

Springer Series in Geomechanics & Geoengineering

Wei Wu *Editor*

Recent Advances in Modeling Landslides and Debris Flows

 Springer

Springer Series in Geomechanics and Geoenvironmental Engineering

Series editors

Wei Wu, Universität für Bodenkultur, Vienna, Austria
e-mail: wei.wu@boku.ac.at

Ronaldo I. Borja, Stanford University, Stanford, USA
e-mail: borja@stanford.edu

About this Series

Geomechanics deals with the application of the principle of mechanics to geomaterials including experimental, analytical and numerical investigations into the mechanical, physical, hydraulic and thermal properties of geomaterials as multiphase media. Geoengineering covers a wide range of engineering disciplines related to geomaterials from traditional to emerging areas.

The objective of the book series is to publish monographs, handbooks, workshop proceedings and textbooks. The book series is intended to cover both the state-of-the-art and the recent developments in geomechanics and geoengineering. Besides researchers, the series provides valuable references for engineering practitioners and graduate students.

More information about this series at <http://www.springer.com/series/8069>

Wei Wu
Editor

Recent Advances in Modeling Landslides and Debris Flows

 Springer

Editor
Wei Wu
Institut für Geotechnik
Universität für Bodenkultur
Vienna
Austria

ISSN 1866-8755 ISSN 1866-8763 (electronic)
ISBN 978-3-319-11052-3 ISBN 978-3-319-11053-0 (eBook)
DOI 10.1007/978-3-319-11053-0

Library of Congress Control Number: 2014948180

Springer Cham Heidelberg New York Dordrecht London

© Springer International Publishing Switzerland 2015

This work is subject to copyright. All rights are reserved by the Publisher, whether the whole or part of the material is concerned, specifically the rights of translation, reprinting, reuse of illustrations, recitation, broadcasting, reproduction on microfilms or in any other physical way, and transmission or information storage and retrieval, electronic adaptation, computer software, or by similar or dissimilar methodology now known or hereafter developed. Exempted from this legal reservation are brief excerpts in connection with reviews or scholarly analysis or material supplied specifically for the purpose of being entered and executed on a computer system, for exclusive use by the purchaser of the work. Duplication of this publication or parts thereof is permitted only under the provisions of the Copyright Law of the Publisher's location, in its current version, and permission for use must always be obtained from Springer. Permissions for use may be obtained through RightsLink at the Copyright Clearance Center. Violations are liable to prosecution under the respective Copyright Law.

The use of general descriptive names, registered names, trademarks, service marks, etc. in this publication does not imply, even in the absence of a specific statement, that such names are exempt from the relevant protective laws and regulations and therefore free for general use.

While the advice and information in this book are believed to be true and accurate at the date of publication, neither the authors nor the editors nor the publisher can accept any legal responsibility for any errors or omissions that may be made. The publisher makes no warranty, express or implied, with respect to the material contained herein.

Printed on acid-free paper

Springer is part of Springer Science+Business Media (www.springer.com)

Preface

The spontaneous nature of landslides and debris flows makes them extremely difficult to predict. Landslides often emerge as loss of stability, where monitoring and observation are of limited informative value. Numerical and physical modelling plays an important role in understanding the mechanisms and may provide reliable prediction and early warning. However, the spatial and temporal multi-scale nature of landslides and debris flows poses a great challenge for the research.

This book presents contributions to the workshop on Recent Developments in the Analysis, Monitoring and Forecast of Landslides and Debris Flow, in Vienna, Austria, September 9, 2013. The contributions cover a broad spectrum of topics from material behavior, physical modelling over numerical simulation to applications and case studies. The workshop is a joint event of three research projects funded by the European Commission within the 7th Framework Program: MUMOLADE (“Multiscale modelling of landslides and debris flows”, Contract Agreement No. 289911 within Marie Curie ITN, www.mumolade.com), REVENUES (“Numerical Analysis of Slopes with Vegetations”, Grant Agreement No.: 324466, within the Industry-Academia Partnerships and Pathways (IAPP), <http://www.revenues-eu.com>) and HYDRODRIL (“Integrated Risk Assessment of Hydrologically-Driven Landslides”, Grant Agreement Number: 295225, within the International Research Staff Exchange Scheme (IRSES), www.boku.ac.at/igt/). This book is characterized by the synergy among the research projects and the many contributions from the young researchers.

The financial support from the European Commission is gratefully acknowledged. I wish to thank Jenny Allén, Enrico Soranzo and Dr. Guofang Xu at our institute for their help.

Wei Wu
Vienna, 16. June 2014

Contents

Material Behavior: Tests and Theories

Some Ideas on Constitutive Modeling of Debris Materials	1
<i>Xiaogang Guo, Wei Wu</i>	

Theoretical and Experimental Investigation into Unsaturated Soil Constitutive Relationship – Preliminary Studies	11
<i>Aleksandra Jakubczyk, Xia Li, Hai-Sui Yu</i>	

Shear Behaviors of Saturated Loess in Naturally Drained Ring-Shear Tests	19
<i>Shun Wang, Wei Wu, Wei Xiang, Qingbing Liu</i>	

Soil Aggregate Stability in Eco-engineering: Comparison of Field and Laboratory Data with an Outlook on a New Modelling Approach	29
<i>Frank Graf, Lothar te Kamp, Michael Auer, Madhu Sudan Acharya, Wei Wu</i>	

Physical Modelling

Centrifuge Model Test of a Bamboo Crib Wall	49
<i>Madhu Sudan Acharya, Wei Wu, Michael Auer, Lothar te Kamp</i>	

Viscous Effects on Granular Mixtures in a Rotating Drum	57
<i>Miguel Angel Cabrera, Devis Gollin, Roland Kaitna, Wei Wu</i>	

Centrifuge Model Tests of Rainfall-Induced Landslides	73
<i>Vasileios Matziaris, Alec M. Marshall, Hai-Sui Yu</i>	

Shallow Tunnelling in Partially Saturated Soil Numerical Analysis of the Contribution of Dewatering to the Enhancement of Face Stability	85
<i>Enrico Soranzo, Roberto Tamagnini, Wei Wu</i>	

Numerical and Analytical Methods

- Modeling the Impact of Granular Flow against an Obstacle** 95
Adel Albaba, Stéphane Lambert, François Nicot, Bruno Chareyre
- One-Dimensional Transient Analysis of Rainfall Infiltration in Unsaturated Volcanic Ash** 107
James Fern, John Eichenberger, Alessio Ferrari, Lyesse Laloui
- Investigations of Gravity-Driven Two-Phase Debris Flows** 119
Xiannan Meng, Yongqi Wang
- Lattice-Boltzmann Method for Geophysical Plastic Flows** 131
Alessandro Leonardi, Falk K. Wittel, Miller Mendoza, Hans J. Herrmann
- Modelling of a Free Surface Flow at Variable Gravity Conditions with SPH** 141
Chong Peng, Miguel Angel Cabrera, Wei Wu
- The Role of Phase Transition in Slope Stability Analyses** 151
Roberto Tamagnini, Wei Wu
- Effect of Vegetation on Stability of Soil Slopes: Numerical Aspect** 163
Wei Wu, Barbara Maria Switala, Madhu Sudan Acharya, Roberto Tamagnini, Michael Auer, Frank Graf, Lothar te Kamp, Wei Xiang

Applications and Case Studies

- Landslide Susceptibility Analysis and Mapping Using Statistical Multivariate Techniques: Pahuatlán, Puebla, Mexico** 179
Franny Giselle Murillo-García, Irasema Alcántara-Ayala
- Application of the Program PCSiWaPro[®] for the Stability Analysis in Earth Dams and Dikes Considering the Influence from Vegetation and Precipitation—A Case Study in China** 195
Jinxing Guo, Issa Hasan, Peter-Wolfgang Graeber
- A Pile-Soil Separation Concerned Model for Laterally Loaded Piles in Layered Soils** 211
Guoping Lei, Huiming Tang, Wei Wu
- The Effect of Overconsolidation and Particle Shape on the CPT End Resistance of Granular Soils** 229
Qingbing Liu, Wei Xiang, Barry Michael Lehane
- Depositional Regularities Analysis of Incompetent Beds in Dam Foundation of Xiaonanhai Reservoir Using Markov Chain** 239
Nie Qiong, Wei Xiang, Du Shuixiang

Physically – Based Critical Rainfall Thresholds for Unsaturated Soil Slopes	253
<i>Diana Salciarini, Claudio Tamagnini</i>	
Numerical Simulations of the Mechanical Contribution of the Plant Roots to Slope Stability	265
<i>Barbara Maria Switala, Wei Wu</i>	
Study on Morphological Characteristics of Coarse Particles in Sliding Zones of Huangtupo Landslide in Three Gorges Reservoir Area, China	275
<i>Jinge Wang, Wei Xiang, Shun Wang</i>	
Study of a Model Slope Reinforced with Jute	289
<i>Aniruddha Sengupta, Saurabh Kumar</i>	
Soil Nailing, the Variable Static System of the Future	307
<i>Michael Auer</i>	
Author Index	323

Some Ideas on Constitutive Modeling of Debris Materials

Xiaogang Guo and Wei Wu

Institut für Geotechnik, Universität für Bodenkultur,
Vienna, Austria
Xiaogang.guo@boku.ac.at

Abstract. Debris flows are dangerous natural hazards in countries with mountainous terrains. Debris materials show complex behavior depending on material composition and loading condition. Constitutive model plays an important role in better understanding the triggering mechanisms and reliable prediction of runout and deposition behavior. This paper reviews some constitutive models for debris materials in particular the Bingham fluid model. The hypoplastic constitutive model with critical state for granular materials is briefly recapitulated. Some ideas are presented to integrate the Bingham model into the hypoplastic constitutive model to account for both slow and fast flow of debris materials. The structure of this combined model and some specific formulations are discussed.

Keywords: debris materials, constitutive equation, hypoplasticity, Bingham fluid, yielding.

1 Introduction

Debris flows are fast moving, liquefied landslides of mixed and unconsolidated water and debris similar to flowing concrete. The complex behavior of debris materials is often described by nonnewtonian and Bingham fluid model. Debris flows can carry material ranging in size from clay to boulders, and may contain a large amount of woody debris such as logs and tree stumps. Both solid and fluid phases have major influence on the motion, distinguishing debris flows from other gravity driven flows such as rock avalanches and sediment-laden water floods [1].

Much research effort has been devoted to modelling the mechanical behaviour of debris materials. In early stage, a viscoplastic model of debris flow was proposed by Johnson [2]. Debris flow was simplified as a single phase continuum with Bingham or Coulomb yield strength. The rheological parameters, such as yield strength, cohesion and Bingham viscosity coefficient, were assumed by field investigation. However, this model cannot describe some important kinetic characteristics of debris flow, e.g. the interaction between particles and water. Takahashi [3] proposed a dilatant fluid model based on Bagnold's research. This model is considered equivalent to the two-phase mixture model in which the

dynamic fluid effects are negligibly small. Some assumptions are applied in the model derivation leading to large discrepancy between the model predictions and field results. The Savage-Hutter avalanche model is a depth averaged model with the following simplifying assumptions: (i) density preserving, (ii) shallowness of the avalanche piles and small topographic curvatures, (iii) Coulomb-type sliding with bed friction angle δ and (iv) Mohr-Coulomb behaviour in the interior with the friction angle $\varphi \geq \delta$ and an ad-hoc assumption reducing the number of Mohr's circles in three dimensional stress states to one [4]. A constitutive model capable of describing the salient features of geophysical flows across three-dimensional terrain is still lacking because conceptual and computational problems have thwarted efforts to combine the influences of Coulomb friction, pore fluid stresses, bed topography, and flow inertia in a satisfactory manner. Iverson and Denlinger [5] suggested a Coulomb mixture model applicable to diverse geophysical flows, from dry granular avalanches to liquefied slurry floods. Use of a single model to describe the material behavior in different flow regimes helps clarify the physical basis of similarities and differences among the events. This model is a generalization of a previous mixture model of Iverson.

A perusal of the relevant models for debris flows in the past shows that most works focused on the simulation of the flow state rather than the mechanical behavior of debris materials. The hypoplastic model is a relatively new constitutive theory which has been developed to mathematically describe the non-linear and irreversible behavior of geomaterials. As compared to elastoplasticity, it does not a priori distinguish between elastic and plastic deformations. The model can be easily implemented into numerical algorithms. The hypoplastic model is well suitable to describe the complex behavior of debris materials before liquefaction. Because debris flows characteristically originate as solid-like sediment masses, transform at least partly to fluid-like flows, and then transform back to solid-like deposits, reasonable models must simulate an evolution of material behavior without invoking preternatural changes in material properties [1]. In this paper we make use of hypoplasticity combined with rheological model to simulate this evolution of debris material.

2 Integration of Bingham Fluid Model and Hypoplastic Model

2.1 Bingham Fluid Model [6]

In the early rheological descriptions, debris flows were treated as Bingham fluid with the following concepts: 1) the shear stress exhibits a linear dependence on the shear rate; 2) the shear stress is independent of the normal stress; 3) debris material behaves like a one-phase homogeneous material; 4) when the shear stress is below a threshold, Bingham materials behave like rigid or elastic bodies. These concepts can be described by the following equation,

$$\begin{cases} \dot{\gamma} = 0, \tau \leq \tau_c \\ \dot{\gamma} > 0, \tau = \tau_c + \mu\dot{\gamma}, \end{cases} \quad (1)$$

where $\dot{\gamma}$ is shear rate, μ is viscosity, τ and τ_c denote shear stress and yield stress, respectively. The three-dimensional representation of yielding of Bingham fluid model shown above has been summarized by Ancy (2007).

During debris flow the material is subjected to large shear deformation. For developing and evaluating constitutive models the planar simple shear motion is particularly relevant. In the case of simple shear, the stress tensor in a Cartesian frame can be written as follows (see Fig.1),

$$\boldsymbol{\sigma} = \begin{bmatrix} \sigma & \tau & 0 \\ \tau & \sigma & 0 \\ 0 & 0 & \sigma \end{bmatrix}, \quad (2)$$

The three stress invariants can be readily obtained, $I_1 = 3\sigma$, $I_2 = \tau^2$ and $I_3 = 0$.

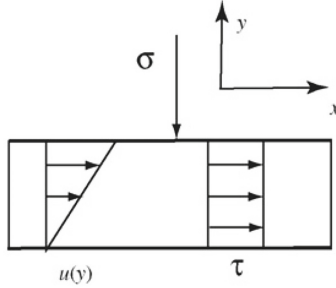


Fig. 1. Simple shear experiment [6]

According to the experimental observations, if the shear stress exceeds a critical value, the material yields. The yielding condition can be described by a scalar function of the stress-tensor invariant $f(I_1, I_2, I_3)$, frequently as a function of I_2 . So the yield surface can be expressed as

$$f(I_1, I_2, I_3) = 0, \quad (3)$$

where f is called the plastic rule.

As shown in equation (1), the yield condition of Bingham fluid model is $\tau = \tau_c$. So the yield function of Bingham fluid model can be expressed as

$$f(I_2) = \sqrt{I_2} - \tau_c. \quad (4)$$

It is easy to show that the above function is the von Mises criterion in which the yield stress is a constant. Ancy (2007) summarized the derivation of the constitutive equation in tensorial form for a Bingham fluid. For debris flows it is important to know what happens beyond yielding. To this end, we assume that the following two conditions remain valid in the regime beyond yielding.

(1) Coaxiality principle: the principal directions of the extra-stress and strain-rate tensors coincide.

(2) Associate flow rule: the strain-rate tensor is directly proportional to the surplus of stress, i.e. the distance between the point representing the stress state and the yield surface, $\sqrt{I_2} - \tau_c$.

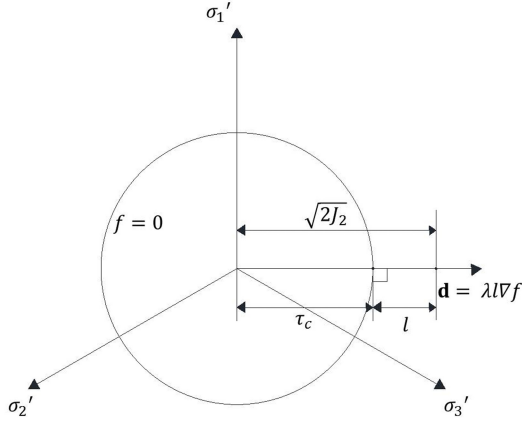


Fig. 2. Yield surface of Bingham fluid model on π -plane

As shown in Fig.2, the shear stress on π -plane is $\tau_\pi = \sqrt{2J_2}$. So the yield surface of Bingham fluid model can be described as

$$f(\boldsymbol{\sigma}) = \sqrt{2J_2} - \tau_c = 0. \quad (5)$$

Here, J_2 is the second deviatoric stress invariant, τ_c is the yield stress.

The surplus of stress is denoted by l . Translated into mathematical terms, the two principles mentioned above lead to: $\mathbf{d} = \lambda l \nabla f$, with λ a proportionality coefficient and $\lambda^{-1} = \mu$, μ is viscosity, \mathbf{d} is the strain rate tensor, ∇f denotes gradient of the yield surface. When $f > 0$, we obtain

$$\mathbf{s} = \mu \left(\frac{\sqrt{2J_2}}{\sqrt{2J_2} - \tau_c} \right) \mathbf{d} \quad (6)$$

in which $\mathbf{s} = \boldsymbol{\sigma} - \text{tr}(\boldsymbol{\sigma})\mathbf{1}/3$ is the stress deviator. Throughout this paper, we use bold letters to denote tensors and matrices. Equation (6) is the constitutive equation in tensorial form for Bingham fluid.

2.2 The Hypoplastic Constitutive Model [7]

In the expression of the Bingham model, debris materials behave like rigid bodies before yielding. This assumption impedes reliable predictions of yielding of

debris materials. We try to use hypoplastic theory to depict the stress-strain relationship of debris materials in this stage. As compared to elastoplasticity, the distinctive feature of hypoplasticity is the continuously non-linear dependence of the material response on the direction of strain rate. Consider the following specific version of hypoplastic constitutive equation (Wu 1992),

$$\dot{\boldsymbol{\sigma}} = c_1(\text{tr}\boldsymbol{\sigma})\dot{\boldsymbol{\epsilon}} + c_2\frac{\text{tr}(\boldsymbol{\sigma}\dot{\boldsymbol{\epsilon}})}{\text{tr}\boldsymbol{\sigma}} + (c_3\frac{\boldsymbol{\sigma}^2}{\text{tr}\boldsymbol{\sigma}} + c_4\frac{\boldsymbol{\sigma}^{*2}}{\text{tr}\boldsymbol{\sigma}}) \|\dot{\boldsymbol{\epsilon}}\|. \quad (7)$$

In the extended model, the variation of the void ratio had been taken into account by introducing the density function, I_e . So the extended model can be expressed as

$$\dot{\boldsymbol{\sigma}} = c_1(\text{tr}\boldsymbol{\sigma})\dot{\boldsymbol{\epsilon}} + c_2\frac{\text{tr}(\boldsymbol{\sigma}\dot{\boldsymbol{\epsilon}})}{\text{tr}\boldsymbol{\sigma}} + (c_3\frac{\boldsymbol{\sigma}^2}{\text{tr}\boldsymbol{\sigma}} + c_4\frac{\boldsymbol{\sigma}^{*2}}{\text{tr}\boldsymbol{\sigma}}) \|\dot{\boldsymbol{\epsilon}}\| I_e, \quad (8)$$

where

$$I_e = (a - 1)D_c + 1, D_c = \frac{e_{crt} - e}{e_{crt} - e_{min}}. \quad (9)$$

In the above equations, a is a material constant, D_c is the modified relative density, e_{min} and e_{crt} are the minimum and the critical void ratio, respectively.

In the framework of hypoplasticity, when stress rate tensor vanishes, strain rate does not vanish and the volume remains unchanged, a material element is said to be at failure. The flow rule and equation of failure surface derived from Equation (8) can be expressed as

$$F(\boldsymbol{\sigma}, e) = \frac{\{\dot{\boldsymbol{\epsilon}}\}}{\|\dot{\boldsymbol{\epsilon}}\|} = [\mathbf{L}]^{-1}\{\mathbf{N}\}I_e \quad (10)$$

and

$$f(\boldsymbol{\sigma}, e) = \{\mathbf{N}\}^T([\mathbf{L}]^T)^{-1}[\mathbf{L}]^{-1}\{\mathbf{N}\}I_e^2 - 1 = 0, \quad (11)$$

respectively. \mathbf{L} and \mathbf{N} is the linear and nonlinear stiffness matrix, which depend on the specific constitutive equation, e.g. Equation (7).

The yield surface and direction of strain rate on π -plane are shown in Fig.3, which are obtained for dense sand.

2.3 Structure of a New Model for Debris Materials

We proceed to develop a new model by combining hypoplastic model with Bingham model. To this end, hypoplasticity will be used to describe debris materials before yielding, and the Bingham model will depict the rapid flow. It means that the new model is composed of a hypoplastic part and a Bingham fluid part in series. The structure of the new model is shown in Fig.4.

Before yielding, the Bingham fluid part behaves like a rigid body, the deformation is only due to the hypoplastic part. After yielding, the stress in the friction element exceeds the yield value and this allows deformation in all elements.

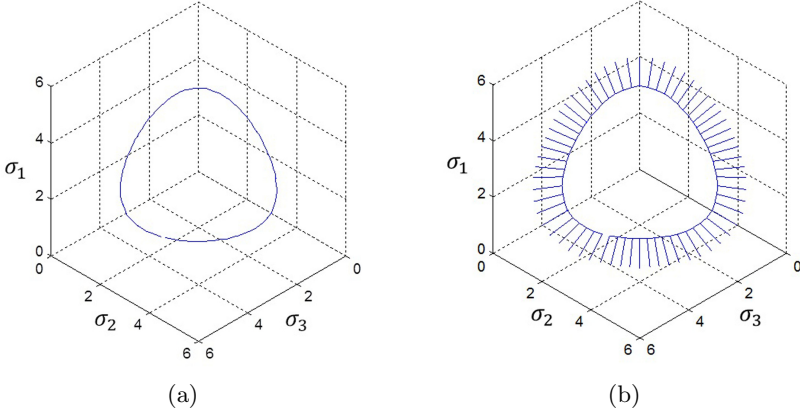


Fig. 3. Failure surface and flow rule of hypoplastic model: (a) failure surface; (b) flow rule

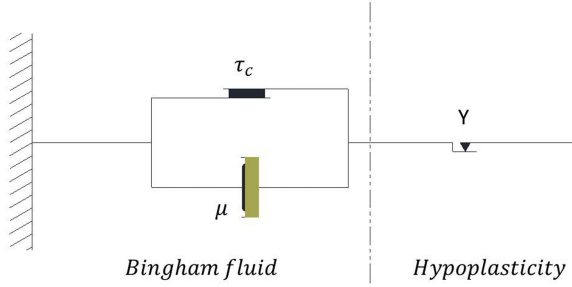


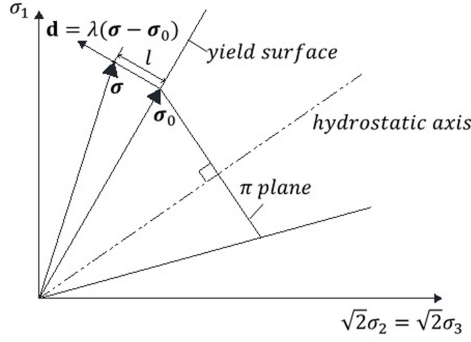
Fig. 4. Schematic diagram of the new model

As mentioned before, the yield stress τ_c is a constant. Equation (5) and (6) are derived under this condition. In hypoplasticity, however, the yield stress is usually a function of normal stress. So, in the new model, the yield condition should be determined by the yield function of the hypoplastic part, and Equation (6) should be modified based on the new yield condition by combining these two models.

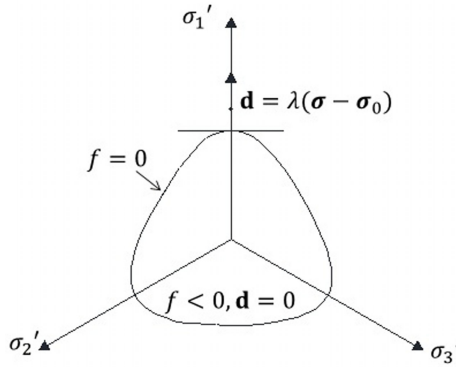
As shown in Fig.5, material yield at the stress state σ_0 and then reach a new stress state σ . We assume that the former mentioned coaxiality principle still holds. The strain rate after yielding has the same direction with the vector $(\sigma - \sigma_0)$ and is proportional to the module of this vector, $\|\sigma - \sigma_0\|$, rather than the distance between the point σ and the yield surface since hypoplastic model has non-associate flow rule. Translated into mathematical terms, the strain rate tensor can be expressed as

$$\mathbf{d} = \lambda(\boldsymbol{\sigma} - \boldsymbol{\sigma}_0), \tag{12}$$

where λ is a proportionality coefficient.



(a)



(b)

Fig. 5. Schematic diagram of strain rate on (a) Rendulic plane and (b) π -plane beyond yielding

Substitution Equation (10) into Equation (12) yields the expression of stress tensor beyond yielding,

$$\boldsymbol{\sigma} = \mu F(\boldsymbol{\sigma}_0, e) \|\dot{\boldsymbol{\epsilon}}\| + \boldsymbol{\sigma}_0, \quad (13)$$

in which μ is viscosity, $\boldsymbol{\sigma}_0$ is yield stress tensor and $\dot{\boldsymbol{\epsilon}}$ substitutes \mathbf{d} to denote strain rate tensor.

The derivative of Equation (13) with respect to time is

$$\dot{\boldsymbol{\sigma}} = \mu F(\boldsymbol{\sigma}_0, e) \|\dot{\boldsymbol{\epsilon}}\|. \quad (14)$$

This is the constitutive equation in tensorial form for Bingham fluid based on the yield condition of the extended hypoplastic model, and can be used to integrate with this model. So the new model for debris materials can be expressed as

$$\begin{aligned} \dot{\sigma} = & (1 - k)[c_1(tr\sigma)\dot{\epsilon} + c_2\frac{tr(\sigma\dot{\epsilon})}{tr\sigma} + (c_3\frac{\sigma^2}{tr\sigma} + c_4\frac{\sigma^{*2}}{tr\sigma}) \|\dot{\epsilon}\| I_e] \\ & + k\mu F(\sigma_0, e) \|\ddot{\epsilon}\|, \end{aligned} \quad (15)$$

where k is the phase changing coefficient and can be expressed as

$$k = [|0.5 - 5R_e| + (0.5 - 5R_e)]^2. \quad (16)$$

R_e is the ratio of mean effective stresses

$$R_e = \frac{tr\sigma}{tr\sigma_i}, \quad (17)$$

where σ and σ_i are the instantaneous effective stress tensor and initial effective stress tensor, respectively. It is assumed that, when R_e is less than 0.1, the effect of the hypoplastic part becomes negligible and the Bingham part dominates the motion progressively.

From the Bingham fluid part, it can be predicted that, when $\|\ddot{\epsilon}\| = 0$ or the angle between vector $F(\sigma_0, e)$ and $\dot{\sigma}$ is greater than 90° , the debris material will cease to flow.

3 Conclusions

Based on the yield criterion and flow rule of hypoplastic model, a new model for debris materials is presented. After yielding, the value of stress rate is assumed proportional to the magnitude of strain acceleration with a proportional coefficient μ , which represents viscosity, and the direction of strain rate is determined by the flow rule of the integrated hypoplastic model. Equation (15) shows the form of the new model, in which the specific version of the hypoplastic part can be determined by matching the experiment results from element tests, e.g. annular shear tests and channel flow tests. Some experimental data of annular shear tests by Savage (1984) and Daniel (1985) can be used for the calibration of the new model. One problem of Equation (15) is that the phase change is controlled artificially. The phase changing coefficient varies from 0 to 1 to trigger the Bingham part beyond materials yield. As a matter of fact, flow of debris materials is subjected to the combined influence of material properties, boundary condition, the path of loading and so on.

Acknowledgement. The authors wish to thank the European Commission for the financial support to the following projects: MUMOLADE (Multiscale Modelling of Landslides and Debris Flows), Contract Agreement No. 289911 within the program Marie Curie ITN, 7th Framework Program.

References

1. Iverson, R.M.: The Physics of Debris Flows. *Reviews of Geophysics* 35, 245–296 (1997)
2. Johnson, A.M.: *Physical processes in geology*. Freeman, Cooper & Company (1970)
3. Takahashi, T.: Debris flow. *Annual Review of Fluid Mechanics* 13, 57–77 (1981)
4. Hutter, K., Wang, Y., Pudasaini, S.P.: The savage-Hutter avalanche model: how far can it be pushed? *Phil. Trans. R. Soc. London* 363(1832), 1507–1528 (2005)
5. Iverson, R.M., Denlinger, R.P.: Flow of variably fluidized granular masses across three-dimensional terrain: 1. coulomb mixture theory. *Journal of Geophysical Research* 106(B1), 537–552 (2001)
6. Ancey, C.: Plasticity and geophysical flows: A review. *Journal of Non-Newtonian Fluid Mechanics* 142, 4–35 (2007)
7. Wu, W., Niemunis, A.: Failure criterion, flow rule and dissipation function derived from hypoplasticity. *Mechanics of Cohesive-frictional Materials* 1, 145–163 (1996)

Theoretical and Experimental Investigation into Unsaturated Soil Constitutive Relationship – Preliminary Studies

Aleksandra Jakubczyk*, Xia Li, and Hai-Sui Yu

Mechanical, Materials and Manufacture Research Division, Faculty of Engineering,
University Park, Nottingham University, United Kingdom
Nottingham, NG7 2RD, UK

aleksandra.jakubczyk@nottingham.ac.uk

Abstract. This article presents the objective of current research to conduct experimental testing on the chosen set of granular materials composed of sand, silt and clay as the reference test materials used in the project, and to develop the advance constitutive model to predict the stress-strain behaviour of materials with diversified properties.

Keywords: unsaturated soil, sand, silt, clay, constitutive model, SWCC.

1 Introduction

An unsaturated soil is defined as a soil which has four phases (i.e., solid, water, air and contractile skin) and the pore-water pressure is negative relative to the pore-air pressure [9]. Its constitutive relationship is complicated by the existence of liquid, air and, moreover, the interface in between. Nature provides a variety of soil types with different particle sizes, shapes and properties. Different types of soil characterise varied capillarity and suction. Coarser soils (sand, silt) have much less capillary action than finer soils (clay). That is why it is important to focus on the material behaviour of the hazard area to investigate its properties. The main goal of current research is to develop an advanced constitutive model together with high quality test data for calibration and validation. In this project, a set of granular materials composed of sand, silt and clay was carefully chosen. It will be used throughout the whole project as reference material to investigate the key scientific issues. Laboratory tests will be performed to study the mechanical and hydrological properties of the reference materials. A constitutive model for unsaturated soil will be developed considering the hysteretic soil-water characteristic curves and incorporating inter-particle bonding. The laboratory dataset will be used to calibrate the constitutive model for unsaturated soil. Research will be used by other fellows from MUMOLADE (Multiscale Modeling of Landslides and Debris Flows) Marie Curie ITN (Initial Training Networks) in their projects. The reference material and collected database will be used in laboratory model tests and centrifuge tests by Early Stage Researchers from WP 4 (work package). The constitutive model will be used for the numerical simulations in WP2 and WP3.

* Corresponding author.

2 Aspects of Constitutive Modelling

Constitutive behaviour of unsaturated soil has been developed within the critical state-based frameworks [1, 2], [25], [27], [30]. They can be categorised in three main classes:

1. Models, where the constitutive stress variables (mechanical and capillary) includes part of the capillary effects. The stress path is complex, but the yield locus is unique, e.g. [10], [22].
2. Models where the stress variables (i.e., net stress and suction) are simpler, but for which a single yield locus of the LC type is insufficient. These models often feature a Suction Increase (SI) and Suction Decrease (SD) yield limit, e.g. [2].
3. Models where the stress variables are not the experimental ones, yet requiring additional yield limits of the SI and SD type, e.g. [16], [29].

A constitutive model for an unsaturated soil was developed to answer the need for a comprehensive stress-strain and water retention framework. The fundamental information required for describing mechanical behaviours of unsaturated soil is delivered from a soil- water characteristic curve (SWCC) [9]. SWCC relates the water content or degree of saturation to the matric suction of a soil. The water content or degree of saturation indicates the volume of water in the soil voids. Experimental investigation shows that there is a relationship between the soil behaviour and the soil water characteristic curve of the soil [9]. It is an important relationship closely associated with the strength, deformation and permeability of unsaturated soil. Many researchers have tried to produce a relationship between the water content or volumetric water content and matrix suction. It presents ability to draw water at various water contents, and suctions, and it is an important relationship closely associated with the strength, deformation and permeability of unsaturated soil. Figure 1 illustrates the curves for soils of different textures.

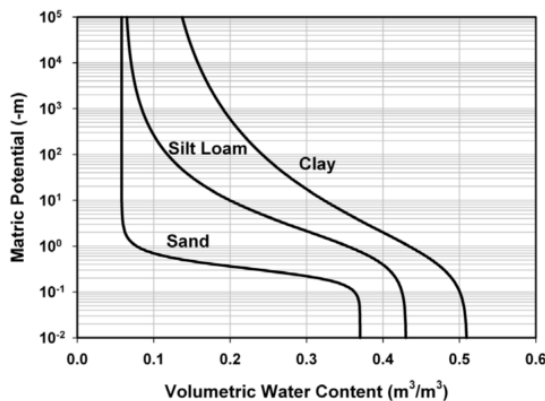


Fig. 1. A typical SWCC (modified from [26])

Vanapalli, Fredlund and Pufahl [28] have reported that the soil water characteristic curve depends on several factors such as soil structure, initial water content, void ratio, type of soil, texture, mineralogy, stress history and method of compaction. According to them, the initial water content profile and the stress history have most influence on the soil structure, which in turn dominates the nature of the soil water characteristic for fine grained soils. Vanapalli, Fredlund, et al. [28] stated that "specimens of a particular soil, in spite of having the same texture and mineralogy, can exhibit different soil water characteristics if they are prepared at different initial moulding water contents and possess different stress histories".

In order to obtain a realistic soil water characteristic curve therefore, the soil aggregation or structure and stress history that exists in the field should be reasonably simulated in the laboratory. Fredlund and Morgenstern [8] proposed that net normal stress and matric suction are the two stress state variables of an unsaturated soil. Data on the SWCC characteristics curve remains limited; that is why, currently it will be a focus on laboratory investigation.

Even though the proposed models integrate many of the essential features of unsaturated soil behaviour, there is a gap for enhancement. Some fundamental issues related to unsaturated soil modelling, such as the selection of stress-strain variables and hydro-mechanical coupling, are still under development. Most of the available models for unsaturated soils are not complete in the sense that some models do not account for the water content variation, e.g. [2], some models cannot describe the hysteresis of SWCCs, e.g. [24], and some models do not provide information on unsaturated soil behaviour under cyclic loading. Furthermore, many models that predict coupled hydro-mechanical behavior, e.g. [29], are restricted to isotropic stress states only. The coupling effects between hydro- and mechanical behaviour have not been thoroughly investigated and experimentally validated.

Nowadays researchers are also keen to establish the macro-micro relations linking up the physical quantities between the two different scales, and to develop macro constitutive relationships in light of the microscopic behaviour [12, 13]. Nottingham Center for Geomechanics (NCG) widely carries out research in the direction to establish the macro-micro relations in granular mechanics [13] in terms of defining the stress and strain tensors, which link the macro-stress tensor with the contact forces, and the macro-strain tensor with the relative displacements at contact. In my work I will try to highlight that aspect.

More experimental data is still needed to complete their validation. The present investigation raised a need for a comprehensive database, which will be further used to develop a current constitutive model for unsaturated soil. It will be the main deliverable from my project.

3 Reference Material

The SWCC curve is highly sensitive to the soil characteristics, such as particle shape, size and gradation. Current constitutive models are not adjusted to describe everything for each kind of soil. It is important to investigate three types of material availa-

ble in nature, to provide a comprehensive database for a constitutive model for unsaturated soil. The reference materials were chosen by taking into account properties, but also on the basis of availability and frequency in research among researchers. They are listed in Table 1.

Table 1. List of reference materials

Type	Reference material
Sand	Leighton Buzzard fraction E
Silt	Loess
Clay	Speswhite kaolin

3.1 Properties

The Leighton Buzzard of Fraction E is classified as fine and uniform uncrushed silica sand. It is deposited around Leighton Buzzard, Bedfordshire in the east of England and is supplied by the David Ball Group, Cambridge, U.K. The index of properties of LB sand is dictated by Cai [5]. All tests were determined in accordance with British Standard 1377 (1990). The grain size ranges from 90 to 150 μ m. D10 and D50 are found to be 125 μ m and 150 μ m, respectively. The specific gravity of the sand is 2.65. The maximum and minimum void ratios are found to be 1.008 and 0.667, respectively. The saturated permeability is in the order of 10⁻⁴ m/s. Behaviour has been well understood and is verified in many geotechnical studies [5], [6]. Cai conducted a consolidated undrained compression triaxial test of dry and saturated sand [6], but more data, particularly for unsaturated state, is required.

Reference material two; silt, Loess silt (from BOKU, Vienna) is used in the research. The Loess is sedimentary yellowish slightly cemented silt that can be found in huge deposits across China and in central Asia. Loess is also present along the banks of the Danube River, in the former inland icecap of the German-Polish plain and in the basin of Paris. Landslides in Loess have been studied by [7] and [32]. These works deal with the analysis of the triggering mechanisms of landslides in the Loess Plateau in China and they discuss the influence of the variation of the water content due to rainfall, water irrigation and engineering activities. The grain size ranges from 0.02-0.05 mm [21]. Specific gravity is influenced by local variations, values range from 2.57 to 2.78 with an average value of 2.66 [4], [11], [17]. Permeability of loess changes from 1 x 10⁻⁵ to 1 x 10⁻³ cm/s, determined after consolidation was complete under a given load [17]. The geo-material characteristic has been investigated from a mechanical point of view by laboratory tests in both saturated and unsaturated conditions [19, 20]. To get all parameters required for development of constitutive model more experiments should be completed (tests in different suctions, permeability test).

Reference material three; clay, Speswhite kaolin it is highly refined kaolin of ultrafine particle size and high brightness from deposits in the South West of England and it is provided by the IMERYS minerals Ltd. The unit weight of the Speswhite kaolin is 17.9 kN/m³, according to Take & Bolton [23]. The grain size range is smaller

than 2 μm , specific gravity 2.6. This material is investigated in detail by many researchers. Experimental investigation on the coefficient of permeability of Speswhite kaolin was conducted by Al-Tabbaa & Wood [3]. Take & Bolton [23] derived the effective shear stress parameters for the Speswhite kaolin. Typical SWCC is presented together with the variation of the maximum elastic modulus (E_{max}) and maximum shear modulus (G_{max}) with respect to soil suction (data from Mendoza et al, [14]; reprinted by Oh & Vanapalli, [15]). Gallipoli et al [10] predicted the soil water characteristic curves (in respect to the degree of saturation) for the Speswhite kaolin, based on the experimental data of Sivakumar [18], at different values of specific gravity. A series of tests on Speswhite kaolin, conducted by Wheeler & Sivakumar [31] under different suction values (0, 100, and 300 kPa) are presented in three planes, $q:\bar{p}$, $v:\bar{p}$ and $v_w:\bar{p}$, where q is the deviator stress, \bar{p} is the mean net stress, v is the specific volume and v_w the specific water volume. Literature provides a broad range of experimental parameters, only one test to check repetitiveness will be carried out.

4 Conclusions

A constitutive model for unsaturated soil is very complex, it depends on many parameters. To answer the need for a comprehensive stress- strain and water retention framework for unsaturated soil more experimental data should be obtained. In the literature database for saturated Leighton Buzzard, fraction E can be found; unsaturated condition will be performed. Loess silt is being studied at the BOKU, permeability will be checked and geotechnical parameters validated. Clay (Speswhite) is very well investigated by researchers, only a few tests will be performed to compare results.

Experimental data- base of reference material will be collected using Unsaturated Triaxial Testing of Soil (UNSAT). It is an extension to traditional triaxial testing in those soils from above the water table. It may be tested under conditions approaching the in-situ stress state and degree of saturation or partial saturation.

Collected laboratory database will be further used by other fellows from MUMOLADE ITN to establish macro-micro relationship and will be available for numerical modelling of slopes and debris flows. Laboratory input is needed to understand particle behaviour to propose improvement in a constitutive model. Applicability of current constitutive modelling will be carried out. Constitutive Model with particle-scale inputs will be developed in my research.

References

1. Alonso, E., Gens, A., Hight, D.: Special problem soils. General report. In: Proc. 9th European Conf. on Soil Mechanics and Foundation Engineering, Dublin, vol. 3, pp. 1087–1146 (1987)
2. Alonso, E.E., Gens, A., Josa, A.: A constitutive model for partially saturated soils. *Geotechnique* 40, 405–430 (1990)
3. Al-Tabbaa, A., Wood, D.M.: Some measurements of the permeability of kaolin. *Geotechnique* 37(4), 499–514 (1987)

4. Bandyopadhyay, S.: Geotechnical Evaluation of Loessial Soils in Kansas. Transportation Research Record 945, Washington D.C. Journal of the Transportation Research Board, 29–36 (1983)
5. Cai, Z.Y.: A comprehensive study of state-dependent dilatancy and its application in shear band formation analysis. PhD thesis, The Hong Kong University of Science Technology (2001)
6. Cai, Y.: An experimental study of non-coaxial soil behaviour using hollow cylinder testing. PhD thesis, The University of Nottingham (2010)
7. Derbyshire, E.: Geological hazards in loess terrain, with particular reference to the loess regions of China. *Earth-Science Reviews* 54, 231–260 (2001)
8. Fredlund, D., Morgenstern, N.: Stress state variables for unsaturated soils. *Journal of the Geotechnical Engineering Division* 103, 447–466 (1977)
9. Fredlund, D., Rahardjo, H.: Soil mechanics for unsaturated soils. John Wiley & Sons, New York (1993)
10. Gallipoli, D., Wheeler, S.J., Karstunen, M.: Modelling the variation of degree of saturation in a deformable unsaturated soil. *Geotechnique* 53(1), 105–112 (2003)
11. Gibbs, H.J., Holland, W.Y.: Petrographic and Engineering Properties of Loess. Engineer Monograph No. 28, p. 37. U.S. Bureau of Reclamation, Denver (1960)
12. Li, X.S.: Effective stress in unsaturated soil: a microstructural analysis. *Géotechnique* 53(2), 273–277 (2003)
13. Li, X., Yu, H.S.: Macro-micro relations in granular mechanics. *International Journal of Solids and Structures* 46, 4331–4341 (2009)
14. Mendoza, C.E., Colmenares, J.E., Merchán, V.E.: Stiffness of unsaturated compacted clayey soils at very small strains. In: Proc. Int. Symp. on Advanced Experimental Unsaturated Soil Mechanics, Trento, Italy, June 27–29, pp. 199–204 (2005)
15. Oh, W.T., Vanapalli, S.K.: Relationship between Poisson’s ratio and soil suction for unsaturated soils. In: Jotisanakasa, A., Sawangsuriya, A., Soralump, S., et al. (eds.) *Unsaturated Soils: Theory and Practise 2011*, pp. 239–245. Kasetsart University, Thailand (2011)
16. Sheng, D., Sloan, S.W., Gens, A.: A constitutive model for unsaturated soils: thermomechanical and computational aspects. *Computational Mechanics* 33, 453–465 (2004)
17. Sheeler, J.B.: Summarization and Comparison of Engineering Properties of Loess in the United States. In: Conference on Loess: Design and Construction. Highway Research Record 212, pp. 1–9. Highway Research Board, Washington, DC (1968)
18. Sivakumar, V.: A critical state framework for unsaturated soil. PhD thesis, University of Sheffield, UK (1993)
19. Soranzo, E., Wu, W.: Experimental and Numerical Investigation on Shallow Tunnelling in Unsaturated Soils. In: EURO:TUN 2013 3rd International Conference on Computational Methods in Tunnelling and Subsurface Engineering. Ruhr University, Bochum (2013)
20. Soranzo, E.: Standsicherheit seichter Tunnel in teilgesättigtem Boden mittels der geotechnischen Zentrifuge und der numerischen Methoden. *Mitteilungsblatt des Fördervereins der Freunde des Instituts für Geotechnik*, Ausgabe 7 (2012)
21. Swineford, A., Frye, J.C.: Petrography of the Peoria Loess in Kansas. *Journal of Geology* 59(4), 306–322 (1951)
22. Tamagnini, R.: An extended cam-clay model for unsaturated soils with hydraulic hysteresis. *Geotechnique* 54(3), 223–228 (2004)
23. Take, W.A., Bolton, M.D.: Seasonal ratcheting and softening in clay slopes, leading to first-time failure. *Géotechnique* 61(9), 757–769 (2011)

24. Thu, T.M., Rahardjo, H., Leong, E.C.: Elastoplastic model for unsaturated soil with incorporation of the soil-water characteristic curve. *Canadian Geotechnical Journal* 44, 67–77 (2007a)
25. Toll, D.G.: A framework for unsaturated soil behavior. *Géotechnique* 40(1), 31–44 (1990)
26. Tuller, M., Or, D.: Water Retention and Characteristic Curve. In: Hillel, D. (ed.) *Encyclopedia of Soils in the Environment*, pp. 278–289. Elsevier Ltd., Oxford (2004)
27. Vaunat, J., Romero, E., Jommi, C.: An elastoplastic hydromechanical model for unsaturated soils. In: Tarantino, A., Mancuso, C. (eds.) *Experimental Evidence & Theoretical Approaches in Unsaturated Soils*, pp. 121–138. Balkema, Rotterdam (2000)
28. Vanapalli, S.K., Fredlund, D.G., Pufahl, D.E.: The influence of soil structure and stress history on the soil-water characteristic of a compacted till. *Geotechnique* 49(2), 143–159 (1999)
29. Wheeler, S.J., Sharma, R.S., Buisson, M.S.R.: Coupling of hydraulic hysteresis and stress–strain behaviour in unsaturated soils. *Géotechnique* 53, 41–54 (2003)
30. Wheeler, S.J., Sivakumar, V.: An elasto-plastic critical state framework for unsaturated soil. *Géotechnique* 45(1), 35–53 (1995)
31. Wheeler, S.J., Sivakumar, V.: Influence of compaction procedure on the mechanical behaviour of an unsaturated compacted clay. Part 2: shearing and constitutive modelling. *Geotechnique* 50(4), 369–376 (2000)
32. Zhang, M., Liu, J.: Controlling factors of loess landslides in western China. *Environmental Earth Sciences* 59, 1671–1680 (2010)

Shear Behaviors of Saturated Loess in Naturally Drained Ring-Shear Tests

Shun Wang¹, Wei Wu¹, Wei Xiang², and Qingbing Liu²

¹ Institut für Geotechnik, Universität für Bodenkultur,
Vienna, Austria

{shun.wang, wei.wu}@boku.ac.at

² Three Gorges Research Center for Geo-hazard, Ministry of Education,
China University of Geosciences, Wuhan, China

{Xiang.wei, liu.QB}@cug.edu.cn

Abstract. A series of ring-shear tests was conducted on saturated loess to investigate the effects of shear rates and normal stress levels on the shear behaviors. The test results revealed that the effect of shear rate on shear strength of loess is strongly dependent on the normal stress levels. The peak friction coefficient of the samples is positively dependent on the shear rate when relatively low normal stress was imposed, whereas shear rate do not significantly affect the peak or residual friction coefficient for samples under high normal stress levels. But on the contrary, the residual shear strength of samples with pre-existing failure surface increase slightly with increased shear rate under high normal stress level while kept constant under low normal stress level. Excess pore pressure was estimated to have built up within the shear zone and then can lead to a reduction in the shear strength after failure occur and the degree of reduction in post-failure shear strength was evaluated by the brittleness index.

Keywords: shear behavior, loess slope, ring-shear test, localized liquefaction.

1 Introduction

The Chinese second west-east gas pipeline project, which starts from Xinjiang in the west and reaches Shanghai in the east, passes through the 279km long Loess Plateau where loess gullies and loess slopes are the most common landforms [1]. The slope disasters, such as landslides and debris flows occur frequently in loess regions due to changes in triggering factors such as rainfall [2], climate [3], earthquakes [4] or human activities. For instance, 7 large-scale loess landslides have been determined in the Luiliang Mountain where the gas pipeline crosses. Furthermore, the existence of failure-prone slopes along the pipeline is a potential threat to the gas pipeline. Therefore, a deep understanding of the shear behaviors of loess is important.

In the survey of the project, a steep loess slope with local failures has been determined. To clarify the potential failure forms of this slope, we took samples from the slope area and investigated their shear behaviors by means of ring shear tests.

According to the field survey, infiltration condition of this slope is well, therefore, ring-shear tests were conducted in naturally drained condition to mimic the naturally drainage of loess slopes. These tests were performed at various normal stress levels and shear rates to examine possible effects on shear strength and localized liquefaction characteristics.

2 Materials and Test Program

2.1 Materials

Three samples from different parts of the selected slope were collected for physical properties and grain size distribution tests. Table 1 shows index properties of the samples. The physical properties listed in Table 1 are obtained following the procedures of Chinese Soil Testing Specification (SL237-1999). The grain size distributions of three samples were almost the same and approximately consisted of 85% silt, 7% sand, and 8% clay fraction by weight, respectively. Note that particles with diameter greater than 3mm were removed from the loess samples due to the size limitation of the shear box.

Table 1. Physical properties of loess samples

Properties	Water content	Natural density	Liquid limit	Plastic limit	Void ratio
	$\omega/\%$	$\gamma/(\text{g}\cdot\text{cm}^{-3})$	$W_L/\%$	$W_p/\%$	
Value range	2.70~6.10	1.41~1.50	26.1~26.5	17.1~18.2	0.90~0.94

2.2 Test Program

The ring-shear test program involved 12 specimens is shown in Table 2.

Table 2. Ring-shear test program of loess samples

Shear rate mm/min	Normal stress level /kpa			Shearing method
	100	300	600	
0.1-1.0-5.0-10.0	RS_1	RS_5	RS_9	Reversal shearing
1.0	RS_2	RS_6	RS_10	Single stage shearing
5.0	RS_3	RS_7	RS_11	Single stage shearing
10.0	RS_4	RS_8	RS_12	Single stage shearing

All specimens were prepared and saturated using the same method as Wang, Sassa [5]. For specimen named RS_1(5,9), reversal shearing test was conducted, that is, after shearing test at the previous stage of shear rate, the specimen was consolidated to stable condition and then sheared again at the next stage of shear rate. Each consolidation duration is approximate 6 hours. For other specimens, shearing tests

were conducted in corresponding conditions using single stage shearing [6]. All the specimens were sheared to steady state in which the shear residence kept constant [7]. Tests were terminated when the shear displacement exceeded approximate 1000mm, at which time the shear residences were still changing slightly with progress of shearing for some specimens.

3 Results

The test results are summarized in Table 3. The variation of shear stress and sample height reduction with shear displacement at the shear rate of 0.1mm/min is shown in Figure 1, which is taken as a typical example to illustrate the test results.

Table 3. Summary of drained ring-shear tests

Specimen number	Shearing condition		Shearing state value				
	Shear rate	Normal stress	τ_p	τ_m	τ_r	L_d	H_d
RS_1	0.1-10.0	100	77.5	62.77	71.5	2127	0.52
RS_2	1	100	70.3	56.8	62.6	606	0.59
RS_3	5	100	77.5	57.9	62.7	837	0.74
RS_4	10	100	91.3	59.1	64.6	1318	0.59
RS_5	0.1-10.0	300	194.8	177.5	178.3	3200	0.74
RS_6	1	300	180.4	164.6	177	885	1.36
RS_7	5	300	192.4	169.6	185.9	887	1.23
RS_8	10	300	181.2	165.7	189.9	1165	1.35
RS_9	0.1-10.0	600	373.8	332.1	348.4	2500	0.8
RS_10	1	600	383.9	348.8	378.9	670	1.94
RS_11	5	600	385.8	354.5	355.5	976	1.52
RS_12	10	600	358.7	325.1	366.1	1001	1.94

Note: τ_p =drained peak shear strength; τ_m =the minimum shear strength after failure; τ_r =residual strength; and L_d , H_d = shear displacement and height reduction of specimen when the shear was stopped, respectively; Stress unit: kPa. Speed unit: mm/min Length unit: mm; For specimen of RS_1/5/9, reversal shearing were conducted using different shear rates, which are 0.1mm/min, 1.0mm/min, 5.0mm/min and 10.0mm/min, respectively, and shearing state values of specimen RS_1/5/9 in this table are the values after the first time of shearing.

As shown in Fig.1, after the shear stress, taking specimen RS_9 for example, was increased to peak (point A, 373.8kPa), shear failure occurred. The post failure process is consisted of two parts, a strain softening phase of fast decrease in shear stress and a strain-hardening phase of gentle increase in shear stress [5], that is, the shear strength of specimen suffered a certain amount of reduction after the shear failure occurred and attained the lowest value (point B,332.1kPa), and then rose slowly to the steady state (point C, 348.4kPa). The other specimens have shown the same

characteristic but with some differences. Usually, specimens under higher normal stress underwent much more amount of reduction and recovery in shear strength after failure. That means the post-failure process curve from point B to point C changed dramatically when high normal stresses were imposed and changed gently under relatively low normal stress levels.

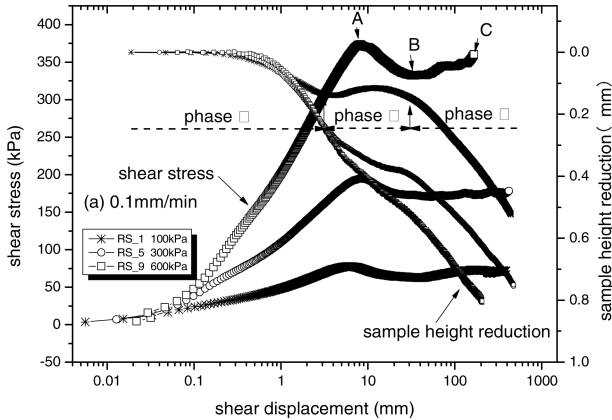


Fig. 1. Shear displacement vs. shear stress and sample height reduction at 0.1mm/min shear rate

The sample height reduction, to some extent, reflected the grain crushing properties in samples. During the entire shearing process, vertical displacement continue to increase. As shown in Fig.1, the height reduction in specimen RS_1 underwent three phases during shearing. According to the study of Wang, Sassa [8], the three phases can be defined as (I) initial negative dilatancy phase, (II) initial positive dilatancy phase (III) negative dilatancy phase due to grain migration, respectively. The positive dilatancy in the second phase was only observed in sample RS_1 which was sheared under the lowest normal stress level.

4 Discussion

4.1 Peak and Residual Shear Strength

The two naturally drained shear strengths considered herein are the peak and residual shear strengths [9]. Fig.2 shows plots of the variation of stress ratio τ / σ' with shear rate under various normal stress levels. It reveals that the peak friction coefficient (τ_p / σ') is relatively greater when the normal stress level is lower, and the peak friction coefficients (τ_p / σ') remain almost invariant for specimens under 300kPa and 600kPa normal stress levels. The peak friction coefficients appear to increase with increasing shear rate when normal stress level is 100kPa, while declined slightly under higher normal stresses [see Fig.2 (a)].

The relation between residual friction coefficient (τ_r/σ') and shear rate at different normal stress levels is shown in Fig.2 (b). As shown in this figure, the curves have slight changes with shear rate of 0.1mm/min, while remain almost flat with increased shear rate. It indicates that the shear rate and normal stress level have not significant effect on the residual friction coefficient (τ_r/σ'). This suggests that the peak failure envelope exhibits a larger stress and shear rate dependency than the residual failure envelope. This is probably because the normal stress and shear rate are the only factors that affect initial particle crushing and orientation in shear zone, whereas shear displacement predominantly affects the particle orientation in the residual strength condition.

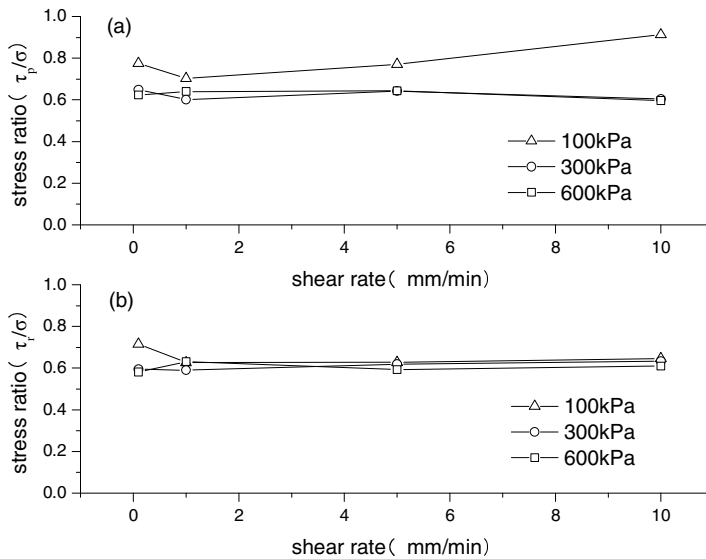


Fig. 2. The variation of stress ratio $\tau_{p(r)}/\sigma'$ with shear rate

4.2 Reversal Shearing Behavior

The reversal shearing test was performed to investigate the shear behaviors of loess sample with a pre-existing shear surface that has attained a residual strength condition. The results are shown in Fig.3.

The stress-strain curves display different characteristics for samples under different normal stress levels in the reversal shearing process. The residual strength remained almost constant under normal stresses of 100kPa and 300kPa, whereas it appeared a fluctuant rising trend with increased shear rate under normal stress of 600kPa. It demonstrates that shear rate do not significantly affect residual strength when the normal stress is relatively low.

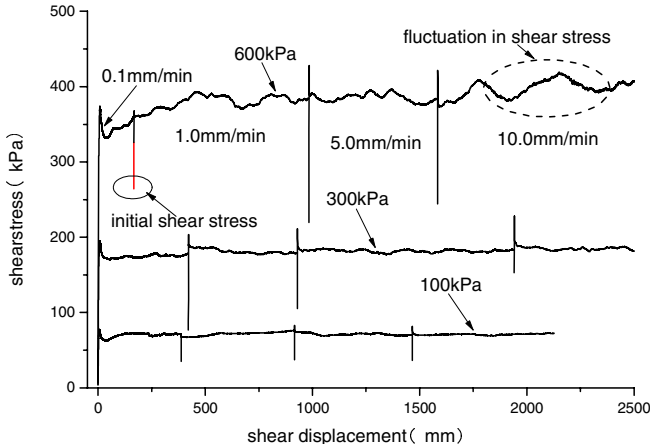


Fig. 3. Relation of shear displacement vs. shear stress for reversal ring shear tests

In the reversal shearing tests, loess samples had undergone previous shearing to generate a continuous shear surface and then consolidated to a stable condition. When restarted shearing at a greater shear rate, the shear stress rose perpendicularly from an initial shear stress to peak value which is larger than the peak strength gained in the previous shearing, and then drop to steady state, which referred to a residual strength condition (see Fig.3). It demonstrates that the shear surface in loess sample had undergone a healing process in the duration of consolidation, but the strength gained due to healing appeared to be lost after very small shear displacement, this is in accordance with the research of Stark, Choi [8], who studied the healing of shear surface on Duck Creek shale in ring shear apparatus with a long duration of consolidation. The mechanism of healing is not fully understood, and it is important to note that no significant generation of bond in the consolidation process due to the less content of clay fraction in loess samples.

4.3 Localized Liquefaction

The concept of localized liquefaction was first proposed by Sassa [10] in the undrained cyclic loading ring shear test. Localized liquefaction is induced by the shrinkage of soil volume due to crushing of grains with a consequence of the generation of excess pore-water pressure in the shear zone and reduction of shear resistance. It is commonly realized that liquefaction failure is mainly caused by cyclic or static undrained loading, however, occurrences of many long run-out landslides have been reported for which no significant source of cyclic loading has ever been identified [11]. In fact, for soils in a natural slope, loading was applied in such a short time that the generated pore-water pressure could not dissipated immediately, and the generation of excess pore-water pressure is inevitable. Thus, generation and dissipation of pore-water pressure occurred simultaneously in the shear zone [5].

Bishop [12] expressed the reduction in undrained strength of a strain-softening material in terms of a brittleness index, which can be used to evaluate the magnitude

of the strength loss and show relate post-failure behavior of a sample. The brittleness index I_B is defined as follows:

$$I_B = (\tau_p - \tau_m) / \tau_p$$

in which τ_p = peak shear strength; and τ_m = minimum shear strength after failure. The occurrence of localized liquefaction results in a reduction of shear strength in soil that may be large or small. Therefore, brittleness index could be adopted as a form of index in liquefaction analysis. A large brittleness index indicates a large reduction in shear strength that could lead to the progressive development of deformation after initiation liquefaction. On the contrary, the initial liquefaction in a material with a low brittleness index may not lead to significant deformations [11].

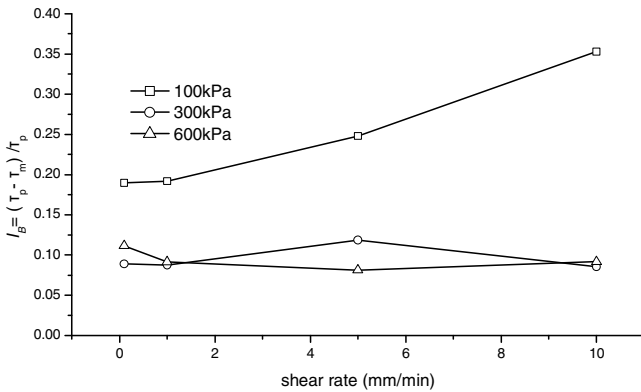


Fig. 4. Brittleness index against shear rate for different normal stress levels

As can be observed in Fig.1, each sample in this naturally drained shearing tests suffered a certain amount of reduction in shear strength after failure occur, and this reduction differed in various test conditions. To analyze the relative value between the peak shear strength and minimum shear strength after failure, the brittleness index against shear rate for various normal stress levels is presented in Fig.4. In all range of shear rate tests, the brittleness index for specimens under normal stress of 100kPa increased with increasing of shear rate. However, the brittleness indexes for specimens under normal stress of 300kPa and 600kPa are located in approximately the same level without an obvious tendency of change with the change of shear rate, probably due to the low initial void ratio. In addition, it can be noted that the cases of specimens under normal stress of 300kPa exhibit a convex and a concave pattern at shear rate of 1.0mm/min and 5.0mm/min, respectively. On the other hand, normal stress level has a negative effect on the brittleness index. This suggests that shallow loess slopes are more likely to suffer a large amount of deformation after initiation liquefaction. It is noted that this kind of localized liquefaction phenomenon has also been identified along the failure surfaces of some landslides triggered by earthquakes or heavy rainfall [13].

5 Conclusion

A series of ring-shear tests was performed on saturated loess taken from a loess slope. The shear behaviors of these loess samples was investigated by shearing them at different normal stress and shear rates in naturally drained condition. Conclusions were drawn as follow.

1. In the single stage shearing tests, the effect of shear rate on friction coefficient of loess is strongly dependent on the normal stress level. The peak friction coefficient of samples under low normal stress levels increase with increase of shear rate, while the shear rate do not significant affeted the peak or residual friction coefficient when relatively high normal stress was imposed.
2. In the reversal shearing tests, the residual shear strength for samples with pre-existing failure surface increase slightly with increased shear rate under high normal stress levels while kept constant under low normal stress levels. In addition, shear residence on the shear surface in loess specimens had undergone a healing after the consolidation, but the grained strength due to healing appears to be lost after very small shear displacement.
3. Excess pore pressure was estimated to have built up within the shear zone and then can lead to a reduction in the shear strength after failure occurred. The reduction of shear strength in post-failure process was evaluated by the brittleness index. The brittleness index increase with the increase of shear rate under relatively low normal stress level while keep constant under high normal stress level.

Acknowledgements. This study was partially supported by the Natural Science Foundation of China (No.41202199).

References

1. Yumin, W.: Loess Landslide in “West to East Gas Pipeline Project”. Oil&Gas Transporlation and Sponage 4, 8–11 (2005)
2. Dahal, R.K., et al.: Comparative analysis of contributing parameters for rainfall-triggered landslides in the Lesser Himalaya of Nepal. *Environmental Geology* 58, 567–586 (2008)
3. Buma, J., Dehn, M.: A method for predicting the impact of climate change on slope stability. *Environmental Geology* 35, 190–196 (1998)
4. Sassa, K., et al.: Dynamic properties of earthquake-induced large-scale rapid landslides within past landslide masses. *Landslides* 2, 125–134 (2005)
5. Wang, G., et al.: Experimental study on the shearing behavior of saturated silty soils based on ring-shear tests. *Journal of Geotechnical and Geoenvironmental Engineering* 133, 319–333 (2007)
6. Dai, F.-C., Wang, S.-J., Lee, C.F.: The drained residual strength of volcanics derived soil sampled on Lantau island, Hong Kong. *Journal of Engineering Geology* 6, 223–229 (1998)
7. Poulos, S.J.: The steady state of deformation. *Journal of the Geotechnical Engineering Division* 107, 553–562 (1981)

8. Wang, F., Sassa, K.: Relationship between grain crushing and excess pore pressure generation by sandy soils in ring-shear tests. *Journal of Natural Disaster Science* 22, 87–96 (2000)
9. Stark, T.D., Choi, H., McCone, S.: Drained shear strength parameters for analysis of landslides. *Journal of Geotechnical and Geoenvironmental Engineering* 131, 575–588 (2005)
10. Sassa, K.: Prediction of earthquake induced landslides. In: Senneset, K. (ed.) *Landslides. Proceedings of the 7th International Symposium on Landslides*, vol. 1, pp. 115–132. Balkema, Rotterdam (1996)
11. Kramer, S.L., Seed, H.B.: Initiation of soil liquefaction under static loading conditions. *Journal of Geotechnical Engineering* 114, 412–430 (1988)
12. Bishop, A.W.: Progressive failure with special reference to the mechanism causing it. In: *Proceedings of the Geotechnical Conference on Shear Strength Properties of Natural Soils and Rocks*, vol. 2, pp. 142–150. Norwegian Geotechnical Institute, Oslo (1976)
13. Fukuoka, H., et al.: Observation of shear zone development in ring-shear apparatus with a transparent shear box. *Landslides* 3, 239–251 (2006)

Soil Aggregate Stability in Eco-engineering: Comparison of Field and Laboratory Data with an Outlook on a New Modelling Approach

Frank Graf¹, Lothar te Kamp², Michael Auer³, Madhu Sudan Acharya⁴, and Wei Wu⁴

¹ WSL Institute for Snow and Avalanche Research SLF, Davos Dorf, Switzerland
graf@slf.ch

² ITASCA Consultants GmbH, Gelsenkirchen, Germany
LteKamp@itasca.de

³ J. Krismer Handels GmbH, Rum, Austria
office@krismer.at

⁴ Institut für Geotechnik, Universität für Bodenkultur,
Vienna, Austria
wei.wu@boku.ac.at

Abstract. Stabilisation effects of plants are developing as a function of time. Within this scope, soil aggregation processes play a decisive role in re-establishing a protective vegetation cover. From this perspective we compared bare and vegetated soil, on the one hand artificially prepared and, on the other hand, derived from a recently landslide affected slope and an adjacent gully with 25 year old eco-engineering measures, respectively.

In both cases, the planted specimens had a significantly higher soil aggregate stability compared to their respective control samples, with the relative increase from control to planted equal for both the natural and artificial samples.

Aspects of the development and succession processes of plants are compared as well as rooting and the degree of mycorrhization. Additionally, soil development and the methodical approach are discussed as well as a new approach to modelling soil aggregate stability in respect of eco-engineering measures for slope stabilisation presented.

Keywords: soil aggregate stability, root length, mycorrhiza, field and laboratory samples, modelling, particle flow code (PFC).

1 Introduction

Eco-engineering combines technical and biological measures in order to re-colonise and re-stabilise slopes affected by heavy erosion or landslide processes [1]. For the engineering part several guidelines and standards exist for structural safety as well as maintenance of the technical constructions [2]. However, in respect of the biological part such information is almost completely missing.

In recent years the need to quantify and monitor the effectiveness of the vegetation has been postulated time and again, in particular with regard to the re-stabilisation of

slopes affected by landslides [3, 4, 5, 6, 7, 8]. Latest concepts in restoration ecology favour an integrated monitoring approach considering different important parameters which is, however, often too time consuming and expensive [9, 10]. Consequently, indicators reflecting multiple aspects are of particular interest in order to overcome the too complex approaches. Besides the fractal dimension of soil particle size distribution and several microbiological parameters, soil aggregate stability has been proposed [11, 12, 13, 14, 15, 16].

The strength of soil aggregates is not only critical to the stability of slopes but plays a key role in ecosystem functioning in general. It mirrors the trait of soil to withstand whatsoever stresses, including superficial soil failure [17, 18] but is additionally a key parameter in ecosystem functioning in general with regard to water, gas, and nutrient fluxes affecting growth and development of all soil organisms [17, 20, 21, 22]. Not by chance, therefore, soil aggregate stability has been suggested as an indicator reflecting multiple aspects allowing extensive information on ecosystem status to be gathered in a relatively short time, in particular in respect of protecting slopes from erosion and shallow mass movements.

With respect to the re-stabilisation of steep slopes affected by superficial soil failure with eco-engineering methods, soil aggregate stability seems preferentially suited. It represents both critical states of plant growth and soil [23, 24]. Furthermore, it seems possible to link this parameter to traditional slope failure models such as the criterion of Mohr-Coulomb [25, 26]. Based on triaxial compression tests with planted and unplanted samples, it was found that soil aggregate stability correlates with the shear strength of the soil, which is a most critical factor of slope stability [27, 28]. This finding implies that soil aggregate stability may reflect the plants' contribution to superficial slope stability and, as a consequence, spurs the development of new approaches for modelling soil stability in general and for slope failure calculations in particular under due consideration of biological effects [29, 30, 31, 32].

Soil aggregate stability is addressed in various ways, differing methodologically and in scale [33, 34, 35, 36]. The variety of approaches, the lack of standardisation, and the application on field as well as laboratory samples complicates the comparison of results from different investigations.

Unlike proposed for other methods assessing soil aggregate stability, we did not focus on small aggregates < 2 mm and, consequently, did not distinguish macro- (> 250 μm) from micro-aggregates (≤ 250 μm) as suggested by [37]. Differently, the starting soil material was composed from a coarse moraine sieved to grain sizes ≤ 10 mm and, in terms of soil aggregate stability, only components > 20 mm were considered, representing the next higher class of grain size from a geotechnical point of view [32], [38]. This approach is particularly advantageous in order to be compatible with conventional methods addressing soil stability, e.g. triaxial compression test, as well as due to biological reasons. In order to test biological effects on aggregate stability in terms of resistance against slaking [34] a certain volume of the specimen is required to fit for appropriate root development and to ensure the vadose zone is representative in view of natural superficial soil conditions, i.e. distribution of macro-, meso-, and micro-pores according to the relevant soil classification [32].

The focus of this article is on the comparison of soil aggregate stability of natural specimens taken from a recent sliding area with samples artificially prepared and maintained in the laboratory using the pure soil material from the same location. A main goal of this analysis was to determine whether soil aggregate stability, naturally increased along with soil and vegetation development over years in a landslide area, is correlated with artificially planted samples developing within months under laboratory conditions. The results are discussed under consideration of methodological aspects, natural soil and plant development including succession processes as well as in view of eco-engineering measures for slope stabilisation. Furthermore, a new approach to modelling superficial soil failure based on a concept of soil aggregate stability and plant development is presented.

2 Material and Methods

2.1 Investigation Area, Soil Material, and Vegetation

The soil material for preparing the laboratory samples was taken from the moraine of the subalpine landslide area "Hexenrübi" (Dallenwil-Wirzweli, Central Switzerland) in 2005. The natural samples, serving as non-planted control, originated from this area, too. In the same year the natural samples representing the planted stage were collected in the adjacent gully "Schwandrübi" which was stabilised with combined technical and biological measures in 1982. The eco-engineering measures particularly consisted of gabions, log cribwalls as well as *Salix purpurea* cuttings and plantlets of *Alnus incana* [38]. At the time of soil sampling the vegetation of the Hexenrübi was represented by a few and sparsely distributed pioneer herb and grass species with a coverage of < 3% whereas in the Schwandrübi a well-developed *Alnetum incanae* (Lüdi) with a considerable number of tree, brush, herb and grass species covered 153% [39].

The moraine was analysed physically and chemically as well as geotechnically classified including particle size distribution, liquid limit, and plasticity index [40, 41, 42]. Furthermore, proctor standard compaction tests were conducted [43]. From oven dried material (24 h at 105°C) the fractions ≤ 10 mm were used to prepare the laboratory samples.

2.2 Laboratory Sample Preparation

All samples were prepared with a water content of 6 % in PVC- plastic tubes (diam.: 70 mm; height: 140 mm) aiming for an average dry unit weight of $\sim 15 \text{ kN m}^{-3}$. The planted samples were planted with *Alnus incana* (L.) Moench (White Alder) and inoculated with the mycorrhizal fungus *Melanogaster variegatus* s.l. (Vittad.) Tul. & Tul. Fifteen alder seeds were applied to each sample and reduced to three seedlings after four weeks of growing. Inoculation was performed according to [32]. The samples were maintained in a greenhouse for 20 weeks with 16 h of daylight and a temperature of 17°C (day) and 10°C (night), respectively. Finally, 20 samples each of the control and planted treatment were used for the soil aggregate stability test.

2.3 Field Sample Preparation

According to [38] a steel soil-coring apparatus was used to collect the field samples. Twenty samples of non- planted moraine from "Hexenrübi" (control) and planted soil from the same moraine in "Schwandrübi" (planted) were taken. Following this procedure, each sample was pushed into a plastic tube (diameter: 50 mm; height: 200 mm) placed inside the steel corer. Subsequently, the samples were maintained for 3 to 5 days in a refrigerator at 4°C until further processing continued. Prior to the soil aggregate stability test, the samples were divided into two parts of about 100 mm of which only the parts corresponding to the soil depth 0-10 cm were considered.

2.4 Soil Aggregate Stability Analysis

The determination of the water stability of soil aggregates followed the protocol described in [38] for the field samples and [32] for those artificially produced. This wet-sieving method using a sieve with mesh openings of 20 mm was applied 3-5 days after sampling in the field and after the greenhouse period of 20 weeks with regard to the laboratory samples. Each sample was tested individually and the aggregated portion remaining on the sieve (aggregates > 20 mm) and the passing part (components ≤ 20 mm) were separately oven dried for 24 h at 105 °C. Soil aggregate stability for the laboratory samples was defined as the dry weight ratio between the components above the sieve (aggregates > 20 mm) and the sum of all components.

With respect to the field samples a correction for non-aggregated particles > 20 mm was applied (Equation 1).

$$agg = \frac{m_{20} - m_{stones}}{m_{tot} - m_{stones}} \left[\frac{g}{g} \right] \quad (1)$$

agg	=	soil aggregate stability [g g ⁻¹]
m_{20}	=	dry weight of the soil material remaining on the sieve [g]
m_{stones}	=	dry weight of stones with a diameter > 20 mm [g]
m_{tot}	=	dry weight of the entire soil sample [g]

2.5 Root Length and Mycorrhization Degree

Immediately after the soil aggregate stability test the roots of the samples were carefully cleaned from soil, spread in a water-filled transparent plastic container, and analysed with a flat-bed scanner using the software WinRhizo[®] [44]. Total root length was addressed and the root length per sample volume [cm cm⁻³] calculated. The degree of colonisation by ecto-mycorrhizal fungi (alder roots) was determined under a stereo microscope (Wild M8) applying the gridline intersection method after [45].

With regard to the field samples only alder roots were considered for ecto-mycorrhizal quantification and, therefore, all other roots, particularly those of grasses and herbs (arbuscular mycorrhiza) were not included in the evaluation. A rough estimation of arbuscular mycorrhiza is given by their spore abundance (Equation 2).

Spores were isolated from four samples per plot (control, planted) each of 30 g by centrifugation using a 70%-sucrose gradient [39], [46].

$$abundance = \frac{n_{spores}}{m_{dw\ soil}} \left[\frac{n}{1\ g} \right] \quad (2)$$

with n_{spores} as the number of spores of arbuscular fungi and m_{dwsoil} the dry weight of the soil sample.

2.6 Statistical Analysis

All statistical calculations were performed with the software R 3.0.2 [47]. Differences in soil aggregate stability, rooting, and mycorrhization degree were analysed with robust statistics applying Kruskal-Wallis and pair-wise Wilcoxon rank sum tests considering p-value adjustment for multiple testing in the latter case [48]. In respect of soil aggregate stability additional analysis was conducted with scaled data [49]. Furthermore, mean values and standard deviation, median and median absolute deviation (mad) as well as the Spearman correlation between aggregate stability, rooting, and mycorrhization degree were calculated [50]. In respect of the mycorrhization degree, field samples were not taken into account as only roots of alder were considered but not those of arbuscular mycorrhized grasses and herbs.

3 Results

3.1 Soil Material

The moraine was geotechnically classified as a clayey gravel with sand (GC-CL). The liquid limit was 21.5%, the plasticity index 8.6%, the maximum dry unit weight 21.9 kN m⁻³ at an optimum water content of 7.9%, and the porosity 0.467 m³ m⁻³.

The pH_[CaCl] of the soil material was 7.7 and the organic matter content 0.2 ± 0.1 % by weight. The total cation exchange capacity amounted to 141.17 mval kg⁻¹. The corresponding contributions of the individual ions were: 132.7 mval kg⁻¹ (93.97%) for Ca²⁺, 6.97 mval kg⁻¹ (4.94%) for Mg²⁺, 1.04 mval kg⁻¹ (0.74%) for K⁺, and 0.50 mval kg⁻¹ (0.35%) for Na⁺.

3.2 Location and Dispersion Parameters

With regard to the soil aggregate stability, there was no obvious difference between mean value and median and standard deviation (sd) and median absolute deviation (mad), respectively, except for the control samples of the laboratory where mean and sd were an order of magnitude higher than the corresponding median and mad (Tab. 1).

Table 1. Mean, standard deviation (sd), median, and median absolute value (mad) of soil aggregate stability [0,1] in terms of the four different treatments (field control, field planted, laboratory control, laboratory planted)

Soil aggregate stability	mean	sd	median	mad
field samples control	0.378	0.171	0.385	0.104
field samples planted	0.729	0.192	0.710	0.208
laboratory samples control	0.028	0.039	0.005	0.007
laboratory samples planted	0.374	0.208	0.350	0.245

Mean and sd and median and mad of root length per soil volume from the field control samples, respectively, differed again an order of magnitude. No obvious deviation was observed for the other treatments as far as root length is concerned. The same holds true for the corresponding values of the ecto-mycorrhization degree of *Alnus incana* (Tab. 2)

Table 2. Mean, standard deviation (sd), median, and median absolute value (mad) of root length [cm cm⁻³] and mycorrhization degree [0,1] in terms of the four different treatments (field control, field planted, laboratory control, laboratory planted). *: in the planted field samples only the roots of *Alnus incana* were considered for determining the ecto-mycorrhization degree.

Root length, mycorrhization	mean	sd	median	mad
root: field samples control	0.105	0.214	0.010	0.015
root: field samples planted	1.506	0.666	1.535	0.445
root: lab samples planted	1.482	0.740	1.375	0.927
mycorrhiza: field samples planted *	0.643	0.097	0.605	0.096
mycorrhiza: lab samples planted	0.454	0.224	0.415	0.282

3.3 Correlations and Tests

Correlation between soil aggregate stability and root length per soil volume was generally high but considerably higher in the planted laboratory samples. If control and planted samples of the field are considered together, due to the reason that in the control samples a few roots were observed too, the correlation increases substantially, however, still stays below the coefficient of planted laboratory samples (Tab. 3).

In respect of mycorrhization in the planted laboratory samples, the comparison with soil aggregate stability and root length per soil volume resulted in correlations of 0.88 and 0.89, respectively (Tab. 3). Planted field samples were not considered for this comparison, as the quantification of mycorrhization was restricted to alder roots, which only constituted a certain part of the whole root system in each sample.

Root length per soil volume significantly differed between planted samples of both laboratory and field samples and the control samples of the field (p-values = $3.6 \cdot 10^{-07}$) – no roots were present in the laboratory control samples. However, no such significance was observed between planted samples of the laboratory and the field (Fig. 1).

Table 3. Spearman correlation between soil aggregate stability and root length / mycorrhization as well as between root length and mycorrhization for different sets of samples (all = planted + control)

variables	samples	correlation
aggregate stability x root length	lab samples (planted)	0.87
	field samples (planted)	0.51
	field samples (all)	0.68
aggregate stability x mycorrhization	lab samples (planted)	0.88
root length x mycorrhization	lab samples (planted)	0.89

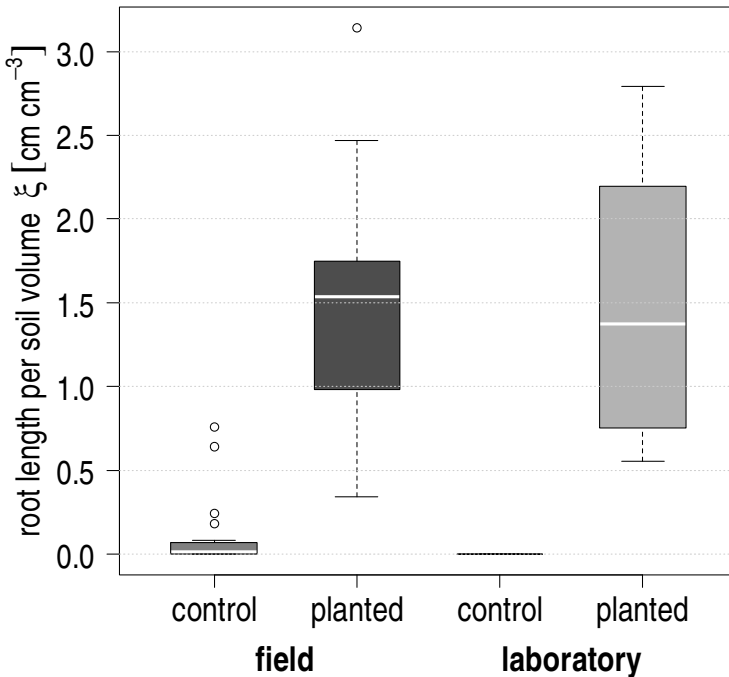


Fig. 1. Boxplots showing the data distribution of root length per soil volume of all samples

The mycorrhization degree of the planted laboratory samples, which consisted exclusively of ecto-mycorrhizal alder roots, was significantly lower (p -value = 0.015) compared to the ecto-mycorrhization degree of alder roots in the planted samples of the field (Fig. 2). In the latter samples arbuscular mycorrhizal roots were present too, however not considered for evaluation of the mycorrhization degree.

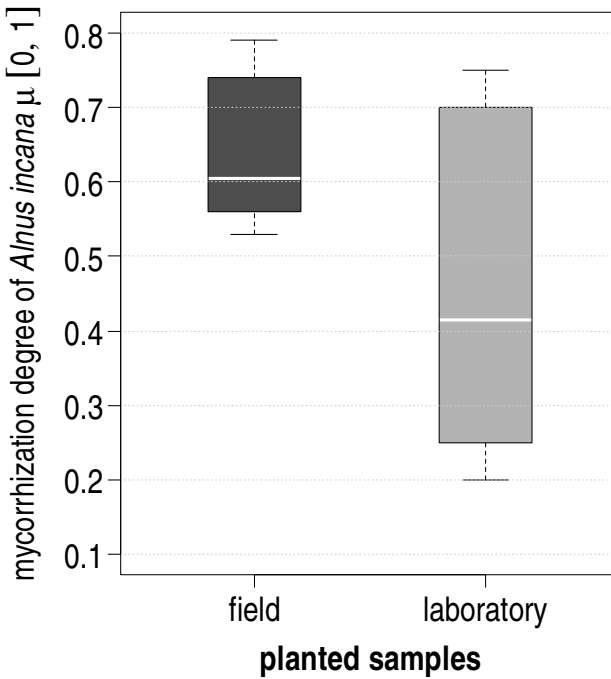


Fig. 2. Boxplots showing the distribution of the mycorrhization degree of *Alnus incana* of the planted samples (field and laboratory)

A significant increase (p-value = 0.013) in spores of arbuscular mycorrhizal fungi was found between the control and the planted field samples. Whereas in the former only $2 (\pm 2)$ spores per Gram dry weight of the soil material were found, $30 (\pm 6)$ spores were counted in the latter. A comparison with regard to the ecto-mycorrhiza in these samples was not meaningful as no ecto-mycorrhizal roots were found in the control samples and, therefore, the degree of ecto-mycorrhization was zero for all specimens (Fig. 3). The mean of the ecto-mycorrhization degree of alder roots in the planted field samples was $0.63 (\pm 0.14)$.

Asymptotic Kruskal-Wallis tests applied to the soil aggregate stability data of both original and scaled data sets indicate significant differences with p-values of $1.15 \cdot 10^{-12}$ ($\chi^2 = 58.63$) and $6.3 \cdot 10^{-11}$ ($\chi^2 = 50.48$), respectively. The significances of the pairwise Wilcoxon comparisons are shown in Table 4.

In respect of the original data, all sample categories differ significantly from each other except the control samples of the field and the planted samples of the laboratory (p-value = 1.0). Differently, the scaled data show significant differences between planted and control samples but not among themselves (p-value_{control} = 0.64, p-value_{planted} = 0.95). In Figure 4 the distribution of original and scaled data is illustrated.

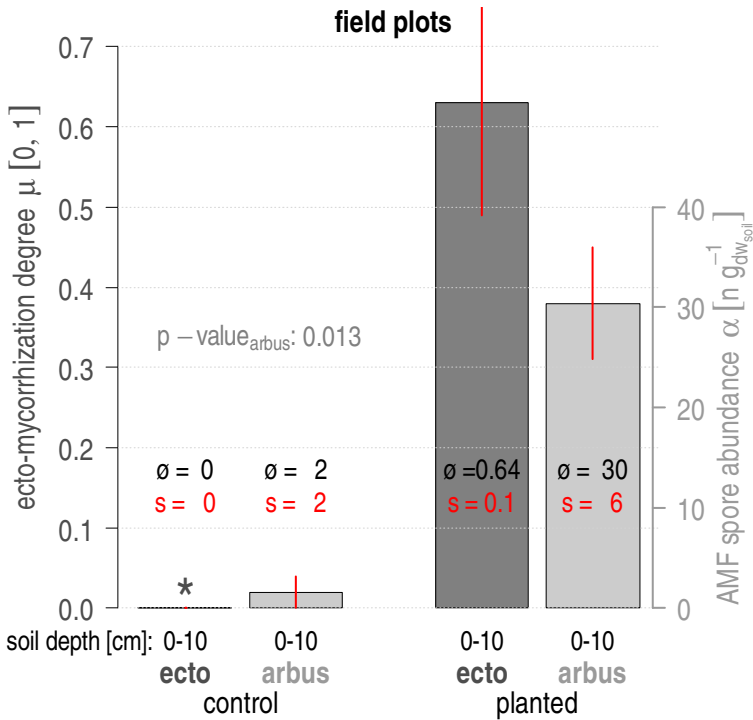


Fig. 3. Barplots with information on distribution, mean ($\bar{\theta}$), and standard deviation (s) of the degree of ecto-mycorrhization (ecto, left y-axis, dark grey bars) and the abundance of spores (arbus, right y-axis, light grey bars) of arbuscular mycorrhizal fungi (AMF) in the control and planted samples of the field. The p-value indicates significant difference of abundance of AMF spores between control and planted samples. *: no ectomycorrhizal plants found.

Table 4. Comparison of soil aggregate stability of the field and laboratory samples (control and planted) applying pairwise Wilcoxon rank sum test with the p-adjustment method of [48] once for original and once for scaled data. Bold numbers indicate non-significant results.

Original data	field (control)	field (planted)	lab (control)
field (planted)	$2.4 \cdot 10^{-05}$		
laboratory (control)	$3.3 \cdot 10^{-07}$	$3.2 \cdot 10^{-07}$	
laboratory (planted)	1.0	$4.9 \cdot 10^{-05}$	$3.2 \cdot 10^{-07}$
Scaled data	field (control)	field (planted)	lab (control)
field (planted)	$2.4 \cdot 10^{-05}$		
laboratory (control)	0.64	$1.2 \cdot 10^{-06}$	
laboratory (planted)	$7.2 \cdot 10^{-06}$	0.95	$3.2 \cdot 10^{-07}$

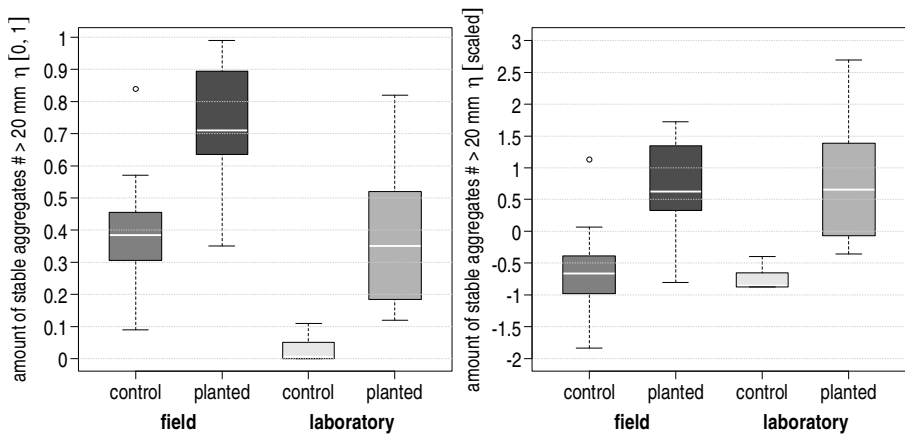


Fig. 4. Boxplots of original (left) and scaled (right) data of soil aggregate stability

4 Discussion

In recent years, the increasing demand for a sound evaluation of the effectiveness of vegetation in respect of their application in eco-engineering in general and slope stabilisation in particular produced different more or less specific approaches and methods [11, 12, 13, 14, 15, 16]. From this development and finding process soil aggregate stability has been emerging as an indicator addressing various aspects in order to quantify biological effects related to restoration and, in particular, in respect of protecting slopes from superficial soil failure [17, 18], [20].

In contrast to other, commonly applied methods addressing soil aggregate stability [23], [33], [36], we did not distinguish macro- ($> 250 \mu\text{m}$) and micro-aggregates ($\leq 250 \mu\text{m}$) of aggregates $< 2 \text{ mm}$ as proposed by [37] but focused on larger scale aggregation processes with components dimensioned $> 20 \text{ mm}$ [32]. The threshold of 20 mm originates from the fact that the grain size of the soil material used for the laboratory samples was limited to $\leq 10 \text{ mm}$ and the next higher fraction in the particle size distribution analysis is $> 20 \text{ mm}$ [41]. In respect of the field samples, the maximum grain size was not known in advance and, therefore, single grains $> 20 \text{ mm}$ (non-aggregated particles) were excluded from the analysis. Consequently, from a geotechnical perspective, all components from laboratory as well as field samples considered as aggregated correspond to the particle size class $> 20 \text{ mm}$.

Compared to other methods, this "large-scale" approach combines several advantages with regard to biological and hydrological processes. Root growth is one of the most important processes in order to increase soil aggregate stability. A positive correlation between the two has been demonstrated for numerous soil types time and again [32], [51, 52] as well as in this study for both laboratory and field derived samples. In order to soundly investigate the effects of roots on soil aggregate stability and, concomitant, on the pore matrix, an adequate size of the specimen allowing for sufficient root amount and development, respectively, is indispensable.

Furthermore, a representative vadose zone is required to reasonably mirror the distribution of the different pore classes. This is not least because the pore water regime, which is directly linked to the pore structure and its stability, plays a key role in triggering superficial landslides. Correspondingly, a certain minimum volume of the samples and maximum size of grains are necessary. Within the presented investigations the concept of triaxial compression tests was followed allowing maximum grain sizes $< \frac{1}{5}$ of the specimen diameter yielding the maximum particle size of 10 mm for both the laboratory and field samples with a diameter of 70 mm and 50 mm, respectively [53, 54]. Due to the correction applied for field samples which omits single grains > 20 mm the requirements were met satisfactorily. In addition, the presented approach for soil aggregate stability analysis allows for comparing results with conventional soil mechanical methods addressing slope stability, e.g. triaxial compression tests [28]. Conclusively, from a methodological point of view, deficiencies due to the different sampling procedure and size of the field and laboratory specimens are hardly distinguishable.

Interestingly, there was no significant difference in root length per soil volume between the planted field and laboratory samples, despite the fact that growth time for alder was up to about 20 years in the former and 20 weeks in the latter (Tab. 2, Fig. 1). Within the 25 year developing period, plant succession processes led the few pioneer plant species of the control plot (*Saxifraga aizoides* L., *Calamagrostis humilis* (Roem. et Schult) O. Schwarz, *Campanula rotundifolia* L., *Tussilago farfara* L.) onto an *Alnetum incanae* (Lüdi) represented by 25 species [39]. Concurrently, soil horizons developed, in particular a humus layer and the soil organic matter content increased tenfold (0.1% vs 1%). None of these developments took place during or was quantifiable after the 20 weeks of growing in the laboratory samples. It may be, therefore, speculated that artificially inoculated alder roots if grown unrivalled and under laboratory conditions develop an equal amount of roots per soil volume in one growth period as is produced by a naturally developed *Alnetum incanae* on a landslide affected slope in its initial phase.

Whereas in the laboratory samples only roots of alder plants were present, the 25 species to be possible for contributing to rooting in the field samples [39] were not distinguished, except for alder. Consequently, there is an uncertainty on the composition of annual and perennial roots within the field samples and, likewise, on the particular contribution of grass, herb, brush, and tree species.

Growth and development of roots are closely related to their associated symbiotic organisms, particularly mycorrhizal fungi, known as essential partners for almost all plants applied in eco-engineering. In general, naturally established partnerships between plant and mycorrhizal fungal species yield an increase in root growth as well as in above ground biomass [55]. This is confirmed in the present study with regard to the mycorrhization degree and the length of alder roots in the laboratory samples resulting in a Spearman correlation of 0.9 (Tab. 3). In this respect no data is available of the field samples as the different roots were not assigned to corresponding plant species, except for White Alder of which, however, the total root length was not addressed separately. Nevertheless, the alder roots of the field samples were significantly stronger mycorrhized than their counterparts of the laboratory samples (Tab. 2,

Fig. 2). This may mainly be attributed to the fact that the alder plants in the field were much older – up to about 20 years – compared to the 20 weeks old laboratory plantlets. Furthermore, the considerably longer development time in the field results in higher production and diversity both of plant and mycorrhizal fungal species. Concurrently, the mycorrhization infection potential (MIP) increases and, additionally, contributes to a higher mycorrhization degree [56]. Further evidence for higher MIP is given by the significant increase in spores of arbuscular mycorrhizal fungi (AMF) within the 25 years of soil and vegetation development (Fig. 3).

The direct and indirect effects of roots as well as their associated mycorrhizal fungi contribute to the stability of aggregates and, therefore, to the strength of the pore matrix [32], [57]. This biological influence on soil aggregate stability is nicely demonstrated in Figure 4 for both the field and laboratory samples, confirmed by the same relative and significant increase from the corresponding control to the planted specimens. The fact that the soil aggregate stability of the field samples is generally higher with their control samples mobilising equal strength as the planted laboratory samples (Tab. 1, 4, Fig. 4) may have different reasons. On the one hand, there was a small amount of roots and, correspondingly, organic matter in the control samples of the field (Fig. 1). On the other hand, the presence of soil micro-organisms, such as bacteria and fungi is beyond debate. For both the contribution to soil aggregation is well known with bacteria particularly contributing to the chemical stabilisation of micro- and fungi to the chemical and mechanical stability of macro-aggregates. Roots stabilise the latter chemically by producing sticky metabolites (polysaccharides) and further reinforce larger scaled soil structures mechanically. Last but not least, soil organic matter contributes by its cementing effects [57]. In respect of the laboratory samples it has to be kept in mind that the soil material was autoclaved, artificially filled into the sample holders and compacted. The material was, therefore, a sterile, single grained mixture and, furthermore, lacking any organic matter. Nevertheless, the scaling of the data clearly demonstrates the equal relative increase in soil aggregate stability from moraine of a recent superficial landslide to a 25 year old *Alnetum incanae*, developed from eco-engineering measures almost exclusively planting alder, and from artificially prepared laboratory samples using the same untreated moraine to identically prepared samples applying alder seeds and the mycorrhizal fungus *Melanogaster variegatus s.l.* after a growth period of 20 weeks (Tab. 1, Fig. 4). This coincidence based on the scaled data set is statistically supported by significant differences between planted and control samples but not among themselves (Tab. 4).

An analysis of covariance (ANCOVA) was applied to compare the effect of the sample location (treatment effect, i.e. field vs laboratory samples) on the response soil aggregate stability (y-variable) while controlling the effect of root length (co-variable, i.e. x-variable). The non-significant interaction of sample location with root length indicates that there is no obvious effect on soil aggregate stability in dependence of sample location, meaning that the slopes of the regression lines are not significantly different. However, the significant intercepts point to substantially different starting levels of aggregate stability depending on the sample location (Tab. 5), strongly supporting the additional stabilisation effects of bacteria, non-mycorrhizal fungi, soil organic matter, and, highly likely, organisms' diversity, too [57, 58].

Table 5. Summary of the linear regression model $\sin^{-1}(\text{aggregate stability})^{1/2} \sim \text{sample}_{\text{loc}} * \log_{10}(\text{root-length})$ showing significant difference in intercepts but not in slopes of field and laboratory samples. Significance codes: *** <math>< 0.001</math>; ** $0.001 \leq$* <math>< 0.05</math>.

Coefficients	Estimate	Std. Error	t value	Pr(> t)	
Intercept (samples _{field})	0.97363	0.04267	22.818	<math>< 2.0 \cdot 10^{-16}</math>	***
Intercept (difference field:lab)	-0.42412	0.05945	-7.135	$2.2 \cdot 10^{-08}$	***
$\log_{10}(\text{root-length}_{\text{field}})$	0.64300	0.16662	3.859	0.000454	***
$\text{samples}_{\text{lab}}:\log_{10}(\text{root-length}_{\text{lab}})$	0.21036	0.23386	0.900	0.374362	

Residual standard error: 0.1647 on 36 DF
Multiple R-squared: 0.7421 Adjusted R-squared: 0.7206
F-statistic: 34.53 on 3 and 36 DF p-value: $1.081 \cdot 10^{-10}$

The undisputed higher diversity in the planted field samples compared to their laboratory counterparts may additionally explain the lower correlation (squared Pearson correlation apparent from the individual linear regression models) between root length and soil aggregate stability as well as the higher variance in the former (Fig. 5).

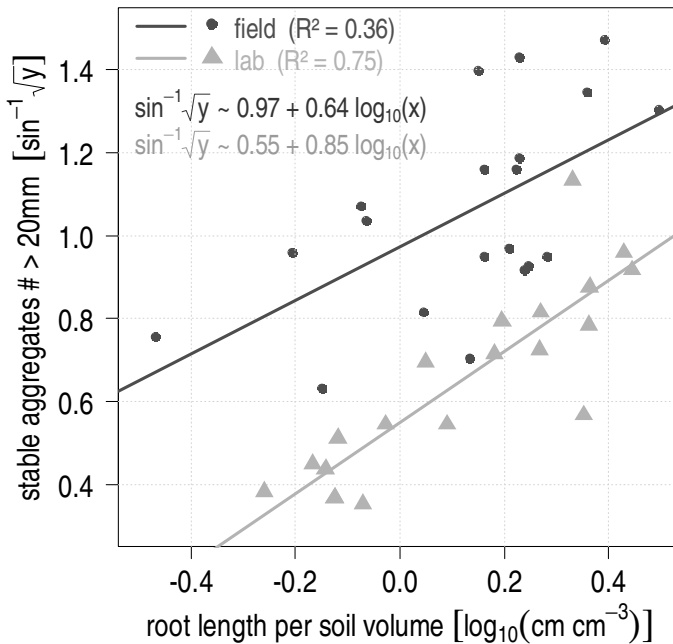


Fig. 5. Linear regression model ($\sin^{-1}(\text{aggregate stability})^{1/2} \sim \text{sample}_{\text{loc}} * \log_{10}(\text{root-length})$) for field (dark grey) and laboratory data (light grey) illustrating almost parallel lines (non-significant slopes), significant difference in intercept as well as the squared Pearson correlation (R^2) and formulas of the individual linear regression models

Nevertheless, root length is a key factor with regard to the strength of soil aggregates in particular and, consequently, in slope stabilisation in general, mirroring the integral effect of the soil rhizosphere including associated mycorrhizal fungi as well as the corresponding community of bacteria and non-mycorrhizal fungi. Associated, soil aggregate stability as addressed in the present article and, for the time being restricted to the corresponding moraine, reflects slope stability reasonably well as it turned out by the comparative study of [32] with shear parameters of triaxial compression tests (angle of internal friction Φ' and cohesion c').

The present comparison of field and laboratory data further suggests the assumption that the underlain "space-for-time-substitution" used for addressing the 25 year succession process in the field is well reflected by the 20 week growth period of the laboratory as related to the relative increase in soil aggregate stability from control to planted samples. Although this is not yet generally applicable on a large scale – local restrictions need to be accepted with reference to soil type, plant associations and eco-engineering measures – it opens an interesting possibility to approach biologically affected slope stability calculation and modelling with relatively short-timed and straightforward laboratory based experiments linked to corresponding field observations. Following this strategy, it will be necessary to develop a new concept integrating in a first minimalistic version the dynamic parameters root growth and soil aggregate stability. Such practice seems adequate as almost all conventional slope stability models finally assign the biological stabilisation part to an additional cohesion coefficient c_r' in the Mohr-Coulomb failure equation as already proposed by [59] in 1984 (Mohr-Coulomb: $\tau_f = c' + \sigma' \tan \Phi'$; Wu: $s_r = c' + \sigma' \tan \Phi' + c_r'$; with s_r as the shear strength τ_f and r for root) regardless of whether root area ratio (RAR), root tensile strength, or root pull-out resistance are considered [29], [31], [60, 61].

5 Outlook

The particle flow code (PFC) of ITASCA [62] is a distinct element code holding the potential to reproduce and model processes of root and soil development considering their manifold interactions in respect of assembling a structured entity starting from loose particles, increasing in stability, yet resilient with regard to biological succession mechanisms. The fact that dynamic motion is supported and interaction of conglomerates differing in size and associated properties as well as allowing for their continuous gradation, makes this software ideally suited to appropriately integrate biological effects into conventional applied slope failure calculations and models. Conclusively, roots can be addressed by their different diameters and tensile strength properties and, therefore, dependent on their spatial-temporal development. The same holds true for soil aggregates in terms of their specific composition of organic and

inorganic components and corresponding binding agents and stabilisation mechanisms, e.g. polysaccharides, glomalin, mechanical reinforcement, and bio-chemical bonds [57].

PFC^{3D}, therefore, looks ready to accept the challenge of modelling soil aggregate stability in dependence of biological (roots, micro-organisms, soil organic matter, ...) and soil mechanical parameters (grain size, pore water pressure, ...) in respect of slope stability. PFC^{3D} allows the creation of groups of particles with individual bonds between and among single parts of all interacting categories (grains, aggregates, root-segments, fungal hyphae, ...) and, therefore, to interlink these ingredients in the course of the simulation as a function of arbitrary conditions. In addition, the possibility to represent such groups as general grain shapes opens the door to soil mechanical methods and concepts, i.e. particle size distribution, direct shear and triaxial compression tests, embankment stability, fracture mechanics. The link to soil mechanics is further supported by the principles of the default contact physics that include among others linear springs and Coulomb sliding as well as a visco-elastic model.

With this given prerequisites, a first simple 2D model of soil reinforcement has been developed, linking biological parameters and processes with the geotechnical contributions to soil and slope stability (Fig. 6). This new approach based on PFC^{3D} will be followed aiming at coupling the joint development of roots and soil aggregation with existing slope failure models.

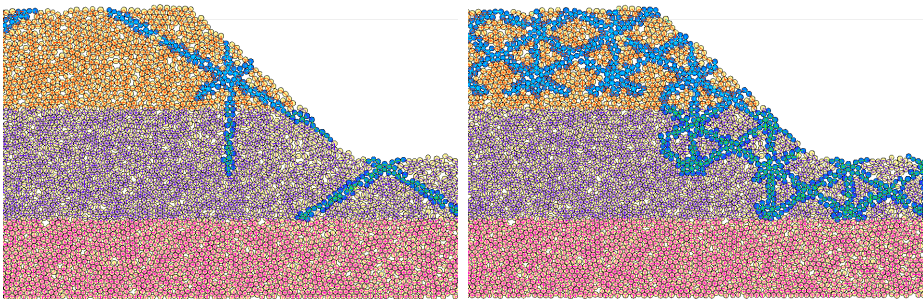


Fig. 6. Simple 2D-PFC models of soil reinforcement with different root densities. Roots are implemented as a group with different strength properties. Blue: roots; orange, purple, red: layers of soil.

Acknowledgments. We are grateful to Anja Bader, Katrin Burri and Martin Frei who provided field and laboratory data, respectively. Parts of the work this article is based upon were supported and financed by the project "SOSTANAH" of the Swiss National Research Programme 68 (grant no 406840_143122) and the EU project "REVENUES" of FP7-PEOPLE-2012-IAPP (Marie Curie Actions – Industry-Academia Partnerships and Pathways: grant no 324466).

References

1. Morgan, R.P.C., Rickson, R.J.: Slope stabilization and erosion control: a bioengineering approach. Spon, London (1995)
2. Czerny, F.: Wildbachsperren. Konstruktionsformen, Belastung, Berechnung. Beton- und Stahlbetonbau 95, 743–749 (2000)
3. Berger, J.J.: A generic framework for evaluating complex restoration and conservation projects. *Environmental Professional* 13, 254–262 (1991)
4. Hobbs, R.J., Norton, D.A.: Towards a conceptual framework for restoration ecology. *Restoration Ecology* 4, 93–110 (1996)
5. Pastorok, R.A., MacDonald, A., Sampson, J.R., Wilber, P., Yozzo, D.J., Titre, J.P.: An ecological decision framework for environmental restoration projects. *Ecological Engineering* 9, 89–107 (1997)
6. Baer, S.G., Kitchen, D.J., Blair, J.M., Rice, C.W.: Changes in ecosystem structure and function along a chronosequence of restored grasslands. *Ecological Applications* 12, 1688–1701 (2002)
7. Anand, M., Desrochers, R.E.: Quantification of restoration success using complex systems concepts and models. *Restoration Ecology* 12, 117–123 (2004)
8. Gretarsdottir, J., Aradottir, A.L., Vandvik, V., Heegaard, E., Birks, H.J.B.: Long-term effects of reclamation treatments on plant succession in Iceland. *Restoration Ecology* 12, 268–278 (2004)
9. SER: The SER International Primer on Ecological Restoration. In: Group, S.f.E.R.I.S.P.W. (ed.) Society for Ecological Restoration International (2004)
<http://www.ser.org/resources/resources-detail-view/ser-international-primer-on-ecological-restoration>
10. Ruiz-Jaen, M.C., Aide, T.M.: Restoration success: How is it being measured? *Restoration Ecology* 13, 569–577 (2005)
11. Arshad, M., Coen, G.: Characterization of soil quality: Physical and chemical criteria. *American Journal of Alternative Agriculture* 7, 25–32 (1992)
12. Alkorta, I., Aizpurua, A., Riga, P., Albizu, I., Amezaga, I., Garbisu, C.: Soil enzyme activities as biological indicators of soil health. *Reviews on Environmental Health* 18, 65–73 (2003)
13. Tian, G.L., Vose, J.M., Coleman, D.C., Geron, C.D., Walker, J.T.: Evaluation of the effectiveness of riparian zone restoration in the southern Appalachians by assessing soil microbial populations. *Applied Soil Ecology* 26, 63–68 (2004)
14. Izquierdo, I., Caravaca, F., Alguacil, M.M., Hernandez, G., Roldan, A.: Use of microbiological indicators for evaluating success in soil restoration after revegetation of a mining area under subtropical conditions. *Applied Soil Ecology* 30, 3–10 (2005)
15. Hernandez-Allica, J., Becerril, J.M., Zarate, O., Garbisu, C.: Assessment of the efficiency of a metal phytoextraction process with biological indicators of soil health. *Plant and Soil* 281, 147–158 (2006)
16. Wang, X.P., Li, X.R., Xiao, H.L., Pan, Y.X.: Evolutionary characteristics of the artificially revegetated shrub ecosystem in the Tengger Desert, northern China. *Ecological Research* 21, 415–424 (2006)
17. Angers, D., Carter, M.: Aggregation and organic matter storage in cool, humid agricultural soils. In: Stewart, M., Stewart, B. (eds.) *Structure and Organic Matter Storage in Agricultural Soils*, pp. 193–211. Lewis Publishers CRC Press Inc., Boca Raton (1996)

18. Diaz-Zorita, M., Perfect, E., Grove, J.H.: Disruptive methods for assessing soil structure. *Soil & Tillage Research* 64, 3–22 (2002)
19. Horn, R., Taubner, H., Wuttke, M., Baumgartl, T.: Soil physical properties related to soil structure. *Soil and Tillage Research* 2, 187–216 (1994)
20. Amezketa, E.: Soil aggregate stability: A review. *Journal of Sustainable Agriculture* 14, 83–151 (1999)
21. Eldridge, D.J., Leys, J.F.: Exploring some relationships between biological soil crusts, soil aggregation and wind erosion. *Journal of Arid Environments* 53, 457–466 (2003)
22. Wick, A.F., Ingram, L.J., Stahl, P.D.: Aggregate and organic matter dynamics in reclaimed soils as indicated by stable carbon isotopes. *Soil Biology & Biochemistry* 41, 201–209 (2009)
23. Barthes, B., Roose, E.: Aggregate stability as an indicator of soil susceptibility to runoff and erosion; validation at several levels. *Catena* 47, 133–149 (2002)
24. Canton, Y., Sole-Benet, A., Asensio, C., Chamizo, S., Puigdefabregas, J.: Aggregate stability in range sandy loam soils. Relationships with runoff and erosion. *Catena* 77, 192–199 (2009)
25. Terzaghi, K., Peck, R.B.: *Soil mechanics in engineering practice*. John Wiley & Sons, New York (1967)
26. Lang, H.J., Huder, J.: *Bodenmechanik und Grundbau* (5. Aufl.), p. 278. Springer, Berlin (1994)
27. Frei, M., Böll, A., Graf, F., Heinimann, H.R., Springman, S.: Quantification of the influence of vegetation on soil stability. In: Lee, C.F., Tham, L.G. (eds.) *Proceedings of the International Conference on Slope Engineering*, Hong Kong, China, December 8-10, pp. 872–877. Department of Civil Engineering, University of Hong Kong (2003)
28. Graf, F., Frei, M., Böll, A.: Effects of vegetation on the angle of internal friction of a moraine. *FOSNOLA* 82, 61–78 (2009)
29. Pollen, N., Simon, A.: Estimating the mechanical effects of riparian vegetation on stream bank stability using a fibre bundle model. *Water Resources Research* 41, W07025 (2005), doi:10.1029/2004WR003801
30. Pollen, N.: Temporal and spatial variability in root reinforcement of streambanks: Accounting for soil shear strength and moisture. *Catena* 69, 197–205 (2007)
31. Schwarz, M., Cohen, D., Or, D.: Spatial characterization of root reinforcement at stand scale: Theory and case study. *Geomorphology* 171-172, 190–200 (2012)
32. Graf, F., Frei, M.: Soil aggregate stability related to soil density, root length, and mycorrhiza using site-specific *Alnus incana* and *Melanogaster variegatus* s.l. *Ecological Engineering* 57, 314–323 (2013)
33. Kemper, W.D., Rosenau, R.C.: Aggregate stability and size distribution. In: Klute, A. (ed.) *Methods of Soil Analysis. Part I, 2nd edn. Physical and mineralogical methods*, pp. 425–442. American Society of Agronomy Inc. Soil Sci. Soc. Am. Inc., Madison (1986)
34. LeBissonnais, Y.: Aggregate stability and assessment of soil crustability and erodibility. I. Theory and methodology. *European Journal of Soil Science* 47, 425–437 (1996)
35. Le Bissonnais, Y., Arrouyas, D.: Stability and assessment of soil crustability and erodibility: II. Application to humic loamy soils with various organic carbon contents. *European Journal of Soil Science* 48, 39–48 (1997)
36. Le Bissonnais, Y., Blavet, D., De Noni, G., Laurent, J.Y., Asseline, J., Chenu, C.: Erodibility of Mediterranean vineyard soils: relevant aggregate stability methods and significant soil variables. *European Journal of Soil Science* 58, 188–195 (2007)
37. Tisdall, J.M., Oades, J.M.: Organic-Matter and Water-Stable Aggregates in Soils. *Journal of Soil Science* 33, 141–163 (1982)

38. Burri, K., Graf, F., Böll, A.: Revegetation measures improve soil aggregate stability: a case study on a landslide area in Central Switzerland. *FOSNOLA* 82, 45–60 (2009)
39. Burri, K.: Boden-Aggregatstabilität als Parameter zur Quantifizierung von Vegetationseffekten auf oberflächennahe Bodenbewegungen. Master's Thesis, ETH, Eidgenössische Technische Hochschule Zürich, Institut für terrestrische Ökosysteme (ITES) (2006), <http://dx.doi.org/10.3929/ethz-a-005326734>
40. ASTM D 2487-00: Practice for classification of soils for engineering purposes (unified classification system). Ann. b. ASTM standards, sect. four: constr., vol. 04(08), pp. 248–259 (2002)
41. ASTM D 422-63: Standard test method for particle size analysis of soils. Ann. b. ASTM standards, sect. four: constr., vol. 04(08), pp. 10–17 (2000)
42. ASTM D 4318-00: Standard test method for liquid limit, plastic limit, and plasticity index of soils. Ann. b. ASTM standards, sect. four: constr., vol. 04(08), pp. 580–593 (2000)
43. ASTM D 698-00a: Standard test method for laboratory compaction characteristics of soil using standard effort (12400 ft-lbf/ft³ (600 kNm/m³)). Ann. b. ASTM standards, sect. four: constr., vol. 04(08), pp. 81–91 (2000)
44. WinRhizo[®]: Régent Instruments Inc., 4040 rue Blain, Quebec, Qc G2B 5C3, Canada (2000), <http://www.regent.qc.ca>
45. Brundrett, M., Bougher, N., Dell, B., Grove, T., Malajczuk, N.: Working with mycorrhizas in forestry and agriculture. ACIAR Monograph 32, p. 380. Australian Centre for International Agricultural Research, Canberra (1996)
46. Sieverding, E.: Vesicular-Arbuscular Mycorrhiza Management in Tropical Agrosystems. Deutsche Gesellschaft für Techn. Zusammenarbeit (GTZ) GmbH, Eschborn (1991)
47. R Development Core Team: R: A language and environment for statistical computing. R Foundation for Statistical Computing, Vienna, Austria (2014), <http://www.R-project.org>, ISBN 3-900051-07-0
48. Holm, S.: A simple sequentially rejective multiple test procedure. *Scandinavian Journal of Statistics* 6, 65–70 (1979)
49. Becker, R.A., Chambers, J.M., Wilks, A.R.: The New S Language. Wadsworth & Brooks/Cole (1988)
50. Stahel, W.A.: Statistische Datenanalyse, 3. Auflage, p. 379. Vieweg Verlag, Braunschweig (2000)
51. Degens, B.P., Sparling, G.P., Abbott, L.K.: The Contribution from Hyphae, Roots and Organic-Carbon Constituents to the Aggregation of a Sandy Loam under Long-Term Clover-Based and Grass Pastures. *European Journal of Soil Science* 45, 459–468 (1994)
52. Gros, R., Monrozier, L.J., Bartoli, F., Chotte, J.L., Faivre, P.: Relationships between soil physico-chemical properties and microbial activity along a restoration chronosequence of alpine grasslands following ski run construction. *Applied Soil Ecology* 27, 7–22 (2004)
53. Arnold, A., Thielen, A., Springman, S.M.: On the stability of active layers in alpine permafrost. In: 11th International Conference and Field Trip on Landslides (ICFL), Trondheim, Norway, September 1–10, pp. 19–25. Taylor & Francis, Netherlands (2005)
54. DIN 18137-2: Baugrund, Untersuchung von Bodenproben - Bestimmung der Scherfestigkeit – Teil 2: Triaxialversuch, p. 48. Beuth Verlag GmbH, Berlin (2011)
55. Smith, S.E., Read, D.J.: Mycorrhizal Symbiosis, p. 787. Academic Press, London (2008)
56. Biondini, M.E., Bonham, C.D., Redente, E.F.: Secondary successional patterns in a sagebrush (*Artemisia tridentata*) community as they relate to soil disturbance and soil biological activity. *Vegetatio* 60, 25–36 (1985)
57. Rillig, M.C., Mummey, D.L.: Mycorrhizas and soil structure. *New Phytologist* 171, 41–53 (2006)

58. Pohl, M., Graf, F., Butler, A., Rixen, C.: The relationship between plant species richness and soil aggregate stability can depend on disturbance. *Plant and Soil* 355, 87–102 (2012)
59. Wu, T.H.: Effect of Vegetation on Slope Stability. Transportation Research Report 965, 37–46 (1984)
60. Bischetti, G.B., Chiaradia, E.A., Simonata, T., Speziali, B., Vitali, B., Vullo, P., Zocco, A.: Root strength and root area ratio of forest species in Lombardy (Northern Italy). *Plant and Soil* 278, 11–22 (2005)
61. Vergani, C., Chiaradia, E.R., Bischetti, G.B.: Variability in the tensile resistance of roots in Alpine forest tree species. *Ecological Engineering* 46, 43–56 (2012)
62. Itasca (2014) PFC^{3D} Particle Flow Code in 3 Dimensions, <http://www.itascacg.com/software/pfc3d> (March 27, 2014)

Centrifuge Model Test of a Bamboo Crib Wall

Madhu Sudan Acharya¹, Wei Wu¹, Michael Auer², and Lothar te Kamp³

¹ Institut für Geotechnik, Universität für Bodenkultur, Vienna, Austria
{madhu_sudan.acharya, wei.wu}@boku.ac.at

² J. Krismer Handels GmbH, Rum, Austria

³ ITASCA Consultants GmbH, Gelsenkirchen, Germany

Abstract. Centrifuge testing is particularly suitable to model geotechnical processes and events because the increase in centrifugal force creates stresses in the model that are equivalent to gravitational force acting on the much larger prototype. The mechanisms of failure and the stresses observed in the model tests are generally the realistic representation of the actual ground movements and accumulation of stresses on prototype. Crib retaining walls made of different materials are used as special form of gravity walls in stabilizing slopes. The centrifuge test results of a model crib retaining wall made of mini bamboo sticks are reported in this paper. The centrifuge model test results are similar to the field test results of concrete crib walls.

Keywords: Centrifuge model, crib retaining wall, bamboo crib wall.

1 Introduction

A geotechnical centrifuge is used to conduct model tests to study geotechnical problems such as the strength, stiffness and bearing capacity of different structures, settlement of embankments, stability of slopes, earth retaining structures etc. Geotechnical materials such as soil and rock have nonlinear mechanical properties that depend on the effective confining stress and stress history. The centrifuge applies an increased "gravitational" acceleration to physical models in order to produce identical self-weight stresses in the model and prototype. This sort of physical model testing allows for a well-controlled and closely monitored real event to investigate the generic response of a geotechnical structure.

Centrifuge testing is particularly suitable to model geotechnical processes and events because the increase in centrifugal force creates stresses in the model that are equivalent to gravitational force acting on the much larger prototype. The mechanisms of failure and the stresses observed in the model tests are generally the realistic representation of ground movements and accumulation of stresses on prototype.

The one to one scaling of stress enhances the similarity of geotechnical models and makes it possible to obtain accurate data which help to solve complex problems such as earthquake-induced liquefaction, soil-structure interaction, analysis of soil slopes etc. Centrifuge model testing provides data to improve our understanding of basic mechanisms of deformation and failure and provides benchmarks useful for

verification of numerical models. Centrifuge tests can also be used to obtain experimental data to verify a design procedure or a computer model.

A crib retaining wall is a structure built up of individual elements to form a series of box-like cells into which infill is placed; the infill acts as an integral part of the structure. A crib cell is formed from headers and stretchers elements. Crib elements may be of concrete, steel or wood. In general, crib walls can be described as a specialized form of gravity-retaining structure using on-site fill material, held within a constructed framework, in order to provide most of the necessary mass to resist overturning by the weight of the slope [5].

Although crib walls are specialized form of a gravity wall, actual failure mechanisms of crib walls are different than other gravity walls. There are different manuals developed for the design and construction of crib walls made of different material based on practical experience and large field tests [1], but there is no generalized method available for designing of crib walls made of different materials and having different geometries.

Conventionally, wooden crib walls were dimensioned based on past experiences. Nowadays, there are several guidelines and design standards for machine finished wooden crib walls available, but only few guidelines are available for the analysis and design of vegetative log crib walls. The limited numbers of available design guidelines are not sufficient for an economic engineering design of wooden crib walls. Analytical methods are generally used to determine the strength of vegetated crib retaining walls based on some assumptions. The crib system is analyzed statically by satisfying the condition of static equilibrium with acceptable level of safety. The crib wall system is checked for internal and external stability using conventional monolithic and silo theories [2]. Due to limitations of available theories, the exact analysis and design of vegetated wooden/bamboo crib wall is rather difficult in static calculation. Therefore, experimental measurements are generally done to verify the static analysis.

In the above context, a centrifuge model test result of a model crib retaining wall (1:20) made of bamboo elements is reported in this paper. This test is mainly carried out to verify the stability analysis and deformation characteristics of a bamboo crib retaining wall.

2 Material and Methods

The tests were performed in the Institute of Geotechnical Engineering at the University of Natural Resources and Life Sciences (BOKU), Vienna. The centrifuge has an effective radius of 1.302 m and a payload of 90.7 kg at up to 200 g. A schematic diagram of the centrifuge is presented in Fig.1.

Basically there are four different configurations for crib construction (see Fig.2). Depending upon the material used and the type of crib elements, crib walls up to a height of 25 meters are possible [2]. In this model, the crib type 2 is used.

Models of crib wall (Fig.3) of dimensions 37x13x10 cm and 37x13x14 cm made from mini bamboos sticks were placed inside a Plexiglas box (Fig.4) having internal dimensions of 42.5x42.5x30 cm and a retaining slope was formed leaving a space about 10 cm in the front.

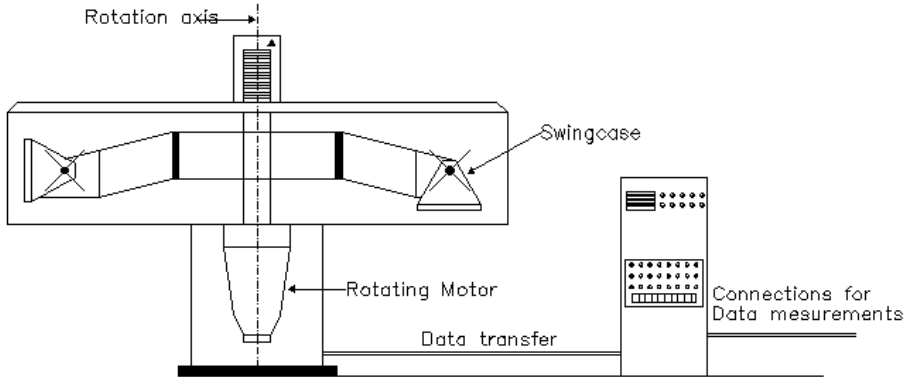


Fig. 1. Schematic diagram of a centrifuge machine

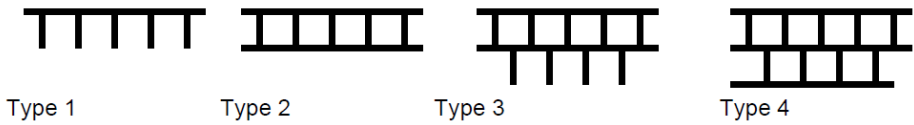


Fig. 2. Different ways of crib construction (ground plan)



Fig. 3. Model bamboo crib wall

The model crib wall tests were all performed at 40-70 times earth's gravity. This means that the 5 mm diameters mini bamboo sticks in model used represents a prototype diameter of 20-35 cm thick bamboos trunk.

The horizontal and vertical displacements were measured with the help of three displacements sensor fixed horizontally and one sensor fixed vertically at the top of the model crib wall (see Fig. 5).



Fig. 4. Placing of model in Plexiglas's box in laboratory at BOKU, June 2006

All together nine tests were carried out with varying model and slope parameters. The variations of model and test parameters are presented in Table 1. Standard medium sand and coarse sand were used as fill material in the testing. Two wall heights variations and three slopes variations were used in the testing. The test model slope was constructed with either compacted or loose filled sand. The compaction in the model was carried out by hand using a steel rod to a density about 90% of the Proctor density. Three different slopes inclinations were used in the tests. For flat slope the slope angle was kept less than 25° , and for steep slope it was between 25° - 35° and for extremely steep slope it was kept more than 35° . The properties of the middle sand and coarse sand used in the test are given in Table 2.



Fig. 5. Measurements arrangements for horizontal and vertical displacement

Table 1. Test parameters for centrifuge test of a bamboo crib wall model

Test No.	Max. Loading	Fill material (Sand)	Compaction	Slope above wall	Model wall height and inclination
0	40 g	Medium	Compacted	Flat slope	Low height/70°
1	70 g	Medium	Compacted	Flat slope	Low height/70°
2	70 g	Medium	Compacted	Steep slope	Low height/70°
3	70 g	Medium	Loose	Extremely Steep	Low height/70°
4	70 g	Medium	Compacted	Extremely Steep	Low height/70°
5	70 g	Medium	Loose	Extremely Steep	High wall /70°
6	70 g	Medium	Compacted	Extremely Steep	High wall /70°
7	70 g	Coarse	Loose	Extremely Steep	High wall /70°
8	70 g	Coarse	Compacted	Flat slope	High wall /70°

Table 2. The properties of medium and coarse sand used in the centrifuge test

Parameters	Medium sand	Coarse sand
Solid density (ρ_s)	2,68	2,64 g/cm ³
Loose density min (ρ_d)	1,39	1,50 g/cm ³
Shake density (ρ_R)	1,79	1,72 g/cm ³
Proctor density (ρ_{Pr})	1,72	1,67 g/cm ³
Proctor moisture content (w_{Pr})	15,3%	8,9 %
Maximum particle size (d_{max})	0,63	2,0 mm
Non uniformity coefficient (U)= d_{60}/d_{10}	2,5	2,0
Coefficient of curvature, $C=(d_{30})^2/(d_{60}*d_{10})$	1,5	1,0
Average particle size (d_{50})	0,4 mm	0,9 mm

3 Results and Discussions

The test results of bamboo crib model (1:20) on centrifuge testing are presented in Fig. 6, which shows the vertical displacements of a bamboo crib wall model placed in a centrifuge testing machine at different loading stages. In most of tests the maximum vertical deformations are attained between 40 g to 50 g. The horizontal displacements at bottom, mid and top of wall are presented in figures, Fig. 7, Fig. 8, and Fig. 9 respectively. In most tests, the maximum horizontal displacements are attained between 10-20 g. In each of these tests, there is a maximum deflection at the middle level followed by bottom and top points. Except in cases of loosely filled slopes, in all other tests no any sign of slope failure was observed during and after the test. Most of the vertical displacement was observed below 20 g of loading.

In most of the tests with moderate slope above the wall, the maximum vertical displacement is about 2 mm which will be 40 mm in prototype wall of 2.60 m high. As the crib model was not fixed on the bottom of box, it may have some movements in

horizontal direction during centrifuge testing. If we assume that the bottom face (toe of wall) did not move outward during the testing, then the actual maximum deformation at the mid of wall will be much less.

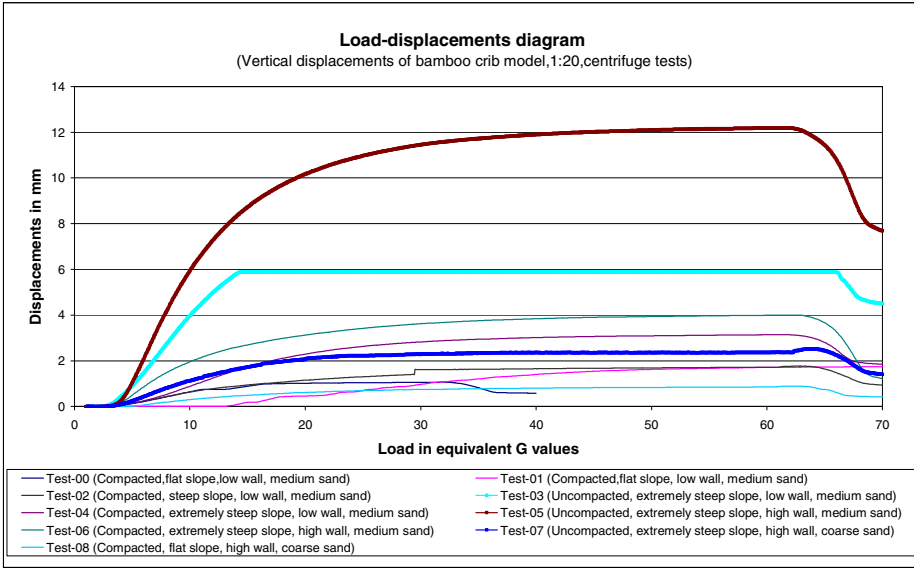


Fig. 6. The load-vertical displacements diagram for a bamboo crib wall model (1:20), centrifuge test results

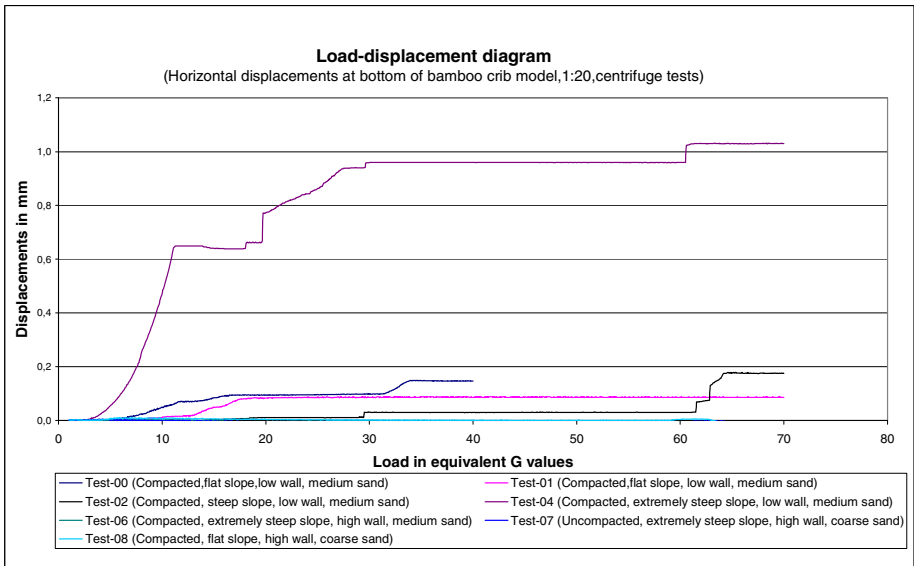


Fig. 7. The load-horizontal displacements at the bottom of a bamboo crib wall model (1:20), centrifuge test results

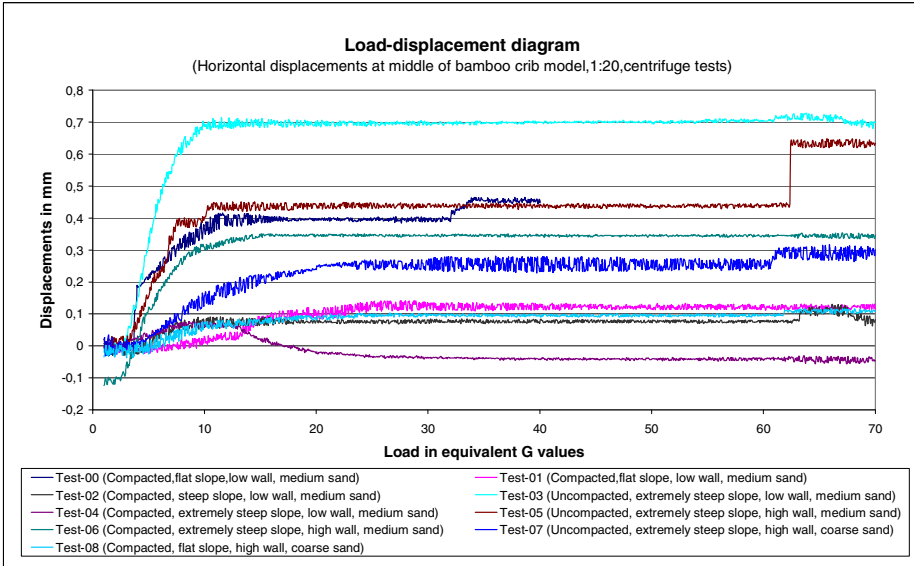


Fig. 8. The load-horizontal displacements at the middle of a bamboo crib wall model (1:20), centrifuge test results

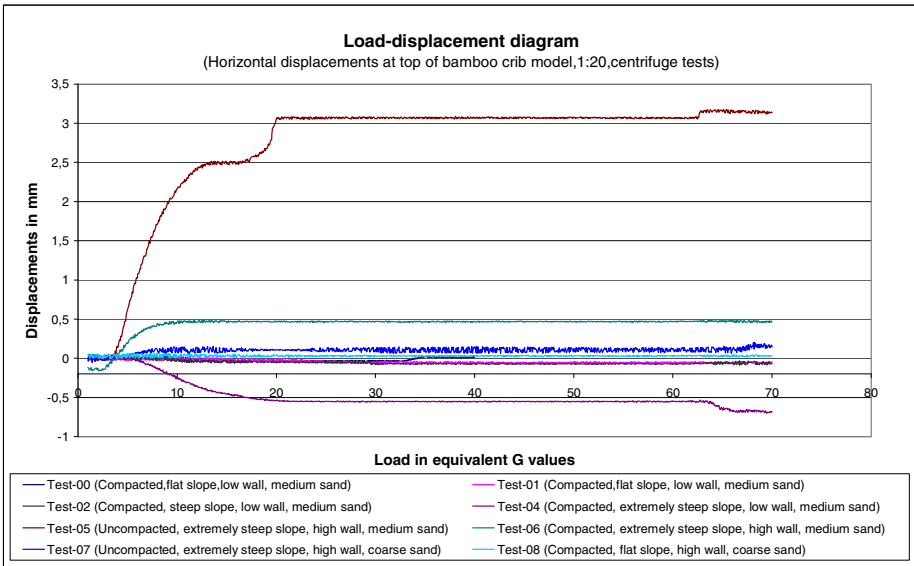


Fig. 9. The load-horizontal displacements at the top of a bamboo crib wall model (1:20), centrifuge test results

4 Conclusions

The results of the centrifugal tests show that the maximum horizontal deformation of the crib wall is at the mid-level followed by bottom and top. From the load displacement chart shown in Fig. 6, it can be seen that the loose backfills have very high vertical displacements compared to compacted backfills. Therefore it is recommended to compact the materials inside the crib cell as much as possible.

In most of tests, the maximum horizontal displacement is attained between 10-20 g beyond which it remained constant and there was no any sign of slope failure observed until 20 g. It shows that, the material inside the crib cell will be compacted during the test until it reaches to its maximum density. After attaining its maximum density, obviously, there will be no significant deformations of crib wall until the crib elements fail in shear or in tension. But in case of vertical displacement the maximum displacement is observed at about 40 g of loading. From these tests, it is clear that the compaction of the backfill/fill material plays a very important role in the strength of the bamboo/wooden crib wall. These results show that bamboo crib wall can accommodate large deformations without affecting its structural integrity. Internal stability of crib cell and crib elements is the governing factors in design of such crib walls.

References

1. Brandl, H.: Raumgitterstützmauern (Krainerwänden) – Großversuche, Baustellenmessungen, Anwendungsbeispiele, Berechnung, Konstruktion und Bauausführung. Bundesministerium für Bauten und Technik, Straßenforschung Heft 208, Vienna, pp. 174–187 (1982)
2. Brandl, H.: Tragverhalten und Dimensionierung von Raumgitterstützmauern (Krainerwänden). Bundesministerium für Bauten und Technik, Straßenforschung Heft 141, Vienna, pp. 115–220 (1980)
3. Brugger, N.: Großversuch an einem Geogitterverbau: Rückrechnungen und vergleichende Modellversuche. Diploma thesis, University of Natural Resources and Applied Life Sciences, Vienna, pp. 18–24 (1997)
4. Koliiji, A., Laloui, L., Cuisinier, O., Vulliet, L.: Modelling suction increase effects on the fabric of a structured soil. In: Mancuso, C., Tarantino, A. (eds.) *Unsaturated Soils, Advances in Testing, Modelling and Engineering Applications*, pp. 83–94. A.A. Balkema Publishers, London (2005)
5. Morgan, R.P.C., Rickson, R.J. (eds.): *Slope Stabilization and Erosion Control: A Bioengineering Approach*, pp. 1–47, 221–248. E & FN Spon, London (1995)

Viscous Effects on Granular Mixtures in a Rotating Drum

Miguel Angel Cabrera¹, Devis Gollin², Roland Kaitna³, and Wei Wu¹

¹ Institut für Geotechnik, Universität für Bodenkultur,
Vienna, Austria

² Department TESAFLand, Environment, Agriculture and Forestry,
University of Padova, Viale dell'Università 16, 35020 Legnaro, PD, Italy

³ Institut für Alpine Naturgefahren, Universität für Bodenkultur,
Vienna, Austria

miguel.cabrera@boku.ac.at

Abstract. In debris flow research, fine particles are considered to be part of the fluid phase of the flow. Nonetheless the particle-size threshold of this phase is not generally clear and could be dependent on the motion-characteristics of the flow itself. In the present study, rotating drum experiments are employed to investigate the effects of kaolin and silt fractions mixed in a fluid phase over a granular mixture of fine and coarse sand. Eight soil mixtures were prepared and tested at variable rotational velocities and water content. The mixtures are subjected to a constant shear that shifts the tested material and due to the action of gravitational forces a recirculating flow is produced inside the rotating drum. Our experiments found evidence of a solid concentration limit value where a shear-dependent behaviour is developed in the mixtures.

Keywords: Granular flows, Rotating drum, kaolin, loess.

1 Introduction

In mountain areas after intense periods of rain or ice melting seasons, the saturation of slopes leads to mass flows involving large volumes of soil, water, and vegetation. These mass flows are often referenced as debris flows, mud flows, debris flood, debris avalanche, and earth flows [9]. A better understanding of those flows will lead to an improvement in prevention systems, saving lives, property, and protecting productive land.

In the case of debris flows, sand, gravel, and larger boulders compose most of the mass of the debris, whereas silt and clay-sized grains commonly constitute less than 10% of the mass [4], [11]. On the other hand, mud flows have a higher fines fraction and fewer boulders [9], [22].

The particle size distribution (PSD) of the mass flow directly affects the evolution of the stresses during motion. In the case of coarse particles, internal forces arise from short-term collisions or long-term frictional forces between the grains. The presence of fine particles suspended in the fluid might increase viscosity and

bulk density of the fluid [5]. Therefore, homogeneous mixtures of water and fine sediment can be described with a simple shear-strain relation [3].

The current work aims, through experimental modelling, to provide evidence of the interaction of a highly viscous fluid in a granular flow. Rotating drum experiments with debris flows (also known as vertical rotating flume experiments [15]) were initially developed by [2] and [8].

In order to clarify the interaction of coarse and fine particles at different water contents a parametric study in the rotating drum was developed. Coarse and fine sand were employed to represent the solid phase of the granular flow, and loess and kaolin (kaolinite clay) were mixed with water to produce a fluid with an increased viscosity. Drum tests were conducted in two sets. The first set of tests focused on the rheological behaviour of the source granular materials as reference tests, while the second set tested the rheological behaviour of the interaction of the granular materials with the addition of kaolin and loess at different water contents.

On dry conditions, granular flows (sand mixtures) are expected to be less affected by the variation of the rotational velocity of the drum. When enduring frictional contacts prevail, resistance is expected to be defined by the grains contact parameters, which show non- or low-shear dependent behaviour following a Coulomb model [11] [14]. With the addition of water and increased viscous water-mixtures it is intended to weaken the particle interactions and obtain a shear-dependent response from the fluid phase. The shear-dependent response of the flow is expected to present a power law distribution as in a non-Newtonian fluid [28].

In this paper section 2 presents the description of the rotating drum, its instrumentation, the characteristics of the soil mixtures, and the test routine. Section 3 discusses the governing equations of granular flows induced in the rotating drum and describes the assumptions adopted in the data analysis. Section 4 presents the results obtained from the measurement system of the drum, discusses the characteristics of the flows tested, and analyses the characteristics of granular flows saturated with a viscous fluid. Section 5 discusses the obtained results, and provides some recommendations for future work.

2 Methods

The rotating drum is composed of a rotating cylindrical channel section connected to an engine that imposes a controlled rotational velocity (see Fig. 1). The material inside the drum is dragged at a constant velocity by the roughened surface and lateral walls, until an avalanche is released at the apex of the flow with an equivalent velocity. This recirculating process is self balancing giving the characteristics of a steady-state flow. The main advantage of employing a rotating drum is the opportunity to establish stationary conditions over an extended period of time [17].

2.1 Apparatus and Instrumentation

The experiments were performed in a rotating drum with an inner diameter of 2.46 m and channel width of 0.45 m at the University of Natural Resources and Life Sciences (BOKU), Vienna, Austria. The rotating drum has a rectangular inner section (Fig. 1). The side-walls are composed at one side of stainless steel and at the opposite side of acrylic glass [17]. The bed of the channel is roughened using a rubber surface with protrusions in a zigzag pattern of approximately 3 mm in height and 5 mm in separation.

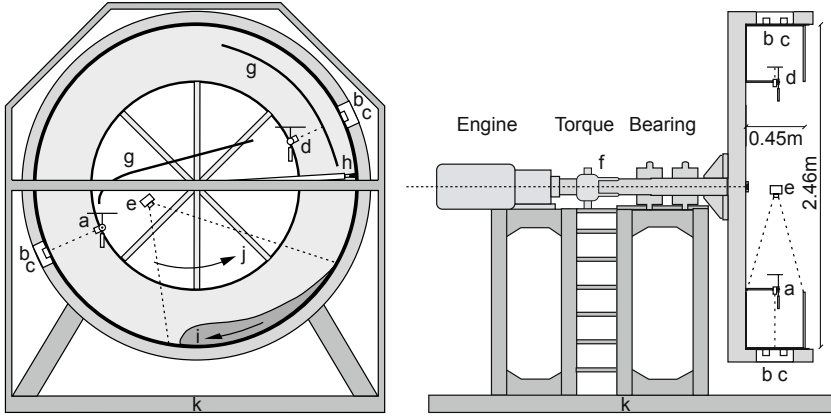


Fig. 1. Rotating drum at BOKU. a) Height point-laser, b) Normal load cell, c) Shear load cell d) Height ultrasonic sensor, e) High-speed camera, f) Sliced ring, g) Inner-roof (drop protection), h) Broom (controls mass up-flow), i) Material flow direction, j) Drum rotating direction, k) Steel frame. Adapted from [17] and [26].

The rotational velocity of the drum is measured with a sliced-ring fixed together with the thrust bearing. A static photo-electric sensor records an impulse at every degree of rotation, thus the angular position of each sensor installed within the drum can be traced. The rotational velocity of the drum is measured at the sliced ring in revolutions per minute (rpm).

Two load cells (HBM PW2GC3) are employed to measure normal forces at the base of the channel section. The load cells are installed at two different locations along the circumference displaced 180° (Fig. 1). Each load cell is connected to a plate, 60 mm in diameter, covered by the same roughened rubber of the drum's bed. This arrangement gives two independent normal force measurements at the third of the drum channel base. In order to prevent leaking and clogging of material the edges of the plates were sealed with a thin silicone layer. Due to the rotation, the recorded signal has a sinusoidal shape caused by the self weight of the assemblage. This sinusoidal effect was removed in the post-processing with a digital signal filtering procedure [26].

Above the load cells, the flow depth was measured by an ultra-sonic sensor (Pepperl und Fuchs UC500-30GM) and a point-laser sensor (Baumer OADM 20) at the same location as the load cells, installed on the central position of the channel cross-section. Near the center of rotation a high-speed camera (Casio EX-ZR15) recorded the full extension of the granular flow at a rate of 232 fps with a frame size of 512×384 pixels (Fig. 1).

The sliced-ring, load cells, and ultrasonic and laser sensors were recorded using a data acquisition system at a sampling frequency of 1200 Hz.

2.2 Soil Mixtures

Mixtures of coarse and fine sand were selected to represent the reference framework, in which the effect of fluid properties are investigated. First with the addition of water, then with the addition of loess and kaolin (kaolinite clay) mixed with water, to produce a fluid with an increased viscosity. Fig. 2 presents the particle size distributions (PSD) of the source materials and mixture compositions.

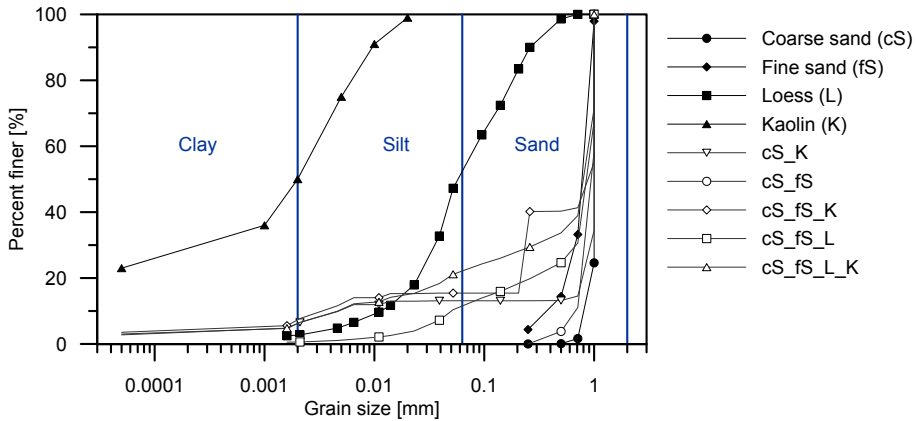


Fig. 2. Particle size distribution (PSD) of the materials tested. Note that the filled dots present the PSD of the source materials, and the empty dots denote the resulting PSD of the mixtures. For more details about the mixtures see table 1.

The sand is a standard naturally rounded siliceous sand (normsand DIN-1164) and a fine high-purity quartz sand. The material is selected because its uniform particle shape and poorly graded PSD (Fig. 2). The mean particle size of the sand samples is 1 mm and 0.71 mm respectively.

Loess is a silty sediment of high porosity, deposited by aeolian action, which can be “draped” across the landscape [13] and known for its high content of silt-size particles [27]. The silt fraction was obtained from a loess deposit in Austria. To define both, the particle size distribution and the silt portion of the loess, a

mechanical gradation and hydrometer method was performed. The results show that 2.6% was composed of clay, 50.6% of silt, and 46.9% of sand (Fig. 2). Note that the silt fraction was not sieved separately from the sample, herein the three fractions employed in tests are presented together in the PSD L on Fig. 2.

Kaolinite clay (Kamig-E1) with mean particle size $2 \mu\text{m}$ (PSD given by the producer) is chosen because of its low reactivity, particularly compared to other common clays (e.g. bentonite) [21], and for the known viscous properties when it is mixed with water [1], [6], [22]. The rheology of the kaolin-water and loess-water dispersions is quantified using a simple co-axial cylinder rheometer (Bohlin Visco 88). In order to measure the viscosity of the silt fraction, the loess sample material is sieved in order to avoid material jamming at the inner cylinder of the rheometer. The solid concentration Cv of the fine-soil-water mixtures, defined as the ratio of the solid volume V_s (fines and coarse particles) over the total volume V_t of the mixture ($Cv = V_s/V_t$), ranges between 0.50 to 0.70.

Fig. 3 shows the shear flow curves for kaolin and loess. The results show a non-Newtonian shear dependent behaviour for both dispersions. In the case of kaolin and loess the viscosity increases with the solid concentration, and decays to a constant value at high shear rates. Note that for the loess dispersion at a Cv value of 0.42 irregular results are obtained at high shear stress values. This could be due to short grain “jams” caused by clogging of material during measurements at this particular Cv .

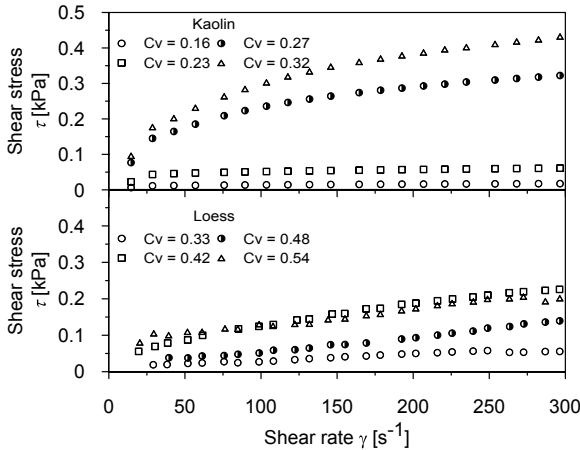


Fig. 3. Viscosity curves for kaolin and loess mixed with water at different solid concentrations (Cv)

2.3 Test Routine

Drum tests were performed in two sets with different grain size fractions (Table 1). For listing purposes the mixture names are followed by the bulk solid concentration of the mixture Cv and the rotational velocity of the test, for example

cS_fS_0.65_7 stands for the mixture of coarse sand and fine sand with a Cv value of 0.65 at 7 rpm. Note that the mixture cS_K1 has a lower content of kaoline than cS_K2 (Cv of kaolin of 0.23 and 0.27 respectively), and thus it is expected that the viscous effects of the mixture cS_K2 become stronger than cS_K1.

Table 1. Rotating drum tests. The abbreviations stands for, cS: coarse sand, fS: fine sand, L: loess, and K: kaolin.

	Set	Mixture name	Mass fraction [%]	Solid Concentration	Cv [-]
		cS	100	<i>dry</i> 0.65 0.60 0.56 0.52 0.49	
1		cS_fS	70-30	<i>dry</i> 0.65 0.60 0.56 0.52 0.49	
		L	100	- 0.53 0.50 0.47 0.45 0.43	
		cS_K1	88.5-11.5	0.71 0.66 0.61 0.57 0.53 0.50	
		cS_K2	87.3-12.7	0.74 0.67 0.61 0.57 0.53 0.50	
2		cS_fS_K	61.9-26.5-11.5	0.71 0.66 0.61 0.57 0.53 0.50	
		cS_fS_L	54.6-23.4-22.0	0.72 0.65 0.60 0.56 0.52 0.48	
		cS_fS_L_K	48.0-20.6-19.4-12	0.69 0.65 0.60 0.56 0.52 0.49	

Every test started with the weighing of the granular material and fluid phase according to a previous defined fraction (Table 1). The total mass of the tested material was approximately 50 kg, and the addition of water to the mixture ranged from 7 to 20 L. Mixtures with different grain size gradation were mixed in a mortar mixer to ensure an homogeneous mixture. During the mixing process, a Cv value was reached by adding a known amount of water. After the mixture become homogeneous, it was added to the rotating drum.

Once the drum was filled a couple of rotations were completed in order to check the sensors response and allow the roughened surface to be uniformly covered by the material. Rotational velocities of 3, 5, 7, and 9 rpm were applied to the mixtures (0.40, 0.65, 0.90, 1.20 ms^{-1} , respectively). The materials were tested over 7 to 10 rotations, during each set of velocities. When the rotational cycle finishes, a previously weighed amount of water is added to the mixture inside the drum (changing the solid concentration Cv of the mixture and of the fluid phase) and the rotational cycle starts again. Five to six cycles of varying the Cv per granular mixture were executed.

3 Governing Principles

Considering a continuum approach, as widely developed by [11], [10], [24], and [25] the governing laws for free surface flows are defined by the balance of mass and momentum (Eq. 1 and 2). A balance of mass considers the flowing material to be fixed to a value and avoid mass changes during flow, and the balance of momentum considers the equilibrium of acting forces during flow. In this case, the physical laws are written as a function of the mixture's density ρ , the velocity

vector \mathbf{v} , the stress tensor \mathbf{T} , and the gravitational field \mathbf{g} . Note that in a two phase flow the contributions of the fluid and solid constituents can be treated independently.

$$\frac{\partial \rho}{\partial t} + \nabla \cdot \rho \mathbf{v} = 0 \quad (1)$$

$$\frac{\partial v}{\partial t} + \nabla \cdot \rho v \otimes v - \nabla \cdot \mathbf{T} + \rho g = 0 \quad (2)$$

The stress tensor is the result of the interactions inside and between the different phases present in the flow. According to [12], [23] and [28] these interactions are identified as:

- short-term collisions of coarse particles,
- enduring particle friction (long-term contacts),
- deformation of the fluid phase (viscous shear),
- stresses between particles and fluid resulting from the relative motion of the fluid and solid constituents (Drag and buoyancy).
- macro turbulent mixing of the fluid phase and coarse particles (inertial velocity fluctuations),

Understanding of the interactions allows recognizing different dominant sources of flow resistance. In dry tests the collisions and frictional forces between particles will be the only interactions present in the flow. While, when a liquid is added to the flow and depending on its viscosity, the fluid interactions start becoming dominant.

Assuming an homogeneous flow and in order to simplify the motion characteristics, the torque (T) is assumed to act at the center of mass of the granular flow and defines the shear applied to the material. The angle (α) between the center of the drum and the center of mass is considered as an equivalent slope angle as presented in Fig. 4 [17], [18], [26]. In this sense, T is computed from the total weight of the granular mixture ($\rho g V$) times the horizontal distance between the center of the drum and the center of mass of the surge ($r_0 \sin \alpha$) (Eq. 3).

$$T = \rho g V r_0 \sin \alpha \quad (3)$$

Then, the mean shear stress (τ_{mean}) is estimated considering a constant distribution of shear through the area in contact with the granular flow [16]. It is assumed an equal distribution of the bed shear stress and a lineal shear stress distribution on the side-walls (Eq. 4).

$$\tau_{mean} = \frac{T}{A_b r + A_s (r - h_{mean}/3)} \quad (4)$$

Where r is the radius of the drum, h_{mean} is the mean height of the flow and, A_b and A_s are the equivalent area of the flow at the base and cross-section of the drum, respectively.

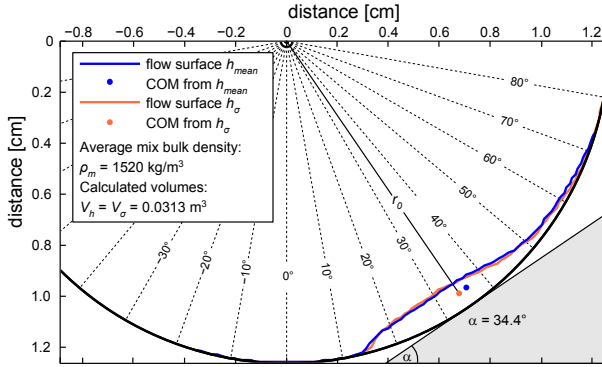


Fig. 4. Calculation of center of mass shown for the mixture cS_fs_0.52_5. Note that the height profiles obtained from the laser measurements (h_{mean}) are in agreement with the post processed load cell measurements (h_{σ}). The 0° point inside the drum is located at 6 o'clock for reference purposes.

4 Results and Analysis

The flow height and normal stress measurements are averaged every degree of rotation. Measured data are found to oscillate more frequently in the tail of the surge profile. These oscillations are considered to be generated by internal development of surges at the tail of the flow.

4.1 General Observations

Granular flows tested in the rotating drum (cS and cS_fs) show specific patterns whether the material was dry or in addition of water. At dry conditions, the pattern of velocities at the surface are affected by the lateral walls generating a middle channel with higher velocities, with a longer body and a shorter tail. Once water is added to the granular material, the effect of the lateral walls decreases and the granular flow transforms into a plug, shortening the body and elongating the tail.

For the coarse grain test (cS) the increase in water content reach a limit level where the mixture of water and soil grains remains in the same bulk flowing mass (Cv of 0.56). At low rotational velocities, the water starts to percolate to the front of the flow and separate from the sand body. Nonetheless, once the rotational velocity of the drum increases, the percolation ceases and the mixture of the two phases is achieved. Similar cases are observed at higher water contents for the mixture of coarse and fine sand (Cv of 0.52), for the mixtures with kaolin (Cv of 0.66 and 0.67), and with loess (Cv of 0.47). Full phase mixing is not evident for the mixture cS_fs_K.L. Therefore, it is possible to conclude that the percolation process (or phase separation) is associated with the porosity of the granular mixture, the viscosity of the fluid phase, and the stress state happening in the flowing mixture as presented in [19].

It is important to note that for the tests with kaolin at high volumetric concentrations ($Cv \geq 0.61$), the losses of material are significant; losing more than 25% of the material in one cycle of rotational velocities. The losses occur due to the clogging of material in the roughened bed followed by dropping and accumulation in the inner roof of the drum (Fig. 1 part f). The losses of material are recognized as one of the biggest limitations of the tests, and are not considered in the following analysis.

At high solid concentrations and high rotational velocities, the thickness of the tail becomes considerably smaller. Then, the drag forces induced by the drum's bed become stronger than the acting forces in the flow direction, generating a separation in the body of the flow. This process caused the creation of internal surges in the tail of the flow at low Cv values, and is considered as one of the reasons for the material losses at high Cv values.

Particle image velocimetry (PIV) analysis were applied on the high-speed recordings. The PIV analyses were computed with the open source code PIVlab (v.1.32). The velocity field obtained on the PIV analysis (Fig. 5.a) enables to infer the location of the front, body and tail of the granular flow. Highest velocities occur at the front mid-section (e.g., zone of 0.2 m/s in Fig. 5.b), then the distribution of the superficial velocities flattens making a transition through the body to the tail where the values are almost negligible.

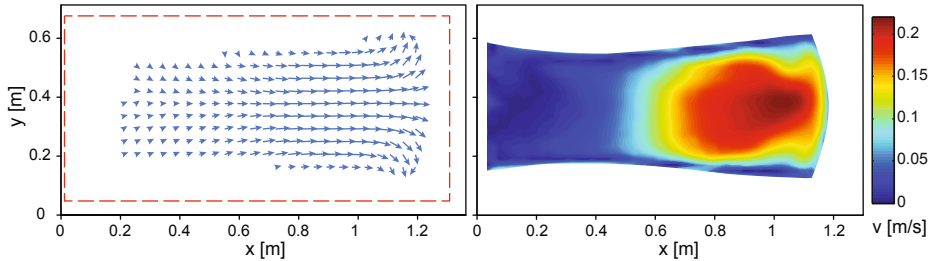


Fig. 5. Particle Image Velocimetry (PIV) of the recorded high-speed videos on the test cS_K1_0.71_3. The left image shows the average velocity field (1304 frames), and the right image shows the distribution of the velocity magnitude on surface.

The velocity field is symmetric across the mid-section of the channel for the flows with high Cv values. When the mixture becomes more fluid the symmetry-axis is displaced. In those cases the front tended to move faster in proximity to the aluminium wall, assumed to have a larger friction coefficient than the acrylic wall.

The velocity field in Fig. 5.a shows that the direction of the velocity vectors varies in space making a strongly non-uniform flow. However the magnitude and direction of the velocity at each point of analysis is usually constant in time. This indicates that the flows induced inside the rotating drum are non-uniform quasi-steady flows.

4.2 Viscous Effects on Granular Mixtures

In order to elucidate the shear-dependent behaviour Fig. 6 presents the height profiles of the mixtures at different rotational velocities for the range of Cv values between 0.67 to 0.69. The obtained results identify the starting point of the flow and the dependence on mixture composition. Granular flows (cS and cS_fs) in the presence of water started at steeper locations inside the drum, while flows with increased viscosity (with the addition of L and K) were found at lower zones. This behaviour might be due to the effect of the induced shear stress inside the drum being supported by the grains in flows with water, rather than in flows where the presence of loess and kaolin increases the density and viscosity of the fluid that surrounds the grains.

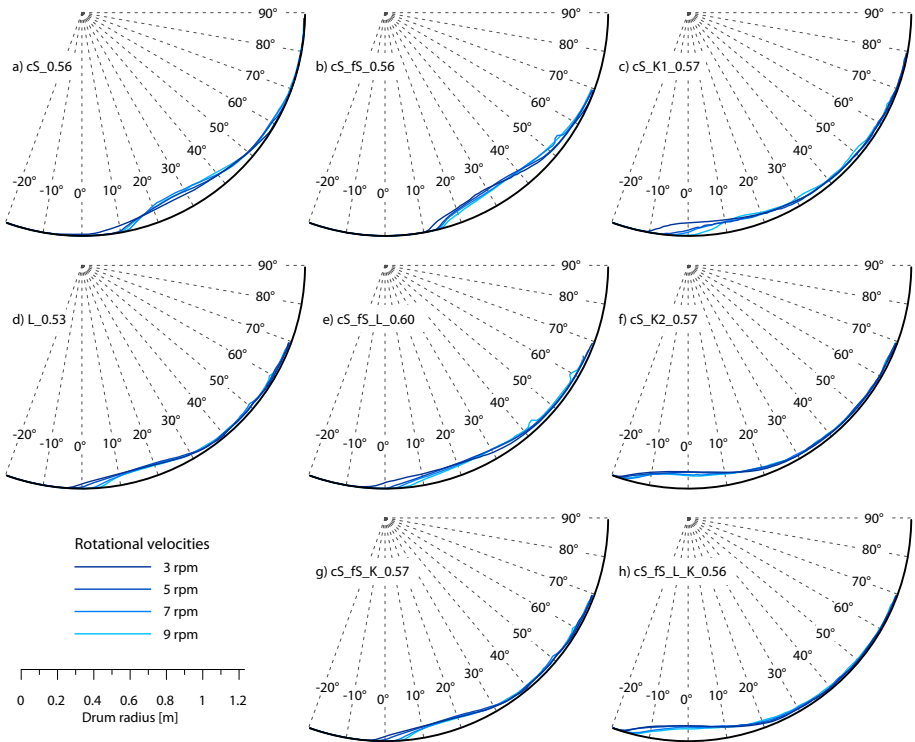


Fig. 6. Mixtures height profiles at different rotational velocities. a) cS_0.69, b) cS_fs_0.69, c) cS_K1_0.68, d) L_0.68, e) cS_fs_L_0.69, f) cS_K2_0.69, g) cS_fs_K_0.68, h) cS_fs_L_K_0.67.

Localization of the front of the flow typically shifts to higher inclinations with the increase of the rotational velocity of the drum, and could be understood as the mixture's response to a change in shear stress resulting in a re-placement of the flow geometry.

Note that for the cS_0.56 test at a rotational velocity of 3 rpm a flat front is developed. Then, as the velocity of the drum is increased, the flow moves up and a bump front is observed. The flat front regards to the percolated water mentioned before and is not obtained in the cS_fS_0.56 test. This is attributed to the reduced porosity of the system, being small enough to keep the volume of water mixed in the soil mixture. For the L_0.53 test, the front of the mixture is located between -5° to 5° .

When the mixture of sand (cS_fS) is tested with the loess the location of the front remains more likely to the L_0.53 test than to the cS_fS_0.56 test, showing that the behaviour of the loess mixture prevails over the sand mixture. In the case of kaolin the two previous behaviours are observed. First, keeping the same amount of kaolin in the mixture and varying the porosity of the sand media (tests cS_K1_0.57 and cS_fS_K_0.57) a compact flowing mass is obtained as an effect of a decreased porosity. Second, the viscous behaviour of kaolin (cS_K1_0.57 and cS_K2_0.57) is observed to be dominant than the sand interactions, even in the case of a wide PSD (cS_fS_L_K_0.56).

Fig. 7 presents the transition of the location of the front for the cS and L test with the addition of water at different rotational velocities. In the dry case of the cS test the location of the front is not strongly affected by the rotational velocity of the drum (variation of 2°). When water is added to the cS mixture, at a Cv value of 0.65, a re-localization of the front moving up inside the drum is observed. Then, at higher water contents (lower Cv values) the front of the mixture moves downward, and match with the loess tests transition surface. The initial re-localization of the front is attributed to the stronger effect of water in the soil mixture, showing a transition where the partial saturation of the mixture strengthens the flow and then dissipates when it reaches and exceeds saturation.

The thin tails observed for flows with an increased viscosity give a probable scenario for mass losses at high solid concentrations (Fig. 6), implying that for the cases where the thickness of the tail is not able to counteract the applied shear stress a fraction of it is dragged upstream.

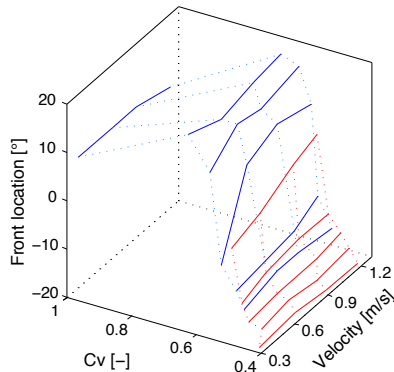


Fig. 7. Localization of the front of the flow for the coarse sand (cS) and loess (L) varying the Cv of the mixture and the rotational velocity of the drum

Considering a constant bulk water content it is possible to infer the following scenarios: a) With the addition of fines mixed with water the density of the fluid rises, the buoyancy of the system increases, and the grain's frictional interactions decreases; and b) As the fines-water mixtures surround the grains, the shear-dependent behaviour induced by the grain-fluid interactions controls the behaviour of the mixture, damping the grain's collisions. Even when it is not possible to differ which of the two scenarios prevails, it is clear that the addition of fines-water mixtures to a granular mass will effect the frictional and collisional interactions of the grains.

As outlined in section 1 the flow behaviour of different mixtures may be connected to the relation of the mean shear stress (τ_{mean}) against the induced shear rate ($\dot{\gamma}$) acting on the flow. Three common behaviours are observed, 1) a shear independent behaviour for the dry coarse sand test (cS_dry) where the variation of the rotational velocity do not vary the shear stress in the mixture. 2) a shear dependent behaviour in which an increase in the rotational velocity increases the shear stresses in the flow, and 3) a shear behaviour in which an increase in the rotational velocity does not increase the shear stress in the flow. Fig. 8 presents the summary of the tests where a shear dependant behaviour was obtained (filled dots and lines).

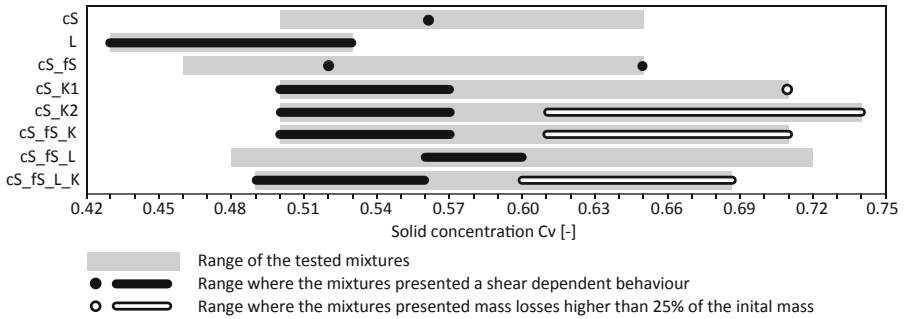


Fig. 8. Experimental range of solid concentrations Cv over the tested mixtures

On the case of the granular mixtures without the addition of an increased viscous fluid (tests cS and cS_fs) it was unexpected to find a shear dependent behaviour (Fig. 8). This is because, it was theorized that sand-flows under low shear stresses were purely frictional, and due to the low viscosity of water (ν of the order of 10^{-3} Pas) the interactions of the grains will prevail over the fluid phase.

On the mixtures with the addition of an increased viscous fluid (tests with kaolin and loess), a shear dependent behaviour is observed at Cv values lower than 0.57 and 0.60 for the kaolin and loess tests (Fig. 8), which shows the apparent threshold in terms of the Cv for non-Newtonian fluids represented by yield pseudo-plastic model.

For the tests cS_K1, cS_K2, cS_fS_K, and cS_fS_L_K the results are somewhat dependent on the strong material losses at low Cv values (Fig. 8), however with the addition of water the system reaches equilibrium, the material losses dissipates, a considerable fraction of material moves back into the drum's channel, and the obtained shear-dependent behaviour is considered reliable.

5 Conclusions

The present study aimed to characterize the interactions of a mixture of coarse and fine sand with the addition of kaolin and loess. The mixtures were tested in a rotating drum by varying the rotational velocity and solid concentration of the mixtures (Cv and Cv_{fluid}). The experiments provide new laboratory evidence of granular mixture behaviour with an increased viscous fluid phase and its characterization. The results show an apparent threshold in terms of Cv where the mixtures started to behave as a shear-dependent material.

The obtained results points that granular flows at high Cv values are controlled by the frictional and collisional interactions. With the addition of water and considering the density and viscosity of the fluid, the grain's interactions are weakened and the stress-strain response of the system is modified. Therefore as the PSD during each test is constant, the classification of the mixture's components as fluid or solid phase is dependent on the stress state inside the flow and not only on a particular particle size threshold.

From the tests developed, the viscous effects of fines-water mixtures on sand granular flows are considered to occur as a result on an increase on the fluid's density which will increase the buoyancy effects on the mixture, and/or the shear-dependent viscous effects originated from the grains-fluid interactions.

Mass losses are a significant limitation, in some cases higher than 25% of the initial mass at high Cv values, and phase separation is significant at low Cv values (presenting a liquid front and a dry tail). These two limits should be considered in future research. While the presented laboratory experiments help to define the experimental field for sand mixtures in the presence of a scaled viscous fluid, the accurate identification of the dominant interactions was not assessed as isolated interactions.

Kaolin and loess were able to induce a non-Newtonian behaviour in the tested mixtures. Their application appears as an interesting alternative to glycerine or other synthetic fluids, in order to represent the solid-fluid interactions in granular flows.

Future studies may focus on the interaction of a scaled viscous fluid with larger granular material components, and on the characteristics of partially saturated flows. Future research may aim to ensure a complete mixture state, in which all the constituents are mixed equally. Furthermore, with the experimental evidence obtained the mechanisms involved in the mass losses are an interesting opportunity to be validated with numerical analysis.

Acknowledgements. The research leading to these results has received funding from the People Programme (Marie Curie Actions) of the European Union's Seventh Framework Programme FP7/2007-2013/ under REA grant agreement n° 289911.

References

1. Barbatoa, C.N., Nelea, M., Pintob, J.C., Franac, S.C.A.: Studies of kaolin rheology. In: IX Jornadas Argentinas de Tratamiento de Minerales, San Juan, Argentina (2008)
2. Brown, S.: The Vertically Rotating Flume for Use as a Rheometer. PhD thesis, University of Missouri-Rolla, USA (1992)
3. Laigle, D., Coussot, P.: Numerical modeling of mudflows. *J. Hydraul. Eng.* 123, 617–623 (1997)
4. Coussot, P., Meunier, M.: Complex viscosity of a kaolin clay. *Clays and Clay Minerals* 17, 101–110 (1996)
5. Einstein, H.A.: The bed-load function at high sediment rates. U.S. Dept. of Agriculture, Tech. Bull. 1026 (1950)
6. Franklin, A.G., Krizek, R.J.: Recognition, classification and mechanical description of debris flows. *Earth-Science Reviews* 40, 209–227 (1996)
7. Gollin, D.: Rheological characterization of debris-flows mixtures using a rotating drum. Master's thesis, Department TESAF Land, Environment, Agriculture and Forestry, University of Padova, Viale dell'Università 16, 35020 Legnaro, PD, Italy (2013)
8. Huizinga, R.: An Analysis of the Two-Dimensional Flow in a Vertically Rotating Flume. PhD thesis, University of Missouri-Rolla, USA (1993)
9. Hungr, O., Evans, S., Bovis, M., Hutchinson, J.: Review of the classification of landslides of the flow type. *Environmental and Engineering Geoscience* 7, 221–238 (2001)
10. Hungr, O., McDougall, S.: Two numerical models for landslide dynamic analysis. *Computers & Geosciences* 35(5), 978–992 (2009)
11. Iverson, R.: The physics of debris flows. *Reviews of Geophysics* 35(3), 245–296 (1997)
12. Iverson, R.M., Denlinger, R.P.: Flow of variably fluidized granular masses across three-dimensional terrain: 1. coulomb mixture theory. *Journal of Geophysical Research: Solid Earth* 106(B1), 537–552 (2001)
13. Jefferson, I.F., Mavlyanova, N., OHara-Dhand, K., Smalley, I.J.: The engineering geology of loess ground: 15 tasks for investigators - the mavlyanov programme of loes research. *Engineering Geology* 74, 33–37 (2004)
14. Jop, P., Forterre, Y., Pouliquen, O.: Crucial role of side walls for granular surface flows: consequences for the rheology. *J. Fluid Mech.* 541, 167–192 (2005)
15. Kaitna, R.: Debris flow experiments in a rotating drum. PhD thesis, University of Natural Resources and Life Sciences, Vienna, Department of Civil Engineering and Natural Hazards, Institute of Mountain Risk Engineering (2006)
16. Kaitna, R., Rickenmann, D., Schneiderbauer, S.: Comparative rheologic investigations in a vertically rotating flume and a moving-bed conveyor belt flume. In: *Monitoring, Simulation, Prevention and Remediation of Dense and Debris Flows*, pp. 89–98. WIT Press (2006)

17. Kaitna, R., Rickenmann, D.: A new experimental facility for laboratory debris flow investigation. *Journal of Hydraulic Research* 45(6), 797–810 (2007)
18. Kaitna, R., Rickenmann, D., Schatzmann, M.: Experimental study on rheologic behaviour of debris flow material. *Acta Geotechnica* 2(2), 71–85 (2007)
19. Kaitna, R., Hsu, L., Rickenmann, D., Dietrich, W.E.: On the development of an unsaturated front of debris flows. In: Genevois, R., Hamilton, D.L., Prestininzi, A. (eds.) *5th International Conference on Debris-Flow Hazards: Mitigation, Mechanics, Prediction and Assessment*, Padua, June 14–17, pp. 351–358 (2011), *Italian Journal of Engineering Geology and Environment*
20. Kaitna, R., Dietrich, W.E., Hsu, L.: Surface slopes, velocity profiles and fluid pressure in shallow, coarse granular flows saturated with water and mud. Manuscript submitted for publication (2013)
21. Parson, J.D., Whipple, K.X., Simon, A.: Experimental study of the grain-flow, fluid-mud transition in debris flows. *The Journal of Geology* 109, 427–447 (2001)
22. O'Brien, J., Julien, P.: Laboratory Analysis of Mudflow Properties. *Journal of Hydraulic Engineering* 114(8), 877–887 (1988)
23. Pudasaini, S., Hutter, K.: *Avalanche Dynamics: Dynamics of Rapid Flows of Dense Granular Avalanches*. Springer, New York (2007)
24. Pudasaini, S.P.: A general two-phase debris flow model. *Journal of Geophysical Research: Earth Surface* 117(F3), 1–28 (2012)
25. Savage, S., Hutter, K.: The motion of a finite mass of granular material down a rough incline. *J. Fluid Mech.* 199, 177–215 (1989)
26. Schneider, D., Kaitna, R., Dietrich, W., Hsu, L., Huggel, C., McArdell, B.: Frictional behavior of granular gravelice mixtures in vertically rotating drum experiments and implications for rockice avalanches. *Cold Regions Science and Technology* 69(1), 70–90 (2011)
27. Smalley, I.J., Jefferson, I.J., OHara-Dhand, K., Evens, R.D.: An approach to the problem of loess deposit formation: Some comments on the in situ or soil-eluvial hypothesis. *Quaternary International* 152–153, 109–117 (2006)
28. Takahashi, T.: *Debris flow: mechanics, prediction and countermeasures*. Taylor & Francis, Leiden (2007)

Centrifuge Model Tests of Rainfall-Induced Landslides

Vasileios Matziaris, Alec M. Marshall, and Hai-Sui Yu

Nottingham Centre for Geomechanics, University of Nottingham, U.K.
Vasileios.Matziaris@nottingham.ac.uk

Abstract. Rainfall-induced landslides and debris flows constitute very serious threats to human lives and infrastructure. In many cases, rainfall characteristics which cause the initiation of landslides are not very well determined and this might lead to the misunderstanding of the failure mechanism, the kinematic characteristics and the run-out distance of the failure. In this paper, the design of three series of centrifuge model tests on soil slopes, subjected to rainfall conditions, is presented. The main goal is to investigate rainfall characteristics which cause failure initiation in soil slopes in respect to soil properties and slope geometry. Tests will be performed in a geotechnical centrifuge at the Nottingham Centre for Geomechanics (NCG) under very well defined initial and boundary conditions. For the accomplishment of these tests, a climatic chamber has been developed which accommodates plane-strain slope models and sufficient instrumentation and embodies a rainfall and an evaporation simulation systems. During the centrifuge tests, changes in pore water pressures and soil state as well as deformations of the slopes will be measured, while rainfall intensity and total rainfall will be accurately defined. Three different soil types will be used to create uniform slope models, i.e. fine sand, silty clay and clay, while rainfall intensity will be proportional to the infiltration capacity. The paper describes, also, the saturation and calibration of Druck PDCR-81 miniature pore pressure transducers and SWT5 tensiometers used for pore water pressure measurements.

Keywords: Centrifuge modelling, rainfall, slope stability.

1 Introduction

Rainfall-induced landslides are devastating phenomena which are responsible for loss of human life and serious damage to infrastructure every year. Although they have a global distribution, a significant segment is observed in areas with tropical and sub-tropical climates [1, 2] where residual and colluvial soils are widespread. The likelihood and time of occurrence, in respect to a triggering rainfall event, is not easy to be defined leading to a major difficulty in predicting small and large-scale disasters. Rainfall characteristics, i.e. duration, intensity and distribution, play a significant role in the pore water pressure changes and therefore influence the stability of natural and man-made slopes. Moreover, slope failures due to rainfall are often rapid phenomena and occur without warning leading to a major lack of reliable field data.

Recent developments in geotechnical centrifuge techniques have heightened scientific interest in slope stability modelling under an increased gravity field. The idea of rainfall simulation in centrifuge slope model tests was introduced in the early '90s, involving the conservation of moisture content of the soil [3]. In another investigation, centrifuge tests of slope models, made of sandy loam, were carried out in order to investigate the effect of heavy rain on their stability [4]. The simulation of seasonal pore pressure cycles of over-consolidated clay embankments, in an increased gravity field, was performed in University of Cambridge [5]. A similar investigation was performed in Dundee University [6], describing the behaviour of a compacted clay embankment under climatic cycles. However, in this case, glacial till was used to form a small-scaled model in order to explore long-term embankment performance in light of the more severe conditions expected due to global climate change. Slope models made of silty sand were prepared in order to be tested under an increased gravity field in order to simulate the behaviour of a full-scale experimental natural slope in Switzerland [7]. The natural slope was subjected to rainfall for several hours until it failed due to a bottom-up saturation mechanism [8]. The initiation of static liquefaction failure mechanism was also investigated by other researchers [9, 10]. Finally, failures of sandy slope models, induced by heavy precipitation, were modelled in a geotechnical centrifuge using liquids with varied viscosity in order to simulate rainfall events [11], paying also attention to the impact pressure of the droplets to the ground surface.

The aim of this research is to evaluate the stability of soil slopes subjected to different types of rainfall conditions. For the accomplishment of the study, a number of centrifuge tests will be conducted on the Nottingham Centre for Geomechanics (NCG). Soil slope models will undergo an increased gravity field under controlled climatic conditions (rainfall, evaporation, relative humidity). The increased gravity field, due to centrifugal acceleration, will create a stress field within slope models similar to a 9m high prototype slope. The intensity of the simulated rainfall events will be proportional to the infiltration capacity of the soils. For this reason, different values of the dimensionless factor I_r/k will be used, where k is the coefficient of permeability of the soil and I_r the rainfall intensity. Changes in pore water pressures, soil state as well as slope deformation will be recorded during the tests.

2 Apparatus

2.1 Geotechnical Centrifuge in the NCG

The geotechnical centrifuge which is based in the Nottingham Centre for Geomechanics (NCG), at University of Nottingham, is a 50g-tonne machine with 2m platform radius able to achieve accelerations up to 150g [12]. It has a maximum payload of 500kg (at 100g) and an automatic "in-flight" balancing system. It includes a data acquisition system which accommodates 32 strain gauge channels and 32 channels for general instrumentation. A swinging model platform is located at the end of the centrifuge arm and is the base where the model box will be fixed. The platform initially is

horizontal for facilitation of the model preparation and the necessary actions concerning instrumentation and connection of the measurement devices. As the centrifuge starts operating and the radial velocity is increased, the platform rotates outwards such that the vertical axis of the model aligns with the beam. In this position, the gravity field within the model is N times greater than g (Ng condition), directed along the vertical axis of the centrifuge model.

2.2 Climatic Chamber

In order to control the climatic conditions during the centrifuge acceleration of the soil slope models, a climatic chamber has been designed (Fig. 1). This comprises a plain-strain rigid container (strong box) with one transparent boundary (Perspex window) which offers the ability to observe and optically measure soil deformations throughout the entire model cross-section. A high speed camera is been placed in front of the Perspex window allowing for optical measurement of soil displacement at small time intervals. In order to ensure absolutely controlled climatic conditions, the climatic chamber is isolated preserving the internal air humidity and preventing wind gusts to affect the model. The skeleton of the container is made of steel and aluminium and it has interior dimensions of 700mm in length, 400mm in height and 200mm in the plain-strain direction.

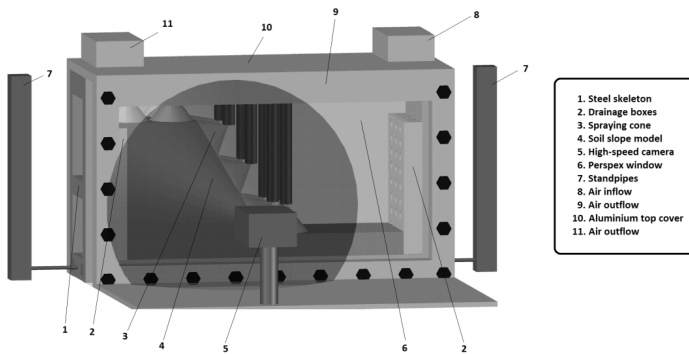


Fig. 1. Climatic chamber, which will be used in centrifuge tests

For the realistic simulation of climatic conditions (i.e. rainfall, evaporation, initial groundwater table and unsaturated conditions) different systems have been designed and constructed. Rainfall simulation takes place through a distribution system which includes a series of atomising mist nozzles located at the top cover. Water, under a pressure of 600kPa, passes through a solenoid valve into the nozzles ensuring that the formed water droplets have a small size. In this pressure, mist nozzles produce water droplets with a mean diameter of $30\mu\text{m}$ and, providing that the designed centrifuge acceleration is $60g$, the mean size of the droplets corresponds to a prototype size of 1.8mm. In nature, rain droplets rarely grow larger than 5mm owing to the stability of the droplet under drag forces [5]. The position of the spraying nozzles depends on two factors, the prevention of soil erosion due to the impact pressure and the minimization

of Coriolis effect. The latter refers to the deformation of the movement projection of an object when this is moved in the plane of rotation and it is an effect which needs to be eliminated. To meet these requirements, the vertical distance between the surface of the model and the spraying nozzles is designed to be between 70 and 100mm.

Based on Dalton's law, the initiation of evaporation process within a climatic chamber requires one of the following conditions to be met: increased wind speed; increased temperature at the surface of the model and as a consequence the saturation vapour pressure; reduction of the vapour pressure on the atmosphere either by reduction of the temperature or the relative humidity (RH) [13]. In the current tests, dryness of the soil model will be driven by air exchange between the climatic chamber and the environment using an air circulation system installed on the top cover. The reduction of the RH of the air within the climatic chamber will cause the evaporation of the pore water, and therefore soil's dryness, as a result of the tendency of the pore air to come into equilibrium with the air above the model.

A groundwater control system will be fixed to ensure a controlled groundwater table within the soil slope and to prevent sufficient drying of the model during the centrifuge flight. This includes the installation of two vertical standpipes at both sides of the model. These will be connected with the climatic chamber, allowing water to drain through the soil. The level of the water inside the tubes will be measured all the time by using LVDTs and it will be controlled by providing or removing water, according to the needs of the test.

A recording system with a high-speed digital camera with a frame rate of 15 fps is going to be used for capturing high-quality images of the slope model through the transparent Perspex window. For the measurement of deformations during the centrifuge tests, Particle Image Velocimetry (PIV) method [14] will be used.

3 Soil Slope Models

Three sets of centrifuge tests will be carried out, each one of them in a different soil type. The soil types used for the formation of the slope models are sand, silty clay and clay.

For the sandy models, Leighton Buzzard Sand (Fraction E) will be used. That is fine-grained sand with D_{10} at 0.095mm and D_{50} at 0.12mm [15]. The maximum dry density and optimum moisture content for compaction were determined using the Heavy Compaction method (BS1377:Part 4:1990). These are 1.61 Mg/m^3 and 11%, respectively. Also, the minimum dry density was determined at 1.33 Mg/m^3 and the maximum and minimum void ratio at 0.99 and 0.65, respectively. The coefficient of permeability is $1.44 \times 10^{-4} \text{ m/s}$ and is estimated using Hazen's approximation ($k = 100D_{10}^2$).

The silty clay soil used in this study comes from the Scrooby Top Quarry in South Yorkshire. It consists of clay (49%), silt (39%) and sand (12%). The petrographic examination showed that the great proportion of the material consists of quartz (68%) and quartzite (19%), with minor proportions of sandstone and chert, and traces of alkali feldspar, ironstone, limestone, opaque minerals, calcitic sandstone, shell, coal

and shale. Its liquid limit was determined to be 51% and the plastic limit 33%, with the plasticity index at 18%.

A third series of tests will be carried out in clayey slopes. The material which will be used in this series is Speswhite kaolin clay, known also as *China Clay*. The specific gravity (G_s) of Speswhite kaolin is 2.60 and its Liquid and Plastic limits are 61% and 27%, respectively [15]. From one-dimensional consolidation tests in Speswhite kaolin, performed in a standard oedometer, the coefficient of compression (C_c) determined at 0.47, Young's Modulus (E_o) ranges between 1.2 and 7.5, coefficient of consolidation (C_v) lies between 1 and 4 (with σ_v between 0 and 200 kPa) and the coefficient of permeability (k) ranges between 1.1×10^{-10} and 5.1×10^{-9} m/s, assuming E_o constant and equal to 7.5 MPa [16].

Two different slope angles will be examined for each soil type. The intensity of rainfall which will be applied to each model will be a function of the soil's permeability. The dimensionless factor k/I_r applied to each model will be set to 0.5 and 1, indicating two different rainfall and, therefore, infiltration conditions within the soil mass.

4 Scaling Laws

Scaling laws are derived from the need to ensure stress similarity between the model and the corresponding prototype. It is well known that soil behaviour depends on the stress level and stress history and, also, that in-situ stresses change with depth, so it is necessary to replicate these features during centrifuge modelling. For this reason, a small-scaled model is placed at one end of the centrifuge arm and is subjected to an inertial radial acceleration field which, for the model, turns to be an increased gravity field.

Table 1. Scaling factors for the testing parameters involved in this study

Parameter	Model	Prototype
Length (macroscopic)	1	N
Seepage velocity	1	$1/N$
Seepage time (macroscopic)	1	N^2
Total rain	1	N
Rain duration	1	N^2
Rain intensity	1	$1/N$
Seepage time (microscopic)	1	N
Hydraulic gradient (macroscopic)	1	$1/N$
Hydraulic gradient (microscopic)	1	$1/N$

Soil model, held in a container, has an unstressed upper surface while in-situ stresses are increasing with depth at a rate which depends on the soil density and the strength of the acceleration field. If the model is subjected to an inertial acceleration field of N times the Earth's gravity, the vertical stresses at a depth h_m will be identical to those in the corresponding depth h_p of the prototype, with $h_p = Nh_m$, providing that the same soil type is used and the stress history has been replicated accurately. This is

the basic scaling law of centrifuge modelling, stating that stress similarity in model and prototype is achieved if the model has been scaled-down by N times, in respect to the prototype, and is subjected into an acceleration of N times Earth's gravity. Seepage velocity is N times higher in the model under Ng centrifugal acceleration, so the velocity of the infiltrated water in the prototype must be scaled down by $1/N$ [18]. Also, the seepage time will be N^2 times less than the prototype as the seepage length is N times shorter in the model.

The duration of the rainfall in the model will be N^2 times less than that of the prototype and the total rainfall (expressed as height of water) will be N times less than that of the prototype. Finally, the rainfall intensity will be N times higher in the model than in the prototype. For example, if a 24h rainfall event with constant intensity of 15mm/hr is to be simulated at an acceleration of 60g, the modelled rainfall event should have intensity of 900mm/hr for a period of 24sec. Scaling factors of the most important parameters involved in this study can be seen in Table 1.

5 Instrumentation

5.1 Relative Humidity and Temperature

The Relative Humidity (RH) and Temperature (T) measurements within the climatic chamber will be performed using a couple of HMP60 Vaisala Humidity and Temperature probes. They consist on an IP65 stainless steel body and a membrane filter which is mounted at one side, while they provide accurate measurements of RH (0-100% measuring range with a typical mean accuracy of $\pm 4\%$) and T (measuring range from -40 up to $+60$ °C, with a typical accuracy of ± 0.6 °C). These sensors are going to be installed at the two ends of the climatic chamber, in positions where no water will be sprayed. This will ensure reliable measurements during the application of rainfall events. Also, their positions will be away from the air inlet and outlet units of the evaporation system in order to prevent the influence of the wind to the measurements.

5.2 Pore Water Pressures

Reliable measurement of pore water pressure before, during and after the application of rainfall events at the soil slope models is crucial for the understanding of their elemental behaviour. Therefore, it is important to use reliable sensors with very small size so as to prevent the disturbance and reinforcement of the soil models.

Two types of sensors are going to be used during this series of tests, the Druck PDCR-81 Pore Pressure Transducers (PPTs) and the SWT5 tensiometers. These sensors are being used primarily for measuring positive pore water pressures; however, they can also be used as negative pore water pressure measurement devices and in order to do so the filter element they bring needs to be very well saturated. To achieve very high degree of saturation, a new apparatus (Fig. 2) has been designed and implemented, based on a previous research work [19]. This device is made of brass and brings 8 slots for the instantaneous saturation and testing of 8 sensors, preventing their drying out during the waiting time between saturation and centrifuge testing.

A de-airing water system has been implemented to this configuration ensuring that the water used for the saturation process contains significantly reduced amount of dissolved oxygen, preventing the formation of large air bubbles at high negative pressures. The de-airing process was applied to distilled water and these results can be seen in Table 2. Compressed air is used for applying positive water pressure in the system, through an air-water interface, while negative pressures are applied through a vacuum pump.

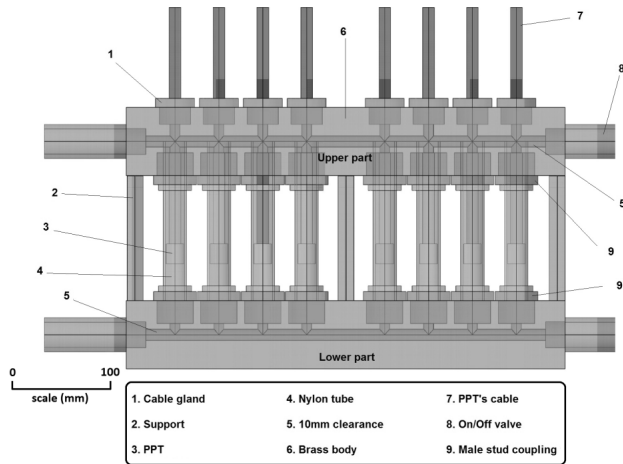


Fig. 2. Saturation and calibration apparatus for PPTs and SWT5 tensiometers (x-ray view)

Table 2. Results from the de-airing of distilled water. The first column contains the percentage of Dissolved Oxygen (DO) in the water in comparison to the amount of oxygen in the air (100%) and the second column milligrams of oxygen per litre of water. The abbreviations T and P stand for temperature of water and pressure within the laboratory, respectively.

	DO (%)	DO (mg/l)	T (°C)	P (mbar)
Distilled water	88.1%	7.61	21	991
De-aired distilled water	56.1%	4.89	21	991

Druck PDCR-81 PPT. The main advantage of the Druck PPTs is their miniature size (Fig. 3) which allow for the minimum disturbance of the small-scaled slope models. Their measuring range is between 3 and 7 bar and they bring a porous stone with an air entry value of 1bar. They are primarily used for measuring positive pore water pressures, but they can also measure negative pore water pressures (suctions) when the filter element (porous stone) is very well saturated. For that reason, a rigorous program of filter saturation has been used to ensure high degree of saturation for the porous stone.

The saturation of these sensors includes the application of repeated cycles of positive and negative pressure [19]. The process involves the application of an initially low pressure (near 0kPa of absolute pressure or -100kPa in respect to the atmospheric) for about 15 minutes and then the application of positive pressure of 100kPa for 30 minutes. The same saturation procedure was applied, also, to this case improving significantly the performance of these sensors at negative pore pressures measurements.

Prior to the centrifuge testing, PPTs were calibrated using the saturation and calibration apparatus. The results can be seen in Fig. 4. In this case, PPTs have been saturated using the procedure described above.

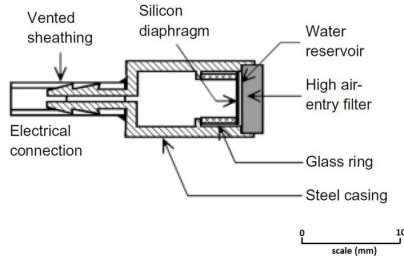


Fig. 3. Druck PDCR-81 Pore Pressure Transducer [20]

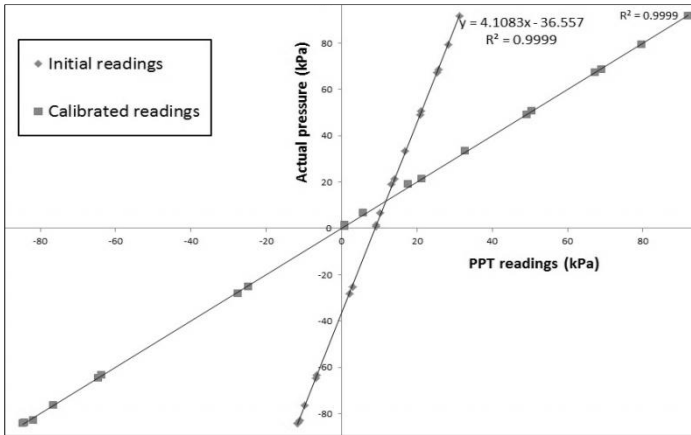


Fig. 4. Calibration of Druck PDCR-81 PPTs

SWT5 Tensiometers. These sensors (Fig. 5) can also be used for measuring negative pore water pressures, while the small size of the saturated shaft and porous stone makes them ideal for centrifuge applications. They consist of a sensor body and a 70mm long shaft fully saturated with water. A porous stone is attached at the edge of the shaft. The thickness of the shaft is 5mm, almost equal to the thickness of the PPT. During the centrifuge tests, the shaft with the porous stone will be inserted within the soil mass through drilled holes at the back wall of the climatic chamber. An aluminum casing will provide adequate strength to the shaft so as to withstand the high stresses

acting due to the centrifuge spinning. The part of the tensiometer which will be inserted inside the model has a length of 3mm, ensuring that reinforcement of the soil is negligible.

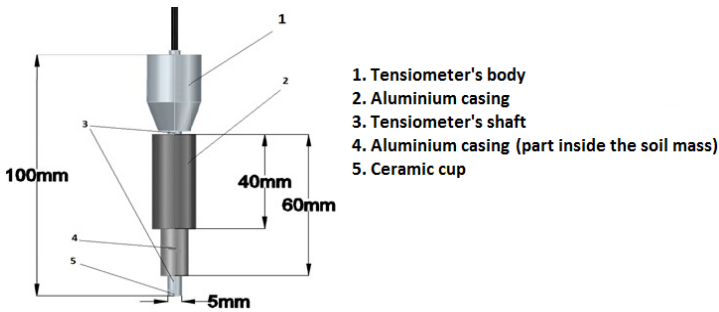


Fig. 5. SWT5 tensiometer and designed aluminum casing

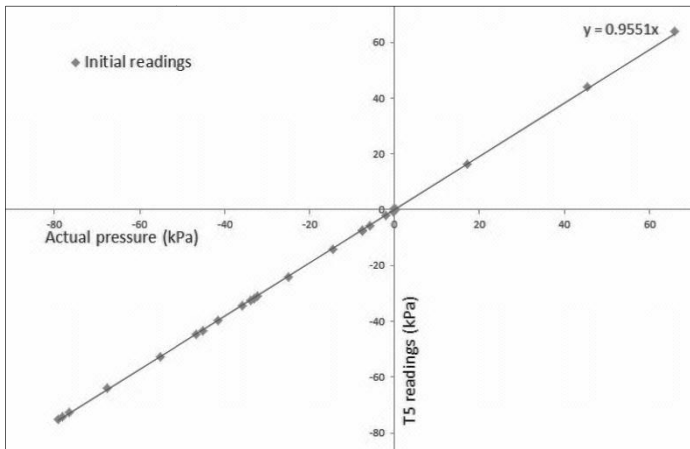


Fig. 6. Calibration of the SWT5 tensiometer and determination of the correction factor

The results from the SWT5 tensiometer testing and calibration can be seen in Fig. 6, where the tensiometer readings have been plotted against the actual readings. In this way, a correction factor of 1.047 has been determined and is used for the correction of the instrument readings.

Tests conducted on these sensors revealed the need for a very good saturation of the sensor body and the shaft. Also, after each test small bubbles appeared inside the shaft leading to incorrect measurements. For all these reasons, it is important to proceed with the saturation of the sensor body and shaft right before each centrifuge test in order to ensure the preservation of porous stone saturation. Finally, due to the fact that the contact of the porous stone with the unsaturated soil causes inevitable desaturation, calibration of the PPTs and T5 tensiometers takes place right before and exactly after each centrifuge test.

6 Conclusions

A series of centrifuge tests for the study of initiation conditions of slope failures, under rainfall, have been designed. These will be performed in the Nottingham Centre for Geomechanics geotechnical centrifuge facility. For the accomplishment of this study, a climatic chamber has been designed in order to accommodate the soil slope models and provide fully control of the climatic conditions. Pore water pressures will be measured by two different types of sensors, Druck PPTs and SWT5 tensiometers. The saturation process of these sensors is very important in order to ensure reliable measurements of both positive and negative pore water pressures throughout the test procedure. Deformations will be observed and optically measured, using PIV, through a transparent boundary and with the use of a high-speed camera. Three different soil types will be used to form the slope models and two different rainfall intensities will be used for the rainfall simulation. Results will form a very well documented database, with well-defined initial and boundary conditions, which can be used as feedback to the validation of numerical models dealing with the prediction of slope stability under rainfall conditions.

Acknowledgement. Authors would like to acknowledge the People Programme (Marie Curie Actions) of the European Union's Seventh Framework Programme FP7/2007-2013/ under REA grant agreement n° 289911 for funding this research.

References

1. Brand, E.W.: Landslides in Southeast Asia: a state-of-the-art report. In: 4th Int. Symposium on Landslides, vol. I, pp. 17–59. Canadian Geotechnical Society, Toronto (1984)
2. Fourier, A.B.: Predicting rainfall-induced slope instability. *Proceedings of the Institution of Civil Engineers / Geotechnical Engineering* 199(4), 211–218 (1996)
3. Craig, W.H., Bujang, B.K.H., Merrifield, C.M.: Simulation of Climatic Conditions in Centrifuge Model Tests. *Geotechnical Testing Journal* 14(4), 406–412 (1991)
4. Kimura, T., Takemura, J., Suemasa, N., Hiro-oka, A.: Failure of fills due to rainfall. In: Ko, H.Y., MvLean, F.G. (eds.) *Centrifuge 91*, Boulder, Colorado, pp. 509–516. Balkema, Rotterdam (1991)
5. Take, A.W.: The Influence of Seasonal Moisture Cycles on Clay Slopes. PhD thesis. University of Cambridge (2003)
6. Hudacsek, P., Bransby, M.F., Hallett, P.D., Bengough, A.G.: Centrifuge Modelling of Climatic Effects on Clay Embankments. *Engineering Sustainability* 162(2), 91–100 (2009)
7. Askarinejad, A., Laue, J., Zweidler, A., Iten, M., Bleiker, E., Buschor, H., Springman, S.M.: Physical modelling of rainfall-induced landslides under controlled climatic conditions. In: *EuroFuge 2012*, Delft, Netherlands (2012)
8. Springman, S.M., Askarinejad, A., Casini, F., Friedel, S., Kienzler, P., Teyssere, P., Thielen, A.: Lessons learnt from field tests in some potentially unstable slopes in Switzerland. *Acta Geotechnica Slovenica* 9, 5–29 (2012)
9. Min, Z.: Centrifuge Modelling of Potentially Liquefiable Loose Fill Slopes with and Without Soil Nails. PhD thesis. Hong Kong University of Science and Technology (2006)

10. Take, W.A., Bolton, M.D., Wong, P.C.P., Yeung, F.J.: Evaluation of landslide triggering mechanisms in model fill slopes. *Landslides* 1(3), 173–184 (2004)
11. Tamate, S., Naoaki, S., Toshiyuki, K.: Simulation of Precipitation on Centrifuge Models of Slopes. *International Journal of Physical Modelling in Geotechnics* 12(3), 89–101 (2012)
12. Ellis, E.A., Cox, C., Yu, H.S., Ainsworth, A., Baker, N.: A new geotechnical centrifuge at the University of Nottingham, UK. In: Ng, Zhang, Wang (eds.) 6th ICPMG 2006, pp. 129–133. Taylor & Francis Group, London (2006)
13. Caicedo, B., Tristancho, J., Thorel, L.: Centrifuge modeling of soil atmosphere interaction using a climatic chamber. In: Springman, S., Laue, J., Seward, L. (eds.) *Physical Modelling in Geotechnics*, pp. 299–305. CRC Press, Leiden (2010)
14. White, D.J., Take, W.A., Bolton, M.D.: Soil deformation measurement using particle image velocimetry (PIV) and photogrammetry. *Géotechnique* 53(7), 619–631 (2003)
15. Zhao, Y.: In situ soil testing for foundation performance prediction. PhD thesis. University of Cambridge (2008)
16. Stewart, D.P.: Lateral Loading of Pile Bridge Abutments Due to Embankment Construction. PhD thesis. University of Western Australia, Perth (1992)
17. Gouvernec, S., Acosta-Martinez, H.E., Randolph, M.F.: Experimental Study of Uplift Resistance of Shallow Skirted Foundations in Clay under Transient and Sustained Concentric Loading. *Géotechnique* 59(6), 525–537 (2009)
18. Schofield, A.N.: Cambridge Geotechnical Centrifuge Operations. *Géotechnique* 30(3), 227–268 (1980)
19. Take, W., Bolton, M.: Tensiometer saturation and the reliable measurement of matric suction. *Geotechnique* 53(2), 159–172 (2002)
20. König, D., Jessberger, H.L., Bolton, M.D., Phillips, R., Bagge, G., Renzi, R., Garnier, J.: Pore pressure measurement during centrifuge model tests: Experience of five laboratories. In: Leung, C.F., Lee, F.H., Tan, T.S. (eds.) *Centrifuge 1994*, pp. 101–108. Balkema, Rotterdam (1994)

Shallow Tunnelling in Partially Saturated Soil Numerical Analysis of the Contribution of Dewatering to the Enhancement of Face Stability

Enrico Soranzo, Roberto Tamagnini, and Wei Wu

Institut für Geotechnik, Universität für Bodenkultur, Vienna, Austria
{enrico.soranzo,roberto.tamagnini,wei.wu}@boku.ac.at
<http://www.baunat.boku.ac.at/igt>

Abstract. Partially saturated soils exhibit higher shear strength than saturated soils. Shallow tunnels are often driven closely to or inside the saturated layers. The water table is sometimes lowered to excavate the tunnel in a partially saturated condition. In doing so, the face stability is improved and the necessary support pressure can be reduced. In this paper a numerical study is performed to assess the effect of dewatering on the face stability of shallow tunnels. The analyses are performed with an advanced constitutive model for partially saturated soil. The model is implemented in a commercial software using the Bishop's effective stress for the equilibrium equation.

Keywords: dewatering, numerical, partially saturated, shallow tunnel.

1 Introduction

Shallow tunnels can be driven below the water table with modern TBMs, whereas with the NATM the water table is lowered below the tunnel invert to generate a layer of partially saturated soil ahead of the tunnel face and to enhance the shear strength of the soils. The stability of the tunnel face has been assessed theoretically, with limit plasticity [2,3],[6] and limit equilibrium methods, and experimentally, both in simple scaled models [4] and in the geotechnical centrifuge [5]. Some numerical parametric studies are also available [9], resulting in approximate solutions for the prediction of the limit support pressure to prevent collapse of the tunnel face. Numerical analysis is certainly the suitable tool in tunnel engineering, especially when dealing with heterogeneous soil properties and complex boundary conditions. The effectiveness of numerical analysis is bounded by two aspects: the capability of the numerical software to reproduce the considered phenomenon and the performance of the constitutive model. In this study, the commercial software ABAQUS is chosen, as the equilibrium equation is written in terms of the Bishop's effective stress tensor, and the extended Cam Clay model by Tamagnini [7] is used for simulations.

2 An Advanced Constitutive Model for Partially Saturated Soil

Tamagnini, R. [7] has formulated an extension to the Cam-clay model for partially saturated soils replacing Terzaghi's mean effective stress by

$$p' = (p - u_a) + S_r(u_a - u_w) \quad (1)$$

where u_a and u_w are the air and water pressure respectively, and S_r replaces the weighting factor χ proposed by Bishop & Blight [1]. The difference $u_a - u_w$ is called *suction* and will be identified by s in the following. Elasticity is defined as in the original Cam-clay model

$$\dot{\varepsilon}_v^e = \frac{1}{K} \dot{p}' \quad (2)$$

$$\dot{\varepsilon}_d^e = \frac{1}{3G} \dot{q} \quad (3)$$

where q is the deviatoric stress, and $\dot{\varepsilon}_v^e$ and $\dot{\varepsilon}_d^e$ are the elastic volumetric and deviatoric strain rate respectively.

$$K = \frac{v}{\kappa} p' \quad (4)$$

is the bulk modulus, v is the specific volume, κ is the slope of the elastic unloading-reloading line, and G is the shear modulus. The yield locus has the usual form:

$$f = q^2 + M^2 p'(p' - p_c) = 0 \quad (5)$$

where M is the slope of the critical state line in the $p' - q$ plane, and p'_c is the preconsolidation pressure describing the isotropic hardening. As associated flow rule and a double hardening mechanism are used:

$$\dot{p}'_c = \dot{p}'_{c_{\text{sat}}} + \dot{p}'_{c_{\text{unsat}}} \quad (6)$$

where

$$\dot{p}'_{c_{\text{sat}}} = \frac{v p'_c}{\lambda - \kappa} \dot{\varepsilon}_v^p \quad (7)$$

and

$$\dot{p}'_{c_{\text{unsat}}} = -b p'_c \dot{S}_r \quad (8)$$

The latter one describes the evolution of the yield function produced by changes in the saturation degree, which may occur even if the current stress lies in the elastic domain. Equation 8 introduces the only new constitutive parameter b

that controls the rate of change in p'_c caused by changes in S_r . Failure is simply modelled by

$$q^f = Mp' \quad (9)$$

The model considers two limit SWCCs for the drying and the wetting case joined by linear scanning curves

$$\dot{S}_r = -k_s \dot{s} \quad (10)$$

2.1 Model Features

Figure 1.a shows an isotropic compression in fully saturated condition ($s = 0$) followed by a suction increase, that expands the yield locus. Figure 1.b depicts an ideal test that has been numerically analysed in order to verify the capability of the constitutive model to overcome mesh dependency in occurrence of softening under wetting collapse. The same numerical test is performed for different mesh refinements in plane strain conditions (Figure 2). In Figure 1.b, isotropic compression \overrightarrow{BC} is followed by the displacement-controlled triaxial compression of the upper boundary of the mesh of Figure 2 (\overrightarrow{CD}). Thereafter, the samples are saturated starting from the boundary, following the path \overrightarrow{DE} , to simulate the wetting collapse and the contribution of partial saturation on the deviatoric component of the stress. The test results are shown in Figure 3 for OC (Overconsolidated) and NC (Normal Consolidated) conditions. The curves descend from the peak value following fairly similar paths, hence suggesting the results are not affected by mesh sensitivity.

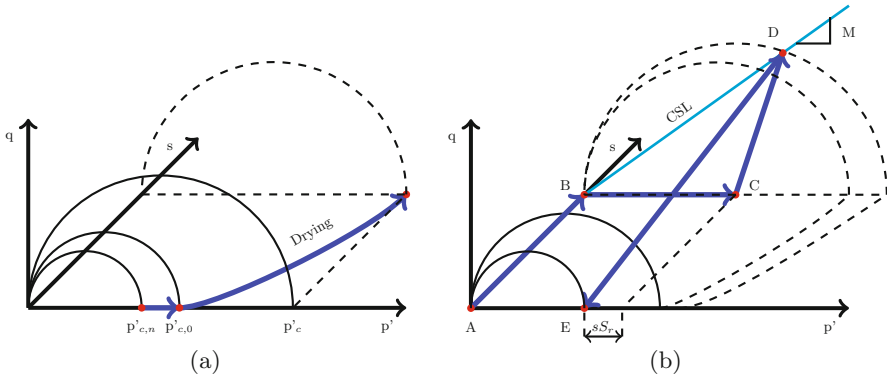


Fig. 1. Model features: (a) mechanical hysteresis, (b) wetting collapse

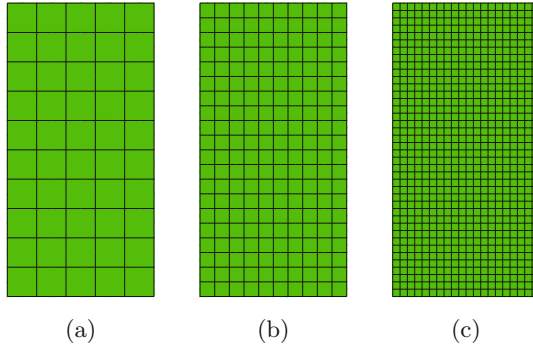


Fig. 2. Mesh refinement: (a) coarse, (b) intermediate, (c) fine

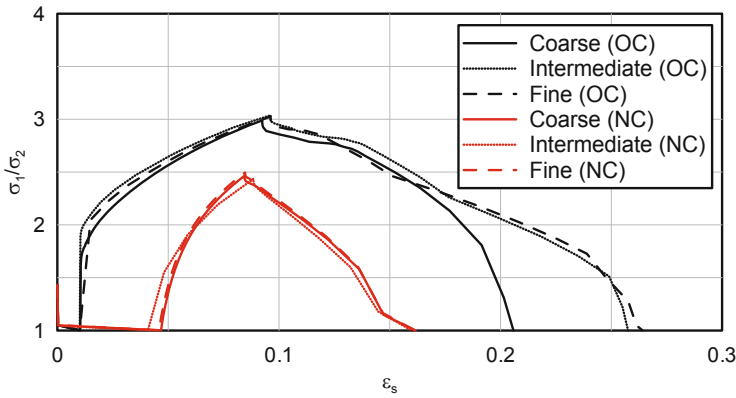


Fig. 3. Drained triaxial compression and wetting of partially saturated soil samples

3 Numerical Analysis

The extended Modified Cam Clay constitutive model was implemented by Tamagnini, R. [8] in a UMAT subroutine with implicit integration scheme for the commercial FE software ABAQUS. A mesh consisting of 1677 nodes and 528 elements is generated, having the geometry indicated in Table 1 and Figure 4. The material parameters of Table 2 are assigned together with SWCC of Figure 5 (the hysteresis is omitted in sake of simplicity) and the water table is set subsequently to the different configurations $W_{0...3}$ of Figure 4, as shown in Figure 6. After the geostatic step, the constraints at the tunnel face are removed stepwise to simulate the release of the support. The horizontal stress and the corresponding displacement are measured at control point CP1 of Figure 4 and the resulting diagrams are shown in Figure 7 for different positions of the water table.

Table 1. Geometry

C	D	W_1	W_2	W_3
(m)	(m)	(m)	(m)	(m)
2.5	5	2.5	3.75	5

Table 2. Soil parameters

ρ_d	k	κ	λ	M	ν	p_{c0}	b
(kg/m^3)	(m/s)					(kPa)	
1700	10^{-6}	0.003	0.071	1	0.3	150	10

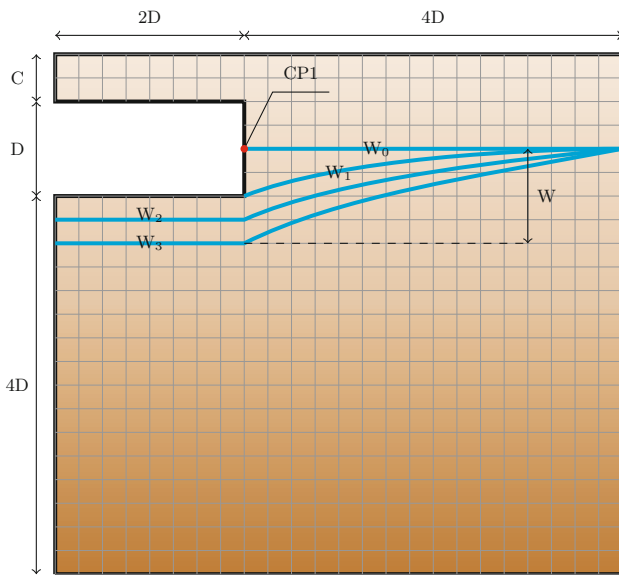


Fig. 4. Dewatering

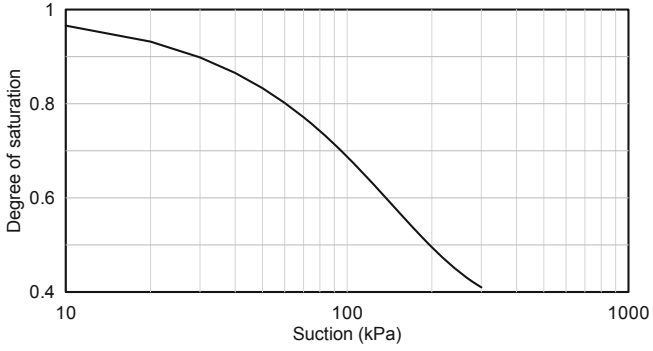


Fig. 5. Soil-Water Characteristic Curve

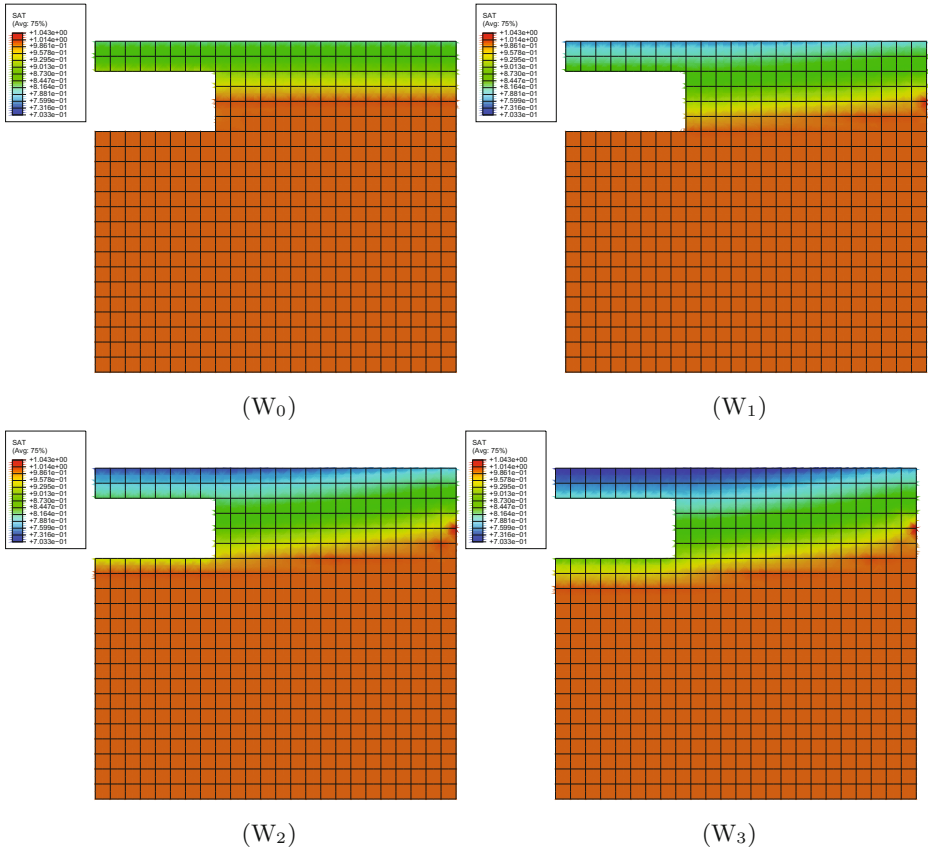


Fig. 6. Degree of saturation for different position of the water table

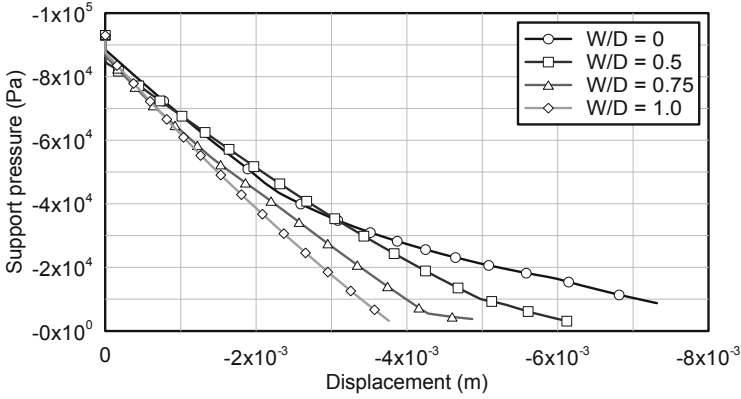


Fig. 7. Support pressure vs. displacement diagram

3.1 Wetting Collapse

To investigate the capability of the extended Cam Clay model by Tamagnini, R. in the simulation of the collapse of the tunnel, the upper boundary is saturated (e.g. as a consequence of heavy rainfall) imposing zero pore water pressure at the ground level. The induced downward water flow saturates the upper layer, inducing the failure of the tunnel face. Two cases were considered: in the first case the constitutive parameter b is set equal to ten and an initial preconsolidation pressure p_{c0} of 250kPa is prescribed and the yield locus is let automatically expand in the geostatic step as an effect of the model; in the second case, the constitutive parameter b is set equal to zero, and the initial preconsolidation pressure is obtained integrating Equation 8, resulting in Equation 11.

$$p_c = p_{c0} e^{b(1-S_r)} \quad (11)$$

The water table is located 2.50m below the tunnel invert and it is supposed to be not affected by the rate of the degree of saturation, and the degree of saturation at the tunnel centreline is 0.76. With this degree of saturation, parameters $p_{c0} = 250\text{kPa}$ and $b = 10$ and $S_r = 0.76$, Equation 11 returns $p_c = 2756\text{kPa}$. This preconsolidation pressure is used in the simulation with $b = 0$ as resumed in Table 3.

Table 3. Wetting simulations

b	p_{c0} (kPa)	p_c (kPa)
0	2756	2756
10	250	$250e^{b(1-S_r)}$

The horizontal, the deviatoric and the mean effective stresses, the void ratio and the yield function are measured at a Gauss point close to CP1 and the resulting diagrams are shown in Figures 8–10. Figure 8 shows the effect of the model: the two lines diverge drastically at a displacement of about 3mm and the Cam-clay for partly saturated soil predicts a collapse of the tunnel, whereas the model with constitutive parameter $b = 0$ allows for an equilibrium condition at an elastic displacement of 4mm. Figure 9 shows that the plastic condition ($f = 0$) is obtained only for the model with $b = 10$ at a value of 40kPa of mean effective stress. The model impact on the volumetric deformation is assessed in Figure 10.

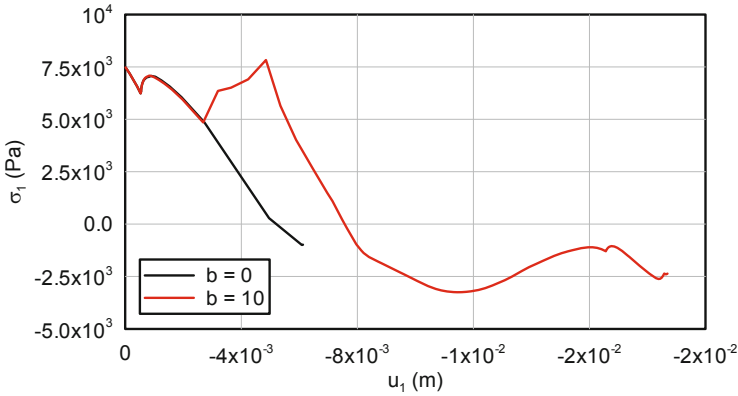


Fig. 8. Horizontal stress vs. mean effective stress

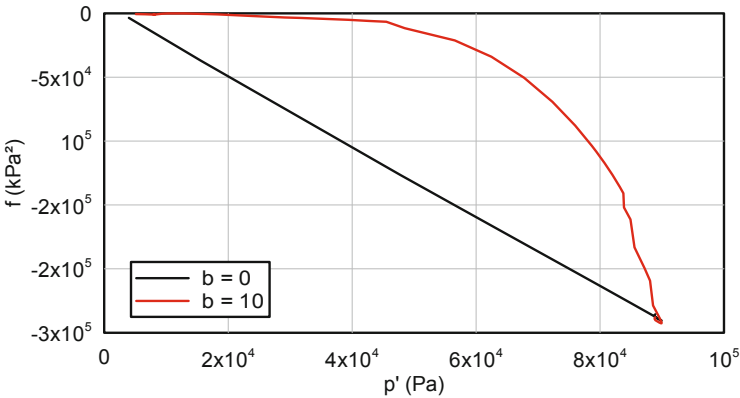


Fig. 9. Yield function vs. mean effective stress

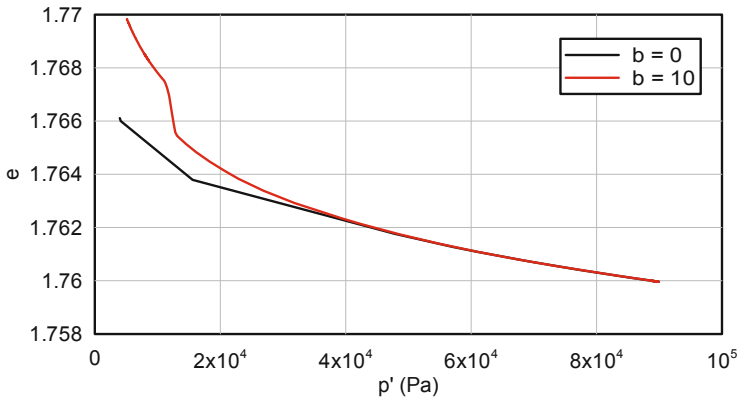


Fig. 10. Void ratio vs. mean effective stress

4 Conclusions

The results demonstrate the capability of numerical analysis in conjunction with appropriate constitutive modelling, to model the positive contribution to local stability of shallow tunnels after dewatering ahead of the face. A prerequisite for such analyses is the use of an appropriate numerical software in which the equilibrium equation is written in terms of Bishop's stress tensor and the adoption of an appropriate constitutive model that is capable of reproducing the stiffening effect of partial saturation. Such a constitutive model should also be able to simulate collapse of the tunnel when the soil ahead of the face of a very shallow tunnel undergoes saturation as a consequence of an intense precipitation. The results obtained with a commercial FE software in conjunction with the extended Cam Clay by Tamagnini, R. are reasonable both in the assessment of the face support pressure and in the prediction of the rainfall-induced collapse of the tunnel face.

References

1. Bishop, A.W., Blight, G.E.: Some aspects of effective stress in saturated and partly saturated soils. *Géotechnique* 13, 177–197 (1963)
2. Davis, E.H., Gunn, M.J., Mair, R.J., Seneviratne, H.N.: The stability of shallow tunnels and underground openings in cohesive material. *Géotechnique* 30, 397–416 (1980)
3. Leca, E., Dormieux, L.: Upper and lower bound solutions for the face stability of shallow circular tunnels in frictional material. *Géotechnique* 40, 581–606 (1990)
4. Kirsch, A.: On the face stability of shallow tunnels in sand. In: *Advances in Geotechnical Engineering and Tunneling*, vol. 16 (2009)
5. Mair, R.J., Taylor, R.N.: Bored tunnelling in the urban environment. In: *Proceedings of the 14th International Conference on Soil Mechanics and Foundation Engineering*, pp. 2353–2385 (1997)

6. Mühlhaus, H.B.: Lower Bound Solutions for circular Tunnels in Two and Three Dimensions. *Rock Mechanics and Rock Engineering* 18, 37–52 (1985)
7. Tamagnini, R.: An extended Cam-Clay model for unsaturated soils with hydraulic hysteresis. *Géotechnique* 54, 223–228 (2004)
8. Tamagnini, R.: The influence of hydraulic hysteresis on unsaturated soils FE analyses. In: *Unsaturated Soils: Numerical and Theoretical Approaches*. Springer Proceedings in Physics, vol. 94, pp. 67–80 (2005)
9. Vermeer, P.A., Ruse, N., Marcher, T.: Tunnel Heading Stability in Drained Ground. *Felsbau* 20, 1–17 (2002)

Modeling the Impact of Granular Flow against an Obstacle

Adel Albaba^{1,2}, Stéphane Lambert¹, François Nicot¹, and Bruno Chareyre²

¹ Irstea, UR ETGR, 2 rue de la papeterie, 38402 St-Martin d'Hères, France

{adel.albaba, stephane.lambert, francois.nicot}@irstea.fr

² 3SR, UJF-INPG-CNRS-UMR5521, DU Grenoble Université, 38041 Grenoble, France

bruno.chareyre@inp-3sr.fr

Abstract. This paper presents a numerical model based on Discrete Element Method (DEM) used to reproduce a series of tests of dry granular flow. The flow was composed of poly-dispersed coarse-grained angular particles flowing in an inclined flume and interacting with a divided rigid wall. The normal impact force against the wall has been studied in details considering the force on each part of the wall. The model has been calibrated based on the flow thickness measurements. By quantitative comparison with experimental data, the model showed good agreement in terms of peak force on each part of the wall, the time of the peak and also the residual force values at the end of the tests.

Keywords: DEM, Granular flow, Obstacle, Impact, Numerical modeling.

1 Introduction

The urbanization of the mountainous areas raised the importance of mitigating the threats to people and infrastructures linked to natural hazards such as rockfalls and granular flows. Several catastrophic granular flow events (Fig. 1) happened in the past resulting in major catastrophes and large loss of lives.

Granular flows has been classified as one of the most hazardous landslides due to its high flow velocity and impact forces, long runout distance and poor temporal predictability [1]. More specifically, dry granular flows produced by shallow slope failures were found to travel long distances destroying infrastructures and blocking vital roads. In terms of formation, they contain large blocks of gravel and rock fragments.

Granular flows hazard can be limited using retention systems similar in principle to rockfall barriers [3]. Different protection structures have been proposed in the literature for the mitigation of natural hazards; they are mainly retaining walls or flexible structures. Retaining walls have been widely used in China and also in Japan [4] for the prevention of rockfalls and granular flows. For the same reason, different types of flexible structures using anti-submarine nets have been developed over the last decades [5,6].



Fig. 1. Dry granular flow after Wenchuan earthquake, China [2]

Several researches have been carried out in order to model granular flows. On one hand, continuum treatment has often been adopted where flows characteristics are analyzed by the Eulerian forms of continuity and momentum equation [7,8,9].

On the other hand, with the use of a Discrete Element Method (DEM), Silbert et al. [10] carried out 2D and 3D simulations of mono-dispersed particles flowing in a chute in a steady-state condition where observations were taken regarding structure and rheology of the flow. DEM was also used to simulate a rock avalanche event that took place in Italy [11]. Faug et al. [12] proposed a hydrodynamic model based on depth-averaged momentum conservation which was used to predict DEM numerical results of a free-surface gravity-driven dense flow overflowing a wall.

On the experimental side, various experiments have been conducted ranging from studies on geological debris flows to well characterized laboratorial granular flows down an inclined plane [13], [8], [14]. Furthermore, Faug et al. [15] experimentally investigated the dead zone formation of glass beads behind an obstacle down an inclined channel. In addition, other DEM models were validated against small tests experiments in different slopes for better prediction of runout distances and impact force against obstacles [16].

However, none of the experiments considered coarse-grained flow of angular particles which is the main case for dry granular flow. To serve this purpose, Jiang and Towhata [2] recently studied the impact behavior of dry granular flow against a rigid retaining wall using poly-dispersed mixture of limestone gravel. Measurements of normal impact force vs. time were recorded along with observations of flow thickness and flow velocity.

The aim of this paper is to present a model capable of simulating the impact of dry coarse-grained flow against a rigid wall taking into account the shape effect of the angular particles. First, we will describe the model in terms of contact law, particles shape and flume characteristics. Afterwards, the model calibration and validation are presented with discussion of obtained results. Finally conclusions of the presented work are drawn.

2 Numerical Modeling

The numerical simulation of the dry granular flow was carried out using Discrete Element Method. Nowadays DEM is widely used for modeling granular media. It is particularly efficient for static and dynamic simulation of granular assemblies where medium can be described at a microscopic scale. The method is based on the molecular dynamics approach proposed by Cundall and Strack [17].

In comparison with Finite Element Method (FEM), DEM makes large displacements between elements easy to simulate. In addition, DEM surpasses FEM when dealing with discontinuous problems where FEM becomes computationally demanding [18].

YADE software has been used as a modeling tool which is an extensible open-source framework for discrete numerical models, focused on Discrete Element Method [19].

2.1 Contact Law

A visco-elastic contact law with Mohr-coulomb failure criterion (Fig. 2) has been adopted where normal and tangential contact forces F_n , F_t between particles were calculated as follows:

$$\vec{F}_n = (k_n u_n - \gamma \dot{u}_n) \vec{n} \quad (1)$$

$$\vec{F}_t = \begin{cases} \frac{k_t \vec{u}_t}{|k_t \vec{u}_t|} |\vec{F}_n| \tan \varphi & \text{if } |k_t \vec{u}_t| > |\vec{F}_n| \tan \varphi, \\ k_t \vec{u}_t & \text{otherwise} \end{cases} \quad (2)$$

Where k_n and k_t are the normal and tangential stiffness parameters, u_n and u_t are the normal and shear displacements, $\tan \varphi$ is the friction coefficient and γ is the viscous damping coefficient. k_t was taken as $(2/7)k_n$ according to what was previously suggested by [10].

Based on Schwager and Pöschel [20], with the restitution coefficient (ε) being the ratio between velocities after and before the impact, It can be calculated as follows:

$$\omega_0^2 = \frac{2k}{m_{eff}} \quad (3)$$

$$\beta = \frac{\gamma}{m} \quad (4)$$

$$\omega = \sqrt{\omega_0^2 - \beta^2} \quad (5)$$

$$\varepsilon = \frac{\dot{u}(t_c^0)}{\dot{u}(0)} = e^{-\beta \pi / \omega} \quad (6)$$

Where $m_{eff} = (1/m_1 + 1/m_2)$ and $\dot{u}(t_c^0)$, $\dot{u}(0)$ are velocities after (at the end of the contact) and before the collision respectively.

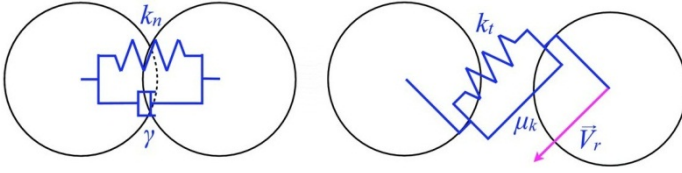


Fig. 2. Normal and tangential interaction forces of the contact [21]

It is worth noting that, in the current study, the tangential viscous damping coefficient has been set to zero (using $\varepsilon_t = 1.0$). This is due to the absence of lubricated contact (as we are dealing with a dry flow), which is usually the proposed physical explanation for accounting for tangential viscous damping coefficient [22]. Particle stiffness $k_{\text{par}} = E D/2$ where E is the Young's modulus (taken as 10^8 Pa) and D is the particle diameter. In order to ensure rigidity, the wall stiffness was taken ten times the stiffness of D_{50} particle. The value of ε was calibrated in Section 3 considering the flow thickness measurements.

2.2 Flowing Particles, Clumping and Shape Effects

Particles in use were of a poly-dispersed mixture with D_{50} of the model being 15 mm and ranging from 10 mm to 20 mm in diameter with an average friction angle of 53° (similar to the one used in [2]). With the aim of simulating angular gravels, a two-spheres clump particle was used which has great advantageous in: controlling rotational velocity, adding interlocking effect between particles and improving shape representation of the angular gravel (section 3.1). Furthermore, the simulation is kept rather inexpensive (with the use of only two particles for forming the clump). The clump consists of two identical spheres (with a radius R) overlapping over a distance R thus having an aspect ratio of $\frac{3}{2} R$.

2.3 Sample Preparation

The samples were prepared in a box with varying lengths (from 14 cm to 44 cm with a 5 cm step) and heights (from 5 cm to 20 cm with a 5 cm step) but with a 30 cm fixed width. The samples were released in a dam-break manner in which the gate was pulled up rapidly and instantaneously. With the total weight of the sample being equal to the weight of a single D_{50} -sphere multiplied by the number of particles, the number of generated particles (num) was calculated as follows:

$$num = \left(\frac{V_t \gamma_t}{V_s \gamma_s} \right) \quad (7)$$

where V_t is the total volume of the sample, γ_t is the specific weight of the sample (13.5 kN/m^3), V_s is the volume of a single D_{50} -sphere and γ_s is the specific weight of gravel particles (taken as 26.5 kN/m^3 for the limestone gravel considered). Afterwards, each spherical particle was replaced with a clump consisting of two equal

spheres. Radii of clumped-spheres were calculated so that the mass and volume of the clump is equal to that of the particle which it replaces.

2.4 Modeling of the Experimental Set Up

The flume dimensions were based on the experimental flume used by [2]. The flume was rectangular in cross section with 219 cm length, 30 cm width and 35 cm height. Different inclination angles α were tested ranging from 35° to 45° . The friction angle specified to the flume base, flume sides and the rigid wall were 25° , 15° and 21° respectively. A frictionless triggering gate was used to initiate the flow. At the end of the flume, a perpendicular rigid wall divided into six horizontal segments (marked from 1 to 6 starting from the bottom) was used. Interaction forces were recorded with each 5-cm height segment of the wall. No overflowing (topping) of the wall took place in all tests.

3 Model Calibration

With our aim being modeling granular flow of angular particles, experimental data [2] has been selected for our model calibration. Three different tests have been carried out: Test L34-H15- $\alpha 45^\circ$, Test L44-H15- $\alpha 40^\circ$ and Test L44-H20- $\alpha 40^\circ$. For instance, Test L44-H15- $\alpha 40^\circ$ represents a sample having 44 cm in length, 15 cm in height and 40° inclinational angle.

3.1 Clumps vs. Spherical Particles

A comparative study is presented showing the effect of using the clumps on capturing the shape effect of the angular particles. Two samples were tested the first having spherical particles and the second having clumped ones. The chosen clump has a lower rotational energy in comparison with the spherical particle (Fig. 3a) resulting in a denser flow. Furthermore, the final shape of the deposit is closer to reality with the clumped particle case in comparison with the spherical one. Consequently, compared with the spherical particles, peak and residual values (Fig. 3b) on the sixth segment of the wall for clumped particles are closer to the experimental (experimental values: $F_{\text{peak}} \approx 14$ N/m, $F_{\text{res}} \approx 10$ N/m). This might be due to the rolling resistance provided by the clump shape which prevents the particles from rolling over the dead zone deposit and accumulate behind part 6 of the wall.

3.2 Flow Thickness and Velocity

The measurements of flow thickness and velocity were considered at the time where the total force on the wall reaches its maximum value in order to be comparative with the experimental data (as done in the experiment). The targeted part of the flow for calculating velocity and thickness were particles within a distance ranging from 40 to 50 cm away from the wall. However, since the flow has two regimes along the flow

thickness-collisional and frictional- cumulative frequency were drawn in which thickness and velocity values were taken at 90% of total frequency. A value of $D_{50}/2$ was added to 90% cumulative frequency of the flow thickness to account for the free surface of the flow.

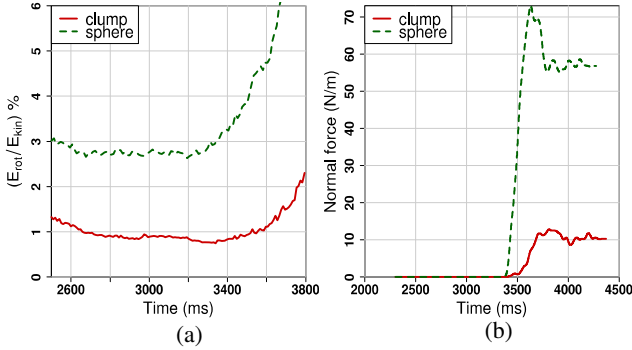


Fig. 3. (a) Ratio of rotational energy to total kinetic energy for clumps and spheres, (b) Normal force on part 6 of the wall

Different values of restitution coefficient were tested and flow thickness values were observed for each corresponding restitution coefficient. It was found that $\epsilon = 0.3$ is suitable for our flow based on flow thickness measurements resulting in a model value of 3.9 cm which well-correspond to the experimental value of 3.9 cm (Fig. 4a).

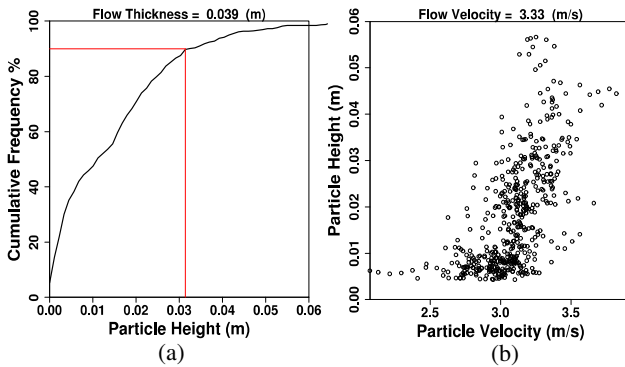


Fig. 4. (a) Cumulative frequency of gravity center of particles height, (b) Variation of particles velocity with heights

However, velocity measurements of test L44-H15- $\alpha 40^\circ$ in the model (Fig. 4b) taken at the considered flow thickness (at 90% for cumulative frequency) was found to be lower than experimental value (4.13 m/s) which still needs improvement. Above all, features of granular flow have been observed by the model showing a dilute front followed by a denser part (Fig. 5).

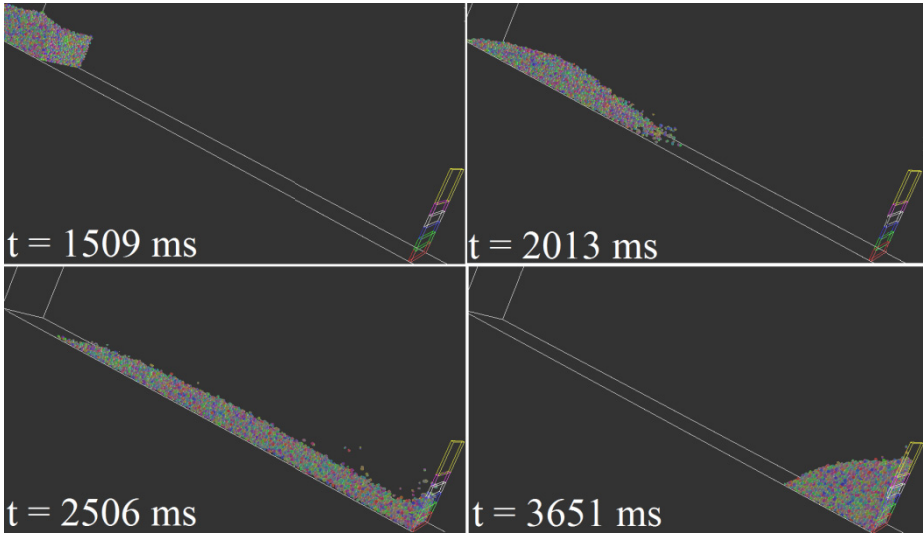


Fig. 5. 3D view of the evolution of simulated flow through time, test L44-H20- $\alpha 40^\circ$

4 Model Validation

The rigid wall response against the granular flow impact has been investigated in details. Indeed, special attention has been given to the normal force applied on each part of the rigid wall where curves of normal impact force vs. time were analyzed. Data treatment was carried out using smooth spline method where a smooth curve is fitted to a set of noisy data using spline function [23].

4.1 Test L34-H15- $\alpha 45^\circ$

In this test (Fig. 6a), the sample had 34 cm length, 15 cm height and 45° inclinational angle. On the first element of the wall (F_1), the peak force was found to be 396 N/m which is fairly close to the experimental value (around 350 N/m). Moreover, the time of the peak force F_1 is relatively similar to the experiment with a value around 3676 ms but with a lower residual force in the model (145 N/m) compared with the experiment (175 N/m) which might be due to the force chain distribution and particles shape arrangement behind the wall. Likewise, in contrast to F_1 , the peak value of F_2 in the model (256 N/m) was lower than the experimental value (300 N/m). For F_3 and F_4 , the model captured the peak time of forces fairly well (being 3883 and 3994 ms for F_3 and F_4 respectively) but with a lower peak value. The peak force and timing of the peak on F_5 and F_6 were fairly captured by the model along with their residual force values.

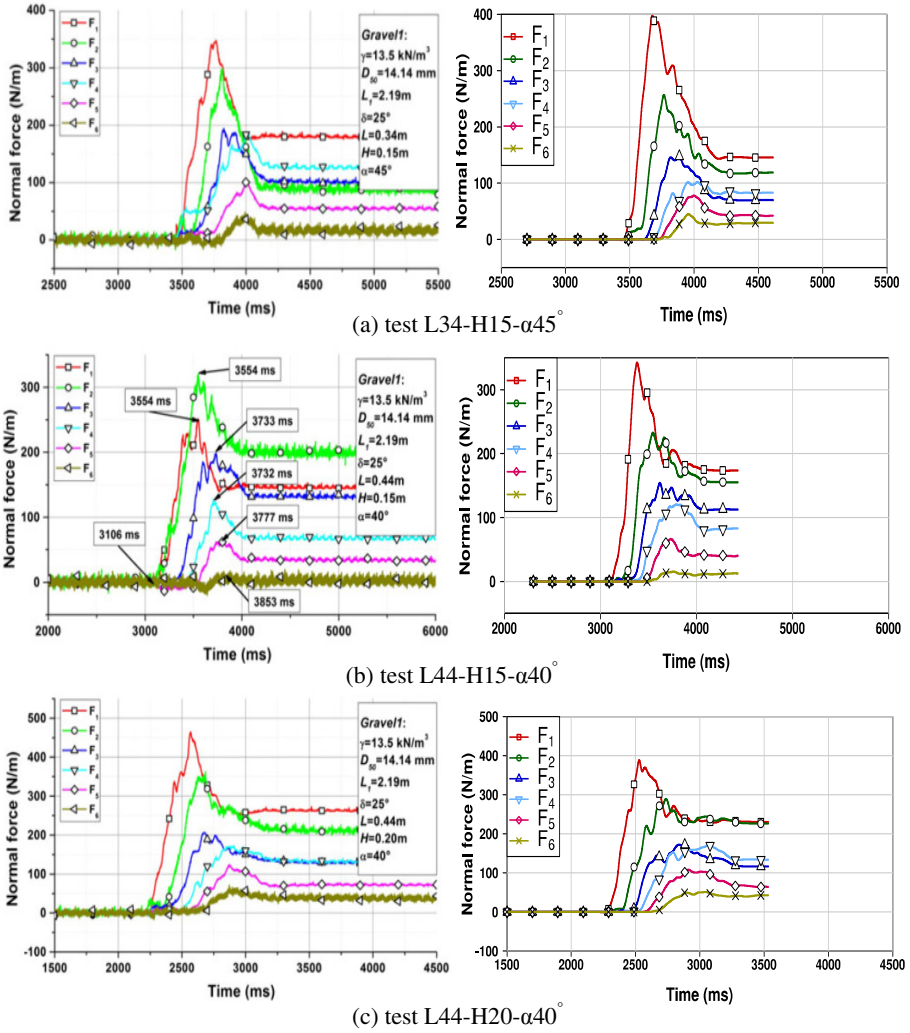


Fig. 6. Time history of normal force variation: experiment (left) [2] and model (right)

4.2 Test L44-H15- $\alpha 40^\circ$

For this test, the model recorded peak impact force values of 341 and 232 N/m for F_1 and F_2 respectively (Fig. 6b). Compared to the experiment, similar values were observed but with a reversed order ($F_2 > F_1$). According to [2], this might be due to an arching effect forming an arch-like protective layer on part 1 of the wall resulting in a non-linear distribution of force with depth. Such a layer is also thought to affect the residual force values of F_1 and F_2 . Concerning the rest parts of the wall, the model managed to capture the peak forces of F_3 , F_4 , F_5 and F_6 (with a small exception for F_3) with values of 154, 120, 66 and 15 N/m respectively along with peak times 3619,

3808, 3733 and 3761 ms respectively. Residual forces on these parts were found to be 112, 82, 40 and 12 N/m respectively which are close to the experimental observations. In terms of total normal force (Fig. 7), the model fairly agrees with the experiment in terms of the peak force (735 N/m), peak time (3733 ms) and residual total force (576 N/m).

4.3 Test L44-H20- $\alpha 40^\circ$

With the use of higher volume of the sample, the trend of the impact force curves was better captured with the model along with the time lag between each force curve. For instance, F_1 peaks at 2523 ms with a value of 387 N/m (450 N/m in the experiment) which is followed by another flow surge leading F_2 to peak with 288 N/m (340 N/m in the experiment) at 2737 ms. Residual forces of F_1 and F_2 were found to be similar to the experiment with values of 227 and 226 N/m respectively. Very good agreement has also been observed for F_3 , F_4 , F_5 and F_6 in terms of peak forces (172, 172, 108 and 51 N/m) the time of the peak (2864, 3070, 2912 and 3043 ms) and residual force values (116, 134, 65 and 43 N/m). Above all, to some extent, arching was managed to be captured in this test, especially for residual forces of F_1 - F_2 and F_3 - F_4 . This might be due to the higher volume of the sample used in this test in comparison with previous tests which permitted better representation of the experiment as larger number of particles is used.

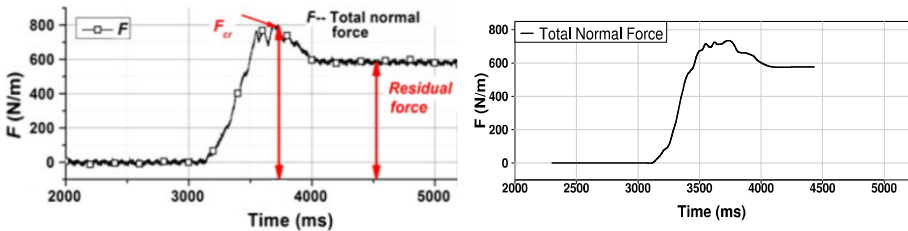


Fig. 7. Time history of total normal force variation, test L44-H15- $\alpha 40^\circ$: experiment (left) [2] and model (right)

5 Conclusions

In this paper, we have numerically studied the impact of granular flow against a rigid wall considering clumped particles. The proposed model has shown capabilities of capturing the main features of normal impact force against a rigid wall. Good agreement has been observed in terms of the peak force on each part of the wall, the time of the peak and the residual force at the end of the test. Moreover, to some extent, the model was able to account for the arching that was observed in the experiment.

Furthermore, the model shows collisional regime in the shallow layer and frictional regime in the deeper ones. The use of clumps was found to be beneficial for accounting for the shape effects caused by sharp angles of coarse-grained particles. It was shown that the use of clumped particles is preferred over the spherical particles in

controlling rotational velocity where it was reduced by 70 % with the use of clumps. Indeed, the shape of the deposition behind the wall was improved by the clumped particles leading to a force distribution which is closer to the experimental values. After being validated against rigid walls, the wall in the model will be replaced by flexible structure (net elements) in which the impact behavior will be studied in details.

Acknowledgment. The research leading to these results has received funding from the People Programme (Marie Curie Actions) of the European Union's Seventh Framework Programme FP7/2007-2013/ under REA grant agreement n° 289911.

References

1. Jakob, M., Hungr, O.: Debris-flow Hazards and Related Phenomena. Springer, Heidelberg (2005)
2. Jiang, Y., Towhata, I.: Experimental Study of Dry Granular Flow and Impact Behavior against a Rigid Retaining Wall. *Rock Mechanics and Rock Engineering* 46(4), 713–729 (2013)
3. Guasti, G., Volkwein, A., Wendeler, C.: Design of Flexible Debris Flow Barriers. In: Genevois, R., Hamilton, D.L., Prestininzi, A. (eds.) 5th International Conference on Debris-Flow Hazard “Mitigation, Mechanics, Prediction and Assessment”, Padua, Italy, June 14-17, pp. 1093–1100. Casa Editrice Università La Sapienza, Rome (2011)
4. Kishi, N., Ikeda, K., Konno, H., Kawase, R.: Prototype Impact Test on Rockfall Retaining Walls and its Numerical Simulation. In: *Proceedings of Structures under Shock and Impact IV*, Cambridge, England, pp. 351–360 (2000)
5. Nicot, F., Cambou, B., Mazzoleni, G.: Design of Rockfall Restraining Nets from a Discrete Element Modeling. *Rock Mechanics and Rock Engineering* 34(2), 99–118 (2001)
6. Volkwein, A.: Numerical Simulation of Flexible Rockfall Protection Systems. In: *Proceedings of the International Conference on Computing in Civil Engineering*, Cancun, Mexico, July 12-15, p. 11. ASCE (2005)
7. Hutter, K., Koch, T., Plüss, C., Savage, S.B.: The Dynamics of Avalanches of Granular Materials from Initiation to Runout. *Acta Mechanica* 109, 127–165 (1995)
8. Azana, E., Chevor, F., Moucheron, P.: Experimental Study of Collisional Granular Flows down an Inclined Plane. *Journal of Fluid Mechanics* 400, 199–227 (1999)
9. Pudasaini, S.P., Hutter, K.: Rapid Shear Flows of Dry Granular Masses down Curved and Twisted Channels. *Journal of Fluid Mechanics* 495, 193–208 (2003)
10. Silbert, L.E., Erta, S.D., Grest, G.S., Halsey, T.C., Levine, D., Plimpton, S.: Granular Flow Down an Inclined Plane: Bagnold Scaling and Rheology. *Physical Review E* 64, 051302 (2001)
11. Calvetti, F., Crosta, G., Tatarella, M.: Numerical Simulation of Dry Granular Flows: From the Reproduction of Small Scale Experiments to the Prediction of Rock Avalanches. *Rivista Italiana di Geotecnica* 21(2), 1–38 (2000)
12. Faug, T., Beguin, R., Benoit, C.: Mean Steady Granular Force on a Wall Over-flowed by Free-surface Gravity-driven Dense Flows. *Physical Review E* 80, 021305 (2009)
13. Campbell, C.S., Cleary, P.W., Hopkins, M.: Large-scale Landslide Simulations: Global Deformation, Velocities and Basal Friction. *Journal of Geophysical Research* 100(B5), 8267–8283 (1995)

14. Lemieux, P.A., Durian, D.J.: From Avalanches to Fluid Flow: a Continuous Picture of Grain Dynamics Down a Heap. *Physical Review Letters* 85, 4273–4276 (2000)
15. Faug, T., Lachamp, P., Naaim, M.: Experimental Investigation on Steady Granular Flows Interacting With an Obstacle Down an Inclined Channel: Study of the Dead Zone Upstream From the Obstacle. Application to Interaction between Dense Snow Avalanches and Defense Structures. *Natural Hazards and Earth System Sciences* 2, 187–191 (2002)
16. Valentino, R., Barla, G., Montrasio, L.: Experimental Analysis and Micromechanical Modeling of Dry Granular Flow and Impacts in Laboratory Flume Tests. *Rock Mechanics and Rock Engineering* 41(1), 153–177 (2008)
17. Cundall, P.A., Strack, O.D.L.: A Discrete Numerical Model for Granular Assemblies. *Géotechnique* 29, 47–65 (1979)
18. Bertrand, D., Trad, A., Limam, A., Silvani, C.: Full-Scale Dynamic Analysis of an Innovative Rockfall Fence Under Impact Using the Discrete Element Method: from the Local Scale to the Structure Scale. *Rock Mechanics and Rock Engineering* 45(5), 885–900 (2012)
19. Šmilauer, V., Catalano, E., Chareyre, B., Dorofeenko, S., Duriez, J., Gladky, A., Kozicki, J., Modenese, C., Scholtès, L., Sibille, L., Stránský, J., Thoeni, K.: Yade Documentation. In: Šmilauer, V. (ed.) *The Yade Project*, 1st edn. (2010), <http://yade-dem.org/doc/>
20. Schwager, T., Pöschel, T.: Coefficient of Restitution and Linear–dashpot Model Revisited. *Granular Matter* 9(6), 465–469 (2007)
21. Sánchez, P., Scheeres, D.J.: Simulating Asteroid Rubble Piles with a Self-gravitating Soft-sphere Distinct Element Method Mode. *The Astrophysical Journal* 727(2), 120–133 (2011)
22. Ghaisas, N., Wassgren, C.R., Sadeghi, F.: Cage Instabilities in Cylindrical Roller Bearings. *Journal of Tribology* 126, 681–689 (2004)
23. Chambers, J.M., Hastie, T.J.: *Statistical Models in S.* Wadsworth & Brooks/Cole, Pacific Grove (1992)

One-Dimensional Transient Analysis of Rainfall Infiltration in Unsaturated Volcanic Ash

James Fern, John Eichenberger, Alessio Ferrari, and Lyesse Laloui

Laboratory of Soil Mechanics,
School of Architecture, Civil and Environmental Engineering,
École Polytechnique Fédérale de Lausanne,
Station 18, 1015 Lausanne, Switzerland
{james.fern, john.eichenberger}@a3.epfl.ch,
{alessio.ferrari, lyesse.laloui}@epfl.ch
<http://lms.epfl.ch>

Abstract. The paper presents a one-dimensional hydro-mechanical analysis of rainfall infiltration in a loose volcanic ash and the utilisation of a factor of safety for the implementation of an early-warning system. Three different rainy seasons with different rainfall patterns were analysed. The analysis aims to understand the influence of the antecedent rainfall on the wetting front, the pore-water pressures and the factor of safety. The analysis was carried out in the context of a Master project of the first author at the Laboratory for Soil Mechanics of EPFL.

Keywords: groundwater seepage, unsaturated volcanic ash, rainfall-induced landslide, infinity slope analysis.

1 Introduction

A shallow rainfall-induced landslide was triggered on 21st November 2005 on the steep slopes of Irazù Volcano, Costa Rica. Three weeks later a second slide took place. The slides did not cause any casualties or extensive damage to property but lead to huge indirect costs due to the lose of productivity of local farmers and industries. Protection measures were already put into place in order to mitigate the risk but turned out to be ineffective [1].

The two slides were located in a thin layer of volcanic ash resting on a layer of clay in some places and or pozzolan in others. The volcanic ash was subjected to seasonal rainfall. The region has a long dry season followed by a short rainy season. Furthermore, this region is subjected to cyclic variation cause by El Niño. The study aims to analyse the influence of the different rainfall patterns on the predisposition of the slope to fail. The analysis is carried out by means of finite element simulation and infinite slope analysis. The simulation considered the field measurements of rainfall of three different years with three very different rainfall patterns.

2 Material Description

The volcanic ash is a cohesionless poorly graded sand of USCS type SC-SM. It is composed of 48% of sand and 50% of silt. The grain-size distribution is shown in figure 1. It has an internal friction angle of 35.5° and a specific gravity of 2.61. The ash is in a very loose state and has a density of 10 kN/m^3 . It was deposited by air-fall during the 1963-65 eruption. This deposition mechanism gave a grading to the deposited material. Boulders are located to the crater and the ashes further on the hillslopes. The USGS [1] reports a large accumulation of ash on the upper part of Irazù volcano despite its proximity to the crater.

A testing programme was set up to investigate the hydro-mechanical behaviour of the ash [2]. The soil water retention curve (SWRC) was obtained with a controlled-suction pressure plate apparatus and no hydric hysteresis was observed. Similar properties were observed on volcanic ash from Italy [4]. The SWRC was fitted with a van Genuchten model [5] and is shown in Fig. 1. The model parameters are summarized in table 1.

$$S_w = S_{w,res} + (1 - S_{w,res}) \left[\frac{1}{1 + (\alpha s)^n} \right]^m \quad (1)$$

where S_w is the degree of saturation, $S_{w,res}$ the residual degree of saturation, s the matric suction and α , n and m the van Genuchten model parameters.

Table 1. The van Genuchten parameters for the volcanic ash

$S_{w,res}$	s_e	n	m	n
3%	2 kPa	2.19	0.42	0.97

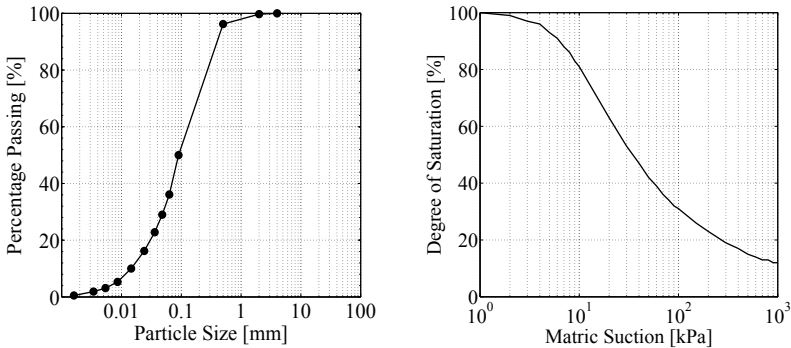


Fig. 1. Grain-size distribution and soil water retention curve

The permeability law was derived from the SWRC as suggested in [5] and shown in Eq. 2. It is a cubic law expressed with the same parameters as the van Genuchten SWRC. The saturated permeability is reported to be $6.4 \cdot 10^{-6}$ m/s.

$$k(s) = \frac{1 - \left(\alpha \frac{s}{\gamma_w}\right)^{n-3} \left[1 + \left(\alpha \frac{s}{\gamma_w}\right)^n\right]^{-m}}{\left[1 + \left(\alpha \frac{s}{\gamma_w}\right)^n\right]^{2m}} \quad (2)$$

where k is the unit permeability and γ_w the unit weight of water.

3 Constitutive Model

The material was modelled with the 'Advanced Constitutive Model for Environmental Geomechanics' for unsaturated soil ACMEG-s [6]. It is a critical state model based set within the generalised effective stress framework [8] and uses Bishop's effective stress [7] with the coupling parameter equal to the degree of saturation [9] (Eq. 3). The main advantages of such a framework are that any change in effective stress result in changes in strain and a smooth transition between saturated and unsaturated conditions.

$$\sigma'_{ij} = \sigma_{ij}^{net} + S_w s \cdot \delta_{ij} \quad (3)$$

where σ'_{ij} is the effective stress, σ_{ij}^{net} the net stress and δ_{ij} the Kronecker delta.

ACMEG-s considers two yielding mechanisms (volumetric and deviatoric) and its yield surface is defined by two yield equations (Eq. 5 and 4). Despite a double yield function, only a single yield surface exists at any given time (Fig. 2).

$$f_{iso} = p' - p'_c \cdot r_{iso} \quad (4)$$

$$f_{dev} = q - Mp' \left[1 - b \cdot \log\left(\frac{d \cdot p'}{p'_c}\right)\right] \cdot r_{dev} \quad (5)$$

where p'_c is the preconsolidation, d and b material parameters and r_{iso} and r_{dev} the deviatoric and isotropic mobilisation factors.

ACMEG-s has a non-associative flow rule for the deviatoric mechanism and an associative for the volumetric. It has a standard Cambridge type flow rule (Eq. 6).

$$\frac{d\varepsilon_v^p}{d\varepsilon_d^p} = \alpha \cdot \left(M - \frac{q}{p'}\right) \quad (6)$$

where $d\varepsilon_v^p$ and $d\varepsilon_d^p$ are respectively the plastic volumetric and deviatoric strain increments, α the dilatancy coefficient, M the critical state stress ratios.

ACMEG-s assumes a volumetric strain driven hardening rule (Eq. 7) in which the compressibility coefficient β is a function of the matric suction (Eq. 8).

$$p'_c = p'_{c0} \cdot \exp(\beta \varepsilon_v^p) \quad (7)$$

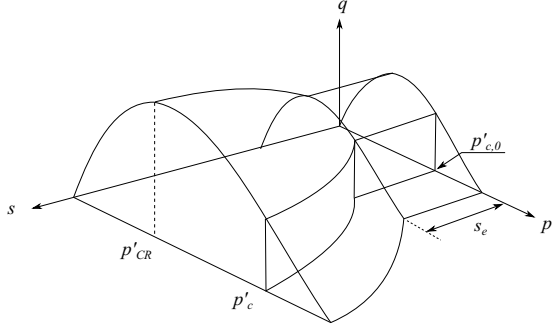


Fig. 2. ACMEG-s yield surface

$$\beta = \beta_0 + \Omega s \tag{8}$$

where p_{c0} and p'_c are respectively the saturated and unsaturated preconsolidation pressures, β_0 the saturated compressibility coefficient and Ω its unsaturated enhancement coefficient.

The evolution of the preconsolidation pressure is defined by the loading-collapse curve (LC) and shown in Eq. 9 and 10.

$$p'_c = p'_{c,0} \left[1 + \gamma_s \cdot \ln \left(\frac{s}{s_e} \right) \right] \text{ for } s \geq s_e \tag{9}$$

$$p_c = p'_{c,0} \text{ for } s < s_e \tag{10}$$

where γ_s are material parameters and s_e the air-entry suction value.

Table 2. ACMEG-s parameters

Bulk modulus	K_{ref}	$2.0 \cdot 10^4$ kPa
Shear modulus	G_{ref}	$1.5 \cdot 10^4$ kPa
Elastic exponent	n	0.5
Friction angle	ϕ'	35.5°
Compressibility Coefficient	β_0	9
Dilatancy coefficient	$alpha$	0.8
Material parameter	a	0.08
Material parameter	b	0.01
Material parameter	c	0.08
Material parameter	d	2
Initialisation of dev. mech.	r_{dev}	0.2
Initialisation of iso. mech.	r_{iso}	0.3
LC-curve coefficient	γ_s	1.6
Compressibility enhancement coefficient	Ω	0

The choice of the constitutive model was motivated by its ability of modelling to model cohesionless material [10]. The model parameters were obtained from an experimental programme consisting in three suction-controlled oedometer tests and three saturated triaxial compression tests [2]. The initial conditions reflected the field observations - loose and at low stresses. The model parameters were derived from these tests and refined by curve-fitting using a single element Gauss point routine [11] and are shown in Table 2.

4 One-Dimensional Transient Analysis of Rainfall Infiltration

The aim of the numerical analysis is to investigate the influence of rainfall patterns on the predisposition of a slope to fail considering both space and time. Rainfall infiltration is a downward gravity-driven mechanism and may be analysed with a one dimensional description of the problem [12]. A 6 m deep and 1 m wide ash-filled column is modelled using the finite element programme LAGAMINE [13,14]. The geometry, mesh and boundary conditions are shown in Fig. 3. A groundwater table is placed at 4 m depth. The bottom surface of the column is has a free drainage boundary condition. The boundary conditions are applied to the surface to prevent water ponding. It aims to replicated the run-off. The steep slopes prevent any ponding and the run-off water is immediately evacuated by gravity. The sides of the column impervious. The initial conditions of the volcanic ash are chosen to replicate the field investigation. The ash has an initial void ratio of 1.6. In order to analysis the influence of the initial pore-water pressure, each simulation is run twice with two different initial conditions. Both have hydrostatic profiles but the second has a cut-off value at -20 kPa of pore-water pressure. Fig. 3 illustrates these initial conditions.

The daily precipitation data was estimated by extrapolation from the daily precipitation of the International Airport of Santamaria located 36 km away. The data was obtained from the NOAA precipitation data base. Due to the unknown duration of each rainfall, the daily precipitation has been discretized throughout the day by applying a maximum intensity at midday and nil precipitation at midnight while conserving the daily precipitation volume. This discretization is conservative as it favours rainfall infiltration. However, The type of precipitation is neglected due to the shear size of the data (e.g. drizzle or storms). Furthermore, it is impossible to predict the local orographic effects in that region [1].

The transient pore-water pressure is obtained for each simulation and a factor of safety is calculated with the infinite slope theory (Eq. 11). It assumes a slip surface parallel to the ground surface and neglects the effect of neighbouring slopes. It takes into account the destabilising effect of weight, the stabilising effect of matric suction and the angle of the slope. The use of the this factor of safety for the implementation of an early-warning system is fully discussed in [11]. A 49° slope is used for all simulations.

$$FS = \frac{c' + (\gamma H \cos^2 \theta + S_w s)}{\gamma z \sin \theta \cos \theta} \quad (11)$$

where c' is the intercept cohesion, ϕ' the shear strength angle, γ the unit weight of the soil, z the depth of the point considered in the analysis, θ the angle of the slope surface.

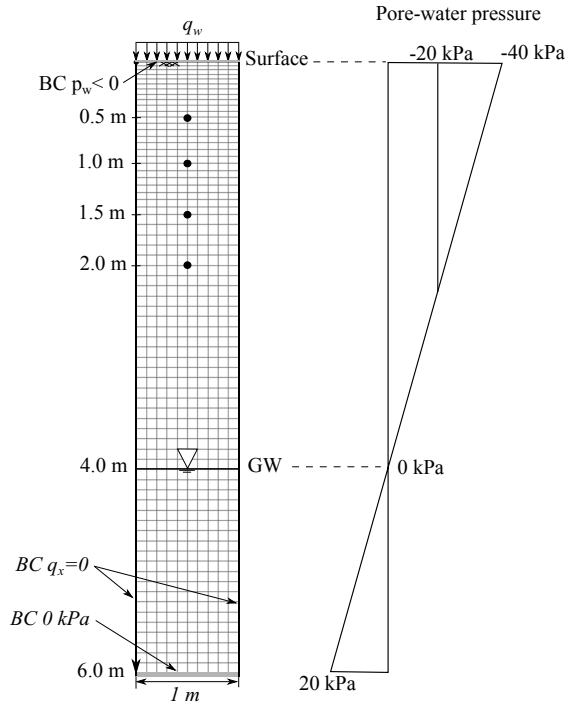


Fig. 3. Geometry, mesh, boundary and initial conditions of the one dimensional analysis

The ash filled column replicates the infiltration process of a 49° slope. The simulation were run as fully coupled meaning that wetting-induced strain was permitted. Four depth are analysed (0.5, 1.0, 1.5 and 2.0 m) and shown in Fig. 4, 5 and 6. The term duration refers to the number of days with some rainfall rather than the actual duration of a rainfall event.

4.1 2005 Rainy Season

The rainy season of year 2005 is simulated using the rainfall pattern shown in Fig. 4a. The cumulative rainfall is 1200 mm and most of it occurred in September and October. Very few days in these two month did not have any rain and the maximum daily precipitation was 56 mm/day. The matric suction and the factor of safety are shown in Fig. 4b and c.

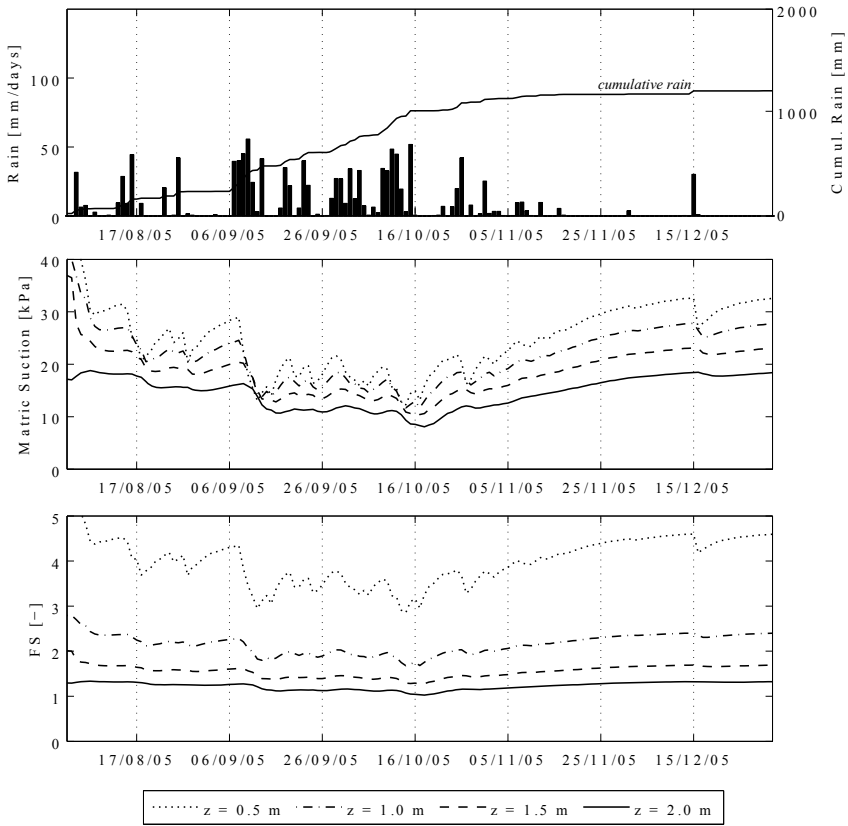


Fig. 4. Rainfall, pore-water pressure and factor of safety for the rainy season 2005

The first few days are subjected to small intensity long duration rainfalls which rule out any influence of the initial conditions after twenty days. The matric suction profiles in the ground are as from then the same. By the end of August, the matric suction is 15 kPa at 2 m depth and 28 kPa at 0.5 m depth and the factors of safety respectively 1.26 and 4.30. The early September showers cause the matric suction and the factors of safety to drop and the rate of drop is more significant at shallow depths. The matric suctions are 13 kPa at all depth while the factor of safety is graded from 2.95 at 0.5m to 1.16 at 2 m. For the following month, the rainfalls are uniform in intensity and duration. A series of high intensity and long duration rainfalls occurs mid-October and is similar to one in September. The matric suctions drop down to 8 kPa at 2m deep with a factor of safety of 1.03. This date corresponds to the date of the actual landslide.

The 2005 results show that a single day of rainfall is not sufficient to affect the stability of the ground at 2m depth. However, a series of rainfalls increases the degree of saturation and the permeability of the ground and decreases the

matric suction. Then only can a high intensity rainfall decrease significantly the matric suction and give a critical factor of safety.

4.2 2008 Rainy Season

The rainy season of year 2008 is simulated using the rainfall pattern shown in Fig. 5a. The cumulative rainfall was 1525 mm most of which occurred in August and September. Unlike 2005, the rainfall is composed of less events but with higher intensities. The maximum rainfall intensity is 133 mm/day. The matric suction and the factor of safety are shown in Fig. 5b and c.

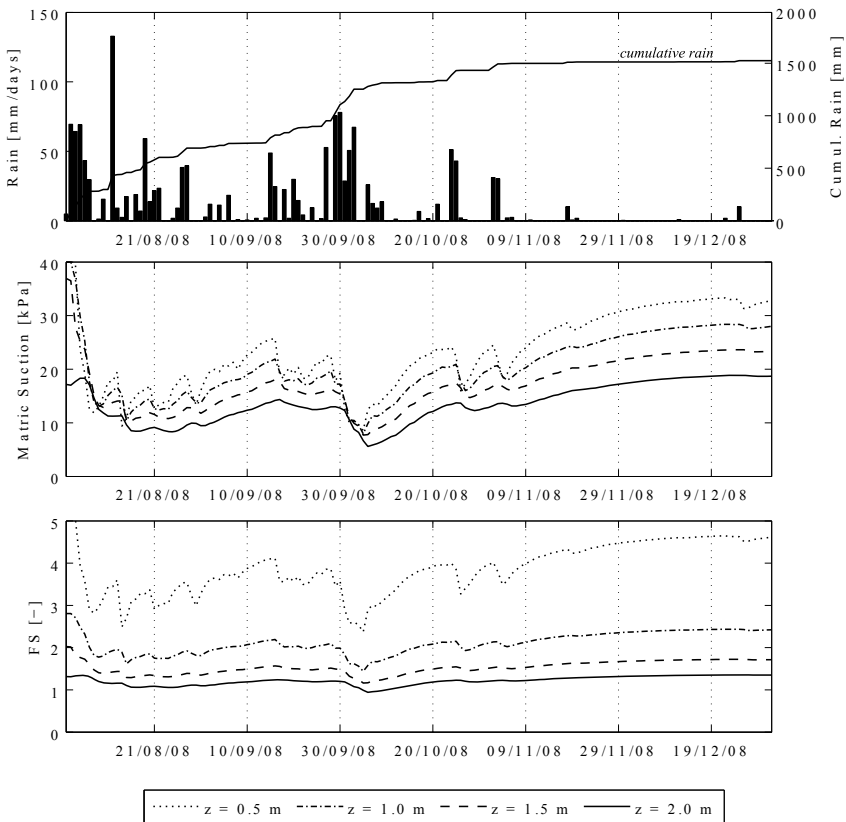


Fig. 5. Rainfall, pore-water pressure and factor of safety for the rainy season 2008

The early August rain remove any influence of the initial matric suction. By mid-August, the heavy rainfall infiltration have set the matric suction to 12 kPa at all depths. The factor of safety at a depth of 2m is 1.12. Then, a single high intensity rainfall occurs. The shallow layers respond to it very quickly with a

rapid decrease in matric suction to 9 kPa while the 12 kPa are maintained at 2 m depth. However, the factor of safety is still high. The following is rather dry and the soil is free to drain. Matric suction increases and stability is gained. A long duration and high intensity series of rainfall occur at the end of September. Despite the lower intensity, the consequence are dramatic. The matric suction is between 5 and 7 kPa at all depth and the factor of safety is 0.94. October and November are subject to sporadic showers which have an effect at shallow depths but none at 2m depth.

The 2008 results show that single events mainly affect shallow depth unless the soil has been subjected to antecedent rainfall. The effect of heavy rainfall are limited by the permeability of the ground. The increase in permeability requires some time while which the water flow is unable to fully saturated the pore space giving a constant matric suction value to the entire profile.

4.3 2010 Rainy Season

The rainy season of year 2010 is simulated using the rainfall pattern shown in Fig. 6a. The cumulative rainfall us 1557 mm and is similar to 2008. It is split into three major events. A small intensity but long lasting series of precipitation occurs in the month of August. It is followed by first high intensity rainfall event with an intensity of 128 mmm/day. After two weeks of dry weather, a second high intensity event occurs with an intensity of 133 mm/day. The matric suction and the factor of safety are shown in Fig. 5b and c.

The first six weeks are subjected to continuous rainfall and both the matric suction and the factor of safety gradually decrease to values of respectively 17 kPa and 3 at 0.5 m depth and 10 kPa and 1.08 at 2 m depth. The total amount of rainfall is 603 mm. It is followed by the first high intensity rainfall event and the matric rapidly drops down to 9 kPa at all depth. The rate of decrease is more significant at shallow depths than at higher depths. The factor of safety reaches its minimum value of 2.1 at 0.5 m depth. A lag-time of two 2 days is required for the deeper soil to respond. It then has a matric suction of 4.5 kPa and a factor of safety 0.9 at 2 m. At the end of this first series of high intensity rainfalls occurs a few lower intensity events but nevertheless non-negligible. This additional water is channelled into the soil because of the high permeability and finally reaches the deeper soil. The matric suction drops to 3 kPa and the factor of safety to 0.82. This event highlights the influence of the antecedent rainfall on the response of the soil to a single event. The following month is rather dry and the matric suction increases in the soil at all depths. The second series of high intensity rainfalls occurs mid-October. The matric suction profile is inversed with a matric suction of 4 kPa at 0.5 m depth and 6 kPa at 2m meters time with a lag-time of 2 days. The factors of safety are respectively 1.51 and 0.97.

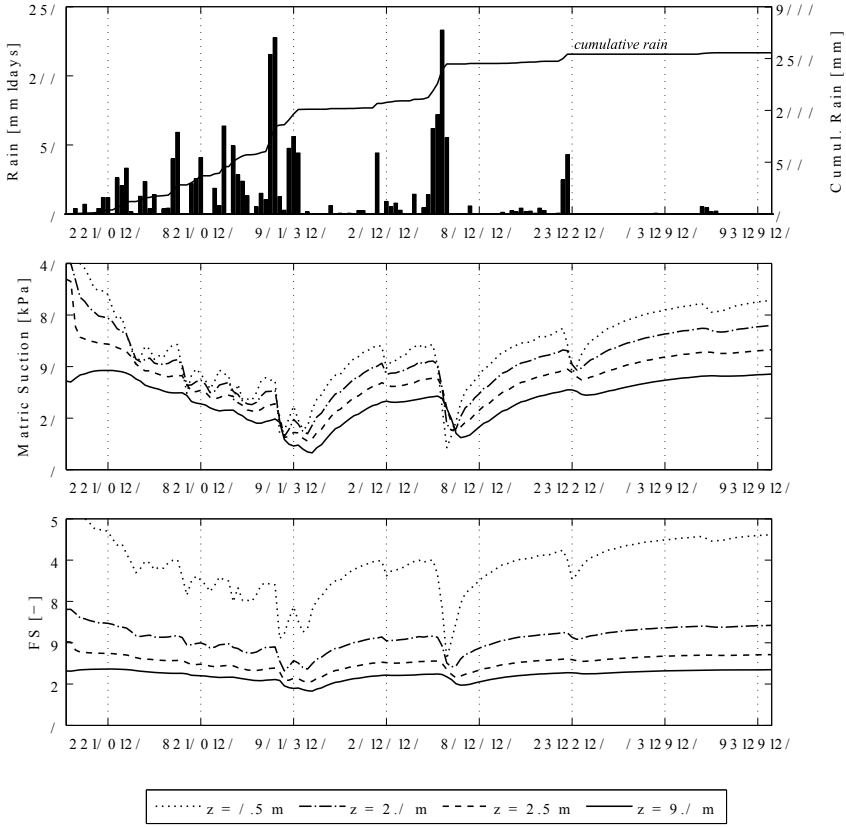


Fig. 6. Rainfall, pore-water pressure and factor of safety for the rainy season 2010

5 Conclusion

The one-dimensional modelling of rainfall infiltration is a suitable approach as long as no perched water tables are formed in the ground [12]. These may be caused by a contrast in permeability between two materials or even within the same material. This simple model excludes any topographic or stratigraphic effects which may be in some cases significant [17,16,15]. Nevertheless, this simple model allows to gain some insight on the hydraulic behaviour of soil subjected to rainfall.

The use of a factor of safety illustrates the predisposition of a soil to fail. It may be seen that deeper soil are less stable but are less sensitive to single events than shallow soils. The actual value of the factor of safety is subjected to some discussion as it relies on many assumptions (e.i. infinity slope analysis and the rainfall patterns). The analysis neglected any anthropogenic or seismic contributions.

The finite element simulation of an ash filled column subjected to the 2005 rainy season rainfall predicted two landslides as observed in the field. However, the 2008 and 2010 simulation also predicted failures which did not occur. It may partly be explained by the estimation of the rainfall and its discretisation. Orographic effects may have also modified the precipitation both in time and in space. Anthropogenic activities or tectonic activity may have also played a role in the 2005 events. Nevertheless, the following conclusion may be drawn from the analysis.

1. Soil is sensitive at shallow depths to single events of rainfall but their predisposition to fail is rather small.
2. Rainfall infiltration increases the permeability allowing more water to penetrate into the ground forming a wetting front.
3. This wetting front is able to reach deeper strata and increases predisposition of soil to fail.
4. Deeper soil is only then sensitive to a single events of rainfall.
5. A lag-time of two days is observed between the rainfall event and the decrease in matric suction at deeper depths.
6. The lag-time means that the risk of a slide is at its most well after the rainfall events rather than during.

Acknowledgments. The authors would like to thank NOAA for sharing their precipitation data.

References

1. Waldron, H.H.: Debris Flow and Erosion Control Problems Caused by the Ash Eruptions of Irazu Volcano, Costa Rica. USGS Numbered Series - Contribution to general geology, vol. 1241, pp. 1–37 (1966)
2. Ferrari, A., Eicheberger, J., Laloui, L.: Hydromechanical Behaviour of a Volcanic Ash. *Géotechnique*, 1–14 (2013)
3. Ferrari, A., Eichenberger, J., Fern, J.: Experimental and Numerical Analysis of an Unsaturated Volcanic Ash Deposit for the Establishment of an Early Warning System in a Quarry in Costa Rica. In: Hryciw, R.D., Athanasopoulos-Zekkos, A. (eds.) *GeoCongress ASCE 2012*, pp. 2512–2521. American Society of Civil Engineers, Oakland (2012)
4. Bilotta, E., Cascini, L., Foresta, V., Sorbinow, G.: Geotechnical Characterisation of Pyroclastic Soils Involved in Huge Flow Slides. *Geotechnical and Geological Engineering* 23, 365–402 (2005)
5. Van Genuchten, M.T.: A Closed Form Equation for Predicting the Hydraulic Conductivity of Unsaturated Soils. *Soil Science Society American Journal* 44, 892–898 (1980)
6. Nuth, M.: *Constitutive Modelling of Unsaturated Soils with Hydro-Geomechanical Couplings*. École Polytechnique Fédérale de Lausanne (2009)
7. Bishop, A.W.: The principles of effective stress. *Tecnisk Ukeblad* 8, 859–863 (1959)
8. Nuth, M., Laloui, L.: Effective Stress Concept in Unsaturated Soils: Clarification and validation of a Unified Framework. *International Journal for Numerical and Analytical Methods in Geomechanics* 32, 771–801 (2008)

9. Schrefler, B.: The Finite Element Method in Soil Consolidation (with applications to surface subsidence). University College of Swansea (1984)
10. D'Onza, F., Gallipoli, D., Wheeler, S.J.: Benchmark of Constitutive Models for Unsaturated Soils. *Geotechnique* 61, 283–302 (2011)
11. Eichenberger, J.: Geomechanical Modelling of Rainfall-Induced Landslides in Partially Saturated Slopes. *École Polytechnique Fédérale de Lausanne* (2013)
12. Fredlund, D.G., Rahardjo, H.: *Soil Mechanics for Unsaturated Soils*. Wiley & Sons, New York (1993)
13. Charlier, R.: Approche Unifiée de Quelques Problèmes non Linéaires de Mécanique des Milieux Continus par la Méthode des éléments finis. *Université de Liège* (1987)
14. Collin, F.: Couplages Thermo-hydro-mécaniques dans les sols et les roches tendres partiellement saturés. *Université de Liège* (2003)
15. Eichenberger, J., Ferrari, A., Laloui, L.: Early Warning Thresholds for Partially Saturated Slopes in Volcanic Ashes. *Computers and Geotechnics* 49, 79–89 (2013)
16. Borja, R.I., White, J.A.: Continuum Deformation and Stability Analyses of a Steep Hillside Slope under Rainfall Infiltration. *Acta Geotechnica* 5, 1–14 (2010)
17. Pirone, M.: Analysis of Slope Failure Mechanism in Unsaturated Pyroclastic Soils, based on Testing Site Monitoring. *Università Degli Studi di Napoli Federico II* (2009)
18. Pagano, L., Picarelli, L., Rianna, G., Urciuoli, G.: A Simple Numerical Procedure for Timely Prediction of Precipitation-Induced Landslides in Unsaturated Pyroclastic Soils. *Landslides* 7, 273–289 (2010)
19. Borja, R.I., White, J.A., Liu, X., Wu, W.: Factor of Safety in a Partially Saturated Slope Inferred from Hydro-mechanical Continuum Modeling. *International Journal for Numerical and Analytical Methods in Geomechanics* 36, 236–248 (2011)

Investigations of Gravity-Driven Two-Phase Debris Flows

Xiannan Meng and Yongqi Wang

Technische Universität Darmstadt, Darmstadt 64287, Germany
{meng,wang}@fdy.tu-darmstadt.de

Abstract. A depth-integrated theory is derived for the gravity-driven two-phase debris flows over complex shallow topography. The mixture theory is adopted to describe the mass and momentum conservation of each phase. The model employs the Mohr-Coulomb plasticity for the solid rheology, and assumes the Newtonian fluid for the fluid phase. The interactive forces assumed here consist of viscous drag force linear to velocity difference between the both phases, and buoyancy force. The well-established governing equations are built in 3D topography; as a result, they are expressed in the curvilinear coordinate system. Considering the characteristics of flows, a shallow layer assumption is made to simplify the depth-integrated equations. The final resulting equations are solved numerically by a high-resolution TVD scheme. The dynamic behaviors of the mixture are investigated. Numerical results indicate that the model can adequately describe the flows of dry granular material, the pure water and general two-phase debris flows.

Keywords: mixture theory, mohr-Coulomb plasticity, newtonian fluid, high-resolution TVD scheme.

1 Introduction

Gravity-driven flows of dense sediment-fluid mixture with free surface occur commonly on the Earth's surface with devastating consequences. There is a significant need for reliable models for predicting the dynamics, runout distances, and deposited areas of such events.

With respect to the modelings, three kinds of typical depth-integrated models so far exist: (i) the model of single phase dry cohesionless granular continuum consisting of particles with a nominal mean, representative size, (ii) quasi-single phase model treating the mixture as a medium combining the contributions of the fluid pressure with those from granular friction, and (iii) two-fluid model fully taking into account the interactive forces between the fluid phase and the granular phase.

The single phase model postulates that the rapidly moving granular material is density preserving and satisfies Mohr-Coulomb friction rheology. Supposing blunt velocity profile, a depth-average is performed to derive the final mass and momentum conservation equations without losing accuracy ([2], [3], [7] and [9]).

For the quasi-single phase model, the role of pore fluid is fully taken into account, and the momentum equation containing solid stress and fluid partial stress, is formulated for the mixture as a whole. Despite the fact of good agreement between the numerical results from quasi-single phase model and experimental results, the following weaknesses have to be mentioned. Firstly, the spatial and temporal distributions of the volume fractions cannot be determined due to the assumption of equality of the velocities of the two constituents. Secondly, the transport equation for the fluid pressure is postulated by means of experimental results. It lacks a theoretical justification.

Taking into account difference of velocities of all phases, the two-fluid model describes each phase in its own conservation equations. The interactive forces are assumed to couple the two sets of conservation equations. The temporal and spatial distributions of volume fractions can be obtained and analyzed (see [4, 5, 6]).

The present proposed model, based on two-fluid model and incorporating the advantages of the existing models, presents a depth-integrated theory for the two-phase debris flows over 3D shallow topography. The granular phase is modeled by Mohr-Coulomb plasticity, and the fluid phase is modeled by Newtonian fluid. The interactive forces consist of viscous drag force and buoyancy force. A friction boundary condition is applied to constrain the basal movement of the fluid phase instead of the no-slip boundary condition (see [6]). Like the previous works, the depth integration is performed, and a shallow layer assumption is made to simplify the governing equations. The resulting non-linear PDEs are solved by a high-resolution scheme taking into account all important effects. Through the analysis of numerical results, some important phenomena are found.

2 Governing Equations and Coordinate System

2.1 Governing Equations

In the framework of the mixture theory, all phases are present at each point of the field with different volume fractions. For each phase, the mass and momentum balance equations are postulated. Through the interactive forces, they are coupled with each other. The conservation equations for mass are given by

$$\partial_t(\tilde{\rho}_s\phi_s) + \nabla \cdot (\tilde{\rho}_s\phi_s\mathbf{u}_s) = 0, \quad (1)$$

$$\partial_t(\tilde{\rho}_f\phi_f) + \nabla \cdot (\tilde{\rho}_f\phi_f\mathbf{u}_f) = 0, \quad (2)$$

and for momentum by

$$\partial_t(\tilde{\rho}_s\phi_s\mathbf{u}_s) + \nabla \cdot (\tilde{\rho}_s\phi_s\mathbf{u}_s\mathbf{u}_s) = \nabla \cdot \hat{\mathbf{T}}_s + \tilde{\rho}_s\phi_s\mathbf{g} + \mathbf{f}_s, \quad (3)$$

$$\partial_t(\tilde{\rho}_f\phi_f\mathbf{u}_f) + \nabla \cdot (\tilde{\rho}_f\phi_f\mathbf{u}_f\mathbf{u}_f) = \nabla \cdot \hat{\mathbf{T}}_f + \tilde{\rho}_f\phi_f\mathbf{g} - \mathbf{f}_s, \quad (4)$$

where the true densities and velocities of the two phases are characterized by $\tilde{\rho}_{s/f}$ and $\mathbf{u}_{s/f}$. ϕ_s and ϕ_f denote the volume fractions of the granular phase and the fluid phase, respectively. $\hat{\mathbf{T}}_s$ and $\hat{\mathbf{T}}_f$ are chosen as the partial stresses of the

granular phase and the fluid phase. The gravity acceleration is denoted by \mathbf{g} . \mathbf{f}_s is used to represent the interactive forces exerted on the granular phase by the fluid phase.

For the granular phase, we assume $\hat{\mathbf{T}}_s = -\phi_s \tilde{\mathbf{T}}_s$, where $\tilde{\mathbf{T}}_s$ is the Coulomb stress tensor for the dry granular material from the work of [9]. For the fluid phase, the relation $\hat{\mathbf{T}}_f = -p\mathbf{I} + \phi_f \tilde{\boldsymbol{\tau}}_f$ is assumed, where p is the pressure of the fluid phase and $\tilde{\boldsymbol{\tau}}_f$ is the shear stress of the pure fluid. In the present investigation, a Newtonian fluid is assumed.

Usually, as in [5], the interactive forces are simply assumed to be composed of the viscous drag force, which has linear relationship with relative velocity expressed as $\beta(\mathbf{u}_f - \mathbf{u}_s)$, and the buoyancy force expressed as $-\phi_s \nabla p$ (see [1]) in the present model. The coefficient of the viscous drag force β follows the expression of [8], based on the experimental data $\beta = \frac{\phi_s \phi_f (\tilde{\rho}_s - \tilde{\rho}_f) \mathbf{g}}{v_T (1 - \phi_s)^m}$. Here v_T is the sedimentation velocity of a single particle, and $m \in [0.39, 2.65]$ is a parameter depending on the particle Reynolds number $Re_p = \frac{v_T d \tilde{\rho}_f}{\mu}$ (d is the diameter of the sphere particle, and μ is the viscosity of the fluid).

Finally the momentum conservation equations are rewritten in the forms:

$$\partial_t(\tilde{\rho}_s \phi_s \mathbf{u}_s) + \nabla \cdot (\tilde{\rho}_s \phi_s \mathbf{u}_s \mathbf{u}_s) = -\nabla \cdot (\phi_s \tilde{\mathbf{T}}_s) + \tilde{\rho}_s \phi_s \mathbf{g} - \phi_s \nabla p + \mathbf{f}_d, \quad (5)$$

$$\partial_t(\tilde{\rho}_f \phi_f \mathbf{u}_f) + \nabla \cdot (\tilde{\rho}_f \phi_f \mathbf{u}_f \mathbf{u}_f) = -\phi_f \nabla p + \nabla \cdot (\phi_f \tilde{\boldsymbol{\tau}}_f) + \tilde{\rho}_f \phi_f \mathbf{g} - \mathbf{f}_d. \quad (6)$$

As illustrated in [2], the granular phase satisfies kinematic boundary condition and stress-free dynamic boundary condition on the free surface, and the Coulomb friction boundary condition

$$\hat{\mathbf{T}}_s \mathbf{n}_b - (\mathbf{n}_b \cdot \hat{\mathbf{T}}_s \mathbf{n}_b) \mathbf{n}_b = \frac{\mathbf{u}_s^b}{|\mathbf{u}_s^b|} (\mathbf{n}_b \cdot \hat{\mathbf{T}}_s \mathbf{n}_b) \tan \delta, \quad (7)$$

and no-penetration boundary condition in the tangential and normal direction of the basal topography, respectively. Here \mathbf{n}_b denotes the normal unit vector of the basal topography, and δ represents Coulomb bed friction angle.

For the fluid phase, besides the kinematic boundary condition and stress-free condition on the free surface and impermeability on the bottom, a friction law linear to its velocity is imposed on the bottom,

$$\hat{\mathbf{T}}_f \mathbf{n}_b - (\mathbf{n}_b \cdot \hat{\mathbf{T}}_f \mathbf{n}_b) \mathbf{n}_b = -k_l \mathbf{u}_f, \quad (8)$$

where k_l represents the friction coefficient depending on the roughness of the slope and the viscosity of the fluid etc. $k_l \rightarrow \infty$ corresponds to a no-slip condition.

2.2 Coordinate System

An orthogonal curvilinear coordinate system, $Oxyz$, is introduced by a two-dimensional reference surface that follows the mean down-slope chute topography. The x -axis is oriented in the down-slope direction, the y -axis lies in the cross-slope direction of the reference surface without lateral variation, and the z -axis

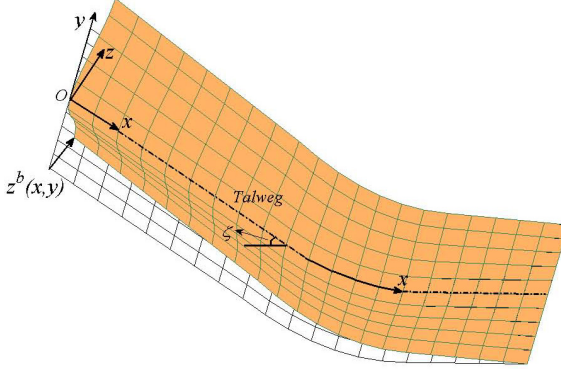


Fig. 1. Curvilinear coordinate system

is normal to them. The down-slope inclination angle of the reference surface ζ changes as a function of the down-slope coordinate x . Its gradient along x -axis is defined by $\kappa = -\frac{d\zeta}{dx}$ representing the curvature of the reference surface, where the negative sign is imposed to guarantee positive value for κ . The complex shallow three-dimensional basal topography is defined by its elevation $z = z^b(x, y)$ above the reference surface as illustrated in Fig. 1.

Following the theory of tensor and [2], the gradient of a scalar field F , the divergences of a vector field \mathbf{l} and a symmetry second-order tensor \mathbf{N} can be represented in terms of the contravariant components. The gradient of a vector field \mathbf{l} , which emerges in the present model due to the Newtonian shear stress for the fluid phase, but not

$$\begin{aligned} \nabla \mathbf{l} = & \left(\partial_x l_x - \frac{\kappa_{,x} z}{1 - \kappa z} l_x - \kappa l_z \right) (1 - \kappa z) \mathbf{e}_1 \mathbf{e}_1 + (\partial_x l_y) (1 - \kappa z) \mathbf{e}_1 \mathbf{e}_2 \\ & + (\partial_x l_z + \kappa l_x) (1 - \kappa z) \mathbf{e}_1 \mathbf{e}_3 + (\partial_y l_x) \mathbf{e}_2 \mathbf{e}_1 + (\partial_y l_y) \mathbf{e}_2 \mathbf{e}_2 + (\partial_y l_z) \mathbf{e}_2 \mathbf{e}_3 \\ & + \left(\partial_z l_x - \frac{\kappa}{1 - \kappa z} l_x \right) \mathbf{e}_3 \mathbf{e}_1 + (\partial_z l_y) \mathbf{e}_3 \mathbf{e}_2 + (\partial_z l_z) \mathbf{e}_3 \mathbf{e}_3, \end{aligned} \quad (9)$$

where \mathbf{e}_1 , \mathbf{e}_2 and \mathbf{e}_3 are unit base vectors along x -, y - and z -axis, respectively.

3 Scaling Analysis

The scaling analysis is performed with the equations:

$$\begin{aligned} (x, y, z, t) &= (Lx^*, Ly^*, Hz^*, \sqrt{L/gt^*}), \\ \kappa &= \frac{1}{\mathcal{R}} \kappa^*, \\ ((u, v, w) |_{f,s}, v_T) &= \sqrt{gL}((u^*, v^*, \epsilon w^*) |_{f,s}, \epsilon v_T^*), \\ (\tilde{T}_s(xx), \tilde{T}_s(yy), \tilde{T}_s(zz), p) &= \tilde{\rho}_s g H (\tilde{T}_s^*(xx), \tilde{T}_s^*(yy), \tilde{T}_s^*(zz), \gamma P^*), \\ (\tilde{T}_s(xy), \tilde{T}_s(xz), \tilde{T}_s(yz)) &= \tilde{\rho}_s g H \tan \delta (\tilde{T}_s^*(xy), \tilde{T}_s^*(xz), \tilde{T}_s^*(yz)), \end{aligned} \quad (10)$$

where the superscript “*” represents dimensionless variables, which will be dropped in the following to simplify the notation. γ represents the ratio of the fluid density to the solid density. The scale for the true stress of the granular phase is introduced in accordance with Coulomb rheology (normal and shear stress are scaled with $\tilde{\rho}_s g H$ and $\tilde{\rho}_s g H \tan \delta$, where δ is Coulomb bed frictional angle). Two non-dimensional parameters arise due to the scaling. The aspect ratio ϵ is expressed by the typical depth of debris flows H over the typical extent L ,

$$\epsilon = \frac{H}{L}, \quad (11)$$

and a characteristic curvature λ is expressed as follows,

$$\lambda = \frac{L}{\mathcal{R}}, \quad (12)$$

where \mathcal{R} is typical radius of curvature.

4 Order Arguments and Depth Integration

In this section, we focus on the evolution of the depth-integrated equations for the two phases. Here we will not present the entire calculation, but only indicate the most important steps. Taking into account the flow characteristics, the ‘thin layer’ approximation is made that the typical down- and cross-slope lengths are much larger than the typical normal thickness, i.e. $\epsilon \ll 1$. Furthermore, following [3], $\lambda = O(\epsilon^\alpha)$ and $\tan \delta = O(\epsilon^\beta)$ with $0 < \alpha, \beta < 1$ are assumed.

4.1 Depth-Integrated for the Fluid Phase

Using the orthogonal coordinates displayed in Fig. 1, and with a scaling analysis as in [7], the contributions of the shear stress for the fluid phase in the down-slope, cross-slope and normal components become

$$f_x(\tilde{\tau}_f) = \frac{\epsilon}{N_R} \left[2 \frac{\partial^2 u_f}{\partial x^2} + \frac{\partial}{\partial y} \left(\frac{\partial v_f}{\partial x} + \frac{\partial u_f}{\partial y} \right) + \frac{1}{\epsilon^2} \frac{\partial^2 u_f}{\partial z^2} \right] + O(\epsilon^{1+\chi}), \quad (13)$$

$$f_y(\tilde{\tau}_f) = \frac{\epsilon}{N_R} \left[2 \frac{\partial^2 v_f}{\partial y^2} + \frac{\partial}{\partial x} \left(\frac{\partial v_f}{\partial x} + \frac{\partial u_f}{\partial y} \right) + \frac{1}{\epsilon^2} \frac{\partial^2 v_f}{\partial z^2} \right] + O(\epsilon^{1+\chi}), \quad (14)$$

$$f_z(\tilde{\tau}_f) = O(\epsilon^{1+\chi}), \quad (15)$$

where $\chi = \min(\alpha, \beta)$. The dimensionless variable N_R is expressed as $N_R = \frac{\tilde{\rho}_f H \sqrt{g L}}{\phi_f \mu}$, and its order is $10^5 \sim 10^6$. Similarly, the friction boundary condition for the fluid phase subject to the simplification of thin layer becomes

$$\frac{\partial u_f^b}{\partial z} = \vartheta u_f^b + O(\epsilon^2), \quad \text{at the bottom } z = b(x, y), \quad (16)$$

$$\frac{\partial v_f^b}{\partial z} = \vartheta v_f^b + O(\epsilon^2), \quad \text{at the bottom } z = b(x, y), \quad (17)$$

where $\vartheta = \frac{k_f H}{\phi_f \mu}$ is a non-dimensional parameter combining frictional coefficient, typical thickness, fluid volume fraction with fluid viscosity.

As usual, it follows from the vertical momentum equation of the fluid phase that the hydrostatic pressure is

$$p(x, y, z, t) = (s - z) \cos \zeta + O(\epsilon^\alpha), \quad (18)$$

where $z = s(x, y, t)$ is the free surface.

The integration is performed for the fluid momentum equations in x - and y -direction along the depth direction from the topography $z = b(x, y)$ to the free surface $z = s(x, y, t)$. In it, the mean value of any quantity $q(x, y, z, t)$ is defined as follows

$$\frac{1}{h} \int_{b(x, y)}^{s(x, y, t)} q(x, y, z, t) dz = \overline{q(x, y, t)}, \quad (19)$$

where $h = s(x, y, t) - b(x, y)$ represents the depth from the basal topography to the free surface.

In the process of depth integration, Leibnitz integral rule and the boundary conditions are exploited repeatedly to simplify the equations. Substituting the hydrostatic pressure (18) into the resulting equations, so that we obtain

$$\begin{aligned} & \frac{\partial}{\partial t}(h\phi_f \bar{u}_f) + \frac{\partial}{\partial x}(h\phi_f \bar{u}_f \bar{u}_f) + \frac{\partial}{\partial y}(h\phi_f \bar{u}_f \bar{v}_f) \\ &= -\phi_f \epsilon \frac{\partial}{\partial x} \left(\frac{1}{2} h^2 \cos \zeta \right) + h\phi_f \sin \zeta - \frac{(1-\gamma)\phi_s \phi_f}{\epsilon v_T (1-\phi_s)^m} \frac{1}{\gamma} h (\bar{u}_f - \bar{u}_s) \\ &+ \frac{\epsilon}{N_R} \left[2h \frac{\partial^2 \bar{u}_f}{\partial x^2} + h \frac{\partial}{\partial y} \left(\frac{\partial \bar{v}_f}{\partial x} + \frac{\partial \bar{u}_f}{\partial y} \right) - \frac{1}{\epsilon^2} \vartheta \bar{u}_f \right] - \phi_f \epsilon h \cos \zeta \frac{\partial b}{\partial x} + O(\epsilon^{1+\chi}), \end{aligned} \quad (20)$$

$$\begin{aligned} & \frac{\partial}{\partial t}(h\phi_f \bar{v}_f) + \frac{\partial}{\partial x}(h\phi_f \bar{u}_f \bar{v}_f) + \frac{\partial}{\partial y}(h\phi_f \bar{v}_f \bar{v}_f) \\ &= -\phi_f \epsilon \frac{\partial}{\partial y} \left(\frac{1}{2} h^2 \cos \zeta \right) - \frac{(1-\gamma)\phi_s \phi_f}{\epsilon v_T (1-\phi_s)^m} \frac{1}{\gamma} h (\bar{v}_f - \bar{v}_s) \\ &+ \frac{\epsilon}{N_R} \left[2h \frac{\partial^2 \bar{v}_f}{\partial x^2} + h \frac{\partial}{\partial x} \left(\frac{\partial \bar{u}_f}{\partial y} + \frac{\partial \bar{v}_f}{\partial x} \right) - \frac{1}{\epsilon^2} \vartheta \bar{v}_f \right] - \phi_f \epsilon h \cos \zeta \frac{\partial b}{\partial y} + O(\epsilon^{1+\chi}), \end{aligned} \quad (21)$$

where in the process of deriving equations (20) and (21), the blunt velocity profile is assumed. The equations (20) and (21) describe the evolutions of the fluid volume fraction ϕ_f , depth-averaged velocities \bar{u}_f and \bar{v}_f , and the total thickness h .

4.2 Depth-Integrated for the Granular Phase

The normal component of the solid momentum equations is firstly integrated along the depth direction, and then becomes the following subject to Leibnitz

integral rule and scaling analysis,

$$\lambda \kappa h \overline{u_s^2} = -\gamma \int_b^s \frac{\partial p}{\partial z} dz - \int_b^s \cos \zeta dz + (\mathbf{n}_b \cdot \tilde{\mathbf{T}}_s \mathbf{n}_b) + O(\epsilon). \quad (22)$$

Substituting the expression of the fluid pressure obtained by approximating the normal momentum equation of the fluid phase to order $O(\epsilon)$ into the equation (22), we can obtain

$$\mathbf{n}_b \cdot \tilde{\mathbf{T}}_s \mathbf{n}_b = \lambda \kappa h \overline{u_s^2} - \gamma \kappa \lambda h \overline{u_f^2} - \gamma h \cos \zeta + h \cos \zeta + O(\epsilon). \quad (23)$$

To proceed, from the normal component of the solid momentum equations, the following equation can be found

$$O(\epsilon^\alpha) = -\phi_s \cos \zeta - \frac{\partial(\phi_s \tilde{T}_{s(zz)})}{\partial z} - \phi_s \gamma \frac{\partial p}{\partial z}. \quad (24)$$

Integrating the equation (24), and substituting the fluid pressure (18), the equation (24) becomes

$$\tilde{T}_{s(zz)} = (1 - \gamma)(s - z) \cos \zeta + O(\epsilon^\alpha). \quad (25)$$

Following [3], the assumption is made that the down-slope and cross-slope normal stress vary linearly with the vertical normal stress, which is fulfilled to leading order

$$\tilde{T}_{s(xx)} = K_x \tilde{T}_{s(zz)} + O(\epsilon^\chi), \quad \tilde{T}_{s(yy)} = K_y \tilde{T}_{s(zz)} + O(\epsilon^\chi), \quad (26)$$

where K_x and K_y are active during dilatational motion and passive during compressional motion. To avoid repeating, the derivations and expressions of K_x and K_y are not mentioned here, and can be found by referring to [3].

The down-slope and cross-slope components of the solid momentum equations are firstly integrated along the depth direction, and then Leibnitz integral rule is performed to simplify the integrated equations. Through substituting equations (18), (23), (25), and (26) into the resulting equations, the depth-integrated

equations for the granular phase finally become

$$\begin{aligned}
& \frac{\partial}{\partial t}(h\phi_s\bar{u}_s) + \frac{\partial}{\partial x}(h\phi_s\bar{u}_s\bar{u}_s) + \frac{\partial}{\partial y}(h\phi_s\bar{u}_s\bar{v}_s) \\
&= h\phi_s \sin \zeta - \epsilon\phi_s\gamma \frac{\partial}{\partial x} \left(\frac{h^2 \cos \zeta}{2} \right) - \epsilon \frac{\partial}{\partial x} \left(\frac{1}{2} K_x \phi_s (1 - \gamma) h^2 \cos \zeta \right) \\
&+ \frac{(1 - \gamma)\phi_s\phi_f}{\epsilon v_T (1 - \phi_s)^m} h(\bar{u}_f - \bar{u}_s) - \frac{\bar{u}_s}{|\bar{\mathbf{u}}_s|} h\phi_s \tan \delta [\lambda\kappa((\bar{u}_s)^2 - \gamma(\bar{u}_f)^2) + (1 - \gamma) \cos \zeta] \\
&- \epsilon h\phi_s \cos \zeta \frac{\partial b}{\partial x} + O(\epsilon^{(1+\chi)}), \tag{27}
\end{aligned}$$

$$\begin{aligned}
& \frac{\partial}{\partial t}(h\phi_s\bar{v}_s) + \frac{\partial}{\partial x}(h\phi_s\bar{u}_s\bar{v}_s) + \frac{\partial}{\partial y}(h\phi_s\bar{v}_s\bar{v}_s) \\
&= -\epsilon\phi_s\gamma \frac{\partial}{\partial y} \left(\frac{h^2 \cos \zeta}{2} \right) - \epsilon \frac{\partial}{\partial y} \left(\frac{1}{2} K_y \phi_s (1 - \gamma) h^2 \cos \zeta \right) \\
&+ \frac{(1 - \gamma)\phi_s\phi_f}{\epsilon v_T (1 - \phi_s)^m} h(\bar{v}_f - \bar{v}_s) - \frac{\bar{v}_s}{|\bar{\mathbf{u}}_s|} h\phi_s \tan \delta [\lambda\kappa((\bar{u}_s)^2 - \gamma(\bar{u}_f)^2) + (1 - \gamma) \cos \zeta] \\
&- \epsilon h\phi_s \cos \zeta \frac{\partial b}{\partial y} + O(\epsilon^{(1+\chi)}). \tag{28}
\end{aligned}$$

Besides the momentum equations, by applying the shallow assumption in the mass conservation equations, and repeating the process of depth integration, the depth-averaged mass conservation equations can read

$$\frac{\partial(h\phi_s)}{\partial t} + \frac{\partial(h\phi_s\bar{u}_s)}{\partial x} + \frac{\partial(h\phi_s\bar{v}_s)}{\partial y} = 0, \tag{29}$$

$$\frac{\partial(h\phi_f)}{\partial t} + \frac{\partial(h\phi_f\bar{u}_f)}{\partial x} + \frac{\partial(h\phi_f\bar{v}_f)}{\partial y} = 0, \tag{30}$$

respectively, for the granular phase and fluid phase.

5 Numerical Investigations

In this section, numerical results of the flows of fluid-sediment mixture are presented. Referring to [10], the NOC, shocking-capture high-resolution scheme, is adopted to discretize the PDEs. The details to implement this scheme can be found in [10]. An example of debris flows with initial hemi-ellipsoidal shape down a rough inclined plane at 40° with Coulomb bed friction angle $\delta = 30^\circ$ and merging continuously into a horizontal plane is studied. The computational domain is $x \in [0, 62]$ and $y \in [-18, 18]$ in dimensionless unit. The inclined section lies in the interval $x \in [0, 20]$ and the horizontal region lies where $x \geq 24$ with a smooth change in the topography in the transition zone, $x \in [20, 24]$. The inclination angle is prescribed by

$$\zeta(x) = \begin{cases} \zeta_0, & 0 \leq x \leq 20, \\ \zeta_0(1 - (x - 20)/4), & 20 < x < 24, \\ 0^\circ, & x \geq 24, \end{cases} \tag{31}$$

where $\zeta_0 = 40^\circ$. The mixture is suddenly released at $t = 0$ from an ellipsoidal shell with a length of the long semi-axis $a = 4$ and that of the short semi-axis $b = 2$. The center of the cap is initially located at $(x_0, y_0) = (5, 0)$ with a maximum total height of $h_{\max}^{\text{ini}} = 1$. The initial total height of the mixture is expressed as

$$h(x, y, t = 0) = h_{\max}^{\text{ini}} \left(1 - \frac{(x - x_0)^2}{a^2} - \frac{(y - y_0)^2}{b^2} \right). \quad (32)$$

As the first case, the numerical results for the dry granular material ($\phi_f = 0$) flow over the defined topography is presented. The internal friction angle within the granular phase is assumed to be $\psi = 35^\circ$. Fig. 2 demonstrates once the cap is opened, the granular mass accelerates downslope due to gravity and the body is elongated until the front reaches the horizontal run-out zone. Then, the front comes to rest due to bottom friction but the tail still accelerates further down, and the body contracts until the final deposition of the granular mass is attained.

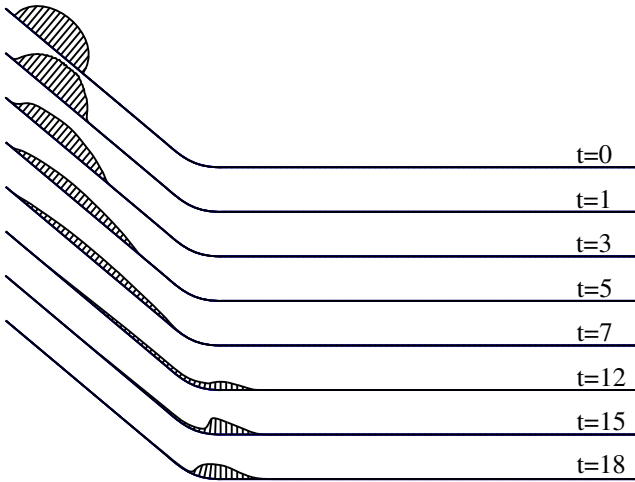


Fig. 2. The evolution for the thickness of the dry granular material along the central line of the flow for various dimensionless times

Furthermore, a general two-phase debris flow over the same topography is investigated. The densities of the fluid phase and the granular phase are chosen as $\rho_f = 1000 \text{ kg/m}^3$ and $\rho_s = 2500 \text{ kg/m}^3$, respectively. Fig. 3 shows the results for debris flow with initial homogenous fluid volume fraction $\phi_f = 0.4$. Comparing with Fig. 2, we observe that the granular phase moves faster, and the deposition is delayed in the presence of the fluid. Also, from the Fig. 3 (b), it is found that the fluid moves faster than the granular phase during the flow. This phenomenon can be explained by the fact that the Coulomb friction exerts a resistive force on

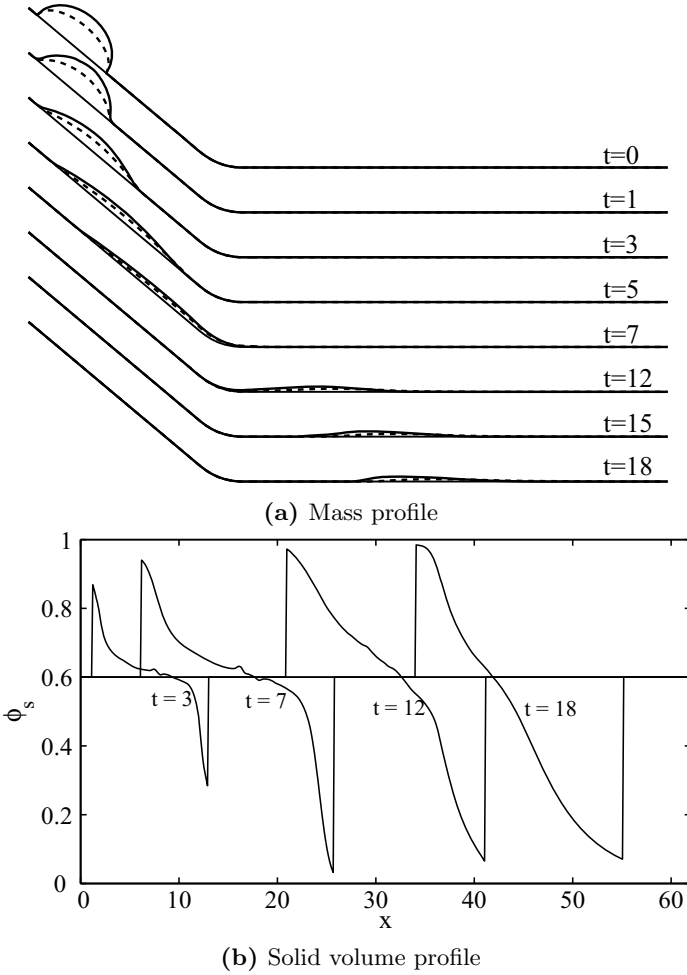


Fig. 3. Evolutions of (a) the heights of the granular phase (solid lines) and the fluid phase (dash lines), and (b) the solid volume fraction along the central line of the flow for various dimensionless times

the granular phase. A more direct overview of the debris flow can be obtained from the evolution of the three-dimensional geometries displayed in Fig. 4.

Last, another limiting situation of the pure fluid flow ($\phi_f = 1$) is investigated, in which the depth-integrated equations are reduced to the shallow water equations. As expected, the pure fluid moves faster than dry granular material, and finally disperses completely, so that the deposition does not occur, as shown in Fig. 5.

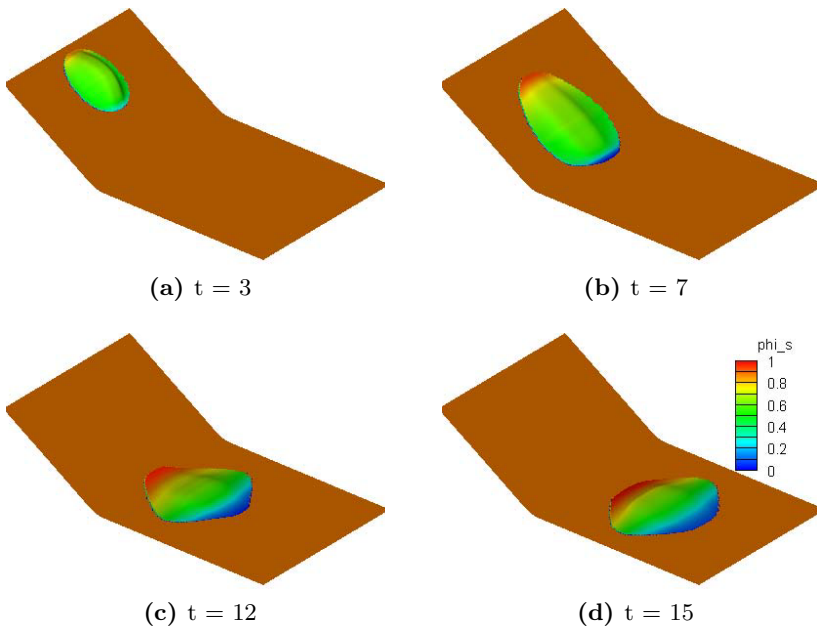


Fig. 4. Three-dimensional geometries of the debris flow at different dimensionless times $t = 3, 7, 12, 15$

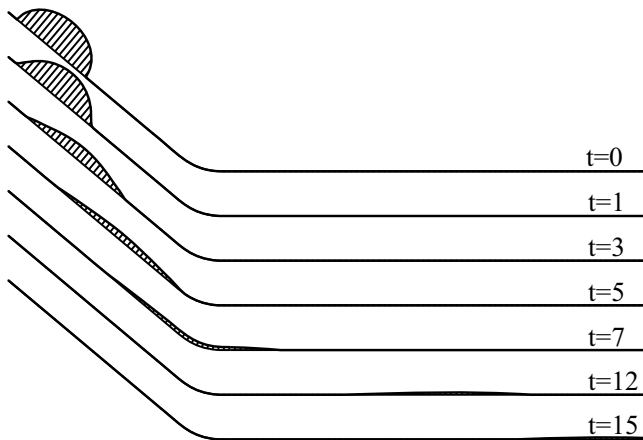


Fig. 5. The evolution of the height for pure water along the central line of the flow for various times

6 Conclusions

In the present study, a shallow two-phase model is proposed to simulate the saturated debris flows over three-dimensional shallow topography. The governing

equations are derived from the mixture theory. The resulting equations are integrated along the depth direction and simplified by shallow layer assumption. The final established equations comprise of a set of non-linear PDEs. The shocking-capture high-resolution scheme is employed to numerically solve the PDEs. Through the analysis of numerical solution, the present model can adequately describe the flows of dry granular material, general two-phase saturated debris flows and pure water. It is found that the granular phase moves faster in the presence of the fluid, and the deposition is further after flowing down an inclined surface. During the flow, the fluid phase moves faster than the granular phase, so that there are more fluid in the front of mixture. The obtained results can help the understanding of natural debris flows.

References

1. Anderson, T.B., Jackson, R.: Fluid mechanical description of fluidized beds. equations of motion. *Ind. Eng. Chem. Fundam.* 6, 527–539 (1967)
2. Gray, J., Wieland, M., Hutter, K.: Gravity-driven free surface flow of granular avalanches over complex basal topography. *Proc. R. Soc. A* 445, 1841–1874 (1999)
3. Geve, R., Koch, T., Hutter, K.: Unconfined flow of granular avalanches along a partly curved surface I. Theory. *Proc. R. Soc. A* 445, 399–413 (1994)
4. Pelanti, M., Bouchut, F., Mangeney, A.: A roe-type scheme for two-phase shallow granular flows over variable topography. *Math. Model Numer. Anal.* 42, 851–885 (2008)
5. Pitman, E.B., Le, L.: A two-fluid model for avalanche and debris flows. *Phil. Trans. R. Soc. A* 363, 1573–1601 (2005)
6. Pudasaini, S.P.: A general two-phase debris flow model. *J. Geophys. Res.* 117, 1–28 (2012)
7. Pudasaini, S.P., Wang, Y., Hutter, K.: Modelling debris flows down general channels. *Nat. Hazards Earth Syst.* 5, 799–819 (2005)
8. Richardson, J.F., Zaki, W.N.: Sedimentation and fluidisation: part 1. *Trans. Inst. Chem. Eng.* 32, 82–100 (1954)
9. Savage, S.B., Hutter, K.: The motion of a finite mass of granular material down a rough incline. *J. Fluid Mech.* 199, 177–215 (1989)
10. Wang, Y., Pudasaini, S.P., Hutter, K.: The Savage-Hutter theory: A system of partial differential equations for avalanche flows of snow, debris, and mud. *J. App. Math. Mech.* 84, 507–527 (2004)

Lattice-Boltzmann Method for Geophysical Plastic Flows

Alessandro Leonardi, Falk K. Wittel, Miller Mendoza, and Hans J. Herrmann

ETH Zurich, Institute for Building Materials,
Schafmattstrasse 6, 8093, Zurich CH
aleonardi@ethz.ch
<http://ifb.ethz.ch/comphys>

Abstract. We explore possible applications of the Lattice-Boltzmann Method for the simulation of geophysical flows. This fluid solver, while successful in other fields, is still rarely used for geotechnical applications. We show how the standard method can be modified to represent free-surface realization of mudflows, debris flows, and in general any plastic flow, through the implementation of a Bingham constitutive model. The chapter is completed by an example of a full-scale simulation of a plastic fluid flowing down an inclined channel and depositing on a flat surface. An application is given, where the fluid interacts with a vertical obstacle in the channel.

Keywords: mudflow, debris flow, non-Newtonian, Bingham, Lattice-Boltzmann.

1 Introduction

Geophysical flows are dangerous natural hazards occurring mostly in mountainous terrain. The most apparent phenomena of this category are debris flows, which originate when heavy rainfall mobilizes a large amount of debris [10]. The resulting mixture comprises water, cohesive sediments, organic matter, silt, sand and in many cases also stones of different sizes. The resulting rheological behavior is known to have a wide variability [24], which makes numerical studies an essential tool to support experimental investigations [9]. Full-scale simulations of geophysical flows are very scarce, since they require a framework that efficiently manages complicated boundary conditions, as well as a powerful and flexible fluid solver. Moreover, the non-Newtonian nature of the material, and in some cases its multiple phases, pose more challenges. Traditional solvers are known to have troubles in tackling this problem, and nowadays alternative solutions are sought by the community.

The Lattice Boltzmann Method (LBM) [23] is becoming increasingly popular and is today considered a valid alternative for categories of flows where traditional solvers exhibit disadvantages, like multiphase fluids, flows through porous media [18], irregular geometries [17], and free-surface realizations [12].

After reviewing the most commonly used rheological model for flowing geomaterials in Sec. 2, we offer an essential overview of the method in Sec. 3, together with a simple but effective formulation for the simulation of geophysical flows. In Sec. 4 and 5 examples are given.

2 Rheology of Geophysical Flows and Simulation

The rheology of geophysical flow materials is a debated issue in the field, due to the extreme variability in natural material parameters and the presence of multiple phases, complicating the classification. Most models therefore adopt simplified solutions based on single-phase descriptions. This can either be a frictional material [21,16] or a viscoplastic fluid [7,26]. The former is used for rock and snow avalanches, while the latter is preferred for mudflows and viscous debris flows [2]. For certain categories of geophysical flows, however, a single-phase approach is insufficient to capture the physics of the phenomena. Debris flows are a typical example of this, because granular and viscous behavior interact, giving rise to unexpected structures and a localization of rheological properties [11]. A continuum-continuum coupling for granular and fluid phase is possible, but is incapable of capturing the localization of flow properties, which is widely recognized to be a key feature of debris flows.

A discrete-continuum approach would of course be able to provide a detailed description, but development of this sort of coupling has been slowed by its demanding computational cost. This is currently challenged, however, by the maturity reached by alternative solvers like Smoothed Particle Hydrodynamics, the Material Point Method, or LBM, which are more flexible in managing complex boundary conditions than traditional tools like Finite Differences and Finite Volumes. In such methods, the granular phase is treated by a separate solver and, for this reason, the fluid model can focus on the nature of the material. This is the reason behind our choice to adopt LBM with a purely viscoplastic rheological law, an approach that can offer:

- An efficient framework for the simulation of geophysical flows of plastic nature, where the complexity of the boundary does not influence the performance.
- A convenient environment for the coupling with a discrete method. This option opens future chances for full realizations of multiphase flows [13].

Regarding the specific rheological law, we adopt the Bingham model, which is widely used to describe plastic fluids due to its conceptual simplicity. It reads:

$$\begin{cases} \dot{\gamma} = 0 & \text{if fluid does not yield } (\sigma < \sigma_y), \\ \sigma = \sigma_y + \mu_{pl}\dot{\gamma} & \text{if fluid flows } (\sigma > \sigma_y), \end{cases} \quad (1)$$

where σ_y and μ_{pl} denote yield stress and plastic viscosity. An analogous way to write the law is through an analogy with Newtonian flow. One defines a parameter, the apparent viscosity μ_{app} , which proportionally relates stress and

rate of strain and is treated as a variable. In the case of a Bingham fluid, μ_{app} takes the form

$$\sigma = \mu_{app} \dot{\gamma} \Rightarrow \mu_{app} = \mu_{pl} + \frac{\sigma_y}{\dot{\gamma}}, \quad (2)$$

where the apparent viscosity μ_{app} (from now on, for simplicity, called viscosity μ), diverges when $\dot{\gamma} \rightarrow 0$, which will require special care in the solver. We are now ready to introduce LBM in the next section, and to incorporate this constitutive law in Sec. 3.1.

3 Lattice-Boltzmann Formulation

LBM has lately emerged as an attractive alternative to traditional fluid solvers, mainly due to its high-level performance and the predisposition to parallelization. LBM is also suitable to the solution of problems involving complex boundary conditions [1]. It is beyond the scope of this chapter to give a complete description of the method. The reader can refer to Refs. [5,23] for a comprehensive review. We will focus on the aspects of the formulation that need to be modified in order to successfully reproduce debris flows.

In LBM, the fluid is described using a distribution function f_i and a set of discrete velocities \mathbf{c}_i . Density ρ and velocity \mathbf{u} of the fluid are computed as the first two moments of the distribution function

$$\rho = \sum_i f_i, \quad \mathbf{u} = \sum_i f_i \mathbf{c}_i / \rho. \quad (3)$$

The evolution of f_i is governed by the Lattice-Boltzmann equation

$$f_i(\mathbf{x} + \delta t \mathbf{c}_i, t + \delta t) = f_i(\mathbf{x}, t) + \Omega_i(\mathbf{x}, t), \quad (4)$$

where Ω_i is the operator that represents the effects of inter-particle collisions in the fluid. A common way to approximate the otherwise complex expression of Ω_i is the Bhatnagar-Gross-Krook operator [3], which relaxes the distribution function to a thermodynamic equilibrium f_i^{eq} . It can be written as

$$\Omega_i = \delta t \left(\frac{f_i^{eq} - f_i}{\tau} \right), \quad (5)$$

and features a constant, the relaxation time τ , which is related to the kinematic viscosity of the fluid μ as

$$\tau = \frac{\delta t}{2} + \frac{\mu}{c_s^2}. \quad (6)$$

With this formulation, and with the setting of a coherent lattice [22], LBM can produce realizations of fluid dynamics in analogy to the Navier-Stokes equations. The method is accurate in the limit of small Mach number, practically $\mathbf{u}_{max} < 0.01 c_s$ with c_s denoting the lattice speed of sound. We will now describe two additions to the model necessary for the simulation of geophysical flows: a non-Newtonian rheology and a free-surface treatment.

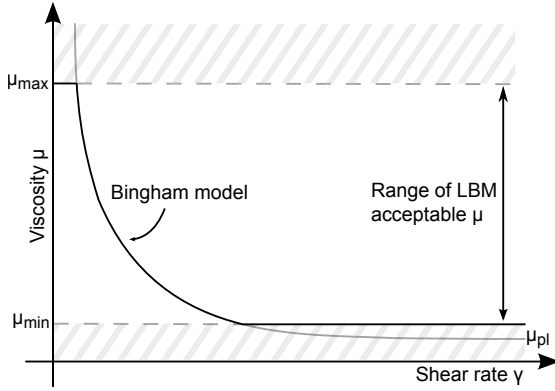


Fig. 1. Representation of the rheology model employed for plastic fluids. The approximation of the Bingham model is limited by the maximum and minimum values for the relaxation time τ imposed by the method. Therefore, also the viscosity μ_f is limited.

3.1 Non-Newtonian Rheology

The LBM described in the previous section yields, after the Chapman-Enskog expansion [4], the Navier-Stokes equation for Newtonian fluids. A simple way to upgrade the method to more general formulations is offered by a local treatment of the relaxation time τ [14,25]. Any rheological law that can be approximated as

$$\sigma = \mu \dot{\gamma}, \tag{7}$$

with $\mu = \mu(\dot{\gamma})$, is suitable for this approach. The relaxation time can in fact be directly related to the viscosity through Equation 6, obtaining ad hoc formulations for different rheological laws. The Bingham fluid, for example, can be written as

$$\sigma = \sigma_y + \mu_{pl} \dot{\gamma} \Rightarrow \tau = \frac{\delta t}{2} + \frac{1}{c_s^2} \left(\mu_{pl} + \frac{\sigma_y}{\dot{\gamma}} \right). \tag{8}$$

This type of formulation requires the computation of the shear rate tensor, which can be done easily in LBM directly from the distribution functions

$$\dot{\gamma}_{ab} = \frac{1}{2\tau c_s^2} \sum_i \mathbf{c}_{i,a} \mathbf{c}_{i,b} (f_i - f_i^{eq}), \tag{9}$$

and the magnitude can be extracted as

$$\dot{\gamma} = \sqrt{2 \sum_a \sum_b \dot{\gamma}_{ab} \dot{\gamma}_{ab}}. \tag{10}$$

The limitation of this approach lies in the range of values given to the relaxation time τ by Equation 8. Accuracy in LBM is guaranteed as long as $\tau_{min} < \tau < \tau_{max}$. Reasonable values for these limits are $\tau_{min} = 0.501$ and

$\tau_{max} = 1.0$. Therefore, also the viscosity μ , which is linearly linked to the relaxation time, is subjected to the same restrictions: $\mu_{min} < \mu < \mu_{max}$. The following considerations are thus necessary:

- The fluid that reaches the maximum allowed value of μ is considered to be in a plastic state. However, with the proposed scheme, the fluid never stops its motion, but rather flows at a much slower rate. The ratio between μ_{max} and μ_{min} determines the effectiveness of this approach. With the proposed limit values for τ , $\mu_{max} = 500\mu_{min}$.
- The best approximation of a Bingham fluid is obtained when $\mu_{min} \leq \mu_{pl}$, because the lower limitation on μ has no effect. However, an eventual transition to turbulent regime can happen when simulating diluted flows, and therefore the value of μ_{min} must be raised to avoid instabilities. In case $\mu_{min} \geq \mu_{pl}$, the approximation of the Bingham constitutive model becomes less accurate.

3.2 Implementation of the Free-Surface Technique

In order to simulate geophysical flows on realistic geometries, we need to include the boundary conditions given by the channel bed and the interface of the flow with air. While the former can be implemented as a standard no-slip boundary condition, as in Ref. [19], the latter is a less common practice in LBM. The free-surface is represented through a classification of the lattice nodes in three categories: liquid, interface and gas nodes. The governing parameter is the liquid fraction λ :

$$\begin{cases} \lambda = \rho & \text{if the node is liquid,} \\ 0 < \lambda < \rho & \text{if the node is interface,} \\ \lambda = 0 & \text{if the node is gas.} \end{cases} \quad (11)$$

The liquid fraction of a node evolves according to the streaming of the distribution function given by Equation 4 as

$$\lambda(t + \delta t) = \lambda(t) + \frac{\delta t}{\rho} \sum \alpha (f_{in} - f_{out}) \quad (12)$$

where f_{in} and f_{out} represent the distribution function streaming respectively in and out of the node, and α is a parameter that depends on whether the distributions are exchanged with a fluid node or another interface node. This method conserves mass exactly, and ensures a smooth evolution of the surface. Further details are found in Ref. [12].

4 Simulation of Mudflow

The full-scale simulation of a plastic geophysical flow is shown in this section. Mimicking the real geometry of a small valley, the simulation features a cylindrical channel inclined at 5° with respect to the horizontal, and a flat deposition

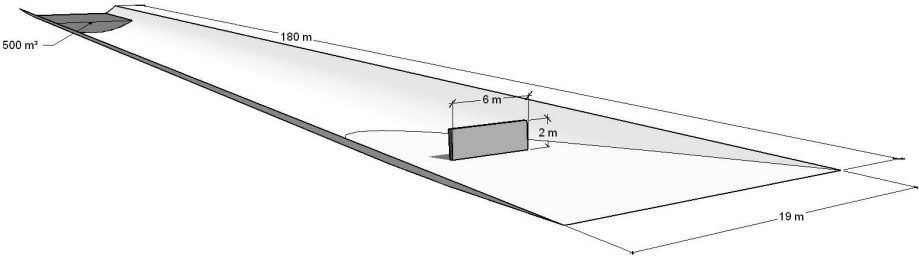


Fig. 2. Geometry of the simulation. The fluid mass lies at the top of a long cylindrical chute. The deposition area at the bottom is flat and features a vertical obstacle.

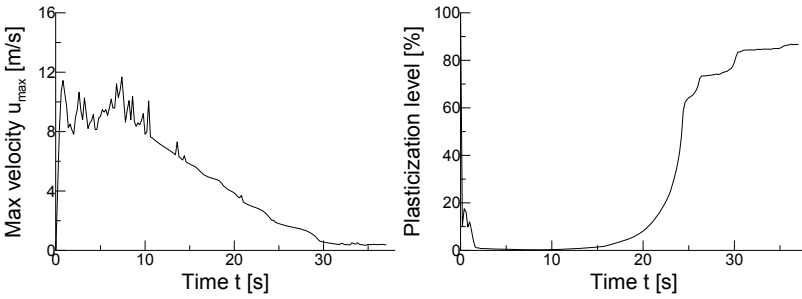


Fig. 3. Evolution of the maximum velocity of the fluid and of the flow plasticization level, computed as ratio between cells that have reached the maximum viscosity and the total number of cells

area at its bottom (Fig. 2). The total volume of the flowing material is 500 m^3 and is fixed, i.e. neither entrainment nor deposition are modeled. While very big events can be of the order of 10^6 m^3 , the size of the most frequent type of geophysical flows lies in the range of 10^3 m^3 , which is big enough to endanger humans and infrastructures. Therefore our simulation proposes a realistic scenario, even though not a particularly dangerous one. The fluid has density $\rho = 2000 \text{ kg/m}^3$ and follows a Bingham-like rheological law, like the one proposed in Sec. 3.1. Yield stress and kinematic plastic viscosity are respectively $\sigma_y = 150 \text{ Pa}$ and $\mu_{pl} = 10 \text{ textrmm}^2/\text{s}$, relating the simulated system to a very dense mudflow or to a debris flow whose granular phase has been homogenized into the fluid, therefore increasing the bulk viscosity [20,6]. Fig. 4 shows how the fluid free surface evolves in time. The fluid is quickly sheared by the effect of gravity and moves until an equilibrium is reached in the deposition area, where the viscosity increases. This technique can be used to estimate the deposition area of the material after an event, and to support the design of hazard maps on real terrain. Fig. 3 shows the evolution of the maximum velocity in the fluid and of the plasticization level of the material, which are the useful parameters to determine the status of the flow.

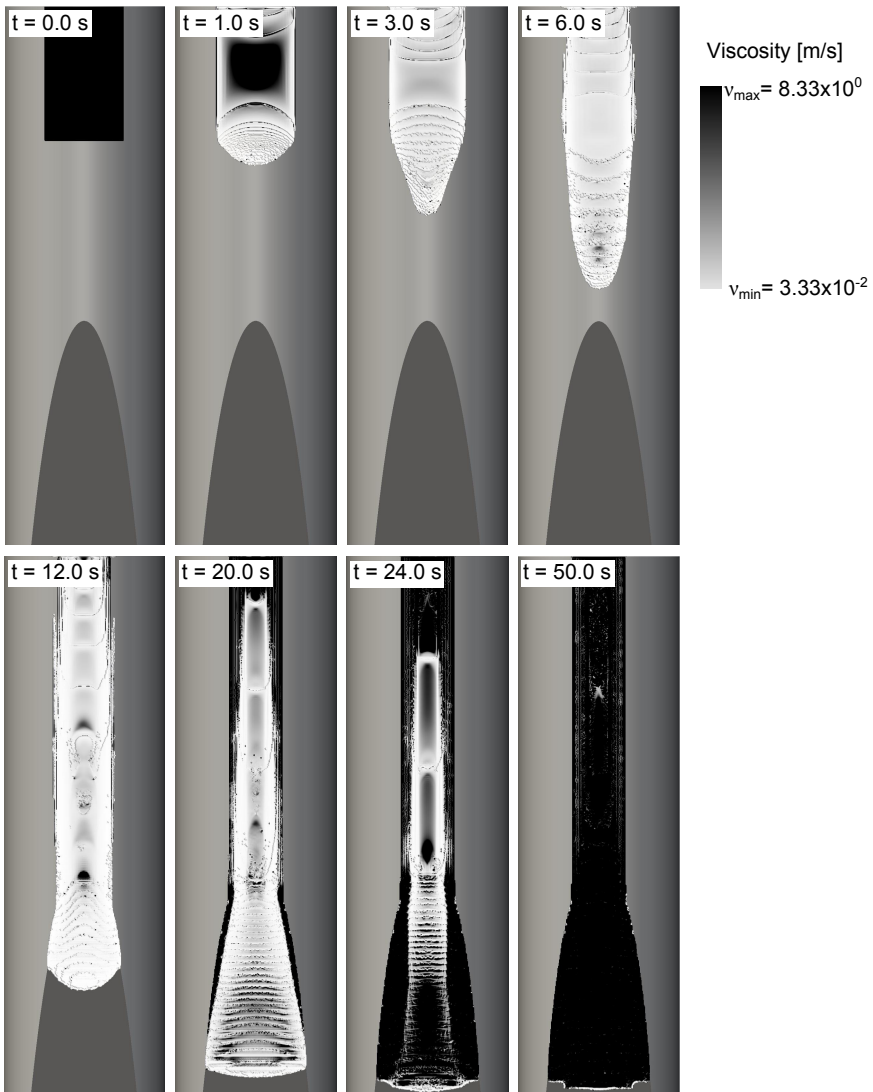


Fig. 4. Evolution of the geometry of the flow. Intensities show the viscosity at the surface, therefore indicating the rate of shearing of the fluid: low (dark) or high (light).

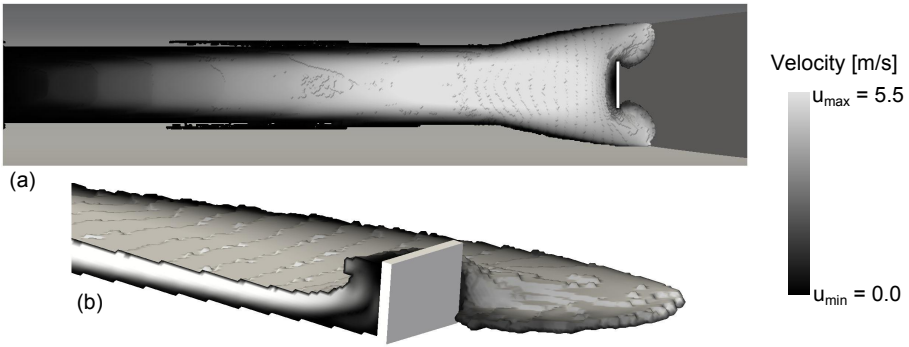


Fig. 5. Image of the flow splashing on the retaining wall, at $t = 14.0$ s. The color contour shows the velocity at the free surface (a) and in the longitudinal section (b).

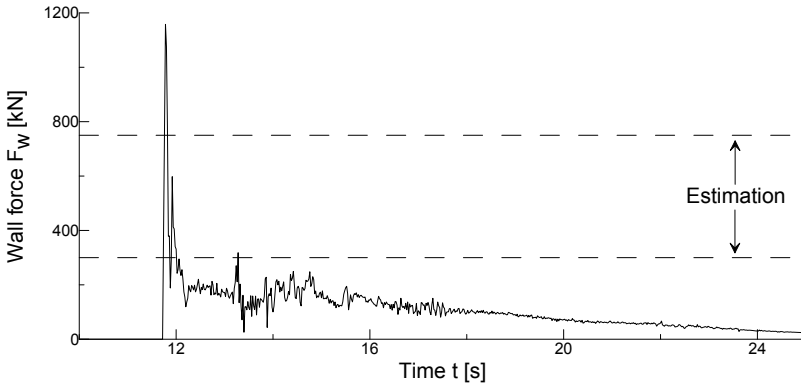


Fig. 6. Force exerted on the obstacle by the flow. The estimation is obtained with the hydrodynamic formula in Eq. 13

5 Obstacle Interaction

To show the possibilities to use LBM to design protection structures, we repeat the simulation of the previous section, this time featuring an obstacle. LBM can in fact be used to calculate the hydrodynamic interactions on solid objects, computing all momentum transfers between the distribution function and the solid boundaries. The procedure, which is found in Ref. [15], does not change significantly the overall efficiency of the method. We add a retaining wall, fixed at the bottom of the channel and of size $H \times L \times S = 3.0 \text{ m} \times 2.0 \text{ m} \times 0.25 \text{ m}$, as in Fig. 2. The shape of the free surface after the impact is shown in Fig. 5, with insight into the longitudinal cross section of the flow.

The force on the wall can be estimated with a hydrodynamic formula [8] as

$$F_{wall} = kA\rho v_{front}^2, \tag{13}$$

where A is the area of the obstacle impacted by the flow. The value of the coefficient k is given by the comparison with experiments and varies, according to different authors, from 2 to 5. In the simulation, when the flow hits the wall, the depth is 0.5m and the front speed is $v_{front} \simeq 5\text{m/s}$, which leads to an estimated force of $F_{wall} = 300 \div 750 \text{ kN}$. Fig. 6 shows the hydrodynamic force as calculated by the solver, highlighting the importance of the dynamic load due to the initial impact. The maximum values match the prediction of the hydrodynamic formula.

6 Outlook

In this chapter we showed how a model based on LBM can be used to simulate geophysical flows and provide a new tool for the rational design of mitigation and protection structures. The model inherits the advantages of the local solution mechanism of LBM, and extends the standard solver with the addition of a Bingham fluid formulation and of the free-surface technique. The resulting framework can be used to simulate homogeneous plastic flows, and provides an optimal environment for the coupling with discrete method, thus opening future chances for the full simulation of multiphase geophysical flows.

Acknowledgements. The research leading to these results has received funding from the European Union (FP7/2007-2013) under grant agreement n. 289911. We acknowledge financial support from the European Research Council (ERC) Advanced Grant 319968-FlowCCS. The authors are grateful for the support of the European research network MUMOLADE (Multiscale Modelling of Landslides and Debris Flows).

References

1. Aidun, C.K., Clausen, J.R.: Lattice-Boltzmann Method for Complex Flows. *Annu. Rev. Fluid Mech.* 42, 439–472 (2010)
2. Ancey, C.: Plasticity and Geophysical Flows: a Review. *J. Nonnewton. Fluid Mech.* 142, 4–35 (2007)
3. Bhatnagar, P.L., Gross, E.P., Krook, M.: A Model for Collision Processes in Gases. I. Small Amplitude Processes in Charged and Neutral One-Component Systems. *Phys. Rev.* 94, 511–525 (1954)
4. Chapman, S., Cowling, T.G.: *The Mathematical Theory of Non-uniform Gases: an Account of the Kinetic Theory of Viscosity, Thermal Conduction and Diffusion in Gases.* Cambridge University Press (1970)
5. Chen, S., Doolen, G.D.: Lattice Boltzmann Method for Fluid Flows. *Annu. Rev. Fluid Mech.* 30, 329–364 (1998)
6. Coussot, P.: *Mudflow Rheology and Dynamics.* A. A. Balkema, Rotterdam (1997)
7. Dent, J.D., Lang, T.E.: A Biviscous Modified Bingham Model of Snow Avalanche Motion. *Ann. Glaciol.*, 42–46 (1983)
8. Hübl, J., Suda, J., Proske, D., Kaitna, R., Scheidl, C.: Debris Flow Impact Estimation. In: *Int. Symp. Water Manag. Hydraul. Eng.*, Ohrid, Macedonia, pp. 137–148 (2009)

9. Hutter, K., Svendsen, B., Rickenmann, D.: Debris Flow Modeling: a Review. *Contin. Mech. Thermodyn.* 8, 1–35 (1996)
10. Iverson, R.M.: The Physics of Debris Flows. *Rev. Geophys.* 35, 245–296 (1997)
11. Iverson, R.M.: The Debris-Flow Rheology Myth. In: *Debris Flow Mech. Mitig. Conf.*, pp. 303–314. Mills, Davos (2003)
12. Körner, C., Thies, M., Hofmann, T., Thürey, N., Rüde, U.: Lattice Boltzmann Model for Free Surface Flow for Modeling Foaming. *J. Stat. Phys.* 121, 179–196 (2005)
13. Leonardi, A., Wittel, F., Mendoza, M., Herrmann, H.J.: Coupled dem-ibm Method for the Free-Surface Simulation of Heterogeneous Suspensions. *Computational Particle Mechanics* (submitted, 2014)
14. Leonardi, C.R., Owen, D.R.J., Feng, Y.T.: Numerical Rheometry of Bulk Materials Using a Power Law Fluid and the Lattice Boltzmann Method. *J. Nonnewton. Fluid Mech.* 166, 628–638 (2011)
15. Li, H., Lu, X., Fang, H., Qian, Y.: Force Evaluations in Lattice Boltzmann Simulations with Moving Boundaries in Two Dimensions. *Phys. Rev. E* 70, 026,701 (2004)
16. Mcdougall, S., Hungr, O.: A Model for the Analysis of Rapid Landslide Motion across Three-Dimensional Terrain. *Can. Geotech. J.* 41, 1084–1097 (2004)
17. Mendoza, M., Succi, S., Herrmann, H.J.: Flow through Randomly Curved Manifolds. *Sci. Rep.* 3, 3106 (2013)
18. Mendoza, M., Wittel, F.K., Herrmann, H.J.: Simulation of Flow of Mixtures through Anisotropic Porous Media Using a Lattice Boltzmann Model. *Eur. Phys. J. E. Soft Matter* 32, 339–348 (2010)
19. Mohamad, A.: *Lattice Boltzmann Method: Fundamentals and Engineering Applications with Computer Codes*. Springer (2011)
20. Phillips, C.J., Davies, T.R.: Determining Rheological Parameters of Debris Flow Material. *Geomorphology* 4, 101–110 (1991)
21. Savage, S.B., Hutter, K.: The Motion of a Finite Mass of Granular Material down a Rough Incline. *J. Fluid Mech.* 199, 177 (2006)
22. Shan, X., He, X.: Discretization of the Velocity Space in the Solution of the Boltzmann Equation. *Phys. Rev. Lett.* 80, 65–68 (1998)
23. Succi, S.: *The Lattice Boltzmann Equation for Fluid Dynamics and Beyond*. Oxford University Press, New York (2001)
24. Takahashi, T.: *Debris Flow, Mechanics, Prediction and Countermeasures*. Taylor & Francis, London (2007)
25. Švec, O., Skoček, J., Stang, H., Geiker, M.R., Roussel, N.: Free Surface Flow of a Suspension of Rigid Particles in a Non-Newtonian Fluid: a Lattice Boltzmann Approach. *J. Nonnewton. Fluid Mech.* 179–180, 32–42 (2012)
26. Whipple, K.X.: Open-Channel Flow of Bingham Fluids: Applications in Debris-Flow Research. *J. Geol.* 105, 243–262 (1997)

Modelling of a Free Surface Flow at Variable Gravity Conditions with SPH

Chong Peng, Miguel Angel Cabrera, and Wei Wu

Institut für Geotechnik, Universität für Bodenkultur,
Vienna, Austria

{pengchong,miguel.cabrera,wei.wu}@boku.ac.at

Abstract. Smoothed Particle Hydrodynamics (SPH) are adapted to model a free surface flow at variable gravity conditions. Implementation of SPH related to high gravity fields are discussed. The analysis shows that the original formulation of SPH needs no modification for the variation of gravity, though a smaller time step must be used. Numerical simulations of a water flow problem show that SPH is consistent at different gravity fields, and produce reasonable results. The scaling principle of the velocity and time of a flowing mass down an incline is discussed.

Keywords: Geotechnical centrifuge, smoothed particle hydrodynamics, water flow, variable gravity.

1 Introduction

Debris flow is a common natural hazard, claiming lots of human lives and properties each year. Due to the difficulties and high cost of large scale physical models and field observations, scaled modelling is a preferable option. Centrifuge modelling is based on the principle of an increased acceleration field acting over a reduced scale-model. The increase of the acceleration field is perceived within the model as an increase of the acting stresses which produces increased strains. Because soil or water are stress dependent materials, the proper consideration of scaling principles allows the modelling of field processes at a reduced scale [6]. Geotechnical centrifuge modelling involves the testing of a $1/N$ scale model under a centrifugal acceleration of N times Earth's gravity (where N is the scale factor defined as the number of earth gravities acting over the model). Thus, centrifuge provides a useful tool for modelling debris flow in lab conditions [1], [5].

Because of the increased gravitational field induced in the model, performing a centrifuge test is not an easy task. The design and preparation of the model and equipment must consider the flow conditions induced by the increased gravity in the centrifuge model. For this reason, numerical modeling is employed to evaluate the characteristic flow conditions as peak velocity, flow duration, flow heights, among others. Moreover, the numerical simulations can also provide validation for the experimental results.

The Smoothed Particle Hydrodynamics (SPH) is a pure Lagrangian meshfree method, mature in the modelling of free surface flow [4]. SPH models continuum by scattered particles, which carry field variables like mass, density, stress, among others, and move with the material velocity. SPH is widely used to study fluid dynamic problems, such as gravity currents [8], wave propagation [10] and fluid-solid interaction [3].

In this study, SPH is adapted to model the free surface flow in centrifuge. As a preliminary study only water is considered. Special attention will be paid to the simulation of flow in a high gravity condition. Some issues related with the high gravity, like time step, viscosity treatment, will be stressed. The strong collisions between fluid and structure will also be discussed.

2 SPH Formulations

2.1 SPH Integral Interpolation

In SPH, the problem domain is discretized by a set of particles, which carry physical properties and move with the fluid. Physical variables on each particle are computed by an interpolation process over its neighbouring particles. In the framework of integral interpolation, a field function $f(\mathbf{x})$ can be approximated by

$$f(\mathbf{x}) = \int_{\Omega} f(\mathbf{x}')W(\mathbf{x} - \mathbf{x}', h)dV \quad (1)$$

where Ω is the integral domain and dV is the element of volume; W is the weighting function called smoothing kernel in SPH, h is the smoothing length. The size of integral domain is dependent on h which determines a support domain surrounding \mathbf{x} . To ensure the accuracy and stability of SPH, it is found by Monaghan that the kernel functions of SPH must satisfy some rules [7]. Here the cubic spline function is applied, by the following form

$$W = \alpha_D \begin{cases} 1 - 1.5q^2 + 0.75q^3 & 0 \leq q < 1 \\ 0.25(1 - q)^3 & 1 \leq q < 2 \\ 0 & q \geq 2 \end{cases} \quad (2)$$

where α_D is a normalization factor, whose value is $10/(7\pi h^2)$ in 2D and $1/(\pi h^3)$ in 3D; q is the normalized distance defined as $q = r/h$ and r is the distance between two particles. It can be observed that the kernel is compactly supported, which means that out of its support domain the value is equal to zero. Based on the concept of integral interpolation, the continuous form in Eq. 1 can be written in the following summation form over the particles in the support domain:

$$\langle f(\mathbf{x}_i) \rangle = \sum_{j=1}^n f(\mathbf{x}_j)W(\mathbf{x}_i - \mathbf{x}_j, h)m_j/\rho_j \quad (3)$$

where n is the number of particles in the support domain of kernel W_{ij} centered at \mathbf{x}_i . The volume of particle j is represented by m_j/ρ_j . Following the same way, the gradient of $f(\mathbf{x})$ can be calculated as

$$\langle \nabla f(\mathbf{x}_i) \rangle = \sum_j^n f(\mathbf{x}_j) \nabla W(\mathbf{x}_i - \mathbf{x}_j, h) m_j / \rho_j \quad (4)$$

2.2 Discretization of Governing Equations

Following the concept of SPH integral interpolation and with some formulation transformation, the governing Navier-Stokes equations of fluid can be expressed in the following summation form over the particles

$$\frac{d\rho_i}{dt} = \sum_{j=1}^n m_j (\mathbf{u}_i - \mathbf{u}_j) \nabla_i W_{ij} \quad (5)$$

$$\frac{d\mathbf{u}_i}{dt} = - \sum_{j=1}^n m_j \left(\frac{p_i}{\rho_i^2} - \frac{p_j}{\rho_j^2} + \Pi_{ij} \right) \nabla_i W_{ij} + \mathbf{g} \quad (6)$$

in which \mathbf{u} is the particle velocity, p the pressure and \mathbf{g} the gravity vector. Eq. 5 is the equation of mass conservation and Eq. 6 the equation of momentum conservation. The term Π_{ij} related to the viscosity treatment will be discussed in section 3.2.

To complete the governing equation, a method for pressure calculation is needed. Usually water is modelled as a weakly compressible fluid in SPH (WC-SPH). The following relationship between pressure and density is applied in most of the SPH formulation, often referred as equation of state [8]

$$p = B \left[\left(\frac{\rho}{\rho_0} \right)^\gamma - 1 \right] \quad (7)$$

where ρ_0 is the reference density (for water $\rho_0 = 1000 \text{ kg/m}^3$) and γ is a constant usually taken as 7. The constant B is linked to the speed of sound of the media, taken as $B = c_0^2 \rho_0 / \gamma$ where c_0 is the reference speed of sound. The determination of the speed of sound in high gravity flow will be discussed in section 3.1.

Fluid particles in simulation are moved in the so called XSPH manner

$$\frac{d\mathbf{x}_i}{dt} = \mathbf{u}_i + \varepsilon \sum_{j=1}^n m_j (\mathbf{u}_i - \mathbf{u}_j) W_{ij} m_j / \bar{\rho}_{ij} \quad (8)$$

where ε is a constant usually taken as 0.5 in fluid simulation, $\bar{\rho}_{ij}$ is the average density of particle i and j . This correction makes the particles move more orderly and prevents fluid penetration [8].

3 Implementation and Discussion at High Gravity

Unlike common fluid dynamics cases such as a dam break and wave propagation in a $1g$ environment, in a geotechnical centrifuge the gravitational field is increased to N times Earth's gravity. The scaling factor N can be in some cases on the order of 10^2 . Therefore, special attention should be paid to some parts of the conventional SPH, to keep the numerical simulation stable and reasonable.

3.1 Equation of State

Water is modelled as a weakly compressible media. The variation of density has the following form

$$\frac{\delta\rho}{\rho} = \frac{v_c^2}{c^2} = \frac{1}{M^2} \quad (9)$$

where v_c is the typical velocity in fluid, c is the speed of sound and M is the Mach number. The application of real speed of sound in water, which is in the order of 10^3m/s , results in a very small time step in SPH simulation. Therefore, a reduced speed of sound is used in practice. If the density fluctuations are of the order 10^{-2} , then M should be of the order 10. The typical estimation of the terminal velocity in a fluid can be obtained by \sqrt{gH} , where H is the still water level. Then the reference speed of sound (speed sound when $\rho = \rho_0$) can be chosen as $c_0 = \lambda\sqrt{gH}$ where λ is a coefficient of the order of 10. In this way M is ≈ 10 and the density fluctuations are $\approx 1\%$.

In the scenario where gravity is increased, if λ keeps unchanged, the density fluctuations should not vary. Without changing the geometry of the model, let the superscripts 1 and N represents the $1g$ and Ng condition, respectively. Since $B = c_0^2\rho_0/\gamma$, we have $B^N = NB^1$. Thus it is clear that $p^N = Np^1$, which means that the pressure scaling principle is satisfied.

The general speed of sound is calculated by

$$c^2 = c_0^2(\rho/\rho_0)^{\gamma-1} \quad (10)$$

It is easily found that at a different gravity the speed of sound scales to $c^N = \sqrt{N}c^1$.

3.2 Artificial Viscosity

The additional term \prod_{ij} in Eq. 6 is related to the viscous term in Navier-Stokes equations. At low Reynolds numbers, this term can be directly derived from the viscous stresses with the SPH discretization [9]. But in an increased gravitational field, the fluid will exhibit strong collisions with the fixed boundaries and frequent water splashes. This behaviour is characterized by high Reynolds numbers and it is more suitable to be modelled as an inviscid flow.

The simulation of an inviscid flow should use Eq. 6 without the viscous term \prod_{ij} . However, this scheme is unstable when solved with explicit time integration. Thus, an artificial viscosity term is usually added, also denoted by \prod_{ij}

$$\prod_{ij} = \begin{cases} -\frac{\alpha h \bar{c}_{ij}}{\bar{\rho}_{ij}} \frac{\mathbf{u}_{ij} \mathbf{r}_{ij}}{r_{ij}^2 + \eta^2} & \mathbf{u}_{ij} \mathbf{r}_{ij} < 0 \\ 0 & \mathbf{u}_{ij} \mathbf{r}_{ij} \geq 0 \end{cases} \quad (11)$$

where $\mathbf{u}_{ij} = \mathbf{u}_i - \mathbf{u}_j$ and $\mathbf{r}_{ij} = \mathbf{x}_i - \mathbf{x}_j$, \bar{c}_{ij} is the average speed of sound of particle i and j , and η is a small number used to avoid singularity. It can be observed that the viscous forces exist only when the particles approach each other and decreases linearly with the smoothing length h . α is a particular constant to the scenario being considered, and need to be tuned in the numerical simulations. Researches revealed that $\alpha > 0.01$ should be satisfied in $1g$ environment [8]. The method to determine α at a Ng condition is discussed below.

According to the scaling laws in centrifuge modelling, the stresses in a Ng condition should be N times of the stresses at $1g$ if the geometry of the system is fixed, i.e., $\prod_{ij}^N = N \prod_{ij}^1$. If we check Eq. 11 carefully, we can find that h , \mathbf{r}_{ij} and $\bar{\rho}_{ij}$ are almost the same at different gravity conditions, while according to section 3.1 $\bar{c}_{ij}^N = \sqrt{N} \bar{c}_{ij}^1$ and $\mathbf{u}_{ij}^N = \sqrt{N} \mathbf{u}_{ij}^1$ are scaled. For this reason, the scaling principle of the viscous term can be satisfied without any modification of the constant α . Therefore, once α is tuned in a $1g$ condition, it can be used for the simulations of an increased gravity.

3.3 Time Step

Explicit time integration is used to march the simulation forward in time, following the discretized SPH formulation given in Eq. 5 and Eq. 6. The time integration scheme used in this study is a second order predictor-corrector method [8]. To keep the numerical process stable, the time step needs to be chosen carefully. In general, the time step depends on the force term, the viscosity term, and on the Courant-Friedrichs-Lewy (CFL) condition [4]. The time step concerning CFL condition and viscosity effect is

$$\Delta t_{cv} = \min_i \left(\frac{h}{c_i + \max_j |h \mathbf{u}_{ij} \mathbf{r}_{ij} / r_{ij}^2|} \right) \quad (12)$$

where i is looped in all the particles in simulation and j is looped in the supported domain of particle i . The time step related to the force term is

$$\Delta t_f = \min_i \left(\sqrt{h / f_i} \right) \quad (13)$$

where f_i is the force per unit mass at the i th particle. Then, based on these two restrains, the time step used in the present study is

$$\Delta t = \chi \min(\Delta t_{cv}, \Delta t_f) \quad (14)$$

where χ is a coefficient ranging from 0.1 to 0.4.

Since the forces exerted on the particles and the speed of sound in an increased gravity condition Ng are larger, it is expected that the time step employed in an increased gravity scenario should be smaller. As discussed in Eq. 12, it is clear that $c^N = \sqrt{N}c^1$ and $\mathbf{u}_{ij}^N = \sqrt{N}\mathbf{u}_{ij}^1$. Therefore, we have $\Delta t_{cv}^N = \Delta t_{cv}^1/\sqrt{N}$. In Eq. 6, each of the three terms on the right side are N times larger in an increased gravity condition, thus, the relationship of force is $f^N = Nf^1$. From this, the time step in different gravitational fields can be derived to

$$\Delta t^N = \Delta t^1/\sqrt{N} \quad (15)$$

4 Numerical Results

Water flow in centrifuge is simulated using SPH. The configuration of the model is shown in Fig. 1. The dimensions of the box are $48 \times 49 \times 8$ cm (L \times H \times W). Other dimensions of the model are: $d = 20$ cm, $l = 40$ cm and $\beta = 30^\circ$. The radius of the inflow tube is 3 cm, and the total water volume is 1.82 L.

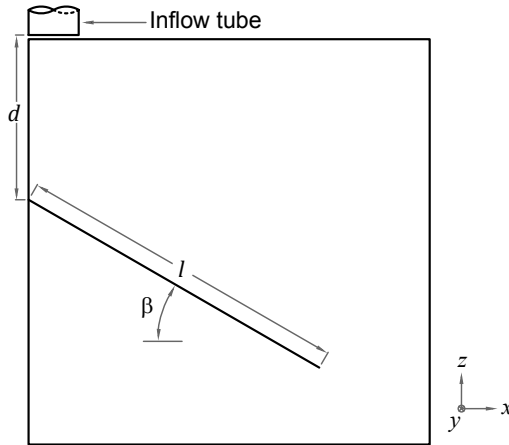


Fig. 1. Configuration of the model. Note that gravity acts in the negative direction of the z axis

The open source code DualSPHysics [2] is adapted to analyse the free surface flow. Particles are placed on a regular grid in a three-dimensional arrangement over the inflow tube. The box and slope are modelled by fixed particles. In the model the particle space is 0.005 m and the smoothing length $h = 0.0075$ m. A total number of 93351 particles are used in the simulation. First a standard case at a $1g$ gravity is modelled. Taking the $1g$ case as a reference, five more cases are performed varying the gravity by a factor of N . $10g$, $20g$, $30g$, $40g$ and $50g$ are used in the five cases, respectively. The artificial viscosity is tuned under $1g$ and taken as $\alpha = 0.1$ for all cases.

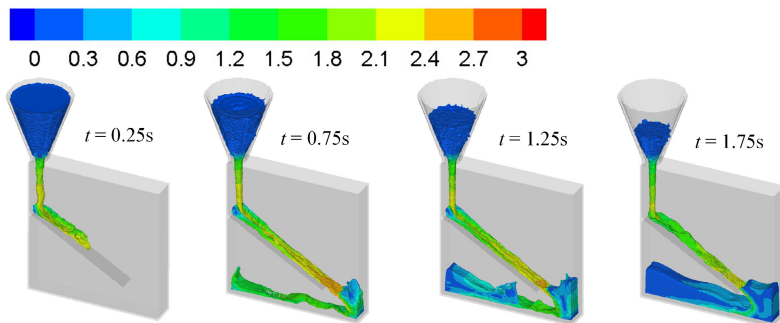


Fig. 2. Water flow in geotechnical centrifuge at $1g$. Note that the color bar is common to all snapshots and its units is in m/s.

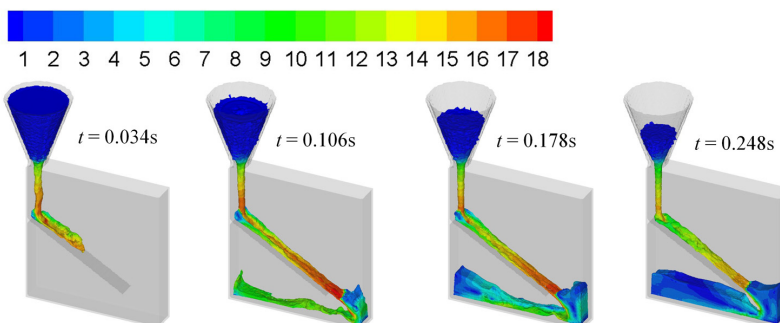


Fig. 3. Water flow in geotechnical centrifuge at $50g$. Note that the color bar is common to all snapshots and its units is in m/s.

Fig. 2 shows the velocity magnitude of the water flow at different instants in a $1g$ environment. Driven by gravity, water accelerates below the inflow tube and collides with, first the slope, then the box vertical wall, and then gets collected at the bottom of the box. The water flow height at the top of the slope is clearly larger than at the end of the slope, where the flow is more uniform. This is caused by the collisions between the flow and the lateral walls. The total duration of the flow is $t^1 = 2.43$ s, with a maximum velocity of $v^1 = 2.99$ m/s.

Based on the numerical simulations, the pattern of the flow at different gravitational fields is almost the same. For this reason, only the result of $50g$ is given in Fig. 3. On it, is clear that the flow pattern is almost identical to its counterpart in Fig. 2. However, the maximum velocity and the duration of the flow are not the same.

The maximum velocity and duration of the flow T are normalized by its equivalent value at $1g$, as shown in Fig. 4. With the intention to differentiate the characteristics of the flow down the incline in the global model, two cases for the maximum velocity and duration of the flow are considered. i.e., the maximum velocity in the slope is obtained just inside the slope domain, while the maximum velocity in the global model refers to the global simulation. The normalized velocity coincides with the velocity analysis given in the above sections, which is $v^N = \sqrt{N}v^1$, with a little difference: the larger the gravity, the bigger the error. Finding the difference bigger for the global simulation and smaller for the in-slope simulation. The reason of this observation lays, probably, in the fact that the maximum velocity is only calculated every hundreds steps, not every time step. Therefore, the given maximum velocity is not the global maximum velocity in the whole flow. Furthermore, the normalized duration of the flow fits to the expected scaling principle of $1/\sqrt{N}$ for the in-slope and global simulations.

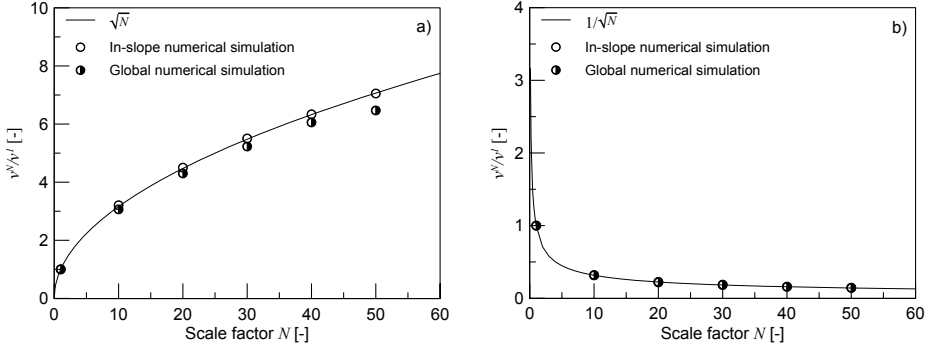


Fig. 4. Scaling effects at different gravity conditions. a) Normalized maximum velocity, b) Normalized flow duration. Note that the normalized flow duration is the same for the in-slope and global simulation.

From Fig. 4.b, it is found that the duration of the flow at different gravity has the following relationship:

$$T^N = T^1/\sqrt{N} \quad (16)$$

From Eq. 15 and Eq. 16, it is obvious that the number of time steps needed for the simulation at different gravity is the same. This means that simulations at different gravity have the same computational cost, since they have identical particle configuration field.

The outcome from the simulations is a valuable information for the design and conception of the centrifuge model. The writers find preliminary simulations as an important tool to understand the expected mechanisms and enhance the

experimental techniques aiming to a more general validation of the assumptions made in the model.

5 Conclusions

The SPH is mainly used at $1g$ environment, while its application at high gravity is seldom. In this paper, the formulation and implementation of classic SPH is carefully reviewed, with additional attention on its application at high gravity.

Free surface water flow at an increased gravity is modelled. The numerical results shows that the formulation of the classic SPH is consistent, in spite of the augmented gravity. The formulated scaling principles regarding the flow of water down an incline are reproduced properly. Future research should consider the validation of experimental data with a general scaling law following the "modelling of models" approach. Also, the outcome of the simulations is a valuable information for the design and conception of the centrifuge model, and can be used as a validation with experimental data.

Acknowledgements. The research leading to these results has received funding from the People Programme (Marie Curie Actions) of the European Union's Seventh Framework Programme FP7/2007-2013/ under REA grant agreement n° 289911.

References

1. Bowman, E., Laue, J., Springman, S.: Experimental modelling of debris flow behaviour using a geotechnical centrifuge. *Canadian Geotechnical Journal* 47(7), 742–762 (2010)
2. Crespo, A.J.C., Dominguez, J., Barreiro, A., Gomez-Gesteira, M., Rogers, B.D.: DualSPHysics, new GPU computing on SPH models. In: Proc. 6th International SPHERIC Workshop, pp. 348–354 (2011)
3. Dalrymple, R.A., Rogers, B.D.: Numerical modeling of water waves with the SPH method. *Coastal Engineering* 53(2), 141–147 (2006)
4. Gomez-Gesteira, M., Rogers, B., Dalrymple, R., Crespo, A.: State-of-the-art of classical SPH for free-surface flows. *Journal of Hydraulic Research* 48(1), 6–27 (2010)
5. Ling, H., Wu, M., Leshchinsky, D., Leshchinsky, B.: Centrifuge modeling of slope instability. *J. Geotech. Geoenviron. Eng.* 135(6), 758–767 (2009)
6. Mitchell, R.J.: The eleventh annual R.M. Hardy Keynote Address, 1997: Centrifugation in geoenvironmental practice and education. *Canadian Geotechnical Journal* 35(4), 630–640 (1998)
7. Monaghan, J.J.: Why particle methods work. *SIAM Journal on Scientific and Statistical Computing* 3(4), 422–433 (1982)
8. Monaghan, J.J.: Simulating free surface flows with SPH. *Journal of Computational Physics* 110(2), 399–406 (1994)
9. Morris, J.P., Monaghan, J.J.: A switch to reduce SPH viscosity. *Journal of Computational Physics* 136(1), 41–50 (1997)
10. Shao, S.: Simulation of breaking wave by SPH method coupled with $k-\epsilon$ model. *Journal of Hydraulic Research* 44(3), 338–349 (2006)

The Role of Phase Transition in Slope Stability Analyses

Roberto Tamagnini and Wei Wu

Institut für Geotechnik, Universität für Bodenkultur,
Vienna, Austria
{roberto.tamagnini,wei.wu}@boku.ac.at

Abstract. The paper presents a thermodynamically consistent analysis of rainfall induced landslides in partly saturated porous materials. The thermodynamic framework is based on non-equilibrium thermodynamics and the theorem of minimum entropy production. The model is implemented in the FE software Abaqus and it is applied in the analysis of an ideal problem in which the role of water condensation is modeled. The analysis is performed in plane strain conditions and it shows as associative plasticity is able to capture the initialization of the mud flow. The numerical algorithm for the constitutive law is derived by the thermodynamics and it is able to describe the collapse induced by wetting. The presented mathematical framework is able to explain the mechanical instability of hill slopes during a coupled strain-diffusion analysis.

1 Introduction

Evapotranspiration and evaporation of water are well-known phenomena that increase the engineering performance of slopes. The extraction of water from soils by vegetation and climate heating increases soil's suction and shear strength. The present paper analyses the inverse phase transition, the condensation of water, as the triggering mechanism of landslides in partially saturated soils. The mathematical framework that describes the material behavior and the slope performance is introduced by thermodynamics. The local equations are derived by non-equilibrium thermodynamics and the system instability is discussed applying the theorem on mechanical equilibrium by Prigogine [1]. The constitutive equations are integrated using a return mapping algorithm that describes the evolution of the affinities of the system. The model is then applied in the simulation of a rainfall induced landslide. The infiltration of water from the slope profile triggers a fluctuation of the equilibrium and drives the system in an overall unstable condition. The principle of minimum entropy production implies that the local equilibrium is obtained for a stationary value of the driving forces. This condition is numerically analyzed.

2 Thermodynamics

Partially saturated soils have been investigated by many authors using thermodynamics [2, 3, 4]. The present paper approaches the identification of the conjugated variables by the principles of non-equilibrium thermodynamics [5, 6]. The specific quantities are defined at the local level with the following symbols:

- Intensive variables: the temperature $T(x,t)$, the fluid pressure $p_\alpha(x,t)$ of the α component of the mixture, the total applied stress tensor $\sigma_{ij}(x,t)$ and the chemical potential $\mu(x,t)$.
- The extensive variables: the entropy $s(x,t)$, the internal energy $u(x,t)$ and the number of mole of the reactant k , $n_k(x,t)$.

The basic hypothesis is that at the local level the laws of equilibrium thermodynamics are satisfied even if the overall system is not in equilibrium. In the following, the system is considered as an open system that can exchange energy and matter with the environment. The second law of thermodynamics can be formulated as:

$$dS = dS_i + dS_e \quad (1)$$

in which dS_e is the change of entropy of the system due to the exchange of energy and matter and dS_i is the internal production of entropy. The restriction on the sign of the entropy, in the case of an open system, applies only to the first term of equation (1):

$$dS_i \geq 0 \quad (2)$$

The local entropy production is defined as:

$$\frac{dS_i}{dt} = \int_V \Phi(x,t) dV \quad \text{with} \quad \Phi(x,t) = \frac{ds_i(x,t)}{dt} \geq 0 \quad (3)$$

in which V is the Reference Elementary Volume (REV) of the system. The change in the number of mole of the component k can be expressed by $dn_k = dn_k^e + dn_k^i$ where the first term is the change of the specific number of mole due to transport and the second term is the internal production due to chemical reactions or phase transition. The mass balance equation of the component k can be expressed by the equation:

$$\frac{\partial n_k}{\partial t} = \frac{\partial n_k^e}{\partial t} + \frac{\partial n_k^i}{\partial t} = -\nabla \cdot (\mathbf{v}_k n_k) + \Theta[n_k] \quad (4)$$

in which \mathbf{v}_k is the velocity of the component k and Θ is the internal production of the component k due to chemical reactions. The velocity of the centre of mass \mathbf{v}

of the mixture (generally associated with the motion of the solid skeleton) can be defined as:

$$\mathbf{v} = \frac{\sum_k M_k n_k \mathbf{v}_k}{\sum_k M_k n_k} \quad (5)$$

in which M_k is the molecular mass of component k . The diffusion flow \mathbf{J}_k of component k is defined as:

$$\mathbf{J}_k = n_k (\mathbf{v}_k - \mathbf{v}) \quad (6)$$

Introducing equation (6) in equation (4) the following expression can be obtained:

$$\frac{\partial n_k}{\partial t} = \frac{\partial n_k^e}{\partial t} + \frac{\partial n_k^i}{\partial t} = -\nabla \mathbf{J}_k - \nabla(n_k \mathbf{v}) + \sum_j \nu_{jk} \nu_j \quad (7)$$

in which the last term is the internal production of the component k and it can be expressed by the product of the stoichiometric coefficient ν_{jk} and the velocity of reaction:

$$\nu_j = \frac{1}{V} \frac{d\xi_j}{dt} \quad (8)$$

ξ_j is the extent of the j^{th} reaction. The equation (7) can be formulated in terms of the material time derivative d/dt with respect to the motion of the centre of mass of the mixture:

$$\frac{dn_k}{dt} = -\nabla \mathbf{J}_k - n_k \nabla \cdot \mathbf{v} + \sum_j \nu_{jk} \nu_j \quad (9)$$

The equation of motion (the mechanical equilibrium) for the system can be written:

$$\sum_k M_k n_k \frac{d\mathbf{v}}{dt} = -\nabla \sigma_{ij} + \sum_k n_k \mathbf{F}_k \quad (10)$$

in which, the overall density:

$$\sum_k M_k n_k = \rho \quad (11)$$

and the force \mathbf{F}_k due to an external field ψ_k :

$$\mathbf{F}_k = \nabla \psi_k \quad (12)$$

have been introduced. The rate of the kinetic energy and potential energy can be defined as [6]:

$$\frac{\partial \rho \left(\frac{1}{2} \mathbf{v}^2 + \psi \right)}{\partial t} = -\nabla \cdot \left\{ \rho \left(\frac{1}{2} \mathbf{v}^2 + \psi \right) \mathbf{v} + \boldsymbol{\sigma} \cdot \mathbf{v} + \sum_k \psi_k \mathbf{J}_k \right\} + \boldsymbol{\sigma} : \nabla \mathbf{v} - \sum_k \mathbf{J}_k \mathbf{F}_k \quad (13)$$

In an open system, the conservation of total energy can be expressed by the equation:

$$\frac{\partial \rho e}{\partial t} + \nabla \mathbf{J}_e = 0 \quad (14)$$

in which e is the total specific energy and \mathbf{J}_e is the energy flux. The specific energy e is the sum of the kinetic energy, the internal energy (the energy that is not associated with the bulk motion) and the potential energy:

$$\rho e = \frac{1}{2} \sum_k M_k n_k \mathbf{v}_k^2 + \rho u + \rho \psi = \frac{1}{2} \rho \mathbf{v}^2 + \frac{1}{2} \sum_k M_k n_k \mathbf{J}_k^2 + \rho u + \rho \psi \quad (15)$$

In the following the kinetic energy of diffusion associated with the vector \mathbf{J}_k will be disregarded. The energy flux can be written as [6]:

$$\mathbf{J}_e = \mathbf{J}_q + \sum_k M_k n_k e_k \mathbf{v}_k + \sum_k \psi_k \mathbf{J}_k + \boldsymbol{\sigma} \cdot \mathbf{v} \quad (16)$$

Using equation (13) and (14) and considering the relation:

$$\rho \frac{da}{dt} = \frac{\partial \rho a}{\partial t} + \nabla(a \rho \mathbf{v}) \quad (17)$$

in which a is a general scalar quantity, the expression of the material time derivative of the specific internal energy can be obtained.

$$\rho \frac{du}{dt} = -\nabla \mathbf{J}_q + \boldsymbol{\sigma} : \nabla \mathbf{v} + \sum_k \mathbf{F}_k \mathbf{J}_k \quad (18)$$

The specific entropy production s can be expressed by the continuity equation:

$$\frac{\partial \rho s}{\partial t} = -\nabla \mathbf{J}_{s, tot} + \Phi \quad (19)$$

in which $\mathbf{J}_{s, tot}$ is the total entropy flux due to exchange of matter and heat flow. By the use of equation (17), the equation (19) results [6]:

$$\rho \frac{ds}{dt} = -\nabla \cdot (\mathbf{J}_{s, tot} - \rho s \mathbf{v}) + \Phi = -\nabla \mathbf{J}_s + \Phi \quad (20)$$

in which \mathbf{J}_s is the entropy flux that does not account for convection.

The second law of thermodynamics can be formulated by the Gibbs equation in its eulerian form:

$$Tds = du - vpdv^e - \sum_k v\mu_k dn_k \quad (21)$$

in which $v = \rho^{-1}$ is the specific volume and v^e is the elastic part of the isotropic strains. Substitution of equations (9) and (18) leads to:

$$\rho \frac{ds}{dt} = -\frac{1}{T} \nabla \mathbf{J}_q + \frac{1}{T} \hat{\boldsymbol{\sigma}} : d\boldsymbol{\varepsilon}^p - \frac{1}{T} \sum_k \mathbf{F}_k \mathbf{J}_k + \frac{1}{T} \sum_k \mu_k \nabla \mathbf{J}_k - \frac{1}{T} \sum_j A_j \mathbf{J}_j \quad (22)$$

in which the affinity A_j is defined as:

$$A_j = \sum_k \mu_k v_{kj} \quad (23)$$

and the effective stress in the second term of equation (22) is formulated as:

$$\hat{\boldsymbol{\sigma}}_{ij} = \left(p + \sum_{\alpha} g_{\alpha} \right) \delta_{ij} + \Pi_{ij} \quad (24)$$

in which p is the first invariant of the total stress tensor and $\boldsymbol{\Pi}$ is the deviator stress tensor.

$$\sum_{\alpha} g_{\alpha} = g_w + g_g = \sum_k \mu_k n_k \quad (25)$$

where the subscript α indicates the water w and the gas g and the rate is:

$$\sum_{\alpha} dg_{\alpha} = \sum_k n_k d\mu_k + \sum_k \mu_k dn_k = -\phi S_g dp_g - \phi S_w dp_w + \sum_k \mu_k dn_k \quad (26)$$

where the porosity ϕ and the degree of saturation S_{α} are introduced as:

$$\phi = \frac{V_v}{V} \quad S_w = \frac{V_w}{V_v} \quad S_g = \frac{V_g}{V_v} = 1 - S_w \quad (27)$$

A simplified version of the equation (26) has been proposed by Lewis and Schrefler [4] in which ϕS_{α} is replaced by S_{α} . In the sake of simplicity this version of the equation (26) will be adopted in the discussion of the numerical analyses. This is also the equation that is implemented in the commercial software Abaqus that has been used for the numerical simulations.

The following relations can be used to rearrange the equation (22):

$$\frac{\mu_k}{T} \nabla \mathbf{J}_k = \nabla \left(\frac{\mu_k \mathbf{J}_k}{T} \right) - \nabla \left(\frac{\mu_k}{T} \right) \mathbf{J}_k \quad (28)$$

$$\frac{1}{T} \nabla \mathbf{J}_q = \nabla \left(\frac{\mathbf{J}_q}{T} \right) - \nabla T \frac{\mathbf{J}_q}{T^2} \quad (29)$$

Then, the specific entropy production can be defined as:

$$\rho \frac{ds}{dt} = -\nabla \left(\frac{\mathbf{J}_q - \mu_k \mathbf{J}_k}{T} \right) + \frac{1}{T^2} \mathbf{J}_q \nabla T + \frac{1}{T} \hat{\boldsymbol{\sigma}} : d\boldsymbol{\varepsilon}^p - \frac{1}{T} \sum_k \mathbf{J}_k \left(T \nabla \left(\frac{\mu_k}{T} \right) - \mathbf{F}_k \right) - \frac{1}{T} \sum_j A_j J_j \quad (30)$$

Comparing the equation (30) and the equation (20) the two components of the entropy rate can be identified:

$$\mathbf{J}_s = -\nabla \left(\frac{\mathbf{J}_q - \mu_k \mathbf{J}_k}{T} \right) \quad (31)$$

$$\Phi = -\frac{1}{T^2} \mathbf{J}_q \nabla T + \frac{1}{T} \hat{\boldsymbol{\sigma}} : d\boldsymbol{\varepsilon}^p - \frac{1}{T} \sum_k \mathbf{J}_k \left(T \nabla \left(\frac{\mu_k}{T} \right) - \mathbf{F}_k \right) - \frac{1}{T} \sum_j A_j J_j \geq 0 \quad (32)$$

The internal production of entropy Φ in isothermal conditions is defined as:

$$\Phi = \hat{\boldsymbol{\sigma}} : d\boldsymbol{\varepsilon}^p - \sum_k (\nabla \mu_k - \mathbf{F}_k) \mathbf{J}_k - \sum_j A_j J_j \geq 0 \quad (33)$$

3 The Prigogine's Theorem

Prigogine [1] has proved that in diffusion problems for each applied arbitrary velocity field \mathbf{v}^a the entropy production in equation (33) remains unchanged. The theorem is valid when the acceleration of the center of mass of the mixture and the gradient of velocity field are negligible and the equation (10) holds. In the present paper we extend this result to the case of an arbitrary velocity field \mathbf{v}^a which gradient value is not negligible. This extension allows discussing the instability that occurs in landslides during water infiltration. The numerical model that is adopted computes the local equilibrium in equation (10) with a fully coupled strain-diffusion approach. The hypothesis of invariance of the entropy production with respect to any applied velocity drift corresponds to a thermodynamically based definition of the mechanical instability of porous materials with two-fluid phase flow.

Let consider an arbitrary velocity drift \mathbf{v}^a that is applied to each component of the mixture. The equation (6) can be rewritten [4]:

$$\mathbf{J}'_k = n_k (\mathbf{v}_k - \mathbf{v}) + n_k \mathbf{v}^a \quad (34)$$

The continuity equation results:

$$\frac{dn_k}{dt} = -\nabla \mathbf{J}'_k - n_k \nabla \cdot \mathbf{v} + \nabla (n_k \mathbf{v}^a) + \sum_j v_{jk} v_j \quad (35)$$

Substitution of equation (35) in equation (21) leads to:

$$\Phi = \hat{\mathbf{g}} : d\boldsymbol{\varepsilon}^p - \sum_k \mu_k \frac{\partial n'_k}{\partial t} + \sum_k (\nabla \mu_k - \mathbf{F}_k) \mathbf{J}'_k - \sum_j A_j \mathbf{J}_j \geq 0 \quad (36)$$

in which the second term is the latent heat produced inside the REV due to the drift velocity. It has the meaning of an enthalpy of phase change, as it is shown below.

The third term in equation (36) can be rewritten using the Gibbs-Duhem equation:

$$\nabla \sigma_{ij} = \sum_k n_k \nabla \mu_k \quad (37)$$

and:

$$\sum_k (\nabla \mu_k - \mathbf{F}_k) \mathbf{J}'_k = \sum_k (\nabla \mu_k - \mathbf{F}_k) \mathbf{J}_k + \sum_k (\nabla \sigma_{ij} - n_k \mathbf{F}_k) \mathbf{v}^a \quad (38)$$

Accounting for the mechanical equilibrium in equation (10) and negligible inertial force the second term in equation (38) vanishes and \mathbf{J}'_k can be replaced by \mathbf{J}_k in the entropy inequality. The second term in equation (36) vanishes if a phase transition inside the REV occurs. This condition is verified when:

$$\mu_g = \mu_w \quad \text{and} \quad \frac{\partial n_w}{\partial t} = -\frac{\partial n_g}{\partial t} \quad (39)$$

The mole fraction of the two components can be expressed with a single equation including the interface between the two phases (see [7]):

$$n_\alpha = n_w + I(n_g - n_w) \quad (40)$$

in which I is the Dirac delta function that has an integral equal to zero when the \mathbf{x} belongs to the water phase and it is equal to one when \mathbf{x} is in the gas phase. Then the equation (39) can be rewritten:

$$\frac{\partial n_w}{\partial t} = -\frac{\partial n_g}{\partial t} - (n_g - n_w) \frac{\partial I}{\partial t} \quad (41)$$

Using equations (27) and (41) the following kinematic constraint is obtained:

$$\frac{\partial(\phi S_w + \phi - \phi S_w)}{\partial t} = \frac{\partial \phi}{\partial t} = (n_w - n_g) \frac{\partial I}{\partial t} = (n_w - n_g) \int_{\Gamma} \mathbf{v}^* \cdot \mathbf{n} \, d\Gamma \quad (42)$$

in which \mathbf{v}^* is the velocity of the moving interface and n is the normal to the interface Γ . Note that interface's velocity is independent with respect to \mathbf{v}^a [8]. The equation (42) states that a collapse of the porous network equal to the phase transition of gas in water must occur to have an invariant expression of the entropy inequality during a so called (in Soils' Mechanics) "bifurcated" solution. Then the entropy preserves the mathematical structure of equation (33):

$$\Phi = \sum_{\alpha} F_{\alpha} J_{\alpha} \geq 0 \quad (43)$$

where F_{α} is the vector of the thermodynamic forces and J_{α} is the vector of the conjugated fluxes. Note that the collapse of the solid matrix does not require any additive term in the phenomenological coefficients that can be expressed as [9]:

$$J_k = \sum_{\alpha} L_{k\alpha} F_{\alpha} \quad (44)$$

in which $L_{k\alpha}$ are the phenomenological coefficients. Osanger [9] has shown that the reciprocal relations hold:

$$L_{k\alpha} = L_{\alpha k} \quad (45)$$

4 Numerical Analyses

The applied model for the numerical analyses is the extended modified Cam clay by Tamagnini R. [10]. The theoretical model is applied in the FE (Finite Element) analysis of the rainfall induced instability of an ideal unsaturated slope. The slope mesh is depicted in figure 1. The figure reports the mesh of the numerical model and the contours show the degree of saturation after half an hour of rainfall infiltration. The model is a typical cut of a motorway. Figure 2 reports the saturation degree distribution after 28 hours of rainfall infiltration from the slope surface. The change in the saturation degree triggers a landslide and the initiation of mass movement is identified by the displacement contours in figure 3. The landslide is triggered starting from the toe of the mesh where the water flows due the infiltration from the atmospheric boundary and due to percolation from the top of the slope. The sliding surface is not circular as generally supposed in limit equilibrium methods.

Figure 4 shows the volumetric behavior of two points: one is at the toe of the slope; one is in the center of the slope and at a depth of two meters. The figure shows as the kinematic constraint of equation (42) is fulfilled by the numerical algorithm. In these two points the condensation of water has produced a structural collapse of the porous network. This condition occurs at a constant value of the isotropic Bishop's stress in equation (24) in agreement with the equations constrains (26) and (39).

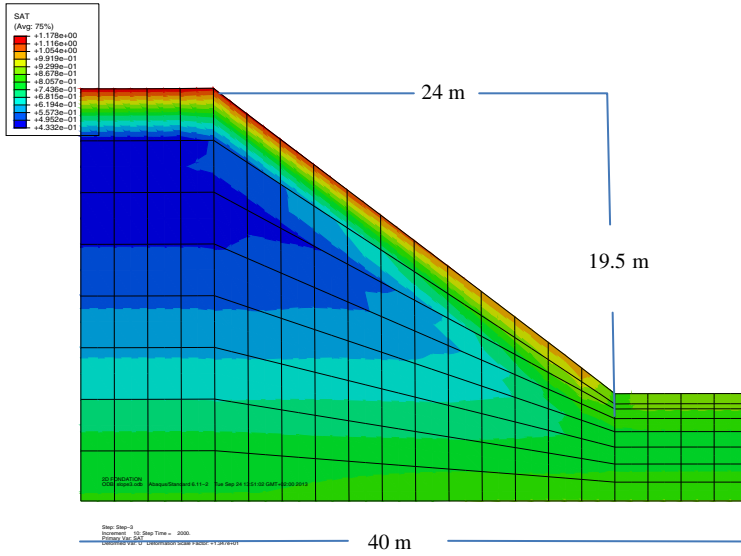


Fig. 1. Mesh and saturation degree distribution after 0.5 hour of rain infiltration

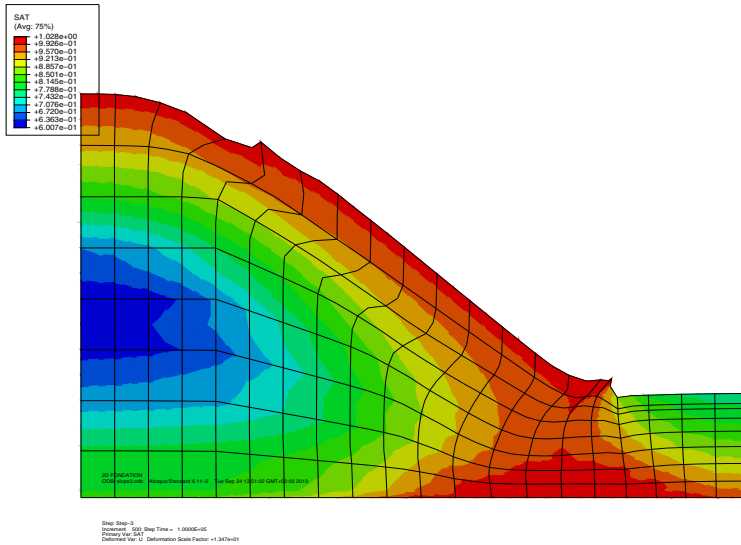


Fig. 2. Deformed mesh and saturation degree distribution after 28 hours of rainfall infiltration

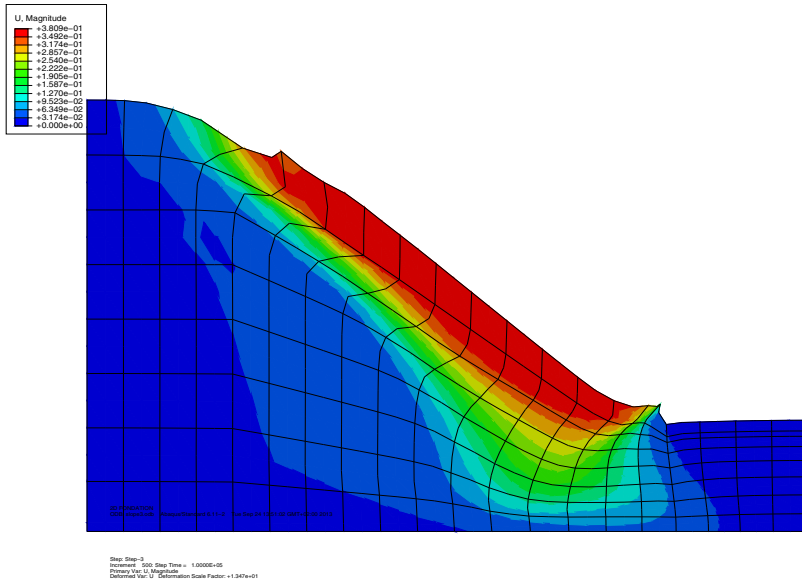


Fig. 3. Displacement contours after 28 hours of rainfall water infiltration into the mesh

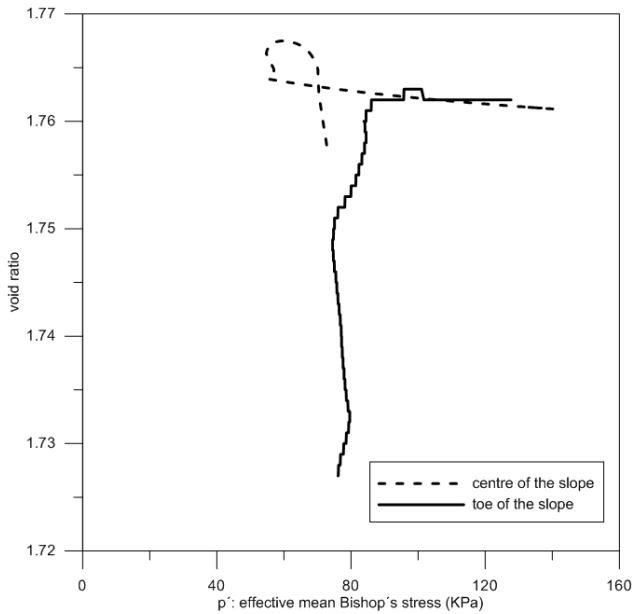


Fig. 4. Volumetric collapse of two points: one at the toe and one at the center of the slope profile

5 Conclusion

The paper has presented a thermodynamically based analysis of rainfall triggered landslides. The paper has provided a criterion based on thermodynamics for the definition of mechanical instability in partially saturated soils. The role of water condensation has been highlighted from a thermodynamic point of view. The theoretical framework has been applied in the simulation of an ideal landslide.

Acknowledgment. The paper is part of a larger research on the analyses of landslides and the role of vegetation and evapotranspiration, funded by the European Commission in the 7th Framework Program for Industry-Academia Partnerships and Pathways FP7-PEOPLE-2012-IAPP Grant no: 324466.

References

1. Prigogine, I.: Etude thermodynamique des phénomènes irréversibles. Thesis, published by Desoer, Liege (1947)
2. Hassanizadeh, S.M., Gray, W.G.: Mechanics and thermodynamics of multiphase flow in porous media including interphase boundaries. *Advances in Water Resource* 13, 169–186 (1990)
3. Coussy, O.: *Mechanics of Porous Continua*. Wiley & Sons Ltd., England (1995)
4. Lewis, R.W., Schrefler, B.A.: *The finite element method in the static and dynamic deformation and consolidation of porous media*. Wiley & Sons Ltd., England (1998)
5. Kondepudi, D., Prigogine, I.: *Modern Thermodynamics: From Heat Engines to Dissipative Structures*. Wiley and Sons Ltd., England (1998)
6. de Groot, S.R., Mazur, S.R.: *Non-equilibrium thermodynamics*. Dover Publications Inc., New York (1984)
7. Juric, D., Tryggvason, G.: Computation of boiling flow. *International Journal of Multiphase Flow* 24(3), 387–410 (1998)
8. Houlsby, G.T.: The Work Input to an Unsaturated Granular Material. *Géotechnique* 47(1), 193–196 (1997)
9. Onsager, L.: Reciprocal Relations in Irreversible Processes I. *Physical Review* 37, 405–426 (1931)
10. Tamagnini, R.: An extended Cam-clay model for un-saturated soils with hydraulic hysteresis. *Geotechnique* 54(3), 223–228 (2004)

Effect of Vegetation on Stability of Soil Slopes: Numerical Aspect

Wei Wu¹, Barbara Maria Switala¹, Madhu Sudan Acharya¹, Roberto Tamagnini¹,
Michael Auer², Frank Graf³, Lothar te Kamp⁴, and Wei Xiang⁵

¹ Institut für Geotechnik, Universität für Bodenkultur, Vienna, Austria

² J. Krismmer Handels GmbH, Rum, Austria

³ WSL Institute for Snow and Avalanche Research SLF, Davos Dorf, Switzerland

⁴ ITASCA Consultants GmbH, Gelsenkirchen, Germany

⁵ China University of Geosciences, Wuhan, China

Abstract. Soil bioengineering makes use of living plants to enhance soil stability against erosion and failure. Its practice is strongly dominated by empiricism. Recently much effort has been made towards quantifying soil bioengineering measures. This paper provides a critical review of the numerical modelling of some soil bioengineering measures. We discuss the application of the numerical methods including the finite element method and the limit equilibrium method for the composite of soil-plant root. A detailed review of the mechanical and hydrological models for the complex interaction between soil, plant, water and atmosphere is provided.

Keywords: soil bioengineering, slope stability, numerical methods, root reinforcement, root water uptake, limit equilibrium methods, finite element method.

1 Introduction

Soil bioengineering (SBE) is becoming increasingly popular in riverbank restoration and in the management of hill and upland slopes. In general, both living and dead plants can be used to stabilize soil against erosion and slope failure. There are numerous successful applications of SBE in different climatic zones worldwide. In spite of this success, however, SBE is still far from the sophistication of conventional engineering practice with the safety factors coded in standards and norms. This state of affairs is mainly due to the difficulties in quantifying the effect of vegetation in the slope stability. Moreover, there are some ambiguities in SBE applications concerning safety level, life time and load combinations. In this paper, some recent developments in the numerical modelling of vegetated slopes are reviewed.

We differentiate between natural slopes and engineered slopes. Typical engineered slopes are met in cuts and embankments. For natural slopes, the probability of slope failure or factor of safety requirements is often not a matter of concern unless there are specific demands from stakeholders. For engineered slopes, however, safety factors for different load combinations and life time are required. Not all SBE measures

can be and need be taken into consideration in the stability analysis. If SBE is used as complimentary to conventional engineering measures, the stability analysis is usually performed without considering the effects of SBE measures, which is on the safer side. However, if SBE is used alone, the stability analysis is to be performed according to the conventional engineering standards. In general, vegetation can be beneficial for slope stability in several ways.

- (a) The leaves of plants cushion the impact of raindrops, reduce the surface runoff and the susceptibility of surface erosion and soil degradation. The canopy of plants provides a protective cover against precipitations. The positive effect of vegetation in erosion control is well recognized but difficult to quantify. Since the safety is usually not relevant for erosion control, a quantitative analysis of the effect of vegetation is not necessary. However, plant canopy has significant influence on the amount of surface runoff and infiltration water, which have important bearing on the stability of slopes. Moreover, the infiltration water is used as boundary condition for some advanced analyses. Often the runoff and infiltration depend on the climatic conditions, vegetation cover and species and soil conditions.
- (b) Plants consume water from ground for their growth by transpiration. The water content in the vicinity of plant roots is often reduced, which gives rise to lower pore water pressure and higher suction force. Transpiration by plants may have large influence on the pore water pressure and water content in soil. A detailed study of the problem requires a coupled analysis of the hydrological and mechanical systems of soil and plant roots. Moreover, climatic boundary conditions and initial conditions of water content need to be specified. Transpiration is most active in dry weather with high temperature but negligible in wet weather with low temperature.
- (c) Plant roots penetrate through soil to acquire water and nutrients, which gives rise to a composite material of soil and fibrous plant roots. Stronger roots can grow across failure surfaces to provide strong anchoring points. Compared with (a) and (b), soil reinforcement by plant roots is highly relevant for the structural stability of slopes and can be reliably quantified. The degree of reinforcement depends mainly on the root architecture and root mass. As plants and their roots grow, the root reinforcement will change along with time. For SBE slopes, the slope stability immediately after the installation of plants is usually the most critical phase since the plants grow and become stronger.

The above mentioned positive effects of vegetation on slope stability are impaired by a number of negative effects. The wind throw of trees on slopes may aggravate the slope stability. Moreover, rotten roots of dead plants may form channels for water flow and eventually lead to piping failure. As a consequence, trees and bushes are not allowed on and near embankments. The so-called grass carpets on embankments provide effective protection against surface erosion and overflow. However, grass carpets of same species with the same root depth are often held responsible for shallow slides along the root tips, below which the permeability soil is usually lower than the root permeated soil above. Because of the limited depth of plant roots, SBE measures are

only relevant for erosion control and prevention of shallow slides. For deeply seated slides, conventional measures remain the only choice e.g. retaining walls, soil nails and dowels. As stated above, the most critical phase for SBE is the time immediately after plant installation. However, if the slope has sufficient safety reserve at this stage, an increase of the longterm safety is a nice-to-have but not a must-have. This is the main reason why SBE measures are seldom used in lieu of conventional measures in construction practice, where a minimum safety factors are required for short and longterm stability.

2 Numerical Methods

The stability analysis of SBE slopes is carried out based on the established methods in soil mechanics. There are mainly two methods available for the analysis of slope stability, i.e. limit equilibrium method (LEM) and finite element method (FEM) [5], [12]. Although the slope stability analysis is a classic topic in soil mechanics, there are still some phenomena that cannot be properly modelled by the numerical methods. Usually slope failure begins as spontaneous formation of shear band from the slope shoulder. The shear band with the thickness of few millimeters (about ten times of the mean grain diameter) propagates, forms a continuous failure surface and eventually leads to slope failure. During this process, the soil within the shear band experience very large shear deformation and volume change. In spite of intensive research in the last decades the localized deformation still cannot be properly modelled. The reason lies in the multi-scale nature of the problem, i.e. the small thickness of the shear band (few millimeters) and the large dimension of the slopes (tens of meters).

2.1 Limit Equilibrium Methods

The LEM assumes the equilibrium along a failure surface, where the soil strength is fully mobilized simultaneously, e.g. the slice method of Bishop. The LEM is easy to use and requires few material parameters (unit weight, friction angle and cohesion). Usually the minimum safety factor is obtained by comparing the safety factors of many possible failure surfaces.

The simplest case of LEM is an infinitely long slope. This failure surface is relevant for shallow slides, where the sliding plane is parallel to the slope surface [6]. Forces due to anchorage (soil nail), geogrid reinforcement, earthquake and seepage can be easily incorporated. The LEM can be easily adapted to consider the reinforcing effect of SBE. Plant roots can be considered individually as discrete elements or collectively as enhancement of the soil shear strength. Individual plant roots can be treated similar to anchor elements and geogrid reinforcement. In this case, the root orientation relative to the sliding surface need be considered. For plants with large number of fibrous roots, a smeared approach of increasing soil cohesion seems more appropriate. The advantage of LEM is its simplicity and the fact that a safety factor can be easily obtained. The major difficulty is the characterization of root architecture and root mass.

The LEM has also its shortcomings. Usually the soil along the sliding surface does not attain its full strength at the same time. This gives rise to the progressive failure of slopes, which cannot be accounted for by LEM. Moreover, the failure patterns of plant roots during pullout tests follow also the pattern of progressive failure. For soil and plant roots, the use of peak strength parameters usually leads to an overestimation of the safety factor. As a consequence, the failure process cannot be modelled by LEM, which considers limit equilibrium on a predefined failure surface. Neither is LEM able to model the coupling between mechanical and hydrological process such as rainfall infiltration process and transpiration by plants.

2.2 Finite Element Methods

Some shortcomings of LEM can be overcome with the methods of finite element or finite difference. These methods allow more sophisticated constitutive models and more realistic initial and boundary conditions. Unlike the LEM, where the soil is regarded as rigid body, the FEM together with sophisticated constitutive models is in the position to describe various soil properties such as nonlinearity, plasticity, anisotropy, viscosity and coupling between mechanical and hydrological processes. The soil above the ground water level can be modelled as partially saturated soil, where suction gives rise to additional strength in form of apparent cohesion. The water content of soil prior to a rainfall event is known to have large influence on the slope stability. This water content can be considered as the initial condition. Rainfall duration and intensity can be modelled as boundary conditions (Fig. 1). In a coupled analysis, the water infiltration into the soil is accompanied by the partial loss of soil strength through the reduction of suction. The propagation of the failure surface and the progressive failure can be modelled, whereas the failure surface is pre-defined in LEM. A further advantage of the FEM is its strength to model construction process. Excavation of soil and installation of structural elements, e.g. anchors, geogrids and plant roots, can be easily simulated through death and birth of elements.

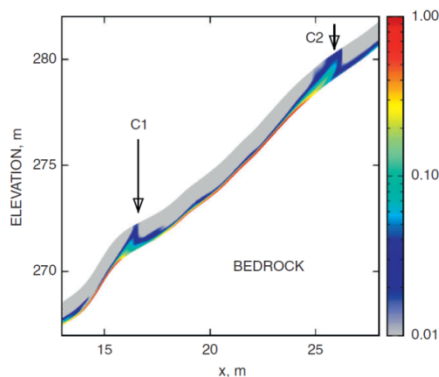


Fig. 1. Plastic strain (color bar) in a shallow slope simulated with a hydro-mechanical continuum model for rainfall rates of 6mm/h for 24h followed by 40mm/h for 1.7 h [1]

However, the sophisticated constitutive models usually require more parameters and their identification goes well beyond the conventional laboratory tests. In practice, however, the test data for the model calibration are often not available, not even for well-designed engineered slopes. The detailed data about initial water content and meteorological situation are also often not available. Moreover, it is very difficult to quantify the wide spatial and temporal variations of the soil parameters. In view of these factors, it remains questionable whether refined numerical methods will provide more reliable results.

The SBE slope parameters such as transpiration and root reinforcement can be easily incorporated into FEM. Fig. 2 shows the effect of plants on the water content of soil in the vadose zone [2]. It is usually assumed that the root density decreases with depth. The mechanical effect of roots can be considered either smeared as an enhancement of soil cohesion [10] or discrete as reinforcing elements [7]. However, the major difficulty is the reliable quantification of effects plant roots. The temporal and spatial distribution of plant roots depends on numerous factors such as species, age and location, which can be hardly described and taken into consideration in numerical calculations [8, 9].

Soil reinforced by plant roots can be regarded as a composite material. For a soil, which is homogeneously permeated by plant roots of the same diameter and strength, the composite properties can be obtained by homogenization of soil and roots similar to steel fiber reinforced concrete [11]. However, the root properties are more complex than fibers. The root density, root size and root strength change with location and depth. Moreover, unlike the random orientation of steel fibers, the roots usually show preferential directions (vertical or horizontal). In what follows, some development in characterizing the mechanical and hydrological properties of the soil-root system is briefly reviewed.

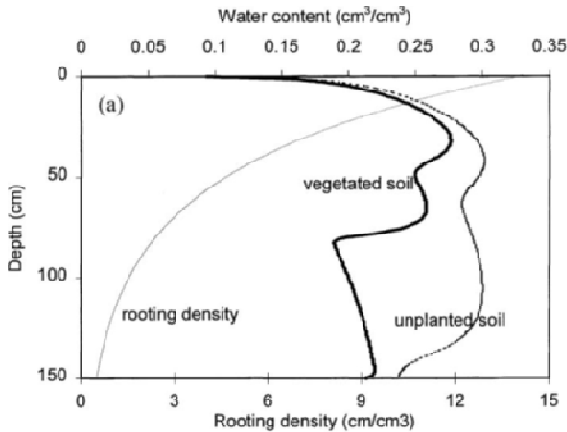


Fig. 2. Effect of plants on water content of soil [2]

3 Mechanical Features of Soil-Plant System

The first studies concerning the impact of vegetation on slope stability were conducted in the 1970s. Laboratory and in situ tests were conducted and analytical models were developed in order to quantitatively assess the mechanical contribution of plant roots to soil strength. The soil reinforcement by plant roots can be compared to reinforced concrete containing steel fibers. Both soil and concrete are strong in compression and weak in tension.

Numerous tests were conducted to study the behavior of the soil-root composite system. Most tests were carried out with direct shear devices [16], [18, 19]. Brenner [20] conducted tests on an inclined model of the vegetated slope, where both live and dead roots after clear-cutting were used. The pull-out behavior of plant roots was also the subject of numerous investigations [18], [21, 22]. The tensile strength of plant roots was shown to be dependent on the root diameter. A threshold diameter exists above which roots are more prone to breakage than pull-out. However, this threshold may change with the soil moisture. In moist soils the friction between root and soil is lower and the threshold diameter for the pull-out resistance increases.

Some pioneer works in the quantitative modelling of root reinforcement were carried out by Wu, Waldron and Wu et al. [16, 17, 18]. The Wu [16] model with some latter amendments is very simple and based on a number of approximations. The enhancement of strength by plant roots is considered as an additional cohesion, which is introduced into the Mohr-Coulomb failure criterion. The cohesion is dictated mainly by two factors, namely the average root tensile strength and root area ratio (RAR), which is the ratio of area occupied by roots on a certain plane. The model assumes that all roots are initially perpendicular to the slip surface and break at the same time.

The contribution of plant roots to the shear strength is dependent on the angle of shear distortion of the root and can be formulated as follows:

$$s_r = \sigma_r \tan \phi' + \tau_r = t_r (\cos \theta \tan \phi' + \sin \theta) \quad (1)$$

where σ_r and τ_r are normal and shear stress respectively, ϕ' is the friction angle of soil, θ is the angle of shear distortion of the root, t_r is the mean traction of plant roots, which is defined by the traction force T_r over the area A

$$t_r = \sum T_{ri}/A \quad (2)$$

Some test results show that the value of $(\cos \theta \tan \phi' + \sin \theta)$ can be taken as 1.2 for the distortion angle θ in the range $48^\circ - 72^\circ$. The contribution of plant roots to the shear strength of the soil can be then included into the Mohr-Coulomb failure criterion as follows:

$$s^* = s + s_r = c' + \sigma' \tan \phi' + s_r \quad (3)$$

where s and c' are the shear strength and cohesion of the bare soil respectively.

The above approach is widely used in simulating the strength of soil-root composite. Recently, some improvements are made towards better understanding of the process and more realistic description of the deformation mechanism of the soil-root

composite [21, 22, 23]. The authors introduced a fiber bundle model (FBM), where the main assumption of the previous model by Wu and Waldron, i.e. the breakage of all roots at the same time is removed. Roots in FBM are assumed to break progressively from the weakest to the strongest. The excessive load due to root breakage is redistributed into the remaining elements. The proposed model works by apportioning the total load applied to the bundle of N parallel fibers and then monitoring whether the load applied to the fiber exceeds its strength. Three different load apportioning methods were reported, i.e. apportioning by root cross section area, by root diameter and by root number. Two failure mechanisms, i.e. breakage and pull-out, can be considered [22].

The recent study by Schwarz et al. [24, 25] showed that the spatial distribution of roots should be taken into account, when considering the reinforcement of the soil with roots. The Root Bundle Model (RBM), proposed by Schwarz is based on the pull-out force – displacement relationship, coupled with the model for lateral root distribution. The RBM, similar to the FBM considers the progressive failure of the roots. The load is apportioned among all the roots by root diameter. RBM allows the estimation of the maximum value of soil reinforcement by plant roots, the root bundle elongation (displacement) as well as the secant Young's modulus.

Recently, a simplified version of the root bundle model was proposed [26] by considering the variability of the root strength. The Weibull survival function was used to describe the strength variation of the roots. This function is also known as complementary cumulative distribution function. All roots in the bundle are assumed to be linear-elastic fibers and break at the threshold displacements. This model is simpler than the previous RBM and can be easily implemented in numerical codes.

An important aspect of modelling the root reinforcement is the characterization of the root architecture. This is very challenging, when taking into account different plant species, growing conditions and available growing space. In numerical modelling, especially in the slope stability models, it is almost impossible to implement complex root architectures, which take into account all these features. Due to this limitation, only simplified root architecture can be used in numerical modelling.

Recently, a new approach to characterize the root growth and distribution was proposed by Dupuy et al. [27, 28], where a density function is introduced to describe the root structure (Fig. 3). This model allows the description of the relationship between the dynamics of meristem distribution and root architecture. Three density distributions are considered: the root length density ρ_n – which defines the geometrical properties of root architecture; the branching density ρ_b – which defines the plant topology; and the root apical meristem density ρ_a – which characterizes the regions of primary growth and links the dynamic of root length and root branching density. The model is based on two concepts. Firstly, root distribution at a given point in space is prescribed by representative volume (typically between 100 cm^3 and 200 cm^3). Secondly, the variations in time and space in the representative volume are assumed to be smooth. This approach has certain advantages over the traditional models. However, the computational time is rather long. Therefore it is mainly restricted to modelling single plant.

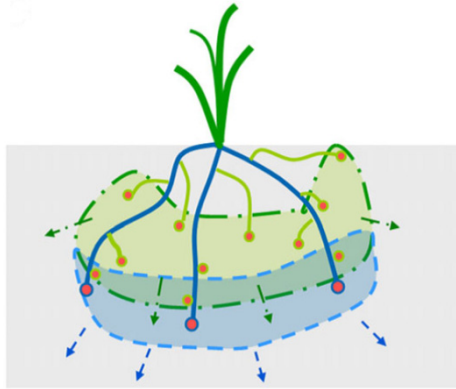


Fig. 3. The development of root systems as waves of meristems [27]

In all models mentioned above the soil-root composite is regarded as continuum. Recently, a discrete approach was presented by Bourrier et al. [29]. They investigated the influence of plant roots on slope stability using the discrete element method (DEM). The DEM code Yade [30] was used to model the direct shear tests on rooted and non-rooted soil samples. This modelling approach requires the development of new specific discrete elements – flexible cylinders which can be connected to model the complete root architecture (Fig. 4). The soil is modelled as an assembly of spheres. The root elements are considered as elastic, perfectly plastic beams, which are capable to sustain normal, shearing, twisting and bending forces. Plant roots are modelled as a set of chained cylinders and spheres. The deformation of the root is defined by the orientations and positions of the nodes, which are defined at the centers of spheres at the end of the cylinders. Three different types of interactions between the discrete elements can be defined: sphere-sphere, sphere-cylinder and cylinder-cylinder. All interactions are assumed to have the same contact formulation with different constitutive parameters.

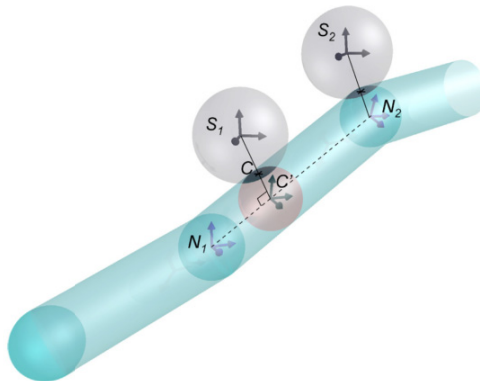


Fig. 4. The geometry of interactions between a sphere and chained cylinders [29]

The failure mechanisms of root reinforcement are tensile breakage, bending loading and pull-out. One of the important observations is that the soil-root reinforcement cannot be considered as constant additional shear resistance, because the mobilization of root strength is dependent on the shear strain.

4 Hydrological Features

Vegetation has great impact on the moisture content of soil and the suction, as well as the permeability and preferential flow paths of ground water. The suction contributes to the development of bonds between soil particles, which gives rise to an increased strength called “apparent cohesion”.

The evapotranspiration is the governing process of water uptake by plant roots and has been investigated by many researchers in agricultural engineering. In geotechnical engineering, however, evapotranspiration has received little attention. A numerical model which accounts for both mechanical and hydrological features of the soil-root system has to be developed. In fact, the increase of apparent cohesion due to water uptake by plant roots can be significant. However, the safety factor of slope is usually obtained without considering the apparent cohesion due to suction. A realistic model is needed, which consider not only mechanical, but also hydrological impact of the roots presence on the slope stability and enable the calculation of realistic FOS.

Evapotranspiration is the water vapor exchange between the vegetated soil surface and atmosphere. Its maximum value, when the soil moisture content is not restricted is called the potential evapotranspiration. In assessing the evapotranspiration, the current atmospheric conditions and the plant characteristics need be considered. This evapotranspiration is defined as the actual evapotranspiration. The estimation of its value is rather complex, and dependent on many factors. The Penman-Monteith equation first formulated by Penman [32] and further modified by Monteith [31] can be used to calculate evapotranspiration from the vegetated surface [33].

The root water uptake depends largely on the matric suction in the soil. The higher the matric suction, the more difficult it is for plant to extract water from soil. Therefore, the matric suction is a reducing factor for the rate of the root water uptake. It is experimentally proved, that for most plants the value of the suction above which a plant cannot extract water is about 15 bars. This threshold is defined as “the permanent wilting point”. The value, at which the water uptake reaches the maximum, is called “field capacity”. It can be defined as the amount of the soil moisture, which remains in the soil a few days after wetting and when free drainage has ceased. A matric potential corresponding to this soil moisture content has a value between 1/10 and 1/3 bar. Between these threshold values, the water is available for plant and becomes more restricted when approaching to the permanent wilting point.

Usually the development of the root water uptake (RWU) models, started from simple analytical models. The first model was based on the analogy to Ohm’s law for the sink term $S(z, t)$ [34]:

$$S(z, t) = [(\Phi_s - \Phi_L)/R_{sl}] S_{act}(z, t) \quad (4)$$

where $\Phi_s - \Phi_L$ is the difference between soil and leaf water potential, R_{sl} is the effective hydraulic resistance to water flow from soil to leaves, dependent on the depth below the soil surface and S_{act} is the specific surface of the active part of roots depth below the surface. The presented concept is rather theoretical, due to the fact that the determination of the hydraulic resistance is rather difficult. Nonetheless, the above simple model provides the basis for the further development of improved models.

Gardner [35] developed an approach which connects the RWU with Darcy's law. The water extraction function describes a steady flow of water into the root zone, which is defined as an infinitely long cylinder. Feddes et al. [36] proposed an equation to describe the root water uptake as a sink term.

The above equations are analytical models and contain many assumptions, which often cause the over- or underestimations of the amount of water uptake by plant roots. Some computer codes, e.g. CHASM, were also developed, which enable the calculation of the slope stability and take into account both mechanical and hydrological influence of the plant roots [37, 38]. In CHASM the forward explicit finite difference scheme is used in calculations. The slope is divided into rectangular columns subdivided into regular cells. The detention storage, water infiltration as well as evapotranspiration can be simulated. Richard's equation with the unsaturated conductivity based on the Millington-Quirk formulation is incorporated in order to model the unsaturated vertical water flow. Darcy's law governs the horizontal water flow between the columns. Unsaturated flow is assumed to take place only in the vertical direction.

In CHASM, slope stability is calculated using limit equilibrium method. The calculations are made at each major time step. Both positive and negative pore pressures are incorporated directly into the effective stress and the Mohr-Coulomb failure criterion. Vegetation can affect the slope hydrology through the evapotranspiration, root water uptake, interception and changes in the soil saturated conductivity. The root reinforcement is considered according to the simple model in [16, 17, 18]. The vegetation-slope interactions are shown in Fig. 5.

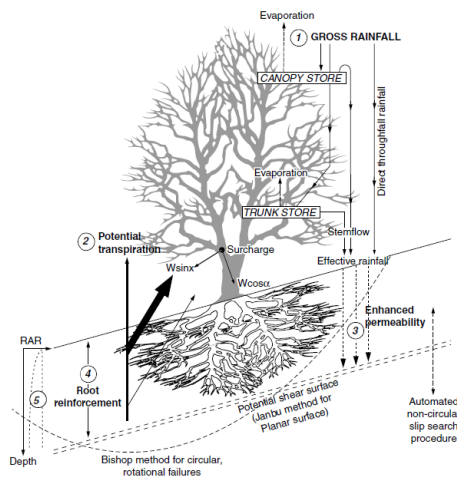


Fig. 5. Vegetation-slope interactions [37]

The extraction of water from the soil via root network and the loss of water from the leaf surface, result in reduced pore-water pressure in the slope, which leads to increase in the effective shear strength and thus enhanced stability of the slope. The maximum rate of water uptake is described using the formula proposed by [36], assuming a homogeneous root distribution:

$$S_{max} = T_v/z_r \quad (5)$$

where S_{max} is maximum uptake rate, T_v is the transpiration rate and z_r is the root depth. The model accounts also for the changes in the soil hydraulic conductivity caused by the root network distribution in the soil mass. The increase in this parameter can be described by relating the RAR to the saturated hydraulic conductivity as follows:

$$\Delta K_s = \alpha + \beta RAR \quad (6)$$

where ΔK_s is the increase in the soil hydraulic conductivity, α and β are material parameters.

The FOS of the slope can be calculated using either Bishop's method for circular slip surface or Janbu's method for non-circular slip surface [39]. Numerical models like CHASM are quite simple, but contain all salient features which should be taken into consideration for stability analysis of vegetated slopes.

Greenwood (2006) developed a simple numerical tool (SLIP4EX), which allows calculations of the stability of the vegetated slope. SLIP4EX is based on MS Excel spread sheet. Due to its simplicity, the program can be used for preliminary analysis of the problem and may serve as a tool for parameter study of the effect of plant on slope stability. The spread sheet computes the change in pore pressure and the increase of apparent cohesion. Moreover, the mass of vegetation, wind forces and mechanical root reinforcement can be considered. The FOS is calculated using different limit equilibrium methods, considering the influence of vegetation on the slice forces.

Fatahi [41] developed the root water uptake model and implemented the model in a finite element code. The RWU is regarded as a sink term in the Richard's equation, which takes the following form:

$$\partial\theta/\partial t = \nabla(k\nabla\psi) - (\partial k_z)/\partial z - S(x, y, z, t) \quad (7)$$

where θ is the soil moisture content, k_z is the vertical permeability and $S(x, y, z, t)$ is the sink term, i.e. the root water uptake. This equation can be applied for both homogenous and heterogeneous porous media.

The three important features which are considered in his model are the change in soil suction, the root distribution in soil and the potential transpiration from the vegetated surface. The rate of transpiration is assumed to be equal to the root water uptake and hence has the following form:

$$T(t) = \int_{v(t)} S(x, y, z, t) dV \quad (8)$$

where $T(t)$ is the transpiration rate at time t , $S(x, y, z, t)$ is the root water uptake at point (x, y, z) at time t and $v(t)$ is the volume of the root zone at time t . The developed RWU model was implemented and tested in the commercial FE code ABAQUS. The numerical results were compared with in-situ measurements. Moreover, Fatahi et al. [42, 43] analyzed the rate of water uptake by plant roots in comparison with the matric suction caused by the prefabricated, vertical, vacuum preloaded drains.

Wan et al. [44] developed a simple, two-dimensional model for the stability analysis of slopes and considered both mechanical and hydrological aspects of plants. The model includes the role of the main vegetation features influencing the stability of slopes, i.e. the root water uptake, the apparent cohesion, i.e. the additional soil shear strength and the increase in the soil hydraulic conductivity. They assumed a linear correlation between the saturated infiltration coefficient of root-permeated soil and the RAR. Moreover, rainfall boundary conditions are also introduced in the model. The mechanical root reinforcement was accounted for, using simple perpendicular model [16, 17, 18].

5 Conclusions

The soil-plant system presents a complex coupled problem, which poses great challenge for numerical modelling. It is not possible to simulate all problems precisely with numerical modelling, because some parameters cannot be put in numbers. A grass carpet is known to be effective against surface erosion. However, it is difficult to prove it through a mathematical model. When SBE measures are considered in slope stability, however, their effect needs to be quantified, e.g. to reach a required FOS. In doing so, some salient features of the soil-vegetation system should be taken into account and combined into a physically consistent model in order to model the complex interaction between soil, plant, water and atmosphere.

Acknowledgement. The authors wish to thank the European Commission for the financial support within its 7th Frame Work Program to the following projects: MUMOLADE (Multiscale Modelling of Landslides and Debris Flows), Contract Agreement No. 289911 within Marie Curie ITN; REVENUES (Reinforced Vegetation Numerical Evaluation of Slopes), Grant Agreement No.: 324466, within the Industry-Academia Partnerships and Pathways (IAPP); HYDRODRIL (Integrated Risk Assessment of Hydrologically-Driven Landslides), Grant Agreement Number: 295225, within the International Research Staff Exchange Scheme (IRSES).

References

1. Borja, R.I., White, J.A., Liu, X.Y., Wu, W.: Factor of safety in a partially saturated slope inferred from hydro-mechanical continuum modeling. *Int. J. Numer. Anal. Meth. Geomech.* 36, 236–248 (2012)

2. Sung, K.J., Yavuz, C.M., Drew, M.C.: Heat and mass transfer in the vadose zone with plant roots. *Journal of Contaminant Hydrology* 57, 99–127 (2002)
3. Bergkamp, G.: A hierarchical view of the interactions of runoff and infiltration with vegetation and microtopography in semiarid shrublands. *Catena* 33, 201–220 (1998)
4. Puigdefàbregas, J.: The role of vegetation patterns in structuring runoff and sediment fluxes in drylands. *Earth Surface Processes and Landforms* 30, 133–147 (2005)
5. Yu, H.S., Salgado, R., Sloan, S.W., Kim, J.M.: Limit analysis versus limit equilibrium for slope stability. *J Geotech. Geoenviron. Eng.* 124, 1–11 (1998)
6. Baum, R.L., Savage, W.Z., Godt, J.W.: TRIGRS—A Fortran program for transient rainfall infiltration and grid-based regional slope-stability analysis, version 2.0. U.S. Geological Survey Open-File Report, 2008-1159, 75 p. (2008)
7. Fan, C.C., Lai, Y.F.: Influence of the spatial layout of vegetation on the stability of slopes. *Plant Soil*, 1–13 (2014), doi:10.1007/s11104-012-1569-9
8. Docker, B.B., Hubble, T.C.T.: Modelling the distribution of enhanced soil shear strength beneath riparian trees of south-eastern Australia. *Ecological Engineering* 35, 921–934 (2009)
9. Rai, R., Shrivastva, B.K.: Effect of grass on soil reinforcement and shear strength. *Ground Improvement* 165, 127–130 (2012)
10. Mao, Z., Bourrier, F., Stokes, A., Fourcaud, T.: Three-dimensional modelling of slope stability in heterogeneous montane forest ecosystems. *Ecological Modelling* 273, 11–22 (2014)
11. Balaguru, N., Shah, S.P.: Fiber reinforced cement composites. McGraw-Hill, New York (1982)
12. Matthews, C., Farook, Z.: Slope stability analysis – limit equilibrium or the finite element method? *Ground Engineering*, 22–28 (May 2014)
13. Eubanks, C.E., Meadows, D., Cremer, J.S.: A Soil Bioengineering Guide for Streambank and Lakeshore Stabilization FS-683. ch. 5, *Soil Bioengineering Techniques*, U.S. Department of Agriculture Forest Service (2002)
14. The Federal Interagency Stream Restoration Working Group: *Stream Corridor Restoration Handbook*. USDA (1998)
15. *National Engineering Handbook, Technical Supplement 14M, Vegetated Rock Walls*, USDA (2007)
16. Waldron, L.J.: Shear resistance of root-permeated homogeneous and stratified soil. *Soil Science Society of America Journal* 41, 843–849 (1977)
17. Wu, T.H.: Investigation of landslides on Prince of Wales Island, Alaska. *Geotechnical Engineering Report 5*, Ohio State University, Department of Civil Engineering (1976)
18. Wu, T.H., McKinnell, W.P., Swanston, D.N.: Strength of tree roots and landslides on Prince of Wales Island, Alaska. *Canadian Geotechnical Journal* 114(12), 19–33 (1979)
19. Gray, D.H., Ohashi, H.: Mechanics of fiber reinforcement in sand. *Journal of Geotechnical Engineering* 109(3), 335–353 (1983)
20. Brenner, R.P.: A hydrological model study of a forested and cutover slope. *Hydrological Sciences* 18, 125–144 (1973)
21. Pollen, N., Simon, A.: Estimating mechanical effects of riparian vegetation on streambank stability using a fiber bundle model. *Water Resources Research* 41(W07025) (2005), doi:10.1029/2004WR003801
22. Pollen, N.: Temporal and spatial variability in root reinforcement of streambanks: Accounting for soil shear strength and moisture. *Catena* 69, 197–205 (2007), doi:10.1016/j.catena.2006.05.004

23. Pollen, N., Simon, A., Jaeger, K., Wohl, E.: Destabilization of streambank by removal of invasive species in Canyon de Chelly national monument, Arizona. *Geomorphology* 103, 363–374 (2009)
24. Schwarz, M., Lehmann, P., Or, D.: Quantifying lateral root reinforcement in steep slopes—from a bundle of roots to tree stands. *Earth Surface Processes and Landforms* 35, 354–367 (2010)
25. Schwarz, M., Cohen, D., Or, D.: Spatial characterization of root reinforcement at stand scale: Theory and case study. *Geomorphology* 171–172, 190–200 (2012)
26. Schwarz, M., Giadrossich, F., Cohen, D.: Modeling root reinforcement using a root-failure Weibull survival function. *Hydrology and Earth System Sciences* 17, 4367–4377 (2013), <http://www.hydrology-earth-syst-sci.net/17/4367/2013/>, doi:10.5194/hess-17-4367-2013
27. Dupuy, L., Gregory, P.J., Bengough, A.G.: Root growth models: towards a new generation of continuous approaches. *Journal of Experimental Botany* 61, 2131–2143 (2010), doi:10.1093/jxb/erp389
28. Dupuy, L., Vignes, M., McKenzie, B.M., White, P.J.: The dynamics of root meristem distribution in the soil. *Plant, Cell and Environment* 33, 358–369 (2010), doi:10.1111/j.1365-3040.2009.02081
29. Bourrier, F., Kneib, F., Chareyre, B., Fourcaud, T.: Discrete modeling of granular soils reinforcement by plant roots. *Ecological Engineering* (2013), <http://dx.doi.org/10.1016/j.ecoleng.2013.05.002>
30. Smilauer, V., Catalano, E., Chareyre, B., Dorofeenko, S., Duriez, J., Gladky, A., Kozicki, J., Modenese, C., Scholtes, L., Sibille, L., Stransky, J., Thoeni, K.: *Yade Documentation*, 1st edn. (2010), *The Yade Project*: <http://yade-dem.org/doc>
31. Monteith, J.L.: Evaporation and environment. *Symposia of the Society for Experimental Biology* 19, 205–234 (1965)
32. Penman, H.L.: Natural evaporation from open water, bare soil and grass. *Proceedings of the Royal Society of London A* 193, 120–145 (1948)
33. Allen, R.G., Pereira, L.S., Raes, D., Smith, M.: *Crop Evapotranspiration- Guidelines for computing crop water requirements - FAO Irrigation and drainage paper 56*. Number 6541. FAO, Rome 300 (1998)
34. Van den Honert, T.H.: Water transport as a catenary process. *Faraday Society Discussion* 3, 146–153 (1948)
35. Gardner, W.R.: Dynamic aspects of water availability to plants. *Soil Science* 89(2), 228–232 (1960)
36. Feddes, R.A., Bresler, E., Neuman, S.P.: Field tests of a modified numerical model for water uptake by plant roots systems. *Water Resources Research* 10, 1199–1206 (1974)
37. Wilkinson, P.L., Anderson, M.G., Lloyd, D.M.: An integrated hydrological model for rain-induced landslide prediction. *Earth Surface Processes and Landforms* 27, 1285–1297 (2002)
38. Wilkinson, P.L., Anderson, M.G., Lloyd, D.M., Renaud, J.-P.: Landslide hazard and bio-engineering: towards providing improved decision support through integrated numerical model development. *Environmental Modelling & Software* 17, 333–344 (2002)
39. Janbu, N.: Application of composite slip surface for stability analysis. In: *Proceedings of the European Conference on the Stability of Earth Slopes*, Stockholm, vol. 3, pp. 43–49 (1954)

40. Greenwood, J.R.: SLIP4EX - a program for routine slope stability analysis to include the effects of vegetation, reinforcement and hydrological changes. *Geotechnical and Geological Engineering* 24, 449–465 (2006)
41. Fatahi, B.: Modelling of influence of matric suction induced by native vegetation on sub-soil improvement. PhD thesis, University of Wollongong, Australia (2007)
42. Fatahi, B., Khabbaz, H., Indraratna, B.: Parametric studies on bioengineering effects of tree-root based suction on ground behaviour. *Ecological Engineering* 35, 1415–1426 (2009)
43. Fatahi, B., Khabbaz, H., Indraratna, B.: Bioengineering ground improvement considering root water uptake model. *Ecological Engineering* 36, 222–229 (2010)
44. Wan, Y., Xue, Q., Zhao, Y.: Mechanism study and numerical simulation on vegetation affecting the slope stability. *Electronic Journal of Geotechnical Engineers* 16, 741–751 (2011)

Landslide Susceptibility Analysis and Mapping Using Statistical Multivariate Techniques: Pahuatlán, Puebla, Mexico

Franny Giselle Murillo-García¹ and Irasema Alcántara-Ayala²

¹ Posgrado en Geografía, Universidad Nacional Autónoma de México, México, Mexico

² Departamento de Geografía Física, Instituto de Geografía,
Universidad Nacional Autónoma de México, Mexico, Mexico

Abstract. Susceptibility analyses are frequently based on the idea that landslides occur in the same areas where they have taken place previously, and also in areas under similar conditions. Based on that assumption, four different statistical techniques—Linear Discriminant Analysis (LDA), Quadratic Discriminant Analysis (QDA), Logistic Regression (LRA), and Neural Networks (NN)—have been applied for the municipality of Pahuatlán, Puebla, México. The base for the analysis was a geomorphological landslide inventory derived from the stereo-interpretation of Very High Resolution (VHR) satellite images.

The quality of each model was controlled by using ROC curves and Cohen's Kappa coefficient. Also, a temporal validation with a data set of landslides occurred on 2012 was carried out for each model. The resulting analysis showed that the aspect, the slope angle and the lithological unit were the variables with the highest weight associated with the occurrence of landslides in the study area.

Keywords: landslides, susceptibility, statistical multivariate techniques.

1 Introduction

Landslides affect human society on a variety of spatial and temporal scales [1]. Its occurrence depends on many factors and geo-environmental conditions. Landslide susceptibility refers to the landslide spatial dimension, as one of the elements comprised within landslide hazard assessments. Landslide susceptibility is very much interconnected to the question where landslides may occur? [2] Susceptibility to landsliding is also related to a set of geo-environmental conditions that influences hillslope stability [2, 3]. Susceptibility analyses are frequently based on the idea that the “past is the key to the future”; meaning that it is more likely that landslides occur in the same areas where they have taken place previously, and also in areas under similar conditions. Based on this, it is possible to predict where landslides can occur.

Landslide susceptibility is the probability of spatial occurrence of landslides [2], [4]. It can be estimated for large areas, even at national scale, or only for a single slope. However, the variety of spatial behaviour requires specifically adapted research

methods [1]. Since the seventies, the number of digital based methods has increased considerably and became more popular as the development of new computer technologies progressed [1]. Pioneering works on landslide susceptibility maps included [5] and [6, 7], but there is not yet a universal methodology [2].

Models for landslide susceptibility estimation can be classified into quantitative (numerical estimates) or qualitative (heuristically, descriptive and subjective estimates) [1, 2]. The heuristic approaches are based on a priori knowledge and depend on the skill and experience of the professional judgment. Approaches using quantitative methods are more objective and repeatable [1].

Five main categories of these methods have been identified by [1]: (1) direct geomorphological mapping; (2) analysis of landslides inventories; (3) heuristic or index based methods; (4) statistical methods and (5) process based conceptual models. Geomorphological mapping relies on the ability of the researcher to recognize the potential slope failures. Analysis of landslide inventories consists of landslide density maps. Process based models are deterministic or based on physically controlling slope instability principles [2].

The statistical methods use functional relationships between instability factors and the past distribution of landslides (landslide inventory) [2], [8]. Most of these methods are based on the relation between the landslide spatial distribution and a set of thematic layers. Such techniques are: (a) Classical statistic techniques include bivariate analysis, factor analysis, discriminant analysis [3], [9], [10], logistic and regression analysis [3], [11, 12, 13, 14, 15, 16, 17, 18, 19, 20, 21, 22]; (b) Modern statistical methods comprise generalized additive models (GAM), weight of evidence methods, weight factors, information value, and modified Bayesian estimation; (c) Fuzzy logic systems; (d) Neuronal networks [3], [11], [13, 14], [19], [21], [23, 24, 25, 26, 27, 28, 29, 30, 31] and support vector machines; and (e) Expert based systems. Many authors have compared and/or combined different statistical methods.

Landslide susceptibility estimations involve several requirements [32], among them, development of landslide inventories, integration of data and maps on a GIS platforms, and data treatment/analysis to establish quantitative ratings and obtaining susceptibility classes. Model or techniques selection depends on tree criteria [33]: (1) the mathematical and conceptual adequacy in describing the system behavior, (2) its robustness to small changes on the input data, and (3) its accuracy in predicting the observed data.

In this research a combination model of statistic techniques has been applied in terms of four different statistical techniques that are frequently used in landslide susceptibility analysis: Linear Discriminant Analysis (LDA), Quadratic Discriminant Analysis (QDA), Logistic Regression (LRA), and Neural Networks (NN). The study area (54 km²) was divided into slope units. In the combination model a probability value (0 to 1) is assigned to each slope unit. The base for the analysis was a geomorphological landslide inventory derived from the stereo-interpretation of Very High Resolution (VHR) satellite images, the review of historical data and field surveys. Temporal validations were applied and compared.

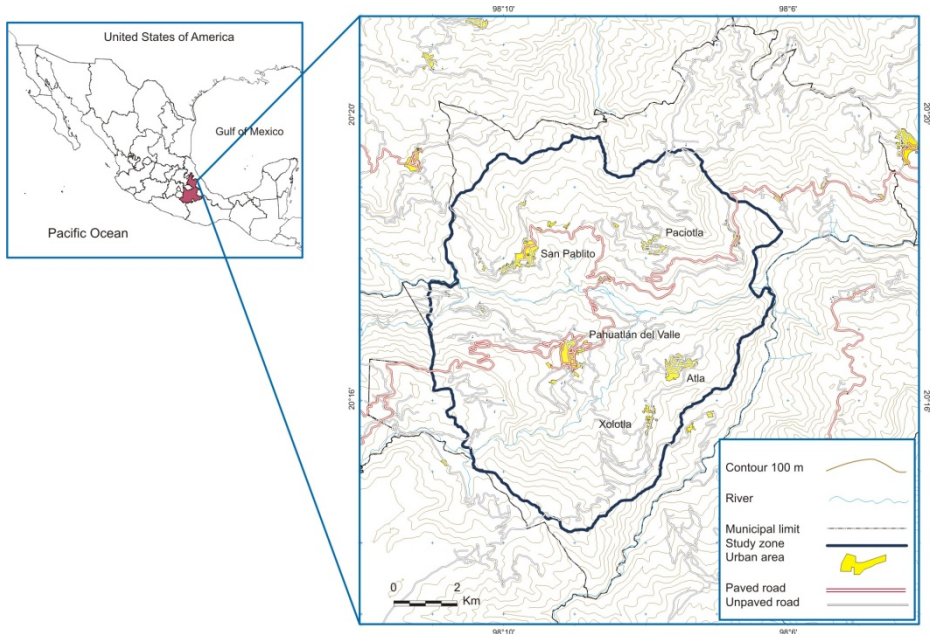


Fig. 1. Location of the studied area, Municipality of Pahuatlán, Puebla, Mexico

2 Study Area

The Pahuatlán municipality covers 89 km² and is situated in the mountainous region of Sierra Norte of Puebla at the Czones River basin. The study area was concentrated on the central portion of the municipality: 54 km² and includes the most populated towns of the region: Pahuatlán del Valle, Xolotla, Atla, San Pablito, Paciotla and Xochimilco towns (Figure 1). Lithological rock units are as follows: (i) Low Jurassic Huayacocotla sandstone and shale sequence; (ii) Cahuas siltstone-sandstone formation; (iii) Middle Jurassic Tepéxic limestone formation; (iv) Late Jurassic Tamán clayey limestone and shale sequence; (v) Late Jurassic Pimienta black limestone-shale sequence; (vi) Low Cretaceous Tamaulipas limestone-shale sequence; (vi) Pliocene basalt, andesite and pyroclastic deposits and recent; (vii) alluvial; and (viii) colluvium deposits [34, 35]. Slopes range from almost zero, along the plain of San Marcos River (alluvial quaternary deposits), to more than 70° at the top of the mountains (Middle Jurassic Tepéxic limestone formation). Most of natural vegetation is rainforest (mesophyll woods) [35], although there is also coniferous forest (pine and oak woods) in the upper mountains of Aila region. This area is highly deforested due to agricultural activity; most of the land use is agricultural land and cattle. Original vegetation can be found on very steep slopes and deep and stretch ravines. Climate is temperate and mean annual rainfall as high as 2500 mm/year. The orientation of Czones River and the strong variation on altitude are additional factors that contribute to the saturation of the soils most of the year in Pahuatlán [35].

Landslides in this area are mainly triggered by heavy rainfall. They have occurred particularly in wet years such as 1955, 1999, 2005 and 2007. These extraordinary rainfall events are usually related to hurricanes and tropical depressions from the Gulf of Mexico. Main types of landslides include flows, slides, rock falls and complex movements [36]. Velocity of the very big large landslides is rather slow; this has allowed evacuation of population. In 2007, a landslide (the 5 de mayo Street landslide) affected the central part of Pahuatlán; a small hospital and other houses were destroyed.

3 Materials and Methods

3.1 Materials: Data Source and Preparation

Any landslide hazard analysis requires an inventory as complete and accurate – in space and time – as possible [7], [37, 38, 39]. In the study area we have compiled a landslide inventory map (LIM) by both visual interpretation of a Very High Resolution (VHR) stereo-pairs satellite images and field surveys carried out in the period 2011-2012. The LIM comprises 385 landslides that occurred in the period 1994-2012 (Figure 2).

A 10 meters high resolution Digital Elevation Model (DEM) was generated on the LPS Automatic Terrain Extraction module from ERDAS IMAGINE© software using a stereo-pair of VHR satellite images GeoEye1 (0.5 m of spatial resolution on panchromatic band). The DEM was used to divide the study area into slope units (SU) and to generate the relief variables for the statistical models.

The SU were generated using a tool developed on GRASS GIS by [40]. The tool allowed i) to identify 259 slope units and ii) to compute average value of different morphometric parameters such as slope angle, slope aspect and slope profile. The most extend SU was 1.1 km² and the smallest 17,344 m².

Additionally, the compilation of variables associated with geo-environmental conditions –relief, lithology, faults and discontinuities, land use and vegetation, and old mass movements- related to landslide occurrence was done using different sources. The selection of geo-environmental conditions depends on the availability and data quality, and is based on the following assumptions: (1) Landslides take place very likely on areas where there is a landsliding history, (2) where the topography dictates that landsliding may occur, (3) where geological and geomorphological conditions are such that landslides are possible, (4) where man-made modifications on slopes enhance failure [32]. These environmental factors are expected to have an effect or influence on the occurrence of landslides and the assumption is that these same factors can be used on the prediction of future landslides [7].

Aspect, curvature, range and slope angle were the components derived from the relief considered as model variables. For the lithology and discontinuities the 1:50 000 scale geology maps (1814_F14D73 and 1814_F14D83) from the study area generated by the Servicio Geológico Mexicano ([34], [41]) were used. The borders of the lithological units were identified more in detail by using the VHR satellite images

stereo-pairs; it allowed the identification of a new fault. Major geological structures are the Huayacocotla anticline, a macrostructure with NNW-SSE axis, and San Pablo synclinal; structural discontinuities are the Paciotla normal fault and Xolotla inverse fault. A buffer of 150 m was generated around these lines on a GIS environment.

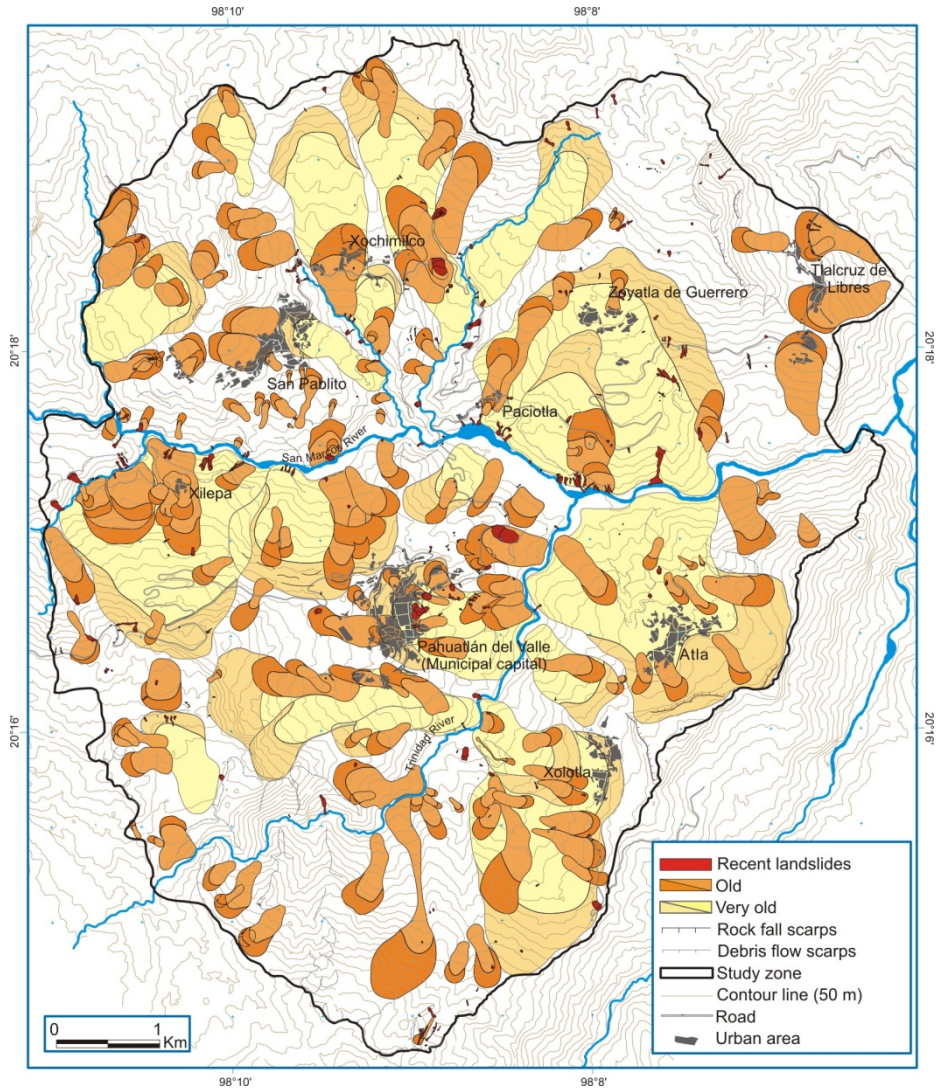


Fig. 2. Landslide inventory map of Pahuatlán. It includes 557 mass movements classified as recent landslides (1994-2012) (385), old failures (171) and very old movements (21).

Table 1. Variables used as explanatory variables on the statistical models

Variable	Source
<i>Weak lithology</i>	Geology maps at 1:50 000 scale
<i>Hard lithology</i>	Geology maps at 1:50 000 scale
<i>Aspect</i>	DEM
<i>Slope angle</i>	DEM
<i>Old and very old landslides area</i>	Geomorphological inventory
<i>Mean elevation</i>	DEM
<i>Falls and fractures</i>	Geology maps at 1:50,000 scale
<i>Standard deviation of slope angle</i>	DEM
<i>Slope curvature</i>	DEM
<i>Urban and roads land use</i>	VHR satellite images
<i>Agricultural land use</i>	VHR satellite images
<i>Areas without vegetation land use</i>	VHR satellite images
<i>Forest land use</i>	VHR satellite images

For land use and vegetation, a supervised classification process was done using the ERDAS 2011© software and the GeoEye1 images. Land use units were classified as: forest, grassland, agriculture, urban area, roads, water and no vegetated areas. Table 1 shows the variables used for the model data set. Lack of information on other geo-environmental conditions for the study zone did not allow its incorporation in the susceptibility models. Information of recent landslides from the inventory was used as response variable, whereas information of the Geo-environmental conditions was considered as explanatory variables.

3.2 Methods

Four statistical multivariate models were selected because of its very extensive used on landslide susceptibility. The models selected were: (1) Linear Discriminant Analysis (LDA), (2) Quadratic Discriminant Analysis (CDA), (3) Logistic Regression (LR), and (4) Neuronal Networks (NN). Percentage of landslide area in each SU was used to classify each as stable or unstable (grouping variable). Slope units with a landslide area larger than 1% were classified as unstable. The models work with a probability range, a degree of certainty value, where zero is a null probability that a landslide occurs, and 1 is the certainly of a landslide occurs. Each SU was assigned with a susceptibility value on each multivariate method. The susceptibility values obtained from the different models were combined by a logistic regression to obtain the combined landslide susceptibility zoning. All the calculations were done on the free statistical software R-Project [42]. Each model was run 200 times, except Neuronal Network which was run 20 times, each time varying the selected slope units.

Landslides are a complex phenomenon and as such, their natural variability results in uncertainties [43, 44]. Therefore, it is important to evaluate the quality of landslide

susceptibility maps. Very common very little or no attention is given to the evaluation of model results; thus, the analysis of the observed data and the presence/absence of landslide on the reality is quite significant [33]. Cross validation, represented by contingency tables based methods is frequently use for validation [44]. Receiver Operator Characteristics' curves (ROC) have been adopted for model evaluation on the landslide literature [3], [11], [13], [33], [45]. For this research, the ROC plot, the Heidke's skill score (Cohen's Kappa coefficient) and contingency tables are presented as confidence parameters of each model. Furthermore, for validating the results the temporal validation of a dataset field survey inventory developed at the end of 2012 was used.

Figure 3 shows the individual results for each model. It includes the frequency histogram with the values divided into five classes: (0-0.2) very low susceptibility; (0.2-0.45) low; (0.45-0.55) medium; (0.55-0.8) high; and (0.8-1) very high. Additionally, the maps portray the five susceptibility categories. Also included are the count of slope units in unequally spaced susceptibility classes, the four-fold plots summarizing the number of true positives true negatives, false positives and false negatives, the Cohen's Kappa Value, the model probability variability (bootstrap) graphic and the receiver operating characteristic curves.

The ROC curve describes the capability of the statistical model to discriminate among two classes of objects [33]. The area under the ROC curve is used as metric to assess the quality of the model [33], [46]. A larger area under the curve implies a better model performance. The points on the ROC curve represent the pairs derived from different contingency tables for different cut-offs. Closer points to the upper-right corner correspond to lower cut-off values. In short, a ROC curve is better than another if it is close to the upper left corner and the ROC value is closer to 1 [33]. On the Cohen's Kappa coefficient the technique measures the fraction of correct classifications after eliminating those classifications which would be correct purely due to random chance [33].

The plots that show the measures of the model error (ϕ) vs mean probability (μ) for each slope unit, provide the results of the application of the "bootstrapping" re-sampling technique obtained from the ensembles of model runs (200 times for LDA, QDA and LR, and 20 for NN) [3]. The points that are closer to the extreme x-axis and to the lower part of the graphic (low standard deviation) show a good performance of the model. Points on the center and with a high standard deviation mean that cases are classified as very high or very low susceptibility indistinctly when the models are running.

The results of the four models have differences. The maps of figure 3 show that an LR, LDA and QDA result are similar but differ from the NN results. NN is the method that shows low dichotomy results (histograms of figure 3). QDA is the model that demonstrates a better capability to divide the SU into two classes, but also shows the highest standard deviation on the bootstrapping graphic. The contingency tables illustrate that the LR and the LDA have an effectiveness of 60%. The AROC value for these models is acceptable (0.75). QDA shows an effectiveness of 73% with the highest AROC value: 0.804. The QDA presents the best performance. NN show low values.

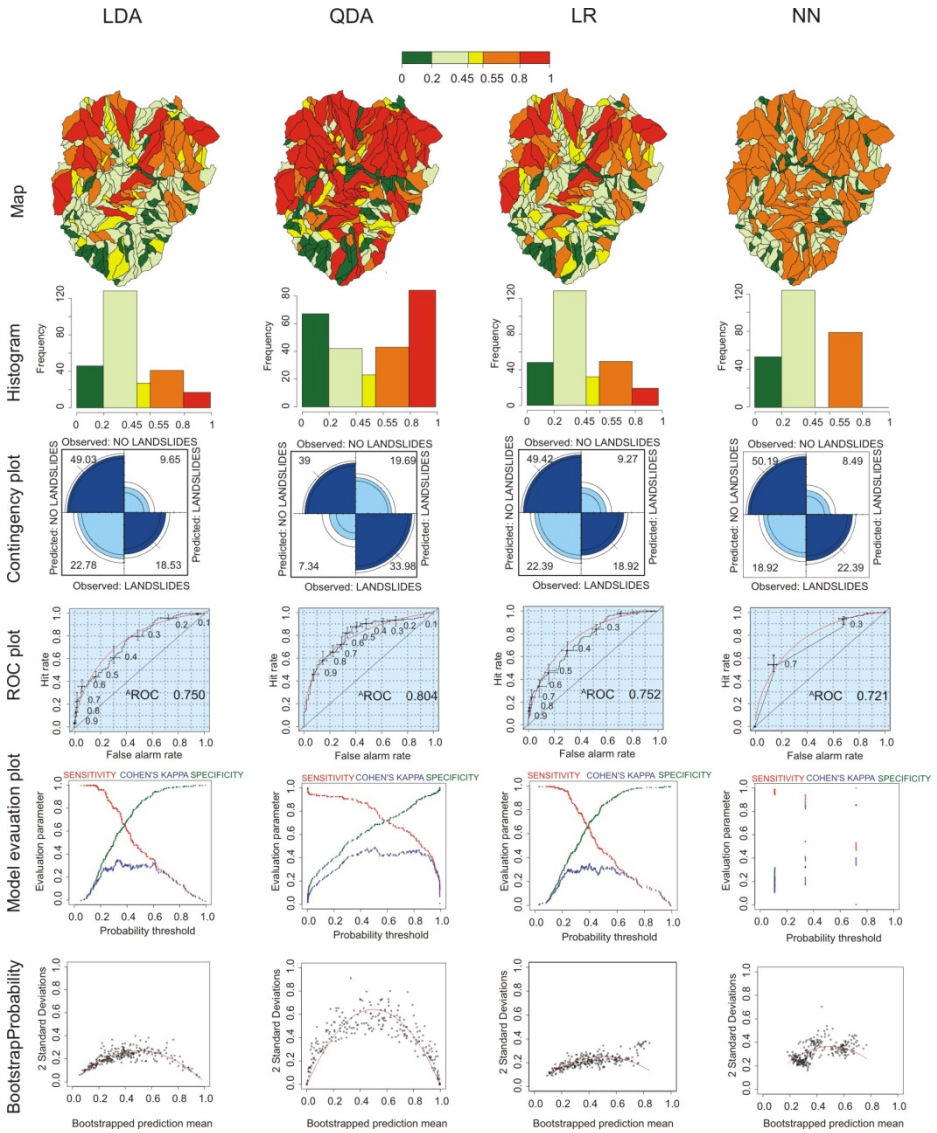


Fig. 3. Model results: 1) maps portraying the four susceptibility zones; 2) count of slope units in unequally spaced susceptibility classes; 3) four-fold plots summarizing the number of true positives true negatives, false positives and false negatives; 4) receiver operating characteristic (ROC) curves; 5) Cohen’s-Kappa coefficient graphic and 6) bootstrap prediction variability plot

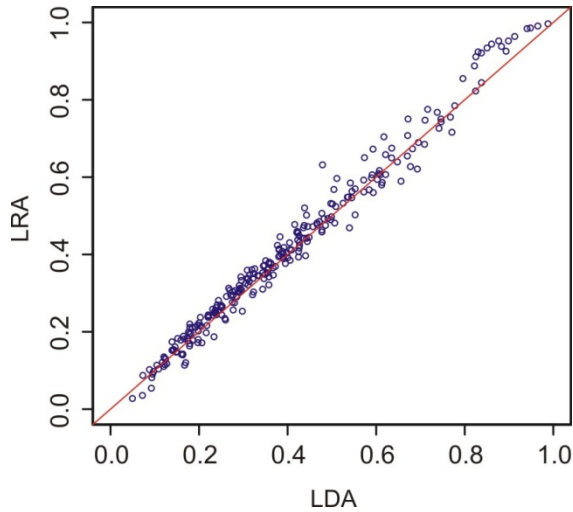


Fig. 4. Dispersion plot for the LDA and the LRA models that shows the linear correlation between the two models

Maps of figure 3 shows that LR and LDA present very similar results and the linear correlation of the two techniques is shown in the dispersion plot (Figure 4). A Pearson correlation value was computed for different couples of models and LRA and LDA show a strong collinearity (Table 2). For these reason, the combination model was run in three different ways: (i) with all the models, (ii) without the LR, and (iii) without LDA.

Table 2. Pearson correlation values among the four individual models

Combination	Pearson correlation (r value)
<i>LR-LDA</i>	0.990
<i>LR-QDA</i>	0.694
<i>LR-NN</i>	0.580
<i>LDA-QDA</i>	0.686
<i>LDA-NN</i>	0.578
<i>QDA-NN</i>	0.586

4 Results

For the LR Combination Model, the dependent variable was the presence or absence of recent landslides, while results of the individual models (LR, LDA, QDA and NN) were considered as “explanatory variables”. In order to choose the best model performance, the Akaike Information Criterion (AIC) was used in combination with the ROC plot area and the effectiveness for training and validation data set (Table 3).

The AIC measures the goodness-of-fit, and at the same time penalizes the model complexity to identify the simpler, but most parsimonious model [44], [47]. The model that includes the four models presents the best AIC value, however, the model lacking of LDA shows better performance on the validation ROC value. In order to eliminate the collinearity problem, the model without LDA was use. Results are shown in Figure 5.

Table 3. Evaluation of the three models run for the analysis

Model	AIC	Effectiveness	ROC	Validation data set effectiveness	ROC validation data set
<i>The four together</i>	260.45	74.51	0.821	67.57	0.706
<i>Without LR</i>	279.11	73.36	0.808	63.71	0.679
<i>Without LDA</i>	272.60	74.13	0.819	63.32	0.780

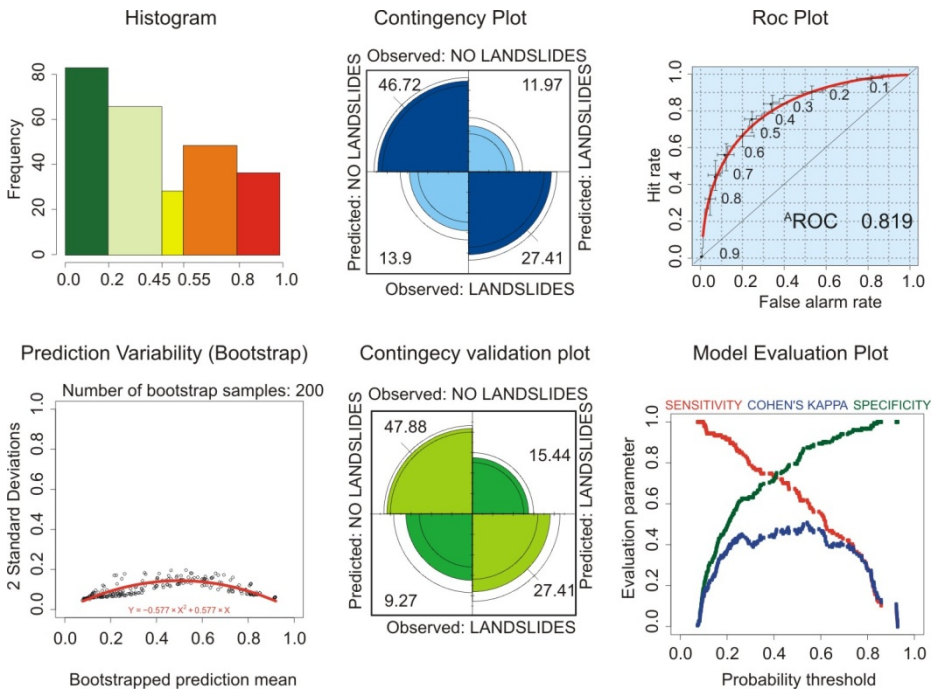


Fig. 5. Results of the Combination model obtained without taking into account LDA

The grouping separation for the final model is acceptable (histogram Figure 5) with few SU on the medium range value. The model has effectiveness of 74.13%. The ROC value is 0.819. On the validation data set a 75.2% of effectiveness was obtained. The ROC value is not the best (0.708). From the individual models the best performance was QDA, whereas the worst, NN. A possible explanation might be that the data base inventory does not include landslides before 1994. The research [3] reports a similar problem when running the NN model only with a recent landslides data set

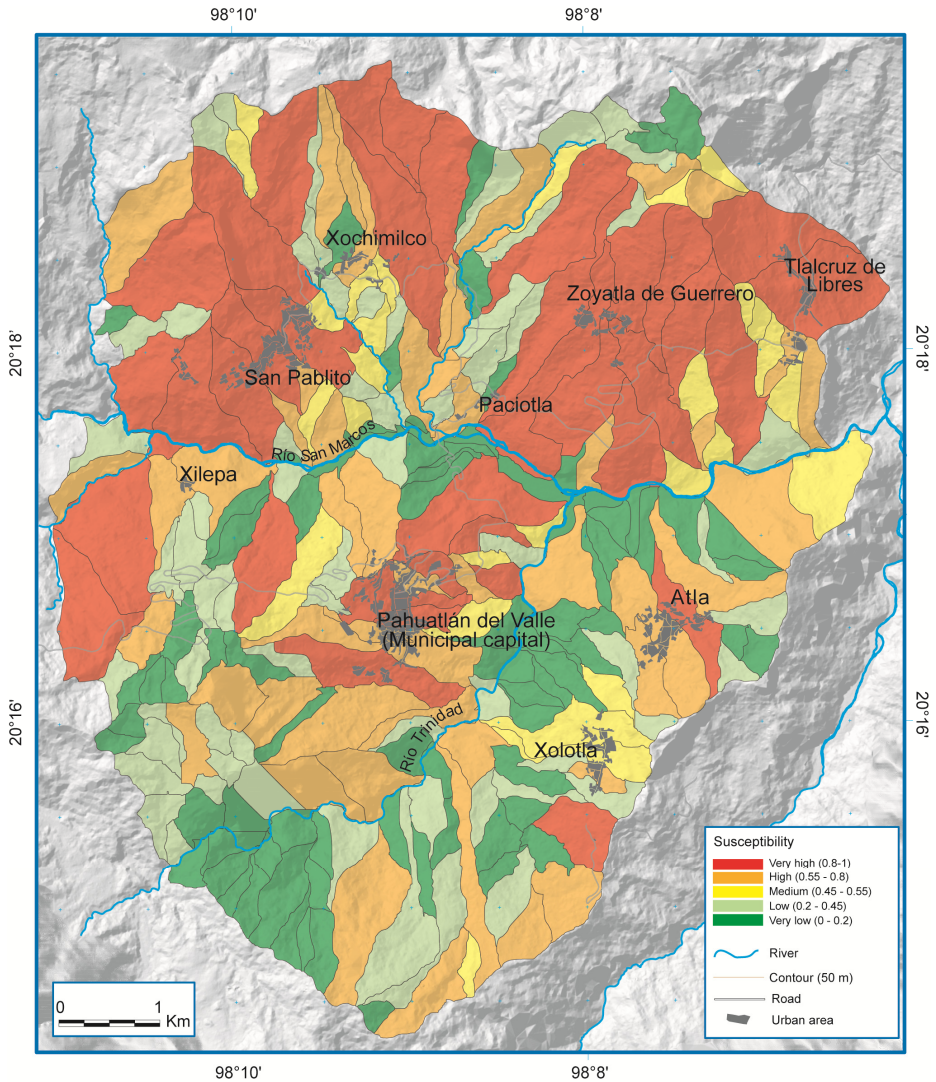


Fig. 6. Susceptibility map for the study area showing the distribution of the slope units where landslide susceptibility is higher. Many of these slope units coincide with the urban area of Pahuatlán.

(1997-2005). In that case, the NN model gives poor results in comparison to those resulting from a large temporal data set (1946-1996). The prediction skill for the others models (LR, QDA and LDA) does not seem to be affected by this issue. Unfortunately, the data set available for this work is not so large—in temporal scale—to be able to produce more comparisons.

The resulting variable analysis showed that the aspect, the slope angle and the lithological unit were the variables with the highest weight associated with the occurrence of landslides in the area of interest. Moreover, the presence of original and dense vegetation and the slope geometry were the variables related to the non-occurrence landslide.

By comparing these results with those obtained by [3] the performance of the application of these models for the present research is not optimal. A possible explanation can be related to the need of a more complete data set used. Also, it is important to consider that results could depend on factors, such as: (i) the geomorphological setting, (ii) the type, quality and abundance of landslide information, (iii) the selection of classification methods, (iv) the ability and the experience of the researcher, and (v) the different methods that implemented the R statistical software on its different versions. Nonetheless, quite clearly, the combination process derived on a reduced number of classification errors [3].

Figure 6 shows that towns like Pahuatlán del Valle, Atla, San Pablito, Zoyatla, Xochimilco and Tlalacruz de Libres are located on SU with high and very high susceptibility classes. This undoubtedly represents a major issue for land use decision-making in Pahuatlán in the near future.

5 Conclusions

Four multivariate analysis statistical techniques (Logistic Regression, Linear Discriminant Analysis, Neuronal Network and Quadratic Discriminant Analysis) were used to run a Logistic Regression Combination Model developed by [3]. The model was applied for a 54 km² study area in the municipality of Pahuatlán, central Mexico, by using the data derived from a geomorphological landslide inventory. Training data set includes the landslides occurred from 1994 to 2010. In order to carry out a temporal validation, a data set derived from a landslide inventory field survey developed in 2012 was used. The information of recent landslide events was used as dependent variable, along with a set of geo-environmental factors used as explanatory variables. The study zone was divided into 259 slope units.

The quality of each model was controlled by using traditional contingency tables, ROC curves and Cohen's Kappa coefficient. Also, a temporal validation with a data set of landslides occurred on 2012 was carried out for each model. Three different combination models were run using: (i) the four simple forecasts, (ii) three forecasts without LRA, and (iii) three forecasts without LDA. Individually, the QDA model was the best performance model, with a 0.804 of AROC value. A collinearity problem was detected on the results of the LDA and LR; a Person Correlation Test was run to measure the level of correlation of the models.

Three models were run: one include all the models, one without the LR model, and another one without LDA. The combination of the four models produced the best Akaike Information Criteria, but the model without LDA showed the best performance for the validation. The susceptibility zonation obtained by the combination Model without LDA classifies correctly 74% of the slope units (ROC 0.819). Some of the urban zones of the area, including the capital, Pahuatlán, are located on SU with high and very high degree of landslide susceptibility. The quality of the models can be considered as acceptable, but evidently the inventory data set is not as complete as desirable due to the lack of sufficient remote sensing tools and historical information. For these reason the temporal extent of the data set is rather short and the information regarding old and very old landslides was not of any use as exact date of occurrence was unknown. However, it is important to point out that the Combination Model allows the reduction of errors for landslide susceptibility estimation. The application of multiple forecasts could be useful to obtain a better approach to landslide susceptibility.

Acknowledgements. This work was developed with the collaboration of the CNR-IRPI, Perugia. We are grateful to Mauro Rossi, Fausto Guzzetti, Francesca Ardizzone, Paola Reichenbach and Ivan Marchesini. Mauro Rossi prepared a script of the Combination Model for the R free software environment for statistical computing. The script is available for download at the universal resource locator address: <http://geomorphology.irpi.cnr.it/tools/landslide-susceptibility-assessment/r-script-for-landslide-susceptibility-assessment-by-mauro-rossi>. Thanks are also due to CONACyT for providing support for the project 156242.

References

1. Glade, T., Crozier, M.J.: A review of scale dependency in landslide hazard and risk analysis. In: Glade, T., Anderson, M.G., Crozier, M.J. (eds.) *Landslide Hazard and Risk*, pp. 75–138. Wiley, Chichester (2005)
2. Guzzetti, F.: *Landslide Hazard and Risk Assessment*. Ph.D. Thesis, Mathematisch-Naturwissenschaftlichen Fakultät der Rheinischen Friedrich-Wilhelms-Universität, University of Bonn, Germany, 389 p. (2006), http://hss.ulb.uni-bonn.de/diss_online/math_nat_fak/2006/guzzetti_fausto/, <http://geomorphology.irpi.cnr.it/Members/fausto/PhD-dissertation>
3. Rossi, M., Guzzetti, F., Reichenbach, P., Mondini, A., Peruccacci, S.: Optimal landslide susceptibility zonation based on multiple forecasts. *Geomorphology* 114, 129–142 (2010)
4. Chung, C.-J.F., Fabbri, A.G.: Probabilistic prediction models for landslide hazard mapping. *Photogrammetric Engineering & Remote Sensing* 65(12), 1389–1399 (1999)
5. Brabb, E.E., Pampeyan, E.H., Bonilla, M.G.: *Landslide susceptibility in San Mateo County, California*. U.S. Geological Survey Miscellaneous Field Studies Map, MF-360, Scale 1, 62,500 (1978)
6. Carrara, A.: *Considerazioni sulla cartografia applicata alla stabilità dei versanti*. Seminario Sottoprogetto Fenomeni Franosi, Bari, 11 p. (March 1978) (in Italian)

7. van Westen, C.J., Castellanos, E., Kuriakose, S.: Spatial data for landslide susceptibility, hazard, and vulnerability assessment: An overview. *Engineering Geology* 102, 112–131 (2008)
8. Carrara, A.: A multivariate model for landslide hazard evaluation. *Mathematical Geology* 15, 403–426 (1983)
9. Guzzetti, F., Reichenbach, P., Ardizzone, F., Cardinali, M., Galli, M.: Estimating the quality of landslide susceptibility models. *Geomorphology* 81, 166–184 (2006)
10. He, S., Pan, P., Dai, L., Wang, H., Liu, J.: Application of kernel-based Fisher discriminant analysis to map landslide susceptibility in the Qinggan River delta, Three Gorges, China. *Geomorphology* 171–172, 30–41 (2012)
11. Yesilnacar, E., Topal, T.: Landslide susceptibility mapping: A comparison of logistic regression and neural networks methods in a medium scale study, Hendek region (Turkey). *Engineering Geology* 79, 251–266 (2005)
12. van Den Eeckhaut, M., Vanwallegem, T., Poesen, J., Govers, G., Verstraeten, G., Vandekerckhove, L.: Prediction of landslide susceptibility using rare events logistic regression: A case-study in the Flemish Ardennes (Belgium). *Geomorphology* 76, 392–410 (2006)
13. Nefeslioglu, H.A., Gokceoglu, C., Sonmez, H.: An assessment on the use of logistic regression and artificial neural networks with different sampling strategies for the preparation of landslide susceptibility maps. *Engineering Geology* 97, 171–191 (2008)
14. Yilmaz, I.: Landslide susceptibility mapping using frequency ratio, logistic regression, artificial neural networks and their comparison: A case study from Kat landslides (Tokat—Turkey). *Computers & Geosciences* 35, 1125–1138 (2009)
15. Bai, S.-B., Wang, J., Lü, G.-N., Zhou, P.-G., Hou, S.-S., Xu, S.-N.: GIS-based logistic regression for landslide susceptibility mapping of the Zhongxian segment in the Three Gorges area, China. *Geomorphology* 115(1–2), 23–31 (2010)
16. Das, I., Sahoo, S., van Westen, C., Stein, A., Hack, R.: Landslide susceptibility assessment using logistic regression and its comparison with a rock mass classification system, along a road section in the northern Himalayas (India). *Geomorphology* 114(4), 627–637 (2010)
17. Nandi, A., Shakoor, A.: A GIS-based landslide susceptibility evaluation using bivariate and multivariate statistical analyses. *Engineering Geology* 110(10), 11–20 (2010)
18. Yalcin, A., Reis, S., Aydinoglu, A.C., Yomralioglu, T.: A GIS-based comparative study of frequency ratio, analytical hierarchy process, bivariate statistics and logistics regression methods for landslide susceptibility mapping in Trabzon, NE Turkey. *CATENA* 85, 274–287 (2011)
19. Choi, J., Oh, H.-J., Lee, H.-J., Lee, C., Lee, S.: Combining landslide susceptibility maps obtained from frequency ratio, logistic regression, and artificial neural network models using ASTER images and GIS. *Engineering Geology* 4, 12–23 (2012)
20. Schicker, R., Moon, V.: Comparison of bivariate and multivariate statistical approaches in landslide susceptibility mapping at a regional scale. *Geomorphology* 161–162, 40–57 (2012)
21. Xu, C., Xu, X., Dai, F., Saraf, A.: Comparison of different models for susceptibility mapping of earthquake triggered landslides related with the 2008 Wenchuan earthquake in China. *Computers & Geosciences* 46, 317–329 (2012)
22. Wang, L.-J., Sawada, K., Moriguchi, S.: Landslide susceptibility analysis with logistic regression model based on FCM sampling strategy. *Computers & Geosciences* 57, 81–92 (2013)

23. Kanungo, D.P., Arora, M.K., Sarkar, S., Gupta, R.P.: A comparative study of conventional, ANN black box, fuzzy and combined neural and fuzzy weighting procedures for landslide susceptibility zonation in Darjeeling Himalayas. *Engineering Geology* 85, 347–366 (2006)
24. Melchiorre, C., Matteucci, M., Azzoni, A., Zanchi, A.: Artificial neural networks and cluster analysis in landslide susceptibility zonation. *Geomorphology* 94, 379–400 (2008)
25. Melchiorre, C., Castellanos-Abella, E.A., van Westen, C.J., Matteucci, M.: Evaluation of prediction capability, robustness, and sensitivity in non-linear landslide susceptibility models, Guantánamo, Cuba. *Computers & Geosciences* 37, 410–425 (2011)
26. Kawabata, D., Bandibas, J.: Landslide susceptibility mapping using geological data, a DEM from ASTER images and an Artificial Neural Network (ANN). *Geomorphology* 113, 97–109 (2009)
27. Pradhan, B., Lee, S.: Landslide susceptibility assessment and factor effect analysis: backpropagation artificial neural networks and their comparison with frequency ratio and bivariate logistic regression modelling. *Environmental Modelling & Software* 25, 747–759 (2010)
28. Vahidnia, M., Alesheikh, A., Alimohammadi, A., Hosseinali, F.: A GIS-based neuro-fuzzy procedure for integrating knowledge and data in landslide susceptibility mapping. *Computers & Geosciences* 36, 1101–1114 (2010)
29. Oh, H.-J., Pradhan, B.: Application of a neuro-fuzzy model to landslide-susceptibility mapping for shallow landslides in a tropical hilly area. *Computers & Geosciences* 37, 1264–1276 (2011)
30. Tien Bui, D., Pradhan, B., Lofman, O., Revhaug, I., Dick, O.: Landslide susceptibility assessment in the Hoa Binh province of Vietnam: A comparison of the Levenberg–Marquardt and Bayesian regularized neural networks. *Geomorphology* 171–172, 12–29 (2012)
31. Pradhan, B.: A comparative study on the predictive ability of the decision tree, support vector machine and neuro-fuzzy models in landslide susceptibility mapping using GIS. *Computers & Geosciences* 51, 350–365 (2013)
32. Fell, R., Corominas, J., Bonnard, C., Cascini, L., Leroi, E., Savage, W.: Guidelines for landslide susceptibility, hazard and risk zoning for land use planning. *Engineering Geology* 102, 85–98 (2008)
33. Frattini, P., Crosta, G., Carrara, A.: Techniques for evaluating the performance of landslide susceptibility models. *Engineering Geology* 111, 62–72 (2010)
34. Sánchez-Rojas, L.E., De la Callejera-Moctezuma, A.E.: Carta Geológico-Minera Pahuatlán F14-D73. Servicio Geológico Mexicano, Escala 1, 50 000 (2004) (in Spanish)
35. Oliva Aguilar, V.R., Garza Merodio, G.G., Alcántara Ayala, I.: Configuration and temporal dimension of vulnerability: spaces and disasters in the Sierra Norte de Puebla. *Investigaciones Geográficas, boletín del Instituto de Geografía. UNAM* 75, 61–74 (2011)
36. Alcántara Ayala, I.: Hazard assessment of rain-fall induced landsliding in Mexico. *Geomorphology* 61, 19–40 (2004)
37. Ibsen, M.-L., Brunsden, D.: The nature, use and problems of historical archives for the temporal occurrence of landslides, with specific reference to the south coast of Britain, Ventnor, Isle of Wight. *Geomorphology* 15, 241–258 (1996)
38. Lang, A., Moya, J., Corominas, J., Schrott, L., Dikau, R.: Classic and new dating methods for assessing the temporal occurrence of mass movements. *Geomorphology* 30(1-2), 33–52 (1999)

39. Glade, T.: Landslide hazard assessment and historical landslide data - an inseparable couple? In: Glade, T., Frances, F., Albini, P. (eds.) *The Use of Historical Data in Natural Hazard Assessments. Advances in Natural and Technological Hazards Research*, vol. 17, pp. 153–168. Springer, Berlin (2001)
40. Marchesini, I., Rossi, M., Alvioli, M., Santangelo, M., Cardinali, M., Reichenbach, P., Ardizzone, F., Fiorucci, F., Balducci, V., Mondini, A., Guzzetti, F.: WPS tools to support geological and geomorphological mapping. In: *HEIG-VD: Open Conference Systems, OGRS 2012* (2012)
41. Loaeza García, J.P., Zárate Barradas, R.G.: *Carta Geológico-Minera Huauchinango F14-D83*. Servicio Geológico Mexicano, Escala 1, 50 000 (2005)
42. R Core Team: *R: A Language and Environment for Statistical Computing*. R Foundation for Statistical Computing, Vienna (2013), <http://www.R-project.org>
43. Ardizzone, F., Cardinali, M., Carrara, A., Guzzetti, F., Reichenbach, P.: Uncertainty and errors in landslide mapping and landslide hazard assessment. *Natural Hazards and Earth System Sciences* 2(1-2), 3–14 (2002)
44. Petschko, H., Bell, R., Glade, T., Brenning, A.: Landslide susceptibility modeling with generalized additive models – facing the heterogeneity of large regions. In: Eberhardt, E., Froese, C., Turner, A.K., Leroueil, S. (eds.) *Landslides and Engineered Slopes: Protecting Society through Improved Understanding*, pp. 769–775. Taylor & Francis, Banff (2012)
45. Gorsevski, P., Gessler, P., Boll, J., Elliot, W., Foltz, R.: Spatially and temporally distributed modeling of landslide susceptibility. *Geomorphology* 80, 178–198 (2006)
46. Hanley, J.A., McNeil, B.J.: The meaning and use of the area under a receiver operating characteristic (ROC) curve. *Radiology* 143(1), 29–36 (1982)
47. Akaike, H.: A new look at the statistical model identification. *IEEE Transactions on Automatic Control* 19(6), 716–723 (1974)

Application of the Program PCSiWaPro[®] for the Stability Analysis in Earth Dams and Dikes Considering the Influence from Vegetation and Precipitation— A Case Study in China

Jinxing Guo¹, Issa Hasan², and Peter-Wolfgang Graeber¹

¹ Institute of Waste Management and Contaminated Site Treatment,
Technische Universität Dresden, Pirna, Germany
{jinxing.guo, peter-wolfgang.graeber}@tu-dresden.de

² Institute of Earth and Environmental Sciences,
Universität Potsdam, Potsdam, Germany
hasan@uni-potsdam.de

Abstract. Earth dams and dikes are always a safety issue, as it can experience catastrophic destruction due to the slope failure caused by various factors, such as construction materials, vegetation, atmospheric conditions and so on. The preliminary tests on a physical model have shown that the security and stability has been already severely compromised in the partially saturated region, i.e. the area above the seepage line is in great danger and it comes quickly to landslides on the air side. Before the stability analysis can be done for those unsaturated zones, the water content and geohydraulic processes in the saturated and partially saturated soil area were simulated using the simulation program PCSiWaPro[®]. The simulation results of several scenarios both in the laboratory and in the field in China clearly demonstrated the impact of building materials and construction on the behavior of water saturation and thus the stability of the dam. The accordance between measured and calculated values for water content using the program PCSiWaPro[®] was very good.

Keywords: earth dam, dike, water balance, stability, seepage line, precipitation, vegetation.

1 Introduction

River regions were always the first cradles of human history. Water plays a crucial role for domestic use and agriculture. Therefore, many cities are close to or even built directly on the banks of a river. However at the same time we are always warned to think about the risk of flooding there. An earth dam and a dike is one kind of hydraulic construction structure built with highly compacted earth and used for the purpose of flood control [1]. Worldwide there are millions kilometers of dams and dikes, while only in the state of Lower Saxony in Germany there are around 645 km of dikes [2]. However, severe flood events occur every year due to the dam collapse, for example, the flood caused by the Elbe River in 2002 [3] and in Fischbeck in July 2013 [4].

Surface erosion (surface overflow) and increase of water saturation in the dam body are the main causes of dam instability risk [5]. There was an early assumption that the landslides and suffusion phenomenon can arise only in the fully saturated soil areas on the air side; however AIGNER [6] showed by physical experiments that this can occur even in the partially saturated soil area of the dam. The surface erosion is relatively easy to be detected and avoided, while the soil moisture increase risk cannot be easily identified. Therefore, these hydraulic structures are more sensitive and dangerous due to the rise and the flow from the ground water in the unsaturated zones [5].

In those unsaturated areas, various factors could influence the water balance and then the stability, for example, construction methods, soil materials, geometry, atmospheric conditions (e.g. precipitation), and even vegetation [7, 8] (see Figure 1). The precipitation has direct influence on the water content change with the infiltration water into the unsaturated slope and then changes seepage line movement regime (especially in an extreme rainfall event). The significant influence of vegetation on slope stability can essentially be attributed to two major aspects: water movement via the soil–plant–atmosphere continuum (SPAC) [9] and soil reinforcement by the root system [10]. Vegetation is a major component of SPAC, responsible for the suction force of water against gravity. By absorbing parts of the soil water, plants thus play a significant role in the drying of slopes [11]. This absorbed soil water will subsequently be removed through the transpiration process into the atmosphere [9]. Ultimately, this water cycle system would result in less saturated and more stable slopes. Concurrently, vegetation also contributes to mass stability by increasing the soil shear strength through root reinforcement [10]. The frequency of slope failures tends to increase when vegetation is cut down and their roots decay [12].

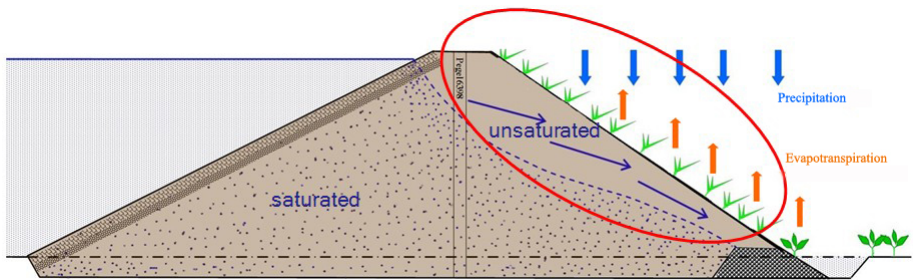


Fig. 1. Water balance in the saturated and partially saturated region [13]

Since now many laboratory experiments have been carried out for the stability analysis in dams and dikes. A physical model from AIGNER [6] clearly shows the hydrological process with the increase of the water level at the left side and the landslides happening in the right slope above the seepage line, i.e. in the partially saturated region (see Figure 2).

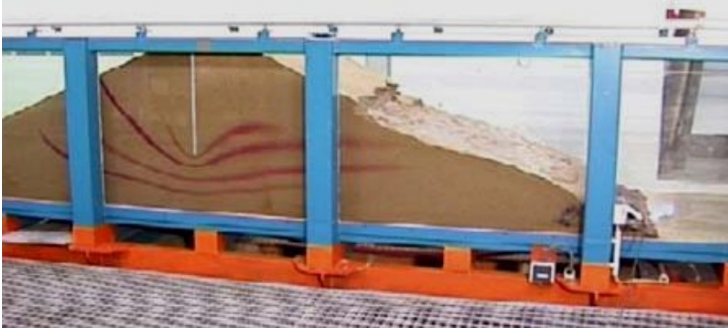


Fig. 2. A physical model dam with slides on the air side [6]

2 Description of Program PCSiWaPro®

The software PCSiWaPro® (developed at the Technical University Dresden, Institute of Waste Management and Contaminated Site Treatment) simulates the distribution of water saturation under transient boundary conditions [14]. It is based on solving the RICHARDS equation in two spatial dimensions using the finite element method. The integration of a weather generator into PCSiWaPro® allows a transient flow calculation with respect to atmospheric conditions (precipitation, evaporation, daily mean temperature and sunshine duration) and removal of water by plant roots [13]. The weather generator's synthetic time series are statistically derived from publicly available weather stations data of the German Weather Service (DWD) [13]. To determine the effects of the above-mentioned factors on the through-flow and the geomechanical instabilities in the partially saturated region of the earth dam, the seepage line as the border between the fully saturated and partially saturated zone in the dam body (Figure 1) was used for validating the simulation results [13]. With PCSiWaPro® a 2D model of the dam could be built, incorporating information of geometry, soil properties, climate parameters and geohydraulic and time-dependent boundary conditions. The water saturation in the dam body and the flow from the air side of the dam are calculated by PCSiWaPro®. For this, an observation point in the model is used in order to compare the measured values of the seepage line depth with the simulated values.

2.1 Theoretical Background of PCSiWaPro®

PCSiWaPro® simulates water flow and contaminant transport processes in variably saturated soils, under both stationary as well as transient boundary conditions. The flow model can be described by the RICHARDS equation (equation 1).

$$\frac{\partial \theta}{\partial t} = \frac{\partial}{\partial x_i} \left[K \left(K_{ij}^A \frac{\partial h}{\partial x_j} + K_{iz}^A \right) \right] - S \quad (1)$$

The equation contains the volumetric water content θ , pressure head h , spatial coordinates x_i ($x_1 = x$ and $x_2 = z$ for vertically-plane simulation), time t , and K_{ij}^A as components of the dimensionless tensor of anisotropy K . S is a source/sink term, which can be partly characterized by the volume of water that is removed from the soil by plant roots. The effects described by this strongly nonlinear partial differential equation are subject to hysteresis, especially the relationship between water content and pressure head [13]. This relationship can be described by the VAN-GENUCHTEN-LUCKNER equation (5).

$$\theta = \theta_{r,w} + \frac{\phi - \theta_{r,w} - \theta_{r,l}}{\left[1 + (\alpha \cdot h_c)^n \right]^{-\frac{1}{n}}} \quad (2)$$

where Φ is the porosity of the soil; $\theta_{r,w}$ is residual water content; $\theta_{r,l}$ is residual air content; h_c characterizes the pressure head difference between the wetting (water) and non-wetting phase (air); α (scale factor) and n (slope) are empirical VAN-GENUCHTEN parameters [15]. The simulation tool PCSiWaPro® implements this relationship and solves the RICHARDS equation in two vertically-plane dimensions with transient boundary conditions, using a numerical finite element approach. For the solution of the linear system of equation originating from discretizing the RICHARDS equation, an iterative preconditioned conjugate gradient solver is used [13].

2.2 Model Setup with PCSiWaPro®

Before the start of the PCSiWaPro® simulation, the various initial and boundary conditions in the earth dams should be identified and then defined in the program. The initial condition is either the distribution of the pressure head or the water content in the whole dam area. This program could define various boundary conditions, e.g. time-dependent boundary conditions, atmospheric boundary conditions, seepage face. Time-dependent boundary conditions are defined by measured water levels at the water side of the dam. Furthermore atmospheric boundary conditions like precipitation or evapotranspiration can be applied. At the air side of the dam a seepage face was defined to allow outflow only when the soil has reached full water saturation [13].

Figure 3 shows an example of boundary condition setup for a physical earth dam with a rubber wall in the middle. On the foot of the left side, there is a yellow line with boundary condition of time dependent potential head which means that this layer has an influence of transient flooding level; on the left slope and in the middle there are impermeable walls allowing no water flux through these two layers; the red vegetation line on the top and on some part of the right slope has atmospheric boundary condition, and can be infiltrated through by rainfall water; lastly the blue line on the foot of the right slope means the seepage face.

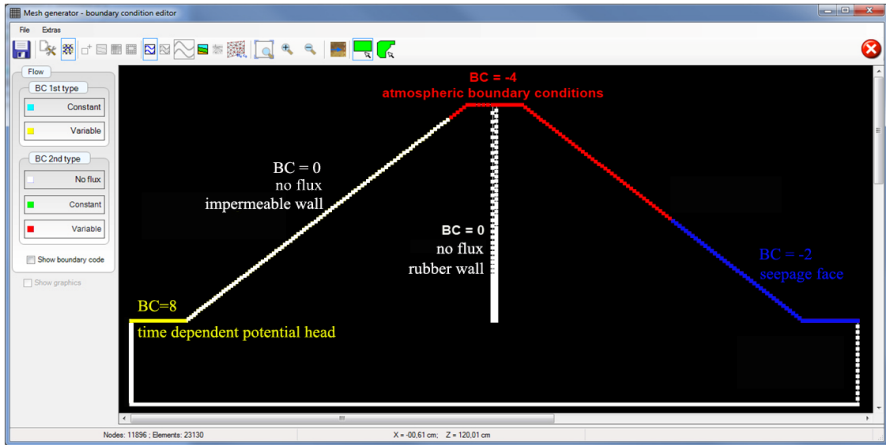


Fig. 3. Setup of various boundary conditions in the program PCSiWaPro®

After setting up the boundary conditions, the parameters of the earth dam materials (dam slope, core if possible, foundation materials, soil materials beyond the dam area) need to be input into PCSiWaPro® (Figure 4). There can be either input from the soil parameter data which have been achieved from the field or laboratory investigation or easily input from existing soil databases DIN4220 which has been installed into the program.

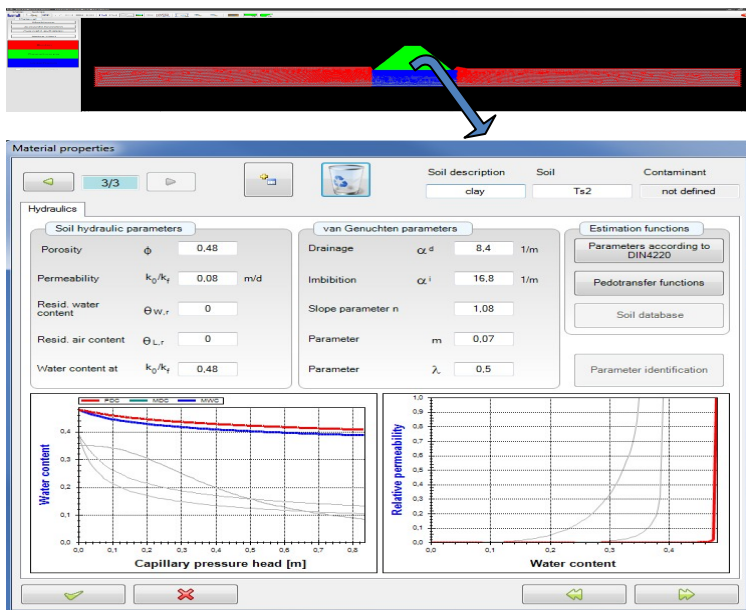


Fig. 4. Input of the soil parameters into the program PCSiWaPro®

Discretization of the model area is required for the calculation with the program PCSiWaPro[®]. In this case, unstructured triangular mesh elements can be specified. This enables the user to adequately map even irregular model areas. The implemented mesh generator uses the "Boundary Representation Modelling Technique" and therefore requires the specification of the model boundaries. Since the range of the dam embankment is of interest for the evaluation, this section of the model was discretized finer (10 cm), which results in a better representation of the change in water contents in the unsaturated zone above the seepage line and enables a better comparison between simulated and measured values [13].

3 Simulation Results

3.1 Simulation of a Laboratory-Scale Dam

The first model simulation is for a physical dam model setup by the Institute of Hydraulic Engineering and Applied Fluid Mechanics at the TU Dresden shown in Figure 2. This model dike had a base width of 3.38 m, a height of 0.77 m and a slope angle of 1:2. In the middle there was an impermeable rubber wall which could hold the dike height (embedding). Beneath the bank, on both air and water side, a berm of 0.3 m height was added to allow an exchange between flowing water through the slope and capillary-rise groundwater. At the air-side slope a drainage system was constructed to dissipate excess water effectively. Aigner [6] carried out a few tests in this physical model with different internal geotechnical structures. During the test, with the increase of water level in the water side (left side of the dam in Figure 2), landslide phenomena could be found in the partially saturated soil above the seepage line (dark color line) in the air side.

With the program PCSiWaPro[®], a simulation with an additional atmospheric boundary condition (i.e. input of rainfall water into the slope) has been carried out during a period of 12 h. The graphical simulation results are shown in Figure 5 for pressure head and water content (5.3 h after the beginning of this simulation). Rainfall water provided an additional flow into the right dam embankment, thereby increasing the water content in this unsaturated slope. In addition, this simulation has been also considered as a test for the efficiency of the rubber wall on the groundwater flow process. As clearly shown in the graphs below, the equipotential lines for pressure head and water content have been decreased by some degree in the right side; in this case, an easy conclusion could be achieved that this impermeable wall could provide a negative force for the water content change in the unsaturated slope.

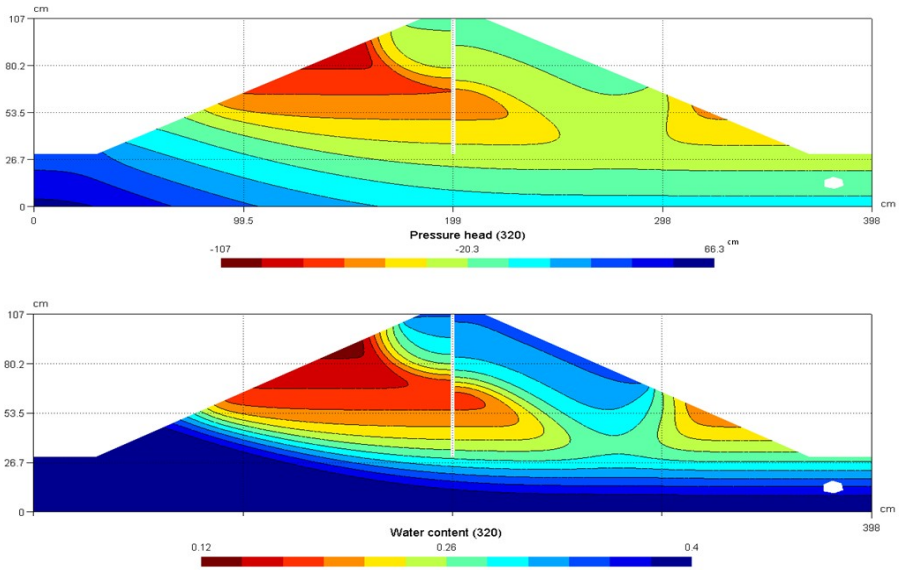


Fig. 5. Simulation of pressure head and water content in a physical earth dam in the laboratory (5.3 h after the beginning of this simulation)

3.2 Simulation for a Real Dam - A Case Study in China

A real earth dam model has been selected in China for the practical application of the program PCSiWaPro® and then for stability analysis. This dam is 600 m wide and 86 m high. Additional basic data, like precipitation, water level change in the reservoir, pore water pressure, have been obtained from the local agencies. There are mainly three parts in the dam body, two cores with slight sandy clay (one is in the middle and the other is closer to the left bottom) and strongly silt sand in the rest dam body.

Figure 6 shows the precipitation data for the year of 2006. As can be seen in this graph, the rainfall event mainly occurred between April and July, especially in the mid-April, late May and early July. Accordingly the water level in the reservoir exhibited a sharp increase from the early May to July due to the rain season, as shown in Figure 7. However from the early January to early May a slow decrease of water level has been detected in the reservoir, which could be explained by the evaporation loss of water and very few rainfall events during this period. In addition, although the rainfall season came from the early April, the water level showed a converse change in April, which was mainly due to the manmade pre-operation of out flow discharge from the reservoir in order to prevent the possible overload water storage in the coming rainfall season and to prevent the dam collapse.

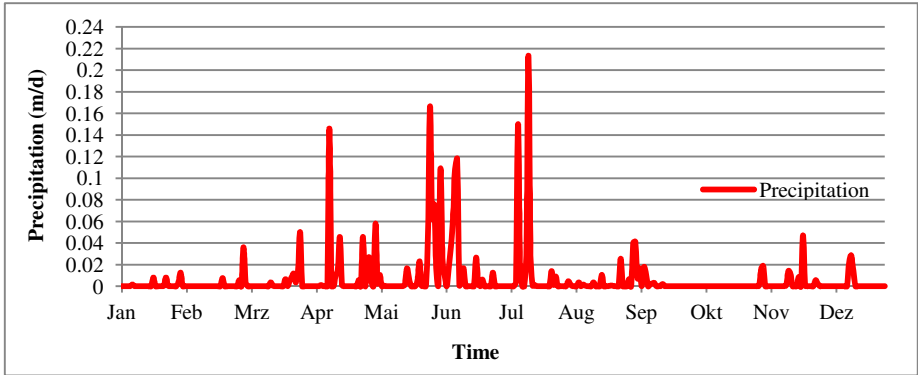


Fig. 6. Yearly precipitation data in 2006

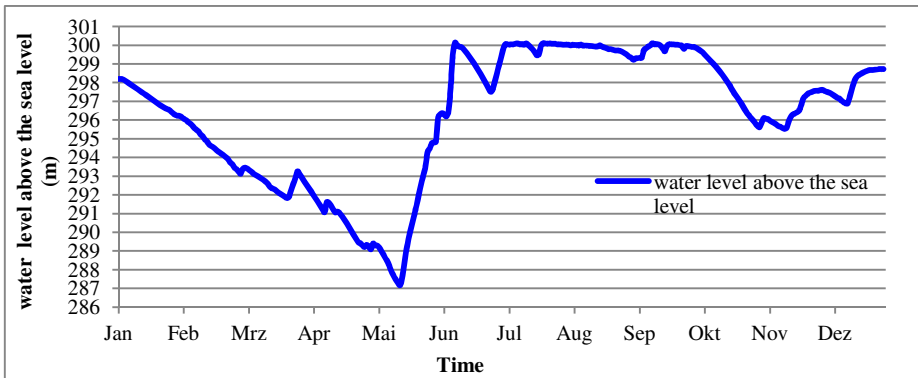


Fig. 7. Water level changes in the reservoir in 2006

After the setup of the model in the program PCSiWaPro[®], a simulation time of 365 days in 2006 was selected. On some part of the right slope, atmospheric boundary condition has been defined and the rest of the right slope was for seepage face; the whole left slope was input by the boundary condition of no flux, which meant no water could pass through the impermeable slope; lastly the left foot of the dam has been given a boundary condition of time depended potential head due to the transient flooding level (similar with Figure 3).

With the daily input data of precipitation and water level in the reservoir, the daily change of pressure head and water content could be easily achieved. Figure 8 shows the simulation result on 29th June of pressure head due to both the groundwater rise and infiltrated rainfall water. The rigid decrease of seepage line in the clay cores could be explained by the fact that the clay material has smaller permeability than the silt sand in the slope.

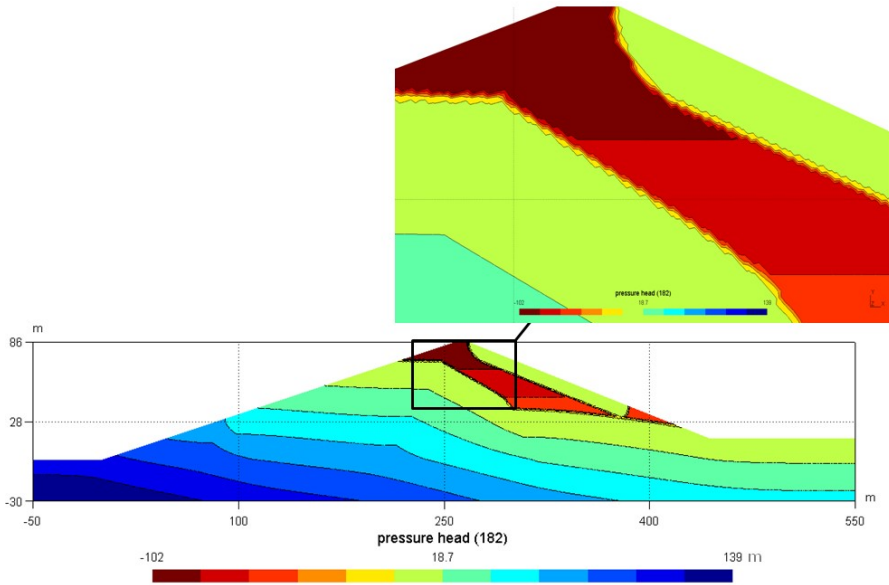


Fig. 8. Pressure head simulation from PCSiWaPro® on 29.06.2006

Figure 9 gives us an image of water content distribution in the dam body, especially in the unsaturated slope and clay core. In the saturated areas, the two clay cores show greater saturated water content (darker blue) than the other part of the dam, which is due to the different soil porosities; the higher the porosity is, the larger the saturated water content will be. The zoom-in image describes the detailed distribution of water content from 2% to 40% near the seepage line in those unsaturated zones;

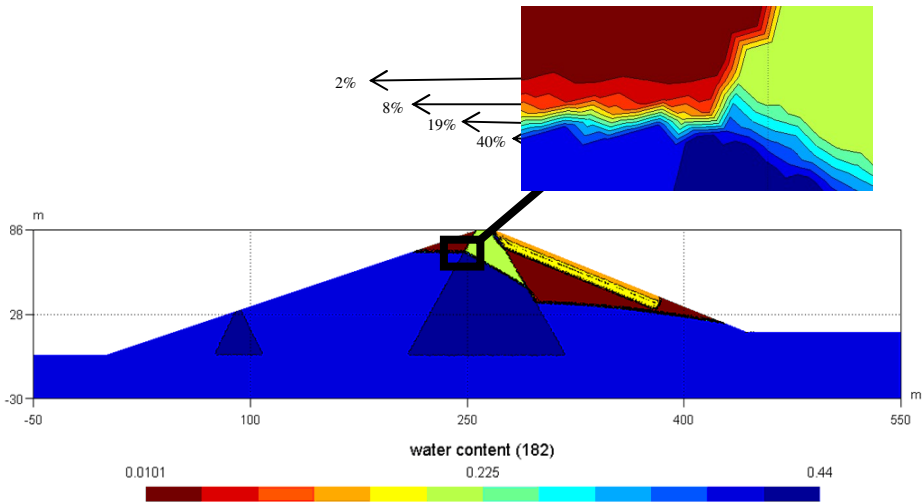


Fig. 9. Water content simulation from PCSiWaPro® on 29.06.2006

however in the middle circled by a black line there is an interesting part which exhibits a smaller degeneration rate of soil water in the core than that in the slope with the falling water level in the reservoir. This could give us a view of clear sensitivity of the model parameters (hydraulic conductivity, pore space diameter); i.e. with the smaller hydraulic conductivity and smaller pore space diameter, the clay soil has larger capillary force to hold the pore water, and then larger hysteresis effect on the water content change.

In addition, a comparison between the measured and simulated water level has been carried out. The accordance between the measured and the computed values using the program PCSiWaPro[®] was good for the case in the clay core shown in Figure 10. However the deviation found in the comparison of simulated with measured values for the water level in the slope (Figure 11) could be explained by the fact that our simulation was mainly based on the soil data base DIN 4220 and not on the exact soil parameters investigation in China.

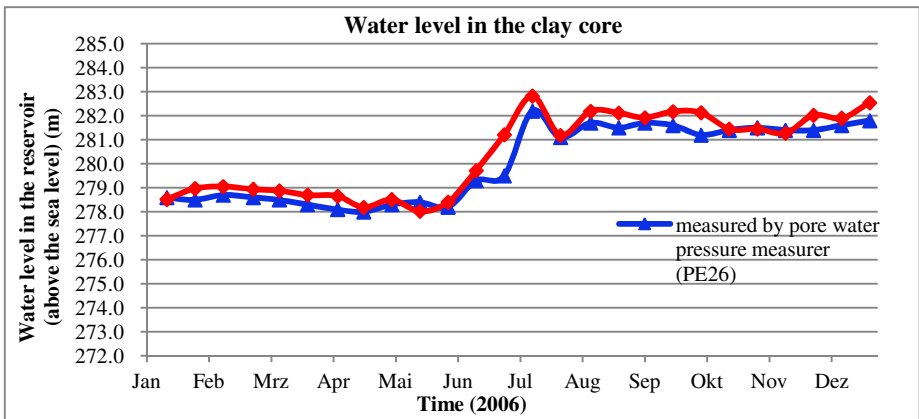


Fig. 10. Comparison between the computed and measured water levels in the clay core

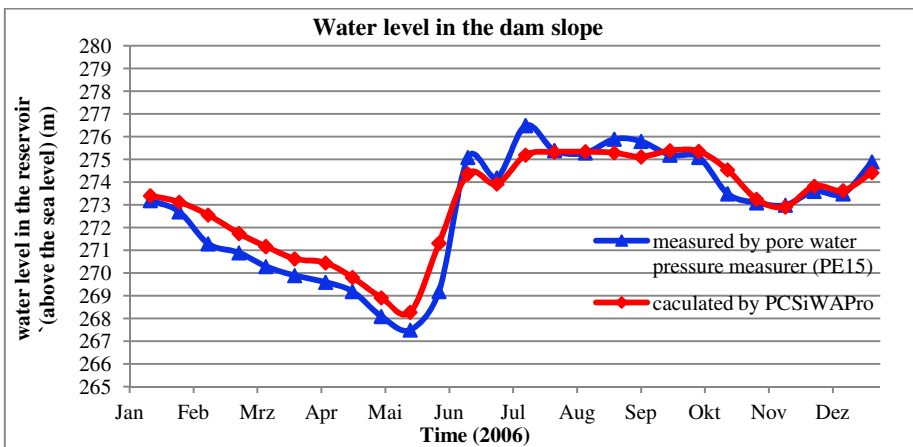


Fig. 11. Comparison between the computed and measured water levels in the dam slope

4 Stability Analysis

4.1 Slope Stability Model

Slope stability problems of dams and dikes are among the most commonly encountered problems in geotechnical and hydraulic engineering. Numerous scientists conducted a large amount of research in this field and several numerical methods were developed for the slope stability analysis. The typical methods are Infinite Slope Equation, Ordinary Method of Slices, JANBU'S Simplified Method, MORGENSTERN-PRICE method and so on. Due to the close relationship between the water content and slope stability, the infinite slope equation is one of the most applicable methods to be used together with water flow simulation in unsaturated dam bodies [16, 17].

The infinite slope model is the oldest and simplest slope stability method that assumes identical conditions occur on any vertical section of the dam; and it is usually implemented with the assumption of homogeneous or averaged soil properties in which geomechanical failures always occur at the base of the slope [16, 17]. The objective of the analysis is to produce estimates of the probability of infinite slope failure in form of the conventional factor of safety (Fs) [18]. The infinite slope equation for the factor of safety (Fs) of a homogeneous soil under the root system, which is defined as the ratio of shear strength to shear stress for a one-dimensional infinite slope under both saturated and unsaturated conditions, is given as equation 3 and 4 [16, 19];

$$\sigma^s = -\frac{\theta - \theta_r}{\theta_s - \theta_r} (u_a - u_w) = -s_e (u_a - u_w) \quad (3)$$

$$Fs_{(z)} = \frac{\tan' \phi}{\tan \beta} + \frac{2c'}{\gamma z \cdot \sin 2\beta} - \frac{\sigma^s}{\gamma z} (\tan \beta + \cot \beta) \tan \phi' \quad (4)$$

where σ^s is defined as the suction stress characteristic curve of the soil with a practical functional form [20]; u_w is the pore water pressure; u_a is the pore air pressure; θ is the volumetric water content; θ_r is the residual volumetric water content; θ_s is the saturated volumetric water content; S_e is the saturation degree; θ is water content; $(u_a - u_w)$ is soil matric suction; z is vertical depth below the ground surface; ϕ' is the angle of internal friction; c' is the soil cohesion; β is the slope angle and γ is the total soil and water unit weight [21].

However for the Fs value within the root area, the root reinforcement should be considered; then

$$Fs_{(z)} = \frac{\tan' \phi}{\tan \beta} + \frac{2(c' + c_r)}{\gamma z \cdot \sin 2\beta} - \frac{\sigma^s}{\gamma z} (\tan \beta + \cot \beta) \tan \phi' \quad (5)$$

c_r is the root reinforcement cohesion [8].

Generally, when the factor of safety (Fs) of a dam slope is reduced to less than unity, landslides will be predicted. Table 1 also shows a reference value for the safe Fs.

Table 1. Typical F_s values for the stable earth dams [22]

Failure Mode	Foundation Type	F_s
Shear	Earthwork for Dams, Fills, etc.	1.2 - 1.6

Since now plenty of researches have been carried out to study the relationship between matric suction and water content in the unsaturated soil. The common result from those researches is that the matric suction increases with the decrease of water content in different kinds of soils (Figure 12).

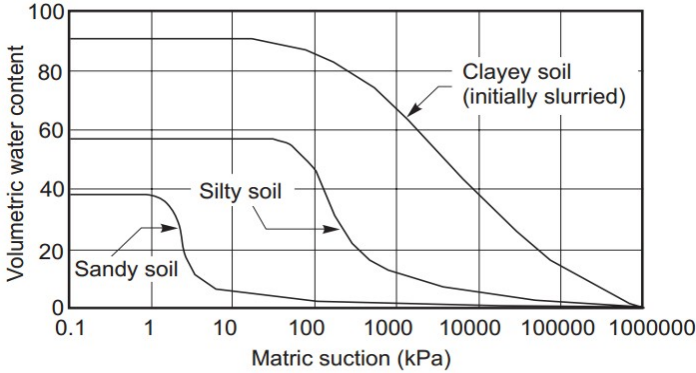


Fig. 12. Relationship between matric suction and water content for different soils [23]

From the VAN GENUCHTEN-LUCKNER equation, the relationship between water content and matrix suction can be easily achieved, as shown below:

$$U_a - U_w = \frac{\left[\left(\frac{\theta_s - \theta_r}{\theta - \theta_r} \right)^{\frac{n}{n-1}} - 1 \right]^{\frac{1}{n}}}{\alpha} \tag{6}$$

where α is scaling factor; n is slope factor.

VAN GENUCHTEN-LUCKNER parameters α and n could be either approximately calculated by the pedotransfer functions shown in the equations 7 and 8 [24] or precisely derived in the laboratory experiment;

$$\ln \alpha = -2.486 + 0.025 \cdot \text{sand\%} - 0.351 \cdot \text{clay\%} \tag{7}$$

$$\ln n = -0.035 - 0.009 \cdot \text{sand\%} - 0.013 \cdot \text{clay\%} + 0.015 \cdot (\text{sand\%})^2 \tag{8}$$

4.2 Stability Analysis Results

Figure 13 shows the simulation of the water content distribution in the slope on 29.06.2006. In this slope five layers with different water contents and different depths have been selected for stability analysis. Then Table 2 shows the general stability analysis results. For the first layer, 0.3 m, with water content of 15% and vegetation root system, the infinite slope model shows a very safe value, 23.3; while with an

assumption of no root system on this layer, a much smaller F_s value, 14.3, could be achieved from this model. This clearly verifies the significant positive effect of vegetation on the stability. In addition, on the next layer of 1 m, three water contents have been given including one simulation data (15%) from the program PCSiWaPro® and two assumed values (5% and 25%). The F_s values for these three conditions clearly indicate the negative influence of water content on the stability of the slope; the higher water content in the slope is followed by the less stability. Last but not least, on the two deepest layers of 20 m and 50 m with different low water contents, the infinite slope model gives us the same F_s value, from which a conclusion could be proposed that in this Chinese dam in the deep layer of the slope with the effect from matric suction, cohesion force, internal friction force and weight of soil – water, the F_s values from the infinite slope model appear no clear difference.

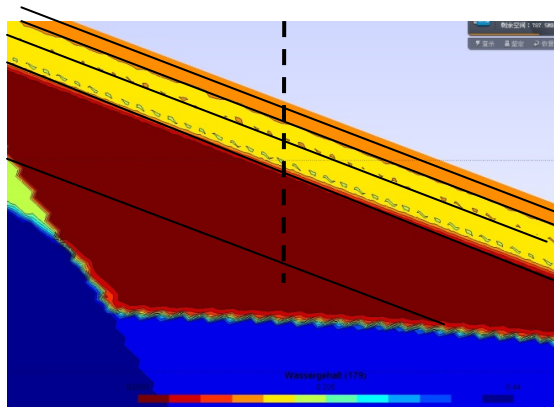


Fig. 13. Water content simulation result for the slope from PCSiWaPro® on 29.06.2006

Table 2. F_s results from the infinite slope model

Depth in the slope* (at air side, m)	Water content θ	F_s value from the infinite slope model
0.3	0.15	23.3
0.3**	0.15	14.3
1***	0.05	10.7
1	0.15	5.6
1***	0.25	5.5
10	0.19	2.0
20	0.1	1.8
50	0.05	1.8

* vegetation root depth = 0.5 m

** no vegetation layer (an assumption)

*** assumption with different water content on the layer of 1 m

5 Conclusions

1. The agreement between the measured water level values and the computed ones using the program PCSiWaPro[®] was very good for the case in the clay core; however there was some deviation between those two values in the dam slope. These deviations could be caused by poorly estimated hydraulic soil parameters, as these were based on the given DIN 4220 values. In this case, the investigation work of those soil parameters in China is in great need in order to get better matching with our program PCSiWaPro[®].
2. The simulation results for the physical dam model in the laboratory indicated clearly that ground water flow had been already detected in the highly partial-saturated dam body, and thus the stability of the dam at the air side was influenced and could cause landslides. This study also has tested the availability of PCSiWaPro[®] to simulate and predicate the water content change during a simulation period with a continuous scale.
3. Vegetation on the air side of dams and dikes has significant influence on the stability of slopes from the root cohesion as well as water uptake by plant roots.
4. Practically, with the water content simulation or prediction results (especially in the heavy rainfall event) from the program PCSiWaPro[®], the infinite slope stability analysis model can be taken as a powerful tool for forecasting the possible landslides (especially the surficial landslides) and the determination of the size and the structure (e.g. the core) of the dam.

Acknowledgement. The authors would like to thank Ms. Ren Zhang for the data collection work for the dams in China.

References

1. Bassell, B.: Earth dam. The engineering News Publication Company, New York (1904)
2. Holger Schuettrumpf: Sea Dikes in Germany. Die Küste, 74 ICCE, 189–199 (2008)
3. LTV of Free State of Saxony, State Reservoir Administration of Saxony, <http://www.smul.sachsen.de/ltv/>
4. Jonkman, B., Schweckendiek, T., Dupuits, G., Heyer, T., de Bijl, J., Labrujere, A.: Floods in Germany (June 2013), Post-flood field investigation. July 2& 3, 2013, Preliminary Findings (2013)
5. Bonelli, S.: Erosion in Geomechanics Applied to Dams and Levees. Wiley-ISTE (2013) ISBN: 978-1-84821-409-5
6. Aigner, D.: Auswertung von Untersuchungen über den Einsatz einer Gummispundwand sowie einer Sickerleitung an einem durchströmten Modelldeich. Institut für Wasserbau und Technische Hydromechanik. Technische Universität Dresden, Dresden (2004)
7. Souliyavong, T., Gallage, C., Egodawatta, P., Maher, B.: Factors affecting the stability analysis of earth dam slopes subjected to reservoir drawdown. In: Second International Conference on Geotechnique, Construction Materials and Environment, Kuala Lumpur, Malaysia (2012) ISBN: 978-4-9905958-1-4 C3051

8. Wu, T.H.: Root reinforcement of soil: Review of analytical models, test results, and applications to design. NRC Research Press (2013)
9. Coppin, N.J., Barker, D.H., Richards, I.: Use of Vegetation in Civil Engineering. Butterworths, Sevenoaks (1990)
10. Gray, D.H.: Influence of vegetation on the stability of slopes. In: Barker, D.H. (ed.) *Vegetation and Slopes Stabilisation, Protection and Ecology*, pp. 2–23. Thomas Telford House, London (1995)
11. Huang, B., Nobel, P.S.: Root hydraulic conductivity and its components with emphasis on desert succulents. *Agron. J.* 86, 767–774 (1994)
12. Abe, K.: A method of evaluating the effect of trees roots on preventing shallow-seated landslides. *Bull. Forest. Forest Prod. Res. Inst.* 1(373), 1105–1181 (1997)
13. Hasan, I., Meyer, M., Guo, J., Graeber, P.-W.: Simulation of the hydrological regime in earth dams and dikes as a basis for stability analysis using the software PCSiWaPro®. In: III Ogólnopolska Konferencja naukowo – Techniczna Zarzadzanie Kryzysowe – Nauka I Praktyka nt. Retencja Wodna Na Obszarach Wiejskich, Opole, Jarnoltowek, Poland (2012)
14. Gräber, P.-W., Blankenburg, R., Kemmesies, O., Krug, S.: SiWaPro DSS Beratungssystem zur Simulation von Prozessen der unterirdischen Zonen. In: Jochen, W., Mike, M. (Hrsg.) *Shaker Verlag, Leipzig* (2006) ISBN 3-8322-5132-4
15. Kemmesies, O.: *Prozessmodellierung und Parameteridentifikation von Mehrphasenströmungsprozessen in porösen Medien.* Dresdner Grundwasserforschungszentrum e.V., Dresden (1995) ISSN 1430-0176
16. Hammond, C., Hall, D.E., Miller, S., Swetik, P.: *Level I Stability Analysis (LISA). Documentation for Version 2.0: U.S. Department of Agriculture, Forest Service, Intermountain Research Station.* General Technical Report INT-285, Ogden, UT (1992)
17. Biondi, G., Cascone, E., Magueri, M., Motta, E.: Seismic response of saturated cohesionless slopes. *Soil Dynam. Earthquake Eng.* 20(1-4), 209–215 (2000)
18. Griffiths, D.V., Huang, J., Fenton, G.A.: Probabilistic infinite slope analysis. *Computers and Geotechnics* 38(2011), 577–584 (2011)
19. Duncan, J.M., Wright, S.G.: *Soil Strength and Slope Stability*, p. 297. John Wiley, Hoboken (2005)
20. Lu, N., Likos, W.J.: Suction stress characteristic curve for unsaturated soil. *J. Geotech. Geoenviron. Eng.* 123, 131–142 (2006)
21. Lu, N., Godt, J.W.: Infinite-slope stability under steady unsaturated conditions. *Water Resour. Res.* 44, W11404 (2008), doi:10.1029/2008WR006976
22. Bowles, J.E.: *Foundation Analysis and Design*, 4th edn. McGraw-Hill (1988)
23. Fredlund, D.G., Rahardjo, H., Ng, T.: Effect of pore air and negative pore water pressures on stability at the end-of-construction (1993)
24. Vereecken, H., Maes, J., Feyen, J., Darius, P.: Estimating the soil moisture retention characteristic from texture, bulk density and carbon content. *Soil Science* 148(6), 389–403 (1989)

A Pile-Soil Separation Concerned Model for Laterally Loaded Piles in Layered Soils

Guoping Lei¹, Huiming Tang², and Wei Wu¹

¹ Institut für Geotechnik, Universität für Bodenkultur,
Vienna, Austria

² Faculty of Engineering, China University of Geosciences, Wuhan, China
guoping.lei@students.boku.ac.at,
tanghm@cug.edu.cn, wei.wu@boku.ac.at

Abstract. A pile-soil separation concerned continuum method is proposed to analyze the response of laterally loaded piles in a homogeneous multilayer elastic medium. The displacement fields of soil vary in the vertical direction and decrease in the radial direction. Variational principles are used to obtain the governing differential equations for the pile and soil displacements. Closed-form solutions are derived and the pile deflection, pile rotation, bending moment and shear force for the entire length of the pile can be obtained. The validity of proposed approach is demonstrated through comparisons with previous methods, 3D FD analysis and data obtained from a published pile test. The influence of pile-soil separation is explicated by the results of a comprehensive parametric study involving the slenderness ratio and flexibility factor of the pile. It can be concluded that the deflection of pile is larger when pile-soil separation happens, and the effect can be reduced for piles with larger slenderness ratio and medium flexibility.

Keywords: pile-soil separation, laterally loaded pile, layered soils.

1 Introduction

Laterally loaded pile, which is one of the complex soil-structure interaction problems in geotechnical engineering, is widely used in high-rise building foundations, bridge pier, offshore structures, and slope or landslide prevention. Response of vertical piles to the action of lateral loads has been studied by a large amount of theoretical and experimental researches for more than six decades. At the beginning, the idea of Winkler subgrade model, which represents soil by discrete springs with the soil subgrade modulus as the spring constant, was developed to analyze piles under lateral loading. This approach was modified to consider plastic deformation of soil by allowing the spring stiffness to vary along the pile [1, 2]. By replacing the linear springs by non-linear p-y curves, the widely used p-y method is developed [3–7].

Various methods have been used to analyze laterally loaded piles: the finite element method [8–11], finite elements coupled with Fourier series [12–14], the finite difference method [15, 16] and the upper-bound method of plasticity [17].

These apart, Douglas and Davis [18] evaluated the soil displacement from the integration of Mindlin equation for horizontal displacement due to a horizontal loaded within a semi-infinite mass, which was also applied to analyze laterally loaded piles [19, 20]. This boundary element method was also developed to consider the non-linear and yielding of soil [21, 22].

Laterally loaded piles were also analyzed by considering the soil surrounding the pile as a continuum. Sun [23] used variational principles to obtain analytical solutions for lateral pile displacements in elastic media. Zhang et al. [24] developed a nonlinear continuum method by assuming the deformation modulus of the soil vary linearly with depth. Guo and Lee [25] assumed a stress field using the Fourier series and obtained a theoretical load transfer method for laterally loaded piles. Basu et al. [26] proposed a continuum-based model in which the displacement fields vary in the vertical, radial and circumferential directions independently.

The above continuum methods are based on the hypothesis of no separation and slippage occurred in the pile-soil contact surface, which may provide very unconservative results when laterally loaded piles socketed in stiff clay or rock mass. Poulos [27] indicates that for practical purposes, the effect of separation is to virtually double the deflection of the pile head under elastic conditions. Guo [28] had analyzed the nonlinear response of laterally loaded rigid piles involving pile-soil gapping.

In order to make the continuum method applicable under such circumstances, in this paper a pile-soil separation concerned continuum method is proposed by using an ellipse to describe the soil boundary around the pile approximately. The displacement fields of soil vary in the vertical direction and decrease in the radial direction. Variational principles are used to obtain the governing differential equations for the pile and soil displacements. Closed-form solutions are derived. Unsurprisingly, pile deflection obtained by this method is larger than those assuming no pile-soil separation, but compares favorably with measured pile deflection and 3D FD analysis which also allow pile-soil separation. Also the impact of pile-soil separation is studied at the end of this paper.

2 Analysis

2.1 Description of Model

Fig.1 shows a typical circular pile of length L_p , radius R , and constant flexibility $E_p I_p$, embedded in a soil deposit that has n layers. Each layer is assumed to be horizontal and extends to infinity in all radial directions, and the bottom (n th) layer extends to infinity in the downward direction. A cylindrical ($r - \theta - z$) coordinate system, whose origin coinciding with the centre of the pile head, is adopted here for analysis. The positive z -axis coincides with the pile axis and points downwards. The value of z for the i th layer base is H_i , which implies that

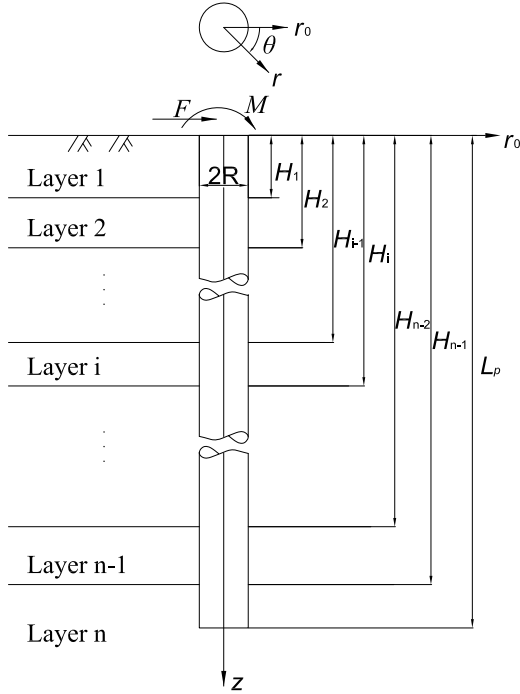


Fig. 1. Laterally loaded pile in layered medium

the thickness of the i th layer is $H_i - H_{i-1}$ with $H_0=0$ and $H_n = \infty$. The pile head is at the ground surface and the pile bottom is embedded in the n th layer. A horizontal force F and a moment M are applied on the pile head.

The surrounded soil is assumed to be an ideal, homogeneous, isotropic, linear elastic material with Young’s modulus E_s and Poisson’s ratio μ . The soil is unaffected by the presence of pile and there is no slippage at the interface of pile and surrounding soil. Meanwhile the interface has no tensile strength, which implies that separation occurs when the interface is in tensile.

2.2 Soil Displacement

As mentioned above, the incapability of tensile stress of the pile-soil interface leads to a gap behind the pile after pile deflection (Fig.2). The circle soil boundary is stretched in the direction of pile movement. In this analysis, the soil boundary after pile deflection is approximately described by an ellipse with

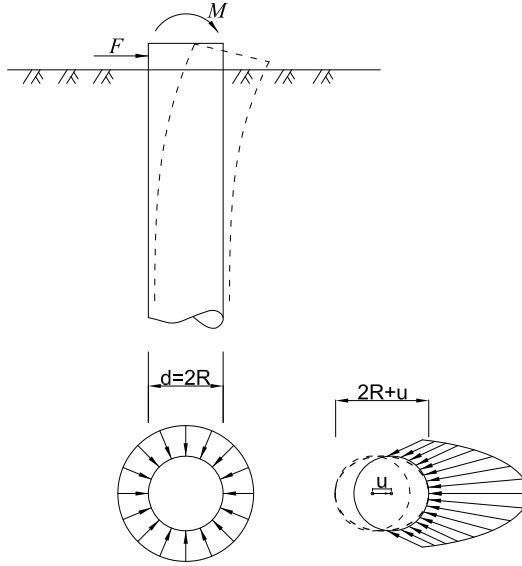


Fig. 2. Pile-soil separation after pile deflection

major axes $2R + u$ (u is the pile displacement) and minor axes $2R$. By adopting the basic idea of Sun [23], the displacement u_r, u_θ, u_z of soil can be approximated by separable functions of the cylindrical coordinates r, θ and z as

$$\begin{cases} u_r(r, \theta, z) = \frac{1}{2} [|u(z)| \cos^2 \theta + u(z) \cos \theta] \phi(r) \\ u_\theta(r, \theta, z) = -\frac{1}{2} [|u(z)| \sin \theta \cos \theta + u(z) \sin \theta] \phi(r) \\ u_z(r, \theta, z) = 0 \end{cases} \quad (1)$$

where $u(z)$ is the deflection of the pile axis, varying with depth z ; $\phi(r)$ is a dimensionless function varying with the radial coordinate r ; and θ is the angle measured clockwise from a vertical reference section that contains the applied force vector F . The vertical displacement of the pile is not considered in this research.

The function $\phi(r)$ describes how the displacements within the soil (due to pile deflection) decrease with increasing radial distance from the pile axis. The boundary condition for this function is $\phi(r) = 1$ at $r = R$ and $\phi(r) = 0$ at $r = \infty$.

2.3 Potential Energy of Pile-Soil System

By using the displacement described in equation (1), the strain of the soil is obtained as

$$\begin{bmatrix} \varepsilon_{rr} \\ \varepsilon_{\theta\theta} \\ \varepsilon_{zz} \\ \gamma_{r\theta} \\ \gamma_{\theta z} \\ \gamma_{zr} \end{bmatrix} = \begin{bmatrix} \frac{\partial u_r}{\partial r} \\ \frac{1}{r} \frac{\partial u_\theta}{\partial \theta} + \frac{u_r}{r} \\ 0 \\ \frac{1}{r} \frac{\partial u_r}{\partial \theta} - \frac{u_\theta}{r} + \frac{\partial u_\theta}{\partial r} \\ \frac{\partial u_\theta}{\partial z} + \frac{1}{r} \frac{\partial u_z}{\partial \theta} \\ \frac{\partial u_z}{\partial r} + \frac{\partial u_r}{\partial z} \end{bmatrix} = \begin{bmatrix} \frac{1}{2} [|u(z)| \cos^2 \theta + u(z) \cos \theta] \frac{d\phi(r)}{dr} \\ \frac{1}{2r} |u(z)| \phi(r) \sin^2 \theta \\ 0 \\ -\frac{1}{4r} |u(z)| \phi(r) \sin 2\theta - \frac{1}{2} [|u(z)| \sin \theta \cos \theta \\ + u(z) \sin \theta] \frac{d\phi}{dr} \\ -\frac{1}{2} \phi(r) \left[\left| \frac{du(z)}{dz} \right| \sin \theta \cos \theta + \frac{du(z)}{dz} \sin \theta \right] \\ \frac{1}{2} \phi(r) \left[\left| \frac{du(z)}{dz} \right| \cos^2 \theta + \frac{du(z)}{dz} \cos \theta \right] \end{bmatrix} \quad (2)$$

The total potential energy (including both the internal and external) of the pile-soil system is given by

$$\begin{aligned}
 \Pi &= \frac{1}{2} E_p I_p \int_0^{L_p} \left(\frac{d^2 u(z)}{dz^2} \right)^2 dz + \int_0^\infty \int_0^{2\pi} \int_R^\infty \frac{1}{2} \sigma_{ij} \varepsilon_{ij} r dr d\theta dz \\
 &+ \int_{L_p}^\infty \int_0^{2\pi} \int_0^R \frac{1}{2} \sigma_{ij} \varepsilon_{ij} r dr d\theta dz - Fu(z)|_{z=0} + M \frac{du(z)}{dz} \Big|_{z=0} \quad (3)
 \end{aligned}$$

where σ_{ij} and ε_{ij} are the stress and strain tensors in the soil. The first integral represents the internal potential energy of the pile. The third integral represents the internal potential energy of the soil with radius R starting at the pile base and extending to infinity downward. The second integral represents the energy of the rest of soil. The remaining two terms represent the external potential energy. The stress tensor σ_{ij} can be obtained from the strain tensor ε_{ij} by applying the generalized Hooke's law. Using the strain expressions in equation (2), the potential energy formula can be rewrite as

$$\begin{aligned}
 \Pi &= \frac{1}{2} E_p I_p \int_0^{L_p} \left(\frac{d^2 u(z)}{dz^2} \right)^2 dz + \frac{\pi}{32} \int_0^\infty \int_R^\infty [(7\lambda_s + 19G_s) u^2 \left(\frac{d\phi}{dr} \right)^2 \\
 &+ \frac{2(\lambda_s + G_s)}{r} u^2 \phi \frac{d\phi}{dr} + \frac{3\lambda_s + 7G_s}{r^2} u^2 \phi^2 + 12G_s \left(\frac{du}{dz} \right)^2 \phi^2] r dr dz \\
 &+ \frac{\pi}{2} R^2 \int_{L_p}^\infty G_s \left(\frac{du}{dz} \right)^2 dz - Fu(z)|_{z=0} + M \frac{du(z)}{dz} \Big|_{z=0} \quad (4)
 \end{aligned}$$

where λ_s is the Lamé's constant and G_s is the shear modulus of the soil. It is noted that the integrands which include $|u(z)|$ all equal to zero after the integration of θ .

2.4 Solutions for Laterally Loaded Piles

The variational approach is adopted here to obtain solutions. The variation of potential energy, $\delta\Pi$, of the pile-soil system can be expressed in terms of δu , $\delta du/dz$ and $\delta\phi$. Applying $\delta\Pi=0$ to equation (4) and collect all the terms associated with δu and $\delta(du/dz)$ and equate their sum to zero. The following equation is obtained

$$\begin{aligned}
& \sum_{i=1}^n \int_{H_{i-1}}^{H_i} \left(E_p I_p \frac{d^4 u_i}{dz^4} - t_i \frac{d^2 u_i}{dz^2} + k_i u_i \right) \delta u_i dz \\
& + \left(E_p I_p \frac{d^3 u_1}{dz^3} - t_1 \frac{du_1}{dz} - F \right) \delta u_1 \Big|_{z=0} - \left(E_p I_p \frac{d^2 u_1}{dz^2} - M \right) \delta \left(\frac{du_1}{dz} \right) \Big|_{z=0} \\
& + \sum_{i=1}^{n-1} \left[\left(-E_p I_p \frac{d^3 u_i}{dz^3} + t_i \frac{du_i}{dz} \right) \delta u_i \Big|_{z=H_i} \right. \\
& + \left. \left(E_p I_p \frac{d^3 u_{i+1}}{dz^3} - t_{i+1} \frac{du_{i+1}}{dz} \right) \delta u_{i+1} \Big|_{z=H_i} \right. \\
& + \left. E_p I_p \frac{d^2 u_i}{dz^2} \delta \left(\frac{du_i}{dz} \right) \Big|_{z=H_i} - E_p I_p \frac{d^2 u_{i+1}}{dz^2} \delta \left(\frac{du_{i+1}}{dz} \right) \Big|_{z=H_i} \right] \\
& + E_p I_p \frac{d^2 u_n}{dz^2} \delta \left(\frac{du_n}{dz} \right) \Big|_{z=L_p} \\
& + \left[\left(-E_p I_p \frac{d^3 u_n}{dz^3} + t_n \frac{du_n}{dz} \right) \Big|_{z=L_p} - t_{n+1} \frac{du_{n+1}}{dz} \Big|_{z=L_p} \right] \\
& + \int_{L_p}^{\infty} \left(-t_{n+1} \frac{d^2 u_{n+1}}{dz^2} + k_n u_{n+1} \right) \delta u_{n+1} dz + t_{n+1} \frac{du_{n+1}}{dz} \delta u_{n+1} \Big|_{z=\infty} = 0 \quad (5)
\end{aligned}$$

where

$$t_i = \begin{cases} \frac{3}{4} \pi G_{si} \left[\int_R^{\infty} \phi^2 r dr \right]; & i = 1, 2, \dots, n \\ \pi G_{sn} \left[\frac{3}{4} \int_R^{\infty} \phi^2 r dr + R^2 \right]; & i = n + 1 \end{cases} \quad (6)$$

$$\begin{aligned}
k_i = \frac{\pi}{16} & \left[(7\lambda_{si} + 19G_{si}) \int_R^{\infty} \left(\frac{d\phi}{dr} \right)^2 r dr + 2(\lambda_{si} + G_{si}) \int_R^{\infty} \phi \frac{d\phi}{dr} dr \right. \\
& \left. + (3\lambda_{si} + 7G_{si}) \int_R^{\infty} \frac{\phi^2}{r} dr \right] \quad (7)
\end{aligned}$$

The subscript i in the above equations refers to the i th layer of the soil (Fig.1); u_i represents the function $u(z)$ in the i th layer with $u_i|_{z=H_i} = u_{i+1}|_{z=H_i}$. Note that the n th layer is split into two parts, with the part below the pile denoted by the subscript $n + 1$; therefore, in the analysis, $H_n = L_p$ and $H_{n+1} \rightarrow \infty$.

For the soil domain below the pile ($L_p \leq z < \infty$), the terms associated with δu and $\delta(du/dz)$ in equation (5) for $L_p \leq z < \infty$ are equated to zero. Since

the variation of $u(z)$ with depth is not known a priori within the interior of the domain $L_p \leq z < \infty$, δu_{n+1} is a non-zero term, so the integrand in the integral between $z = L_p$ and $z = \infty$ must be equal to zero in order to satisfy equation (5). This results in the following differential equation

$$t_{n+1} \frac{d^2 u_{n+1}}{dz^2} - k_n u_{n+1} = 0 \tag{8}$$

The displacement in the soil must vanish for z equal to infinity, which make the boundary condition of u_{n+1} as

$$u_{n+1} = 0 \text{ (at } z = \infty) \tag{9}$$

The solution of equation (8) satisfying boundary condition (12) is

$$u_{n+1} = u_n|_{z=L_p} e^{-\sqrt{(k_n/t_{n+1})}(z-L_p)} \tag{10}$$

For the soil domains surrounding the pile ($0 \leq z \leq H_1$, $H_1 \leq z \leq H_2, \dots$, $H_{n-1} \leq z \leq H_p$), the variations δu_i and $\delta \frac{du_i}{dz}$ are both non-zero terms, which leads to

$$\frac{d^4 \tilde{u}_i}{d\tilde{z}^4} - \tilde{t}_i \frac{d^2 \tilde{u}_i}{d\tilde{z}^2} + \tilde{k}_i \tilde{u}_i = 0 \tag{11}$$

where $\tilde{u} = u/L_p$, $\tilde{z} = z/L_p$, $\tilde{t}_i = t_i L_p^2 / E_p I_p$, $\tilde{k}_i = k_i L_p^4 / E_p I_p$. The boundary conditions for equation (17) are

$$\frac{d^3 \tilde{u}_1}{d\tilde{z}^3} - \tilde{t}_1 \frac{d\tilde{u}_1}{d\tilde{z}} - \tilde{F} = 0 \text{ (at } \tilde{z} = 0) \tag{12a}$$

$$\frac{d^2 \tilde{u}_1}{d\tilde{z}^2} - \tilde{M} = 0 \text{ (at } \tilde{z} = 0) \tag{12b}$$

$$\tilde{u}_i = \tilde{u}_{i+1} \text{ (at } \tilde{z} = \tilde{H}_i) \tag{12c}$$

$$\frac{d\tilde{u}_i}{d\tilde{z}} = \frac{d\tilde{u}_{i+1}}{d\tilde{z}} \text{ (at } \tilde{z} = \tilde{H}_i) \tag{12d}$$

$$\frac{d^2 \tilde{u}_i}{d\tilde{z}^2} = \frac{d^2 \tilde{u}_{i+1}}{d\tilde{z}^2} \text{ (at } \tilde{z} = \tilde{H}_i) \tag{12e}$$

$$\frac{d^3 \tilde{u}_i}{d\tilde{z}^3} - \tilde{t}_i \frac{d\tilde{u}_i}{d\tilde{z}} = \frac{d^3 \tilde{u}_{i+1}}{d\tilde{z}^3} - \tilde{t}_{i+1} \frac{d\tilde{u}_{i+1}}{d\tilde{z}} \text{ (at } \tilde{z} = \tilde{H}_i) \tag{12f}$$

$$\frac{d^2 \tilde{u}_n}{d\tilde{z}^2} = 0 \text{ (at } \tilde{z} = 1) \tag{12g}$$

$$\frac{d^3 \tilde{u}_n}{d\tilde{z}^3} - \tilde{t}_n \frac{d\tilde{u}_n}{d\tilde{z}} = -\tilde{t}_{n+1} \frac{d\tilde{u}_{n+1}}{d\tilde{z}} \text{ (at } \tilde{z} = 1) \tag{12h}$$

where $\tilde{F} = FL_p^2 / E_p I_p$, $\tilde{M} = ML_p / E_p I_p$, $\tilde{H}_i = H_i / L_p$. The general solution of equation (14) is given by

$$\tilde{u}_i(\tilde{z}) = C_1^{(i)} \Phi_1 + C_2^{(i)} \Phi_2 + C_3^{(i)} \Phi_3 + C_4^{(i)} \Phi_4 \tag{13}$$

where $C_1^{(i)}$, $C_2^{(i)}$, $C_3^{(i)}$ and $C_4^{(i)}$ are integration constants for the i th layer, and Φ_1 , Φ_2 , Φ_3 and Φ_4 are individual solutions of the differential equation. The functions Φ_1 , Φ_2 , Φ_3 and Φ_4 are standard trigonometric or hyperbolic functions (detailed discussed by Basu [26]). The integration constants for each layer can be determined by using the boundary conditions given in equations (12), which can be written as a system of linear equations of the form

$$[\Theta][C] = [F] \tag{14}$$

where $[\Theta]$ is a $4n \times 4n$ matrix containing the functions Φ_1 , Φ_2 , Φ_3 and Φ_4 calculated at the top and base of each soil layer, $[C]$ is a $4n \times 1$ column vector of unknown integration constants of all the layers, $[F]$ is a $4n \times 1$ column vector containing the applied force and moment. It is noted that only the pile with free head and free base is presented in this paper, all the matrixes or vectors ($[\Theta]$, $[C]$ and $[F]$) for piles under all kind of head and base conditions are discussed by Basu [26].

The vector $[C]$ can be easily calculated by

$$[C] = [\Theta]^{-1}[F] \tag{15}$$

which substituted in equation (13) can produce the particular solution of pile deflection for a given set of boundary conditions and applied loads. By differentiating the equation (13), the rotation of the pile cross section, the bending moment and shear force of the pile can also be obtained.

2.5 Solutions for Soil Displacement

Applying $\delta II=0$ to equation (4) and collecting all the terms associated with $\delta\phi$, the following equation is obtained

$$\int_R^\infty -m_{s1}(r \frac{d^2\phi}{dr^2} + \frac{d\phi}{dr})\delta\phi dr + \int_R^\infty m_{s3} \frac{\phi}{r} \delta\phi dr + \int_R^\infty n_{sr} \phi \delta\phi dr + (m_{s1}r \frac{d\phi}{dr} + m_{s2}\phi)\delta\phi \Big|_R^\infty = 0 \tag{16}$$

where

$$m_{s1} = \int_0^\infty (7\lambda_s + 19G_s)(u)^2 dz = \sum_{i=1}^{n+1} (7\lambda_{si} + 19G_{si}) \int_{H_{i-1}}^{H_i} u_i^2 dz \tag{17a}$$

$$m_{s2} = \int_0^\infty (\lambda_s + G_s)(u)^2 dz = \sum_{i=1}^{n+1} (\lambda_{si} + G_{si}) \int_{H_{i-1}}^{H_i} u_i^2 dz \tag{17b}$$

$$m_{s3} = \int_0^\infty (3\lambda_s + 7G_s)(u)^2 dz = \sum_{i=1}^{n+1} (3\lambda_{si} + 7G_{si}) \int_{H_{i-1}}^{H_i} u_i^2 dz \tag{17c}$$

$$n_s = 12 \int_0^\infty G_s (\frac{du}{dz})^2 dz = 12 \sum_{i=1}^{n+1} G_{si} \int_{H_{i-1}}^{H_i} (\frac{du_i}{dz})^2 dz \tag{17d}$$

The function ϕ is known at $r = R$ and at $r = \infty$, as a result the last term on the left-hand side of equation (16) is equal to zero. Meanwhile, as $\phi(r)$ is not known a priori in the interval $R < r < \infty$, the variation $\delta\phi$ is a non-zero term, which leads to the differential equation

$$r^2 \frac{d^2\phi}{dr^2} + r \frac{d\phi}{dr} - [N^2 + (\frac{\gamma}{R}r)^2]\phi = 0 \quad (18)$$

where dimensionless contents given by $N^2 = m_{s3}/m_{s1}$ and $(\gamma/R)^2 = n_s/m_{s1}$.

The solution to equation (18), which satisfies the boundary condition $\phi(r) = 1$ at $r = R$ and $\phi(r) = 0$ at $r = \infty$, is

$$\phi(r) = \frac{K_N(\frac{\gamma}{R}r)}{K_N(\gamma)} \quad (19)$$

where $K_N()$ denotes the modified Bessel function of the second kind of order N . The dimensionless parameters γ and N can be expressed by dimensionless displacement \tilde{u} as

$$\gamma = \sqrt{\frac{R^2 \sum_{i=1}^n G_{si} \int_{H_{i-1}}^{H_i} (\frac{du_i}{dz})^2 dz + 12G_{sn} \frac{1}{2} \sqrt{\frac{k_n}{t_{n+1}}} \tilde{u}_n^2|_{\tilde{z}=1}}{L_p^2 \sum_{i=1}^n (7\lambda_{si} + 19G_{si}) \int_{H_{i-1}}^{H_i} u_i^2 dz + (7\lambda_{sn} + 19G_{sn}) \frac{1}{2} \sqrt{\frac{t_{n+1}}{k_n}} \tilde{u}_n^2|_{\tilde{z}=1}}} \quad (20a)$$

$$N = \sqrt{\frac{\sum_{i=1}^n (3\lambda_{si} + 7G_{si}) \int_{H_{i-1}}^{H_i} u_i^2 dz + (3\lambda_{sn} + 7G_{sn}) \frac{1}{2} \sqrt{\frac{t_{n+1}}{k_n}} \tilde{u}_n^2|_{\tilde{z}=1}}{\sum_{i=1}^n (7\lambda_{si} + 19G_{si}) \int_{H_{i-1}}^{H_i} u_i^2 dz + (7\lambda_{sn} + 19G_{sn}) \frac{1}{2} \sqrt{\frac{t_{n+1}}{k_n}} \tilde{u}_n^2|_{\tilde{z}=1}}} \quad (20b)$$

2.6 Determination of Interaction Parameter γ and N

In order to obtain the solution for $\phi(r)$ and $\tilde{u}(\tilde{z})$, the values of the parameter γ and N defined by equations (20) are needed. The function $\phi(r)$ depends on γ and N (see equation 19) while γ and N depend on the function $\tilde{u}(\tilde{z})$ (see equations 20). The coefficients k_i and t_i , which are required to evaluate the function $\tilde{u}(\tilde{z})$, also depend on function $\phi(r)$ (see equations 6 and 7). Since the values of γ and N are not known a priori, iterative technique is required here to solve the problem. At first, initial guesses for $\gamma = 1$ and $N = 1$ are made and k_i and t_i are calculated by numerical integrations. Using the values of k_i and t_i , the pile deflection is calculated, with which the new values of γ and N are obtained. And also the function $\phi(r)$ is recalculated and so on. The entire process is repeated until convergences on γ and N are both attained for a specified tolerance. The details of the solution steps are given in the form of a flow chat in Fig.3. This iterative procedure is also used by Sun [23] and Basu [26], which all claim that convergence can be obtained very fast even if the first estimates of γ and N is far from the exact values.

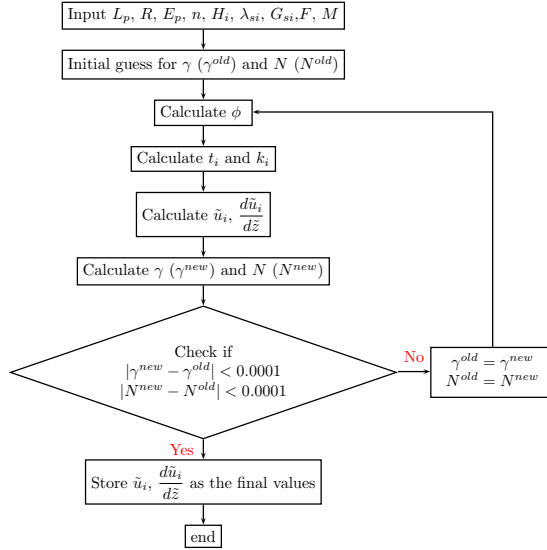


Fig. 3. Solution flowchart

3 Validations of the Analysis

This analysis is a modification on the analysis of Sun [23], and also adopts the analysis method for multi-layered soil in the analysis of Basu [26]. The consideration of pile-soil separation makes the result produced by the proposed method more comparable to the real pile response than those two. To illustrate this point, two examples from the paper of Basu [26] are presented below. Both of the examples are analyzed by methods of Sun [23], Basu [26], 3D FD analysis and method presented in this paper. The 3D FD analyses were performed using *FLAC^{3D}*. In the 3D FD analysis, the soil is modeled by a cylinder with a finite diameter and shearing its center with the pile. The top surface of the soil cylinder is flush with the pile head and the bottom surface is located at a finite distance below the pile tip. The horizontal force F is applied as a concentrate load acting on the center of pile head. The vertical plane passing through the pile axis and parallel to F is a plane of symmetry and divides the numerical model into two equal and symmetrical halves. Only one half is involved in the computational process in order to obtain the solution quickly. Different boundary conditions are prescribed at different boundaries of the FD model: the vertical displacement (z -direction) is assumed to be zero along the bottom surface; the horizontal displacement (both x and y -direction) is assumed to be zero along the outer, curved surface of the soil domain; on the boundary surface created by the plane of symmetry, the displacement perpendicular to the boundary is assumed to be zero. Two kinds of contact between the pile and the surrounding soil are

taken into consideration: first is the contact with no slippage or separation and the second is the contact which allows separation but no slippage (implemented by using high value of frictional coefficient).

The first example is a 15m long pile, with a diameter of 0.6m and pile modulus $E_p = 24 \times 10^6 kN/m^2$, embedded in a four-layer soil deposit (Table 1) with a horizontal force $F = 300kN$ acts on the pile head. The second example is a 40m long pile, with a diameter of 1.7m and pile modulus $E_p = 25 \times 10^6 kN/m^2$, also embedded in a four-layer soil deposit (Table 1) with a horizontal force $F = 3000kN$ acts on the pile head. The pile head is free to deflect and rotate in both of the examples.

In the 3D FD analysis, the radial distance of the outer curved boundary of the soil domain from the pile axis are taken as 20m and 25m for the 15m and 40m piles respectively; the corresponding vertical distance from the pile tip to the bottom boundary of the soil domain are 5m and 20m. The element size in the pile and at the pile-soil interface is approximately 0.1m×0.5m (radical×vertical) for the 15m pile and 0.5m (both radical and vertical) for the 40m pile, and increases gradually with increasing radical distance from the pile axis to 2.0m and 3.8m at the outer curved boundary of the soil domain in the two examples, respectively.

Fig.4 and Fig.5 show the pile deflection profile obtained using the proposed analysis, and the analyses based on the displacement assumption of Sun [23] and Basu [26], and 3D FD analysis. It is obvious that the analyses which share the same pile-soil contact assumptions match better with each other: the pile responses obtained from the analyses of Sun [23] and Basu [26] match more closely to the 3D FD analysis with the first kind of contact (no separation and slippage between pile and soil); and the pile response obtained by the analysis proposed in this paper suits better with the 3D FD analysis with the second kind of contact (allow separation but no slippage). Unsurprisingly, both the pile responses produced by the proposed analysis and 3D FD analysis which allows separation are larger than the rest. Further study about the influence of pile-soil separation is exhibited in the next section.

Table 1. Parameters for the soils and loads in the Examples

Example NO.	layer NO.	Extend of soil layers: m	Young's modulus, E_s : MPa	Poisson's ratio
1	1	0 to 2.0	20	0.35
	2	2.0 to 5.0	35	0.25
	3	5.0 to 8.3	50	0.2
	4	8.3 to ∞	80	0.15
2	1	0 to 1.5	20	0.35
	2	1.5 to 3.5	25	0.3
	3	3.5 to 8.5	40	0.25
	4	8.5 to ∞	80	0.2

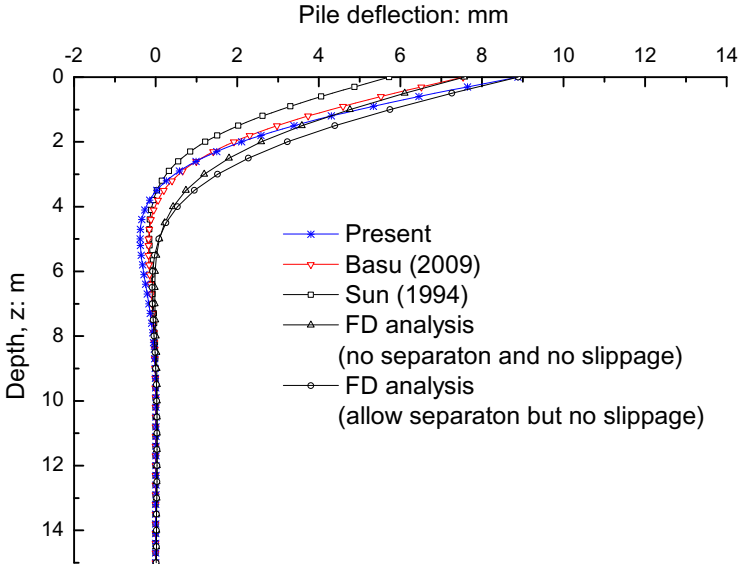


Fig. 4. Deflection profile of a 15m long pile

In order to compare the analysis with measured pile deflection, a lateral loading test on a 0.61m diameter pipe pile, reported by McClelland & Focht [29], is studied here. The pile has a length of 23m and was embedded in a normally consolidated clay. The bending rigidity of the test pile was 465 MN/m^2 giving an effective Young's modulus of $E_p = 68420 \text{ MN/m}^2$. Through the back-analysis of the measured pile deflection, Randolph [12] suggested that the soil shear modulus profile for the soil deposit can be represented as $G_s = 0.8z \times 10^3 \text{ kN/m}^3$ with Poisson's ratio of 0.3. For the purpose of comparing the analysis in this paper to the analysis of Basu [26], same soil properties are used here. The soil profile is divided into four layers and for each layer the shear modulus at the middle of the layer represents the shear modulus for the whole layer (Table 2). From the pile deflection presented in Fig.6, it can be concluded that the pile response produced by the analysis in this paper matches better to the measured data.

4 Effect of Pile-Soil Separation

To illustrate the effect of pile-soil separation on pile response, a comprehensive set of results has been calculated for comparisons between the proposed model and the origin model of Sun [23]. For linear elastic homogeneous soil foundation, Poulos [19] has given the solutions in terms of the slenderness ratio, L_p/d , and the dimensionless flexibility factor K_r , as

$$K_r = \frac{E_p I_p}{E_s L_p^4} \quad (21)$$

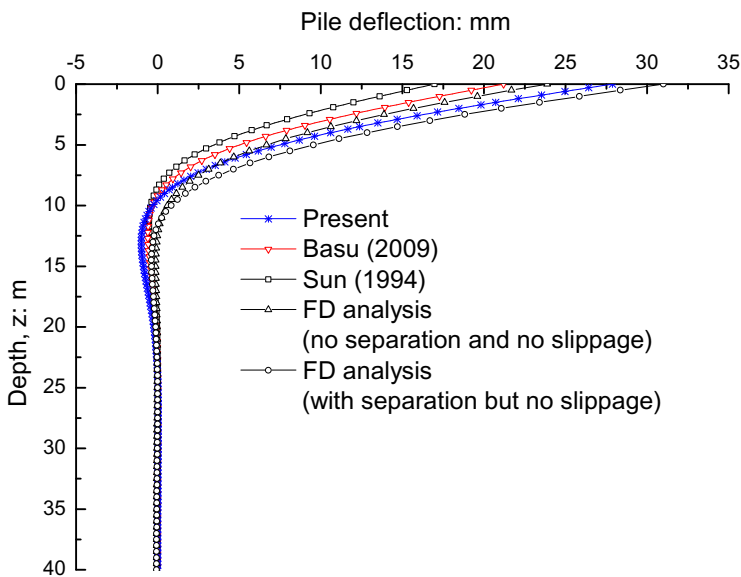


Fig. 5. Deflection profile of a 40m long pile

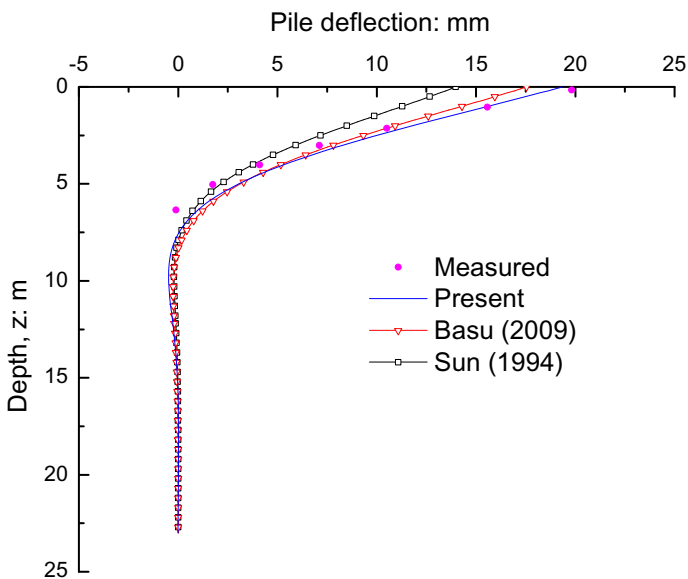


Fig. 6. Deflection profile for the pile load test of McClelland & Focht [29]

Table 2. Soil properties at the pile load test site of McClelland & Focht [29]

layer NO.	Extend of soil layers: Shear modulus, G_s :		
	m	MPa	Poisson's ratio
1	0 to 4.0	1.6	0.3
2	4.0 to 8.0	4.8	0.3
3	8.0 to 12.0	8.0	0.3
4	12.0 to ∞	14.0	0.3

The ground-line displacement of a free-head pile, $u(z = 0)$, can be expressed as

$$u(z = 0) = I_{uF} \frac{F}{E_s L_p} + I_{uM} \frac{M}{E_s L_p^2} \quad (22)$$

where I_{uF} , I_{uM} are elastic influence factors for displacement caused by horizontal load and moment, respectively.

For the cases of a pile having the slenderness ratio of 10, 25, 50 with the uniform Poisson's ratio $\mu = 0.3$ of the surrounded soil, the results of the displacement influence factors I_{uF} and I_{uM} are computed using both the proposed analysis and the analysis of Sun [23]. Values of I_{uF} and I_{uM} are shown as a function of the flexibility factor K_r in Fig.7 and Fig.8, respectively. Both I_{uF} and I_{uM} decrease as K_r increases, and trend to remain stable for relatively rigid piles ($K_r > 10^{-2}$). The effect of pile-soil separation on pile displacement is evident from the two figures, the values of I_{uF} and I_{uM} obtained from the proposed analysis is greater than those from Sun's analysis. And the difference of the two analysis seems to be more outstanding with a smaller slenderness ratio.

Another way to state the above conclusions is using the ratio of the displacement influence factors I_{uF} and I_{uM} calculated by Sun's analysis and the proposed analysis, I_S/I_p , given by:

$$I_S/I_p = \frac{I_{uF}(Sun)}{I_{uF}(proposed)} \text{ or } \frac{I_{uM}(Sun)}{I_{uM}(proposed)} \quad (23)$$

The values of I_S/I_p are displayed in Fig.9, also as a function of the flexibility factor K_r . Due to the influence of pile-soil separation, the ratio I_S/I_p is less than one. The effect of separation is more pronounced for more flexible piles ($K_r < 10^{-2}$). For relatively rigid piles ($K_r > 10^{-2}$), the ratio of the factor I_{uF} has a slight decrease with the increase of K_r while the ratio of the factor I_{uM} declines more significantly. The effect of the slenderness ratio L_p/d on I_S/I_p is also illustrated in Fig.9 that the pile-soil separation has a more significant influence with a smaller slenderness ratio. It is also presented in the figure that the ratio I_S/I_p is bigger than 0.5 unless the slenderness ratio is too small and the pile is extremely flexible. So in most condition it is conservative when consider the pile-soil separation by reducing the soil modulus by a factor of about 2.

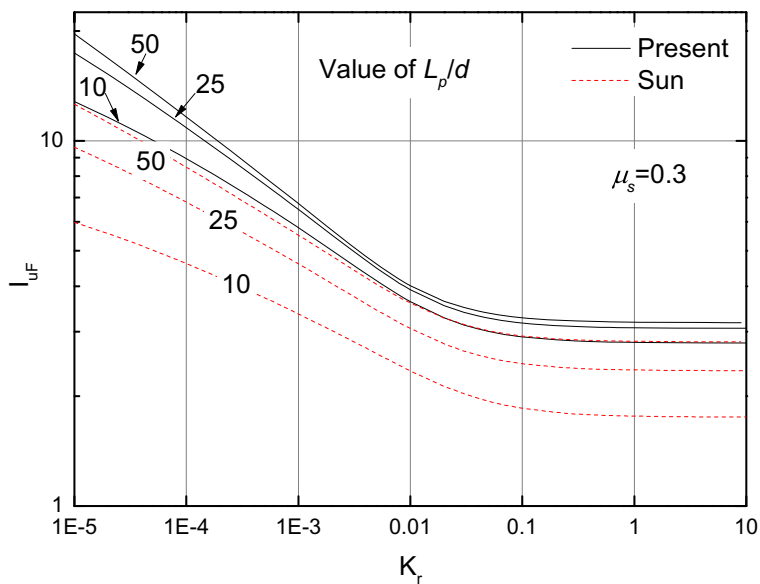


Fig. 7. Displacement influence factor I_{uF}

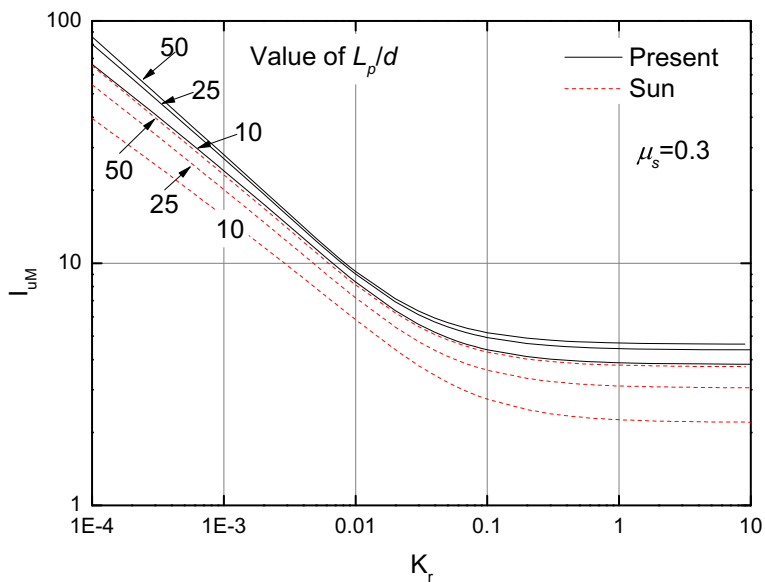


Fig. 8. Displacement influence factor I_{uM}

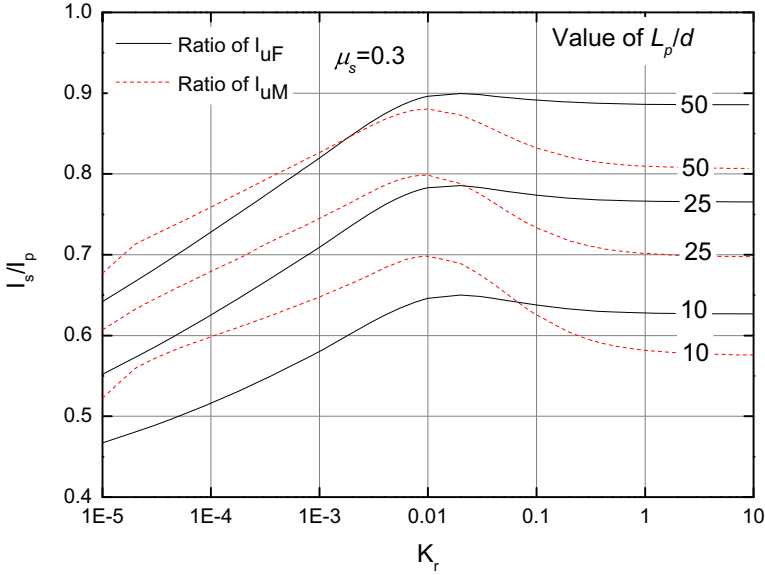


Fig. 9. The ratio of the displacement influence factors I_s/I_p

5 Conclusions

A pile-soil separation concerned continuum method is proposed to analyze the response of laterally loaded piles in a homogeneous elastic layered medium. Sun’s method is modified to consider the influence of pile-soil separation by using an ellipse instead of a circle to describe the soil boundary around the pile approximately. Variational principles are used to obtain the governing differential equations for the pile and soil displacements. Closed-form solutions are derived and the pile deflection, pile rotation, bending moment and shear force for the entire length of the pile can be obtained. The proposed approach has been verified by comparing with previous methods, 3D FD analysis and measured pile deflection. The impact of pile-soil separation is studied by calculating a comprehensive set of cases. It can be concluded that the deflection of pile is larger when pile-soil separation happens, and the effect can be reduced for piles with larger slenderness ratio and medium flexibility. Besides that, this method can be extended to consider the soil non-linearity with depth by dividing the soil layer into more sub layers with constant elastic modulus, and also the local yield near the ground-line.

Acknowledgements. The work was funded by National basic Research Program of China (973 Program) (No.2011CB710604), the National Natural Science Key Foundation Project of China (No.41230637), the National Natural Science Foundation Project of China (No.41302231), the Fundamental Research Funds

for the Central Universities of China(CUGL140408), the Chinese Post Doctoral Science Foundation Project (No.2012M521501 and 2013T60760).

References

1. Reese, L.C., Matlock, H.: Non-dimensional solutions for laterally-loaded piles with soil modulus assumed proportional to depth. In: Proceedings of 8th Texas Conference on Soil Mechanics and Foundation Engineering, Austin, Texas, pp. 1–41 (1956)
2. Matlock, H., Reese, L.C.: Generalized solutions for laterally loaded piles. *Journal of Soil Mechanics and Foundation Division. ASCE* 86, 63–91 (1960)
3. Reese, L., Cox, W.: Soil behavior from analysis of tests of uninstrumented piles under lateral loading. In: Proc. Seventy-first Annual Meeting, pp. 161–176. ASTM, San Francisco (1968)
4. Matlock, H.: Correlations for design of laterally loaded piles in soft clay. In: Proc. 2nd Offshore Technology Conference. TX1, Houston, pp. 577–594 (1970)
5. Reese, L.C., Cox, W.R., Koop, F.D.: Analysis of laterally loaded piles in sand. In: Proc. 6nd Offshore Technology Conference. TX2, Houston, pp. 473–783 (1974)
6. Reese, L.C., Cox, W.R., Koop, F.D.: Field testing and analysis of laterally loaded piles in stiff clay. In: Proc. 7nd Offshore Technology Conference. TX2, Houston, pp. 671–690 (1975)
7. Reese, L.C.: Analysis of laterally loaded piles in weak rock. *Journal of Geotechnical and Geoenvironmental Engineering* 123(11), 1010–1017 (1997)
8. Desai, C.S., Appel, G.C.: 3-D analysis of laterally loaded structures. In: Proc. 2nd International Conference on Numerical Methods in Geomechanics, Blacksburg, VA, pp. 405–418 (1976)
9. Bhowmik, S., Long, J.H.: An analytical investigation of the behavior of laterally loaded piles. In: Proc. Geotechnical Engineering Congress, ASCE, vol. 2(27), pp. 1307–1318 (1991)
10. Bransby, M.F.: Selection of p-y curves for the design of single laterally loaded piles. *International Journal for Numerical and Analytical Methods in Geomechanics* 23(15), 1909–1926 (1999)
11. Hsiung, Y., Chen, Y.: Simplified method for analyzing laterally loaded single piles in clays. *Journal of Geotechnical and Geoenvironmental Engineering* 123(11), 1018–1028 (1997)
12. Randolph, M.F.: The response of flexible piles to lateral loading. *Geotechnique* 31(2), 247–259 (1981)
13. Carter, J.P., Kuihawy, F.H.: Analysis of laterally loaded shafts in rock. *Journal of Geotechnical Engineering* 118(6), 839–855 (1992)
14. Higgins, W., Vasquez, C., Basu, D., Griffiths, D.: Elastic solution for laterally loaded piles. *Journal of Geotechnical and Geoenvironmental Engineering* 139(7), 1096–1103 (2013)
15. Ng, C.W.W., Zhang, L.M.: Three-dimensional analysis of performance of laterally loaded sleeved piles in sloping ground. *Journal of Geotechnical and Geoenvironmental Engineering* 127(6), 499–509 (2001)
16. Klar, A., Frydman, S.: Three-dimensional analysis of lateral pile response using two-dimensional explicit numerical scheme. *Journal of Geotechnical and Geoenvironmental Engineering* 128(9), 775–784 (2002)

17. Murff, J.D., Hamilton, J.M.: P-Ultimate for undrained analysis of laterally loaded piles. *Journal of Geotechnical Engineering* 119(1), 91–107 (1993)
18. Douglas, D.J., Davis, E.H.: The movement of buried footings due to moment and horizontal load and the movement of anchor plates. *Geotechnique* 14, 115–132 (1964)
19. Poulos, H.G.: Behavior of laterally loaded piles:1-single piles. *Journal of the Soil Mechanics and Foundations Division ASCE* 97(SM5), 711–731 (1971a)
20. Banerjee, P.K., Davies, T.G.: The behaviour of axially and laterally loaded single piles embedded in nonhomogeneous soils. *Geotechnique* 28(3), 309–326 (1978)
21. Davies, T.G., Budhu, M.: Nonlinear analysis of laterally loaded piles in heavily overconsolidated clays. *Geotechnique* 36(4), 527–538 (1986)
22. Budhu, M., Davies, T.G.: Analysis of laterally loaded piles in soft clays. *Journal of the Geotechnical Engineering Division ASCE* 114(1), 21–29 (1988)
23. Sun, K.: Laterally loaded piles in elastic media. *Journal of Geotechnical Engineering* 120(8), 1324–1344 (1994)
24. Zhang, L., Ernst, H., Einstein, H.H.: Nonlinear analysis of laterally loaded rock-socketed shafts. *Journal of Geotechnical and Geoenvironmental Engineering* 126(11), 955–968 (2000)
25. Guo, W.D., Lee, F.H.: Load transfer approach for laterally loaded piles. *International Journal for Numerical and Analytical Methods in Geomechanics* 25(11), 1101–1129 (2001)
26. Basu, D., Salgado, R., Prezzi, M.: A continuum-based model for analysis of laterally loaded piles in layered soils. *Geotechnique* 59(2), 127–140 (2009)
27. Poulos, H.G., Davis, E.H.: *Pile foundation analysis and design*. Series in geotechnical engineering. John Wiley and Sons (1980)
28. Guo, W.D.: Laterally loaded rigid piles with rotational constraints. *Computers and Geotechnics* 54, 72–83 (2013)
29. McClelland, B., Focht Jr., J.A.: Soil modulus for laterally loaded piles. *Transactions ASCE* 123, 1049–1063 (1958)

The Effect of Overconsolidation and Particle Shape on the CPT End Resistance of Granular Soils

Qingbing Liu¹, Wei Xiang¹, and Barry Michael Lehane²

¹ Three Gorges Research Center for Geohazard,
Ministry of Education, China University of Geosciences,
Wuhan, China

² School of Civil & Resource Engineering,
The University of Western Australia,
35 Stirling Highway, Crawley WA 6009, Australia
qingbing@cug.edu.cn, liuqingbing_1357@163.com

Abstract. This paper examines the effect of overconsolidation and particle shape on the end resistance (q_c) measured in a series of centrifuge Cone Penetration Tests (CPTs) conducted in three uniformly graded silica materials with distinct particle shape. For each soil type, the end resistances were measured for both normally and overconsolidated soil samples at centrifuge g-level of 100g. All samples were prepared and tested at two different relative density, and the over-consolidated samples were achieved by reducing the centrifuge g-level from 200g to 100g (with over-consolidation ratio, OCR=2). At a given relative density and stress level, the striking dependency of the CPTs end resistance (q_c) on the particle shape can be observed. For a particular material, a tendency for q_c value to increase with the OCR was in evidence. An approach based on the spherical cavity expansion method was proposed to predict the q_c value of each soil, and particularly to investigate how the OCR and particle shape influence on the end bearing resistance. It was found that the predicted q_c are shown to match the measured data well, and the end bearing resistances were significantly affected by the critical friction angle and horizontal stress, which were closely related to the particle shape and overconsolidation ratio.

Keywords: Particle shape, Centrifuge CPT, Cavity expansion method, Over-consolidation, Friction angle.

1 Introduction

The cone penetration test is widely used to assess the end resistance of driven pile in the granular materials. studies have been extensively conducted, aiming to propose the correlations between the CPT end resistance and the soil property indices such as the relative density, vertical stress, and stress history [1], [7], [11], [18, 19, 20]. However, there are significant discrepancies among these correlations. It is generally found that an increase in lateral stress (or overconsolidation ratio, abbreviation as

OCR) can cause q_c value to increase for a particular sand at a given relative density, e.g., [18] proposed the following expression

$$q_c^{OC} / q_c^{NC} = 1 + 0.75 [(k_o^{OC} / k_o^{NC})^{0.42} - 1] \quad (1)$$

where q_c^{OC} and q_c^{NC} are the cone tip resistance in overconsolidated and normally consolidated sand, respectively ; k_o^{OC} and k_o^{NC} are coefficient of the lateral earth pressure at rest in overconsolidated and normally consolidated sand, respectively. The Equation (1), derived from the chamber test data, provides a simple mean to evaluate the effect of stress history on the q_c value. However, [9] showed that Equation (1) overestimate the q_c^{OC} / q_c^{NC} by 20%-40% according to the bearing capacity theory. Further, [9] pointed out that the effect of high in-situ lateral stress caused by overconsolidation is offset by the low bearing capacity factors associated with a more localized failure surface based on the coupled DEM-BEM numerical analysis, and this eventually result in insignificant effect of OCR on the q_c value.

In spite of the above disagreement, the following expressions are currently widely applied to correlate the q_c value and relative density for overconsolidated sand [2], [11] as:

$$D_r = \frac{1}{C_0} \ln \left[\frac{q_c}{C_1 (\sigma'_m)^{C_2}} \right] \quad (2)$$

where σ'_m is the mean norm stress; the C_0 varies from 2.6 to 2.95 while C_1 varies from 180 to 2051; C_2 approximately equal to 0.5. The effect of loading history on q_c are embedded in σ'_m .

The Equation (2) was derived from the extensive chamber tests on ticino sand. However, errors may be expected to arise when it is applied to assess another sand deposit with dissimilar properties to Ticino sand. One such property is the soil particle shape, which is reported to greatly influence the mechanical characteristics such as compressibility and friction angle [4], [16]. Given the uncertainties surrounding the application of Equation (1)-(2) to quantify q_c values of over-consolidated sands with distinct particle shape, A laboratory centrifuge study were undertaken to examine the effect of particle shape and over-consolidation on the cone tip resistance. Three uniformly graded silica materials with various particle shapes are tested in drum centrifuge CPTs. The tests results are interpreted on the basis of cavity expansion method.

2 Granular Materials Investigated

Classification details of the three granular materials tested in this study are given in Table 1. All materials are uniformly graded (uniformity coefficient, $C_u = d_{60}/d_{10} < 1.4$) with mean particle sizes (d_{50}) ranging from 0.12mm to 0.45mm. The UWA-Sand is a

silica sand with a specific gravity (G_s) of 2.65 while the two other “soils” comprise glass particles with $G_s \sim 2.5$. Images of particles from each material are presented in Figure 1. On inspection, the SGB particles are spherical, whereas the UWA-sand and GB soils are more angular and irregular. Three types of particle shape parameters (i.e. Roundness (R), Sphericity (S) and regularity (ρ) = (R+S)/2) are provided in Table 1; further details concerning the measurement of these parameters can be found in [4] and [5].

Table 1. Index properties of three granular materials

Code	Gradation		Void ratio limits		Particle shape			G_s
	d_{50} :mm	C_u :	e_{max}	e_{min}	R	S	ρ	
UWA-Sand	0.15	1.4	0.81	0.52	0.7	0.62	0.66	2.65
SGB	0.12	1.05	0.75	0.51	1	1	1	2.52
GB	0.45	1.13	1.01	0.64	0.62	0.54	0.58	2.48

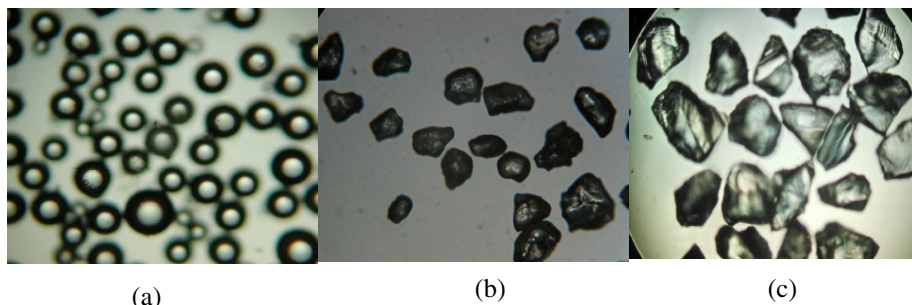


Fig. 1. Light microscope images of granular material used (a) SGB (b) UWA-sand and (c) GB

3 Centrifuge Cone Penetration Tests

3.1 Sample Preparation and Test Programme

Cone Penetration Tests (CPTs) were performed on each soil sample at dense and loose state. The g-level was set at 100g when conducting cone penetration in the drum centrifuge located in the University of Western Australia (technical details of this drum centrifuge referred to [17]).

Loose and dense samples ($Dr=0.2$ and $Dr=0.8$) were prepared in centrifuge strong boxes. For loose samples, the soil was poured into the box using an electrically

controlled bar-type hopper. Consistent loose packing was produced by maintaining a soil drop height of a 20mm, hopper travel speed of 5 mm/s and a hopper aperture opening of 0.5 mm. Care was taken to ensure that the sand surface remained level throughout the complete process. For dense samples, another box was attached to the top of the strongbox to allow loose sand to be placed to a high level. Samples were then densified by placing the strongbox on the vibrating table to achieve the required density.

All samples were saturated slowly by application of a differential water pressure of 0.5kPa (maximum) to a screw hole located at the centre of the base of the strong box. A geofabric were also placed at the base of the soil sample to minimize the disturbance during the saturation. Light suction was then applied to each sample to prevent its collapse while being placed sideways in the centrifuge before centrifuge spinning began. The box samples were firstly spinning at a low g-level (i.e. 50g) and re-saturated for approximately 2 hours prior to commencement of the CPTs. A pause period of at least two hours was also allowed prior to the cone testing at the g-level of 100g. After completing the first round testing at g-level of 100g, the soils were spined to a higher g-level of 200g and re-saturated for another 2 hours. The over-consolidated soils (OCR=2) was then tested in identical circumstances by reducing the g-level from 200g to 100g. The cone has a diameter of 5mm and was installed at a (drained) rate of displacement of 0.1mm/s in the whole process of testing.

3.2 CPT Results

The CPT test results are given in Fig.2, where cone resistance q_c versus model penetration depth were plotted for each soil at different relative densities and OCR. Typically, the cone resistance increases approximately linearly with depth within the first 50mm and then reaches a stage of slowing in the rate of increase. However, no obvious maximum “limiting” end bearing resistance can be seen. At a given depth (vertical stress), as expected, the q_c values increase with the sample relative density.

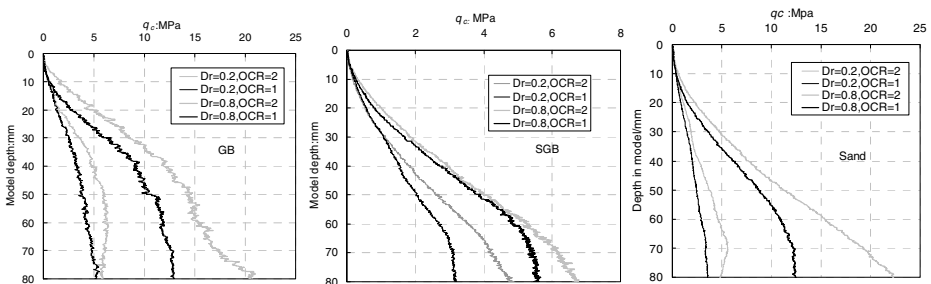


Fig. 2. CPT end resistances (q_c) observed in centrifuge tests

Furthermore, on inspection of Fig.2, it appears that following points applies:

1. For the same relative density and the same vertical stress (overburden pressure from a given penetration depth), the cone end resistance measured in normally consolidated sands is significantly lower than that measured in overconsolidated sands with OCR=2. The difference of q_c values between the normally consolidated and overconsolidated sands typically varies from 1 to 5Mpa for dense samples ($Dr=0.8$) and in the range of 1~3Mpa for loose samples ($Dr=0.2$).Such differences for more angular UWA-sand and GB particles are higher than those for the more rounded SGB particles.
2. The marked dependence of the q_c values on the soil type are in evident. At a given relative density and OCR, The lowest values of q_c are acquired by SGB while the higher values are recorded by UWA-Sand and GB. In view of the similar effective particle size recorded for SGB and UWA-Sand, It is reasonable to attribute this striking difference in q_c values to variations in the particle shape. The q_c values appear to increase with the particle irregularity, regardless of whether the soils are normally consolidated or overconsolidated.

4 Predicting the End Resistance Using Spherical Cavity Expansion Method

In view of the shape of failure model observed beneath a loaded pile tip in the granular soils, the spherical cavity expansion theory firstly proposed by [21] is widely accepted as analytical method for the prediction of the end bearing resistance of pile in the sands. Within the framework of spherical cavity expansion theory, the following equation suggested by [15] was normally adopted to link the limit cavity expansion pressure p_{limit} to the end bearing capacity q_c

$$q_b = p_{limit}(1 + \tan \phi' \tan \alpha) \quad (3)$$

It is assumed that the soil immediately beneath the cone tip has been sheared to its ultimate state, so the friction angles ϕ' should therefore be taken as critical state angle ϕ'_{cv} . the value of α equal to the that of cone angle, as being 60.

The limit expansion pressure for spherical cavity expansion in Equation (3) can be calculated by the expressions from [22], where the values for following input parameters are needed to carefully chosen :

- The in situ mean effective stress p_o , related to the σ'_v and K_o
- The friction angle ϕ' and dilation angle ψ for the sands
- The shear modulus G and possion ratio ν .

The evaluating procedure of these parameters for the three soils investigated in our study is expounded as follows:

(1) *Assessing the p_o* : the mean effective stress p_o is expressed as $\sigma'_v(1+2K_o)/3$. Based on the extensive laboratory tests, [14] suggested the following expression to correlate the K_o with friction angle ϕ' and OCR.

$$K_o = (1 - \sin\phi') (\text{OCR})^{\sin\phi'} \quad (4)$$

(2) *Assessing the ϕ' and ψ* : following the work of [3], the peak friction angle and dilation angle can be determined by linking critical state angle ϕ'_{cv} with the soil relative density and mean effective stress at failure. i.e.:

$$\phi' = \phi'_{cv} + 3I_R \quad (5)$$

$$\psi = 3.75 I_R \quad (6)$$

where the I_R was defined as the relative dilatancy index and expressed as:

$$I_R = 5D_r - 1 \quad \text{for } p' < 150 \text{ kPa} \quad (7a)$$

$$I_R = D_r [10 - \ln p'] - 1 \quad \text{for } p' > 150 \text{ kPa} \quad (7b)$$

Preliminary direct shear box tests results [12] showed that the ϕ'_{cs} is dependent on the soil particle shape, and a linear relationship between ϕ'_{cs} and particle regularity ρ was suggested as:

$$\phi'_{cs} \text{ (degrees)} = 40 - 15.3\rho \quad (8)$$

This expression implies the SGB has the lowest value of ϕ'_{cs} while the more angular GB acquired the highest value of ϕ'_{cs} among three soils.

In view of the very significant increase in stress level beneath a cone as the vertical stress increases from σ'_v to q_c , [8] suggest that the mean effective stress in E_q (7b) should be taken as the geometric mean of the σ'_v and q_c , i.e.

$$p' \approx \sqrt{q_c \sigma'_v} \quad (9)$$

(3) *The practical evaluation of G* : The shear modulus G usually can be derived from the small-strain testing. Many correlations has been proposed to express the G as a function of mean effective stress and either the void ratio or the relative density. The following correlation suggested by [13] proved valid for the silica sand.

$$G_0 / p_a \sim S \exp(C_1 D_r) (p'_o / p_a)^n \quad (10)$$

where parameter S is about 600, C_1 is 0.7 and n equal to 0.43. p_a is atmospheric pressure (100kPa). [15] suggested the value of S should been reduced for more compressible materials. [6] reported that the shear modulus for the SGB is approximately 50%

of the silica sand. Based on this, in the following calculation, the value of S in Equation (10) is taken as 300 for SGB. Furthermore, following the [4], who reported a decrease in particle regularity will lead to increase in the compressibility and decrease in the small-strain stiffness, the value of S is taken as 500 for GB with angular particles.

It needs to be emphasized that the cavity expansion solution is based on an idealized soil model, and the above correlations given for the shear modulus are limited by real behavior that values of the elastic parameters and the correlation index n are all affected by strain level. However, in spite of these limitations, this approach appears to be able to capture the significant effect of stress level on the traditional bearing capacity factor N_q and hence yield relatively realistic estimate of bearing capacity.

Taking the value of the passion ratio ν as to be 0.2, an iteration calculation can be formed using the Equations (1) to (10) to predict the variations of q_c value with vertical stress for each type of soil at different relative density. Prediction of q_c obtained from the cavity expansion method are compared with the measures q_c values in Fig 3. A few points of note were implied on view of the figure 3.

- (a) Although with some scatter, overall, the predicted values of q_c are in good agreement with measured ones. The difference between the predicted and measured q_c values are more striking at low penetration depth (low vertical stress). These differences are mainly due to the higher dilation angle occurring in the low stress levels using the equation (6). Besides, the prediction leads to greater curvature of the end-bearing profiles.
- (b) The predictions conform that the q_c values in overconsolidated soils are typically 13% higher than those in normally consolidated soils. This is approximately consistent with the measured values. [10] showed the marketed dependency of q_c value on the in suit horizontal stress, which is directly related to the k_o . The equation (4) implies higher value of k_o recorded for overconsolidated sand, and therefore the higher horizontal stress is expected to act on the cone tip.
- (c) The predicted data indicated that the “ q_c (OC) / q_c (NC)” is dependent on the soil type and appear to increase with the soil particle irregularity as SGB < UWA-sand < GB. This hierarchy may be attributed to the tendency for the ϕ'_{cs} to increase with particle irregularity (see Eq.8) because the values of ϕ'_{cs} greatly influence the values of ϕ' and k_o , both of which can produce significant effect on the q_c value in the spherical cavity expansion method. The tendency for measured “ q_c (OC) / q_c (NC)” to increase with the particle irregularity can also be observed when comparing data of the SGB with that of UWA-Sand. However, this tendency is indistinct between UWA-Sand and GB, which may be due to the effect of particle size.

It also can be seen from Fig.3 that the “ q_c (OC) / q_c (NC)” is also dependent on the stress level, and the values of “ q_c (OC) / q_c (NC)” increase with the depth. This dependency may arise due to the effect of stress level on the dilation angle and perhaps the stiffness of the soil. The equation (4) show the “ k_o^{OC} / k_o^{NC} ,” varies only with the friction angle for the soils at particular OCR. In view of these , to diminish the effect

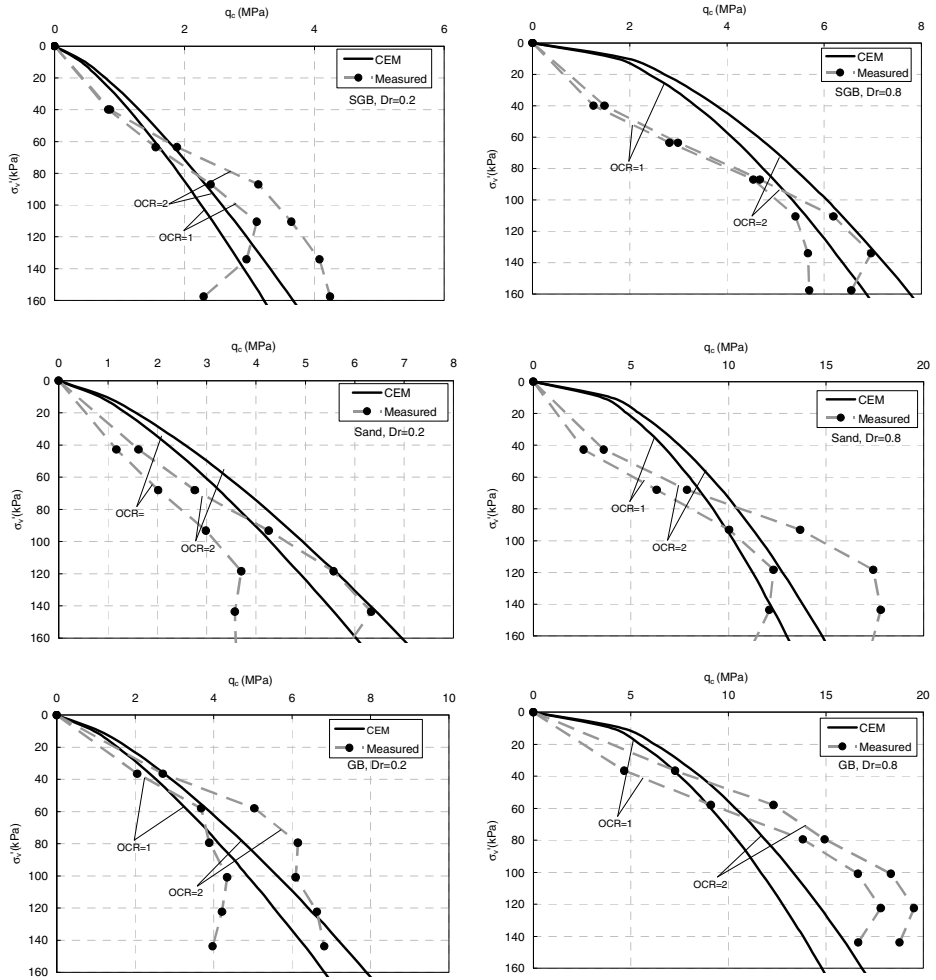


Fig. 3. The comparison of the measured q_c with the CEM predictions for both dense ($Dr=0.8$) and loose ($Dr=0.2$) samples

of dilation angle, the loose soils, of which friction angle approximately equal to the critical state angle, is examined to make a comparison of between “ q_c (OC) / q_c (NC)” from the Centrifuge test, CEM and the Equation (1). The comparison is shown in Fig.4, where the CEM produce the approximately same value for one particular soil in the whole range of depth. The tendency for the “ q_c (OC) / q_c (NC)” to increase with particle irregularity is clear in Fig.4, where both of the two predictions are lower than the measured ones. The best-fit expression to describe the variation of “ q_c (OC) / q_c (NC)” with overconsolidation ratio and particle shape may be concluded as follows:

$$q_c(OC)/q_c(NC) = 0.7(OCR)^{1.5/\exp(0.5p)} \tag{11}$$

It needs to be emphasized that this equation only provides a preliminary and rough description of the effect of the particle shape and OCR on the q_c values, and the actual variation of the “ q_c (OC) / q_c (NC)” with the depth (stress levels) has not been quantified exactly and needs to be studied further.

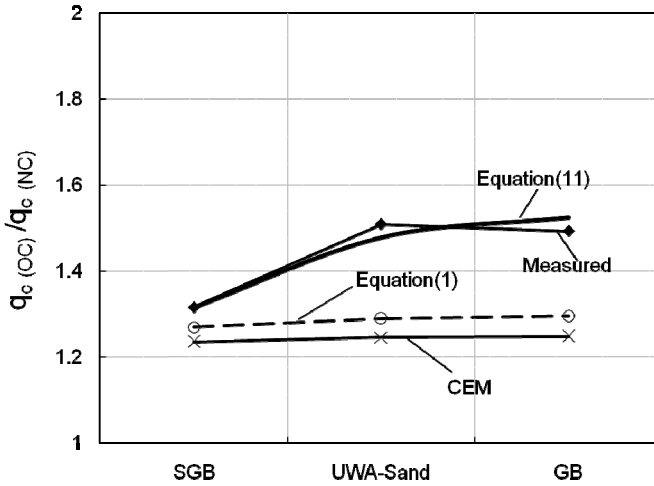


Fig. 4. Comparison of q_c (OC) / q_c (NC) using different methods

5 Conclusions

The effect of the particle shape and overconsolidation on the cone tip resistance is examined in the centrifuge tests. The q_c values in the overconsolidated soils is typically 13% higher than those in the normally consolidated soils. The ratio of the q_c in overconsolidated soils to that in normally consolidated ones is variable with the depth (stress levels) and particularly dependent on the particle shape. An approach based on the spherical expansion method is adopted to predict the q_c values. It can be concluded that the particle shape influence the q_c by the means of its effect on the critical state friction angle, and the over consolidated soils exert a higher in-situ horizontal stress surrounding the cone tip and therefore produce a higher q_c values. An equation (11) is finally proposed to approximately quantify the effect of the particle shape and overconsolidation on the cone tip resistance.

Acknowledgements. Funding for this research was provided by the National Natural Science Foundation of China (Grant No.41202199).

References

1. Baldi, G., Bellotti, R., Ghionna, V., Jamiolkowski, M., Pasqualini, E.: Design parameters for sands from CPT. In: de Ruiter, J. (ed.) Proceedings of the 2nd European Symposium on Penetration Testing, Amsterdam, May 24-27, vol. 2, pp. 425–432. A.A. Balkema, Rotterdam (1982)

2. Baldi, G., Bellotti, R., Ghionna, V., Jamiolkowski, M., Pasqualini, E.: Interpretation of CPT's and CPTU's 2nd part: Drained penetration of sands. In: Proc. 4th Int. Geotechnical Seminar, Singapore, pp. 143–162 (1986)
3. Bolton, M.D.: The strength and dilatancy of sands. *Geotechnique* 36(1), 65–78 (1986)
4. Cho, G.C., Dodds, J., Santamarina, J.C.: Particle shape effects on packing density, stiffness, and strength: natural and crushed sands. *Journal of Geotechnical and Geoenvironmental Engineering* 132(5), 591–602 (2006)
5. Cox, M.R., Budhu, B.: A practical approach to grain shape quantification. *Engineering Geology* 96(1-2), 1–16 (2008)
6. Chen, Y.J.: The Effect of Particle Shape and Grading on the Shearing Characteristics of Granular Materials, undergraduate honor's thesis. Faculty of Engineering, The University of Western Australia (2010)
7. Durgunoglu, H.T., Mitchell, J.K.: Static penetration resistance of soils. I. Analysis. 11. Evaluation of theory and implications for practice. In: Wahls, H.E. (ed.) Proceedings of the Specialty Conference in In-Situ Measurements of Soil Properties, ASCE, Raleigh, NC, June 1-4, vol. 1, pp. 151–189. ASCE, New York (1975)
8. Fleming, W.G.K., Weltman, A.J., Randolph, M.F., Elson, W.K.: *Piling engineering*, 3rd edn., pp. 98–101. Taylor & Francis, New York (2009)
9. Huang, A.B., Ma, M.Y.: An analytical study of cone penetration tests in granular material. *Canadian Geotechnical Journal* 31(1), 91–103 (1994)
10. Houlsby, G.T., Hitchman, R.: Calibration chamber tests of a cone penetrometer in sand. *Geotechnique* 38(1), 39–44 (1988)
11. Jamiolkowski, M., Ghionna, V.N., Lancellotta, R., Pasqualini, E.: New correlations of penetration tests for design practice. In: de Ruiter, J. (ed.) Proceedings of the 1st International Symposium on Penetration Testing, Orlando, Fla, pp. 263–296. A.A. Balkema, Rotterdam (1988)
12. Liu, Q.B., Lehane, B.M.: The influence of particle shape on the (centrifuge) cone penetration test (CPT) end resistance in uniformly graded granular soils. *Géotechnique* 62(11), 973–984 (2012)
13. Lo Presti, D.: Mechanical behaviour of Ticino sand from resonant column tests. Diss. Ph.D. thesis, Politecnico di Torino, Torino, Italy (1987)
14. Mayne, P.W., Kulhawy, F.H.: Ko-OCR Relationships in Soil. *Journal of the Geotechnical Engineering Division* 108(6), 851–872 (1982)
15. Randolph, M.F., Dolwin, J., Beck, R.: Design of driven piles in sand. *Geotechnique* 44(3), 427–448 (1994)
16. Santamarina, J.C., Cho, G.C.: Soil behaviour: the role of particle shape. In: *Advances in Geotechnical Engineering: The Skempton Conference*, vol. 1, pp. 604–617. Thomas Telford, London (2004)
17. Stewart, D.P., Boyle, R.S., Randolph, M.F.: Experience with a new drum centrifuge. In: Proc. Int. Conf. Centrifuge 1998, Tokyo, pp. 35–40 (1998)
18. Schmertmann, J.H.: Guidelines for cone penetration test performance and design. United States Federal Highway Administration Report FHWA-TS-78-209, Washington, DC (1978)
19. Tringale, P.T.: Soil investigation in-situ using an acoustic penetrometer. Ph.D. thesis, University of California at Berkeley, Berkeley (1983)
20. Vilet, W.C.B., Mitchell, J.K.: Cone resistance, relative density and friction angle. In: Norris, G.M., Holtz, R.D. (eds.) *Cone Penetration Testing and Experience*, Proceedings of the ASCE National Conventions, St. Louis, Mo, October 26-30, pp. 178–208. ASCE, New York (1981)
21. Vesic, A.S.: Expansion of cavities in infinite soil mass. *Journal of the Soil Mechanics and Foundations Division* 98(SM3), 265–290 (1972)
22. Yu, H.S., Houlsby, G.T.: Finite cavity expansion in dilatant soils: loading analysis. *Geotechnique* 41, 173–183 (1991)

Depositional Regularities Analysis of Incompetent Beds in Dam Foundation of Xiaonanhai Reservoir Using Markov Chain

Nie Qiong¹, Wei Xiang^{1,2}, and Du Shuixiang¹

¹ Faculty of Engineering, China University of Geosciences, Wuhan, China

² Three Gorges Research Center for Geohazard, Ministry of Education, China University of Geosciences, Wuhan, China

nieqiong520@hotmail.com,
xiangwei@cug.edu.cn,
adue1108@163.com

Abstract. Incompetent beds, which are composed of clastic rocks, are widely distributed in Upper Jurassic red strata in Sichuan Basin. These incompetent beds are prone to lead to the instability of Xiaonanhai Reservoir. The Markovian simulation results show that the semi-rhythmic structures of J_{3S}^{4-1} section are mainly of two types: one is siltstone and argillaceous siltstone alternation with great rhythmic thickness, the other is thin bedded argillaceous siltstone with interbedded mudstone. The incompetent beds are divided into three types: (I) cracked rock; (II) cracked rock with mud interbedded; (III) mudstone with cracked rock interbedded, or mudstone. Type I mainly exists in the thick mudstone or at the junction of thick mudstone and siltstone. Type II generally lies in the soft rock. Type III with more than 30% of clay, frequently appears in the second semi-rhythmic structure mentioned above.

Keywords: Engineering geology, Xiaonanhai Reservoir, Jurassic, Markov chain, incompetent beds, depositional regularity, stability.

1 Introduction

Red beds, which are composed of conglomerates, sandstones, siltstones, argillaceous siltstones and mudstones, exposed more than 460,000 square kilometers in China. They are common bedrocks in hydropower engineering projects [1]. Incompetent beds are prone to be formed in the interbedded sandstone and mudstone formation due to their high clay content, short geological age, weak cementation and low strength [2]. Incompetent beds are regarded as one of the primary engineering geological problems influencing on the stability against sliding of the dam abutment and the dam foundation. A majority of dam-break accidents occurred in red beds areas because of the regardless of the incompetent beds, such as the collapse of the St. Francis Dam [3], Bouzey Dam [4] and Tigra Dam [5].

Previous work on the incompetent beds has concentrated on the engineering properties. Wang [6] analyzed the mechanism of shear failure and strength value for different forms of incompetent beds. The correlations between physical and mechanical

indices and confining pressure were given by Fu [7]. Experimental methods for shear strength of the incompetent beds were discussed in detail [8, 9, 10]. However, only a limited number of publications have been focused on the sedimentary environment. Hu [11] and Li [12] point out that the formation of the incompetent beds is controlled by sedimentation environment and tectonic movement. Red beds are attributed to the lacustrine, fluvial and pluvial facies occurring since the Mesozoic and Cenozoic. Fluvial fining-upward cycles are obvious in such sedimentary rocks [1]. As is known, Markov chain analysis is a statistical technique for the detection of repetitive processes in space or time [13]. This method was used to interpret the results in considerable detail in terms of the evolution through time of the depositional mechanisms occurring in the given sedimentary basin [14, 15, 16]. However, the lithofacies in previous research were subdivided on the basis of lithology, grain size and cross-bedding, without considering the individual bed thickness.

In this paper, Markov chain analysis is applied to the stratigraphic succession in order to point out any depositional regularity of the incompetent beds in the dam foundation of Xiaonanhai Reservoir. Firstly, sedimentary environment of the strata in Upper Jurassic is analyzed in detail. And then take the strata of J_{3s}^{4-1} as an example, the simulation commences with transition count matrix, probability matrix, chi-square test and different matrix, which serve to emphasize vertical lithologic transitions in the given section. Individual bed thickness is taken full consideration in the Markov analysis. After that, considering the grain size, mudding degree and structure characteristics, the incompetent beds are divided into several types, and the depositional regularities of each type will be finally discussed.

2 Geological Setting

The Xiaonanhai Reservoir is a proposed dam on the Yangtze River in Chongqing, which is 40 km upstream of the city, and 700 km upstream from the Three Gorges Dam (Fig. 1). The study area is regarded as one of the most serious landslide hazard region in southwest China. The project is located between the northeast of the Longquan Mountain and the northwest of the Dalou Mountain, which is attributed to the second terrace of the Yangtze River and characterized by low-angle red beds. The area situated in the Guanyinxia anticline and Nanwenquan syncline, showing geological structures of folds, faults, fractures and shear zones. The deposits belong to the Upper Jurassic Suining Formation in Central Sichuan Basin and they are attributed to the fluvial and lacustrine facies. The total thickness of the Suining group is 471.1 m, which are subdivided into 6 sections (J_{3s}^1 – J_{3s}^6), J_{3s}^6 , J_{3s}^5 and J_{3s}^4 are the bedrocks of the dam foundation as shown in Table 1. The bedrocks are characterized by alternations of sandstone, siltstone, argillaceous siltstone and mudstone with veins of gypsum. Red siltstone with interbedded mudstone is particularly recognized in the strata of J_{3s}^4 . Incompetent beds present various lithologies, structures, thickness and lateral continuities because of the significant difference of physical-mechanical properties between the soft and hard rocks.

Table 1. Lithologies of dam foundation rock mass of Xiao Nanhai

Position	Thickness/m	Lithology description
J _{3s} ⁶	239.7	Very thick gray sandstone, thin red mudstone intercalated with thin to medium siltstone. Massive siltstone in the upper part. There are two layers of sandstone with 8 to 9 m thick in the middle, and 6 m sandstone in the lower part.
J _{3s} ⁵	19.3-34.0	Thick gray sandstone with laminated siltstone and mudstone.
J _{3s} ⁴⁻²	20.3	Interbedded red siltstone and mudstone. The thickness of each layer is 3 to 5 centimeters in the upper part, whereas the mudstone in the lower part is 20 to 30 centimeters thick.
J _{3s} ⁴⁻¹	105.2	Alternations with various thicknesses of red mudstone, argillaceous siltstone, siltstone and fine sandstone. Mudstone accounts for a greater percentage than siltstone.

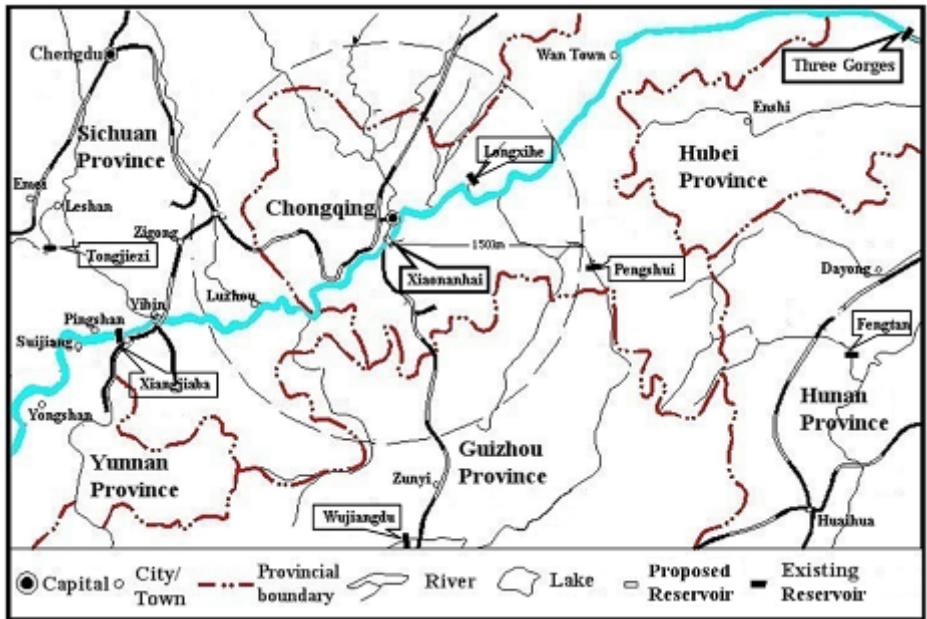


Fig. 1. Location of Xiaonanhai Reservoir

3 Sedimentary Environment

The Early Jurassic in Sichuan Basin was attributed to relatively stable lacustrine deposit. It changed to fluvial sediment until the Middle Jurassic. During the later period of the Middle Jurassic, the area of fluvial facies rapidly increased instead of lacustrine

facies, showing a group of Jurassic Shaximiao Formation which composed of green or gray thick sandstones and red mudstones. At the beginning of the Lower Jurassic, an estimated 300 to 500 m red fine clastic rocks were formed, dominated by the flood plains or intermittent lakes deposits [17].

Generally, sedimentary facies of the study area can be recognized based on lithological association, material composition, sedimentary structure, grain size and palaeobios. Thin section tests show that the red sandstones are poorly or medium sorted, subangular, and with low sphericity, showing diameters from 50 to 60 microns. Quartz is the most abundant with a percentage ranging from 90% to 95%. The second is feldspar accounts for 4% to 5%. Sedimentary lithics are less than 1%. Micas (biotite and muscovite) and heavy minerals are also rare or absent. The matrix content is below 5% and is mainly composed of clay minerals. Grain size and clay content are two crucial factors for the formation of incompetent beds. In this study, fine-grained sediments are analyzed and the results are given in Table 2.

Table 2. Grain size and clay content of fine-grained deposits in the study area

Lithology	Grain size / μm	Clay content (<5 μm) /%
argillaceous siltstone	11-15	24.39-31.85
silt mudstone	5-8	36.31-49.80
mudstone	3-4	60.58-63.91

Five vertically repeated cyclothem are recognised in the strata of J_{3s}^6 - J_{3s}^4 . A cyclical variation is normally 10 metres thick. The lower part is mainly composed of thick sandstones with large-scale through cross-bedding. In the minority, pebbly sandstone units may be found at the bottom. Fine-grained deposits in the higher part show greater thickness and normally contain siltstones and mudstones. Small-scale cross-bedding or horizontal laminations are developed in siltstones, as well as rootlets in mudstones. The succession is interpreted to be fluvial facies, dominated by the point bar and flood plain (basin) sub-facies. However, channels and levee deposits are rarely found in this area.

4 Method

As observed, incompetent beds are prone to be formed in a stratigraphic section, which is composed of various thin beds on account of fluctuating changes in conditions of deposition and in the nature and supply of sediment. Taking the strata of J_{3s}^{4-1} as an example, the given succession is under the control of Markovian process. This method comes to be applied to geological problems to point out subtle relationships in the given succession that would not otherwise be noticed or intuitively sought out. A Markov process is one 'in which the probability of the process being in a given state at a particular time may be deduced from knowledge of the immediately preceding

state' [18]. Markov chain analysis commences with transition count matrix, probability matrix, different matrix and chi-square test, which serve to emphasize vertical lithologic transitions. Procedures are described in detail as follows:

1. Subdivide lithotypes into several states. Andrew [13] noted that there were two different methods available for sampling a stratigraphic section: one is by counting only discrete lithofacies, regardless of individual bed thickness and the other is by sampling at fixed vertical intervals. The author also noted that too few or too many states would obscure or distort the results, from four to six states appear to be ideal.
2. The starting point in Markov chain analysis is the transition count matrix. This is a two-dimensional array which tabulates the number of times that all possible vertical lithologic transitions occur in the given stratigraphic succession. The upper bed of each transition couplet is given by the row number of the matrix, and the lower bed by the column number. Elements in this matrix are hereafter referred to by the symbol M_{ij} , where i = row number and j = column number. It will be noted where $i = j$ zeros are present in the matrix, i.e. transitions have only been recorded where the lithofacies shows an abrupt change in character.
3. From the transition matrix an independent trials probability matrix can be derived. This matrix is composed of E_{ij} , which represents the probability of the given transition occurring randomly. Given any state i the probability of this state being succeeded by any other state j is dependent only on the relative proportions of the various states present.

$$E = E_{ij} = \frac{T_j}{N - S_i}, \quad S_i = \sum_{j=1}^n M_{ij}, \quad N = \sum_{i=1}^n \sum_{j=1}^n M_{ij}.$$

where N is the total number of beds, and T_j is the sum of the M_{ij} for the j th column of matrix M . However, $i = j$ transitions are not permitted, and the total range of possibilities must be set to exclude them..

4. Actual transition probability matrix, containing elements P_{ij} , gives the actual probabilities of the given transition occurring in the given section:

$$P = M_{ij}/S_i$$

The values in the P matrix sum to unity along each row and they will necessarily reflect the presence of any Markovian dependency relationship.

5. Matrix P is also useful to construct a difference matrix D_{ij} , derived thus:

$$D = D_{ij} = P_{ij} - E_{ij}$$

Positive entries in the D matrix serve to emphasize the Markov property by indicating which transitions have occurred with greater than random frequency. Values in each row of the D matrix sum to zero.

6. The nature of the cyclic process can be derived by through the highest values of the P matrix or the positive values in the D matrix. Values that less than 0.1 will be ignored in this paper. The principal transition paths would be recognized from the figure of facies relationships.

7. Although the differences between the *P* matrix and the *E* matrix may seem to be considerable, the differences themselves may be due to random chance, and thus it is important to apply tests of significance to the results. A chi-square test is suitable for the purpose. A formula is given by Harbaugh & Bonham-Carter [18] and Anderson & Goodman [19]:

$$\chi^2 = 2 \sum_{i=1}^n \sum_{j=1}^n M_{ij} \ln(p_{ij}/p_j), \quad p_{ij} = \frac{T_j}{N}$$

This statistic has $(n-1)^2$ degrees of freedom. Null hypothesis is that the vertical succession of strata was derived by random variation in the depositional mechanisms. It is important to ensure the size of the sample conforms to the normal statistical rules concerning sample validity and the repeatability of the results.

5 Results

5.1 Markov Chain Analysis of J_{3s}^{4-1}

In this paper, state-variables are set up by subdividing lithotypes on the basis of color, presence, and cross-bedding. They are designated alphabetically as A, B, C, D, and E. However, bed-thickness is an essential factor reflecting the scale and rate of the sediments. Individual bed-thickness of the sediments is divided into two categories here: one is greater than 5 cm, named as C1, D1, or E1, and the other is less than or equal to 5 cm, named as C2, D2, or E2. State-variables are counted and listed in Table 3. The total thickness of J_{3s}^{4-1} is 45.76 m, including 59 bed transitions.

Table 3. State-variables of J_{3s}^{4-1}

Thickness /cm	State-variables					Total
	A	B	C	D	E	
	1	1	17	25	16	60
>=0.5	1	0	11	12	4	28
<0.5	0	1	6	13	12	32

The geological significance of each state is interpreted as follows:

- A: variegated pebbly sandstones distribute as bands under the thick gray sandstones. The pebbles are 4 to 5 centimeters in diameter, with the color of red, gray and yellow. Generally, they are the products of waning flow in the river channel. The layers overlying commonly belong to the point bar deposits.
- B: gray or red sandstones with great thickness and small proportion of clay. They are attributed to the point bar subfacies, which show a fining-up from coarser

sandstone at the base to finer at the top, as well as larger scale cross-bedding at the base and smaller sets of cross-lamination nearer to the top.

- C: red fine sandstones or siltstones. C1 are widely distributed on the floodplains, between or beyond the channels. The overbank deposits consists mainly of finer-grained sediment with small scale cross-bedding and current ripple or horizontal lamination. C2 are observed in both the floodplain and levee deposits, which are characterized by alternation of thin silt- and clay- sized debris.
- D: red argillaceous siltstones deposited in the floodplain subfacies. The physical and mechanical properties of D1 are weaker than that of C1 because of the high clay content ranging from 24.39% to 31.85%. D2 constantly exists between siltstones and argillaceous siltstones.
- E: red mudstones. During the periods of flooding, muddy sediments will be carried by river flow to the low-lying areas away from the channels and deposit for several meters. Deposits like E1 are formed stably in such situation because the clay is cohesive and cannot be easily eroded. Sheets of mudstones like E2 deposited during floods are close to the channel edge because coarser suspended load is dumped quickly by the floodwaters as soon as they start flowing away from the channel. Repeated deposition of sandstones and mudstones leads to the formation of levee. With more than 60% of clay, the mudstones lying between the permeable sandstones would be prone to form muddy shear zones under the tectonic process.

The transition count matrix is shown in Table 4. A1 and B1, the coarsest particles deposited at the base of the succession, are only presented once in the given strata, overlying by D2. Transitions from D2 to E2 show up the most, which are recorded six times, and the second-most cases are from C1 to D1 with five times. Independent trials probability matrix, actual transition probability matrix, difference matrix, positive value of difference matrix for the given data calculated from the M matrix are presented in Tables 5, 6, 7 and 8. Chi-square test results are given in Table 9, and the presence of the Markov property in these strata is clearly indicated.

Table 4. Transfer count matrix *M*

	A	B	C1	C2	D1	D2	E1	E2
A	0	0	0	0	0	1	0	0
B	0	0	0	0	0	1	0	0
C1	0	0	0	0	5	1	2	2
C2	0	0	0	0	3	2	0	1
D1	1	0	5	3	0	0	0	3
D2	0	1	4	0	0	0	2	6
E1	0	0	0	0	2	2	0	0
E2	0	0	2	3	1	6	0	0

Table 5. Independent trials probability matrix E

	A	B	C1	C2	D1	D2	E1	E2
A	0	0.02	0.19	0.10	0.19	0.22	0.07	0.21
B	0.02	0	0.19	0.10	0.19	0.22	0.07	0.21
C1	0.02	0.02	0	0.12	0.22	0.27	0.08	0.25
C2	0.02	0.02	0.21	0	0.21	0.25	0.08	0.23
D1	0.02	0.02	0.23	0.13	0	0.28	0.09	0.26
D2	0.02	0.02	0.24	0.13	0.24	0	0.09	0.26
E1	0.02	0.02	0.20	0.11	0.20	0.24	0	0.22
E2	0.02	0.02	0.23	0.13	0.23	0.28	0.09	0

Table 6. Actual transition probability matrix P

	A	B	C1	C2	D1	D2	E1	E2
A	0	0	0	0	0	1.00	0	0
B	0	0	0	0	0	1.00	0	0
C1	0	0	0	0	0.50	0.10	0.20	0.20
C2	0	0	0	0	0.50	0.33	0	0.17
D1	0.08	0	0.42	0.25	0	0	0	0.25
D2	0	0.08	0.31	0	0	0	0.15	0.46
E1	0	0	0	0	0.50	0.50	0	0
E2	0	0	0.17	0.25	0.08	0.50	0	0

Table 7. Difference matrix D

	A	B	C1	C2	D1	D2	E1	E2
A	0	-0.02	-0.19	-0.10	-0.19	0.78	-0.07	-0.21
B	-0.02	0	-0.19	-0.10	-0.19	0.78	-0.07	-0.21
C1	-0.02	-0.02	0	-0.12	0.28	-0.17	0.12	-0.05
C2	-0.02	-0.02	-0.21	0	0.29	0.09	-0.08	-0.06
D1	0.06	-0.02	0.18	0.12	0	-0.28	-0.09	-0.01
D2	-0.02	0.06	0.07	-0.13	-0.24	0	0.07	0.20
E1	-0.02	-0.02	-0.20	-0.11	0.30	0.26	0	-0.22
E2	-0.02	-0.02	-0.07	0.12	-0.15	0.22	-0.09	0

Table 8. Positive value of difference matrix *D*

A	(A, D2)=0.78	
B	(B, D2)=0.78	
C1	(C1, D1)=0.28	(C1, E1)=0.18
C2	(C2, D1)=0.29	
D1	(D1, C1)=0.18	(D1, C2)=0.12
D2	(D2, E2)=0.20	
E1	(E1, D1)=0.30	(E1, D2)=0.26
E2	(E2, D2)=0.22	(E2, C2)=0.12

Table 9. Test of significance

Test equation	χ^2	d.f.	Limiting value ¹
8	73.3	49	67.5

The principal transition paths of J_{3s}^{4-1} are shown in Fig.2. The fluvial fining-upward cycle appears as from pebbly sandstone or sandstone to argillaceous siltstone. In a fluvial system, the fining-upward cycles are originated by debris floods sweeping across the pediment surface and create new channels. Waning flow plus the process of lateral accretion acting during periods of more normal, quieter run-off, then combined to deposit beds of successively finer grain size, until the next flood altered the channel pattern once again [20]. Actually, several pebbly sandstone beds observed in the research area could not be fitted into a fining-upward cycle, and these were interpreted as the deposits of debris floods that did not result in the establishment of new channel system, so that once the flood had passed, the original fluvial pattern re-established itself.

The facies relationships also show that the semi-rhythmic structures of J_{3s}^{4-1} are mainly of two types:

- siltstone (C1 and C2) interbedded with thick argillaceous siltstone (D1), showing great rhythmic thickness;
- thin alternations of argillaceous siltstone(D2) and mudstone (E2).

¹ From table of chi-square values with correct number of degrees of freedom, at 5% confidence level.

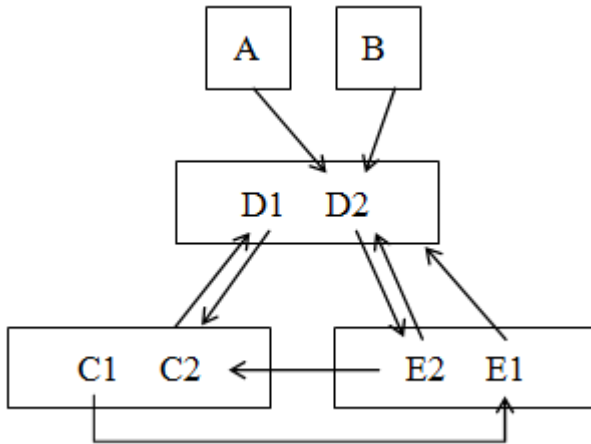


Fig. 2. Facies relationships in J_{3s}^{4-1}

5.2 Classification and Depositional Regularities of Incompetent Beds

Field investigations show that the incompetent beds are acted upon by a set of compressive tectonic forces. Original structures of rocks are destroyed by suffering the physical-chemistry effects: (1) more and more cracks are formed during multiple-period tectonic processes; (2) broken fragments are grounded into finer grained particles, even into powders because of the mechanical frictions; (3) clay minerals are increasingly generated and forming muddy materials under the action of groundwater. As a result, the binding property of the particles reduced, which eventually led to shear failure. Actually, the mineral compositions of these strata make little difference, however, incompetent beds contain much more clay than surrounding rocks. With a thickness ranging from a few centimeters to tens of centimeters, the incompetent beds normally grade from siltstone to mud and may extend for tens to hundreds of meters. Their structure characteristics and depositional regularities are different since they exist in different part of the layers.

In this study, 66 samples are taken from an outcrop of the left bank. Considering the lithology, grain size, mudding degree and depositional structure, incompetent beds are divided into three types: (1) cracked rock; (2) cracked rock with mud interbedded; (3) mudstone with cracked rock interbedded, or mudstone. They are described respectively as follows:

- Type 1: Cracked rocks refer to the fracture zone caused by the shear failure along the interfaces of soft and hard rocks. A continuously undulated shear surface would be formed by massive micro-cracks, as shown in Fig.3 (a). The amplitude of the undulation ranges from a few millimeters to several centimeters. Joints and cleavages with spacing of a few centimeters are perpendicular to the main shear surface, some of which are filled with mud. Field observations reveal that nearly one third of the incompetent beds belong to the first type. Most of them are frequently formed at the junction of siltstones (C1 or C2) and thick argillaceous siltstones (D2), as described

in the first semi-rhythmic structures of J_{3s}^{4-1} . The rest of them exist in E1 (thick mudstones), which is attributed to the flood basin sub-facies. As a result, such incompetent beds distribute discontinuously and cannot extend long distance.

- Type 2: Cracked rocks with mud interbedded are generally formed in E1, as shown in Fig.3 (b). Differing from type 1, they suffer more mechanical frictions and effects of groundwater. A sheet of mud with scratches is common on the top and bottom of the incompetent beds. Clasts are mainly composed of fine-grained materials, such as argillaceous siltstones and mudstones, the clay content (grain size smaller than 5 microns in diameter) of which is less than 10%.
- Type 3: This type of incompetent beds can be subdivided into two categories based on the clay content and mudding degree. (1) The first is mudstone with cracked rock interbedded as shown in Fig.3 (c). Clasts are surrounded by massive mud with the clay content ranging from 10% to 30%. (2) The second with more than 30% of clay, is completely composed of mudstones (Fig.3 (d)). Because of the high permeability of the sandstones, an estimated 1 to 5 mm continuous muddy surface can easily be formed under the effect of groundwater. Both types frequently appear in



(a) 3SZ303



(b) 3SZ104



(c) 3SZ405



(d) 3SZ406

Fig. 3. Classification of incompetent beds

the thin alternations of argillaceous siltstone (D2) and mudstone (E2), exactly as the second semi-rhythmic structure mentioned above. The thickness of the rhythmic layer ranges from 0.05 m to 1.48 m. However, the thicker the rhythmic beds are, the more often incompetent beds could be formed.

In most cases, a sliding surface will be formed by a connection between a gentle-dip incompetent bed and an anti-dip crack downstream, or by several individual incompetent beds. Both situations are detrimental to the local stability of the dam foundation.

6 Conclusions

The study has shown how Markov chain has assisted in clarifying lithofacies relationships by defining these relationships statistically. Based on Markov analysis, the depositional regularities of the incompetent beds have been studied and the following conclusions can be drawn:

1. The strata studied are attributed to the floodplain deposition. Thick-bedded fine-grained particles are widely distributed, providing sufficient materials for the formation of incompetent beds.
2. The analysis of Markov chain shows that the semi-rhythmic structures of J_{3s}^{4-1} are mainly of two types. (1) One is siltstone interbedded with thick argillaceous siltstone, showing great rhythmic thickness. As water leaves the confines of the channel it spreads out and loses velocity very quickly, the drop in velocity prompts the deposition of the sandy and silty suspended load, leaving only clay in suspension. (2) The other is thin alternations of argillaceous siltstone and mudstone. Thin sheets of such sediments are often only a few centimetres thick, but extending for tens to hundreds of metres.
3. Incompetent beds are formed under specific sedimentary environment. They present in various shapes and properties by suffering multiple-period tectonic processes and physical-chemistry effects. In this paper, incompetent beds are divided into three types: (1) cracked rocks; (2) cracked rocks with mud interbedded; (3) mudstones with cracked rocks interbedded, or mudstones.
4. Type 1 is frequently formed at the junction of siltstones and thick argillaceous siltstones, or in thick mudstones. Massive joints and cleavages are densely distributed close to the main shear surface. Type 2 suffers more mechanical friction and effect of groundwater than type 1. More sheets of mud can be recognized on the top and bottom of such incompetent beds. Type 3, with more clay content, frequently appears in the thin alternations of argillaceous siltstone and mudstone. A set of continuous muddy surfaces can easily be formed under the effect of groundwater, which may negatively influence the stability of the dam foundation.

Acknowledgment. This paper is the result of long-time field work completed by the research group of Dr. Prof. W. Xiang at the China University of Geosciences. Thanks to the colleagues and friends for their useful comments. Finally, we would like to thank the Yangtze River Water Resources Commission for their co-operation that makes the study possible.

References

1. Xv, R.C., Zhou, J.J.: Red bed and dam, pp. 4–6. China University of Geosciences Press, Wuhan (2010)
2. Jian, W.X., Wang, Z.J., Yin, K.L.: Mechanism of the Anlesi landslide in the Three Gorges Reservoir, China. *Engineering Geology* 108, 86–95 (2009)
3. Doyce, B.N., Charles, N.J.: The St. Francis Dam Disaster Revisited. *Historical Society of Southern California* 182 (1995)
4. Norman, A.F.S.: The Failure of the Bouzey Dam in 1895. *Construction History* 10, 47–65 (1994)
5. Valdiya, K.S.: *Geology, Environment and Society*, p. 178. Universities Press (2004)
6. Wang, X.F., Nai, L.: The character of strength and the failure mechanism of clay intercalary strata. *Journal of Changchun College of Geology* 4, 90–97 (1984)
7. Fu, W.X., Nie, D.X., Shang, Y.Q., Chen, Y.M.: Study on engineering properties of weak layers under ground stresses. *Chinese Journal of Geotechnical Engineering* 24, 584–587 (2002)
8. Jiang, M.J., Shen, Z.J.: Microscopic analysis of shear band in structured clay. *Chinese Journal of Geotechnical Engineering* 20, 102–108 (1998)
9. Ma, G.Y., Gao, G.L.: Distribution of the clay intercalation in the Xiaolangdi dam and experimental method of shear strength. *Journal of Engineering Geology* 8, 94–99 (2000)
10. Yu, X.H., Nie, D.X., Zhou, H.F.: Study on strength parameters of soft interlayer for large and small direct shears. *Journal of Engineering Geology* 14(suppl.), 126–129 (2006)
11. Hu, T., Ren, G.M., Nie, D.X., Tang, L.Q., Xiang, G.F.: The Chinese Journal of Geological Hazard and Control. *The Chinese Journal of Geological Hazard and Control* 15, 124–128 (2004)
12. Li, S.D., Li, X., Zhang, N.X., Liao, Q.L.: Sedimentation characteristics of the Jurassic sliding-prone stratum in the Three Gorges Reservoir area and their influence in physical and mechanical properties of rock. *Journal of Engineering Geology* 12, 385–389 (2004)
13. Andrew, D.M.: Markov chain analysis applied to an ancient alluvial plain succession. *Sedimentology* 20, 347–364 (1973)
14. Gong, Y.M.: The Quantitative analysis of historical sedimentology for lithofacies successions. *Earth Science – Journal of Wuhan College of Geology* 12, 613–620 (1987)
15. Wang, Q.L., Li, C.G.: Markov chain in quaternary sedimentary environment of Jiangnan plain. *Geological Science and Technology Information* 27, 38–46 (2008)
16. Zhang, C.F., Lv, H.B., Xia, B.D., Fang, Z.: Markov chain simulation on the rhythmic sequences of Middle Triassic flysch in Nanpanjing basin, SW China. *Geological Review* 57, 632–640 (2011)
17. Dong, S.W., Zhang, Y.Q., Long, C.X., Yang, Z.Y., Ji, Q., Wang, T., Hu, J.M., Chen, X.H.: Jurassic tectonic revolution in China and new interpretation of the “Yanshan Movement”. *Acta Geologica Sinica* 82, 334–347 (2008)
18. Harbaugh, J.W., Bonham-Carter, G.: *Computer Simulation in Geology*. R.E. Krieger Pub. Co., 575 Seiten (1981)
19. Anderson, T.W., Goodman, L.A.: Statistical inference about Markov Chains. *Ann. Math. Statist.* 28, 89–110 (1957)
20. Nichols, G.: *Sedimentology and stratigraphy*. SPi Publisher Services, 419 Seiten, Pondicherry (2009)

Physically – Based Critical Rainfall Thresholds for Unsaturated Soil Slopes

Diana Salciarini and Claudio Tamagnini

Dipartimento di Ingegneria Civile e Ambientale, University of Perugia, Perugia, Italy
{diana.salciarini,claudio.tamagnini}@unipg.it
<http://www.dica.unipg.it>

Abstract. In this work, a physically based model for the definition of the critical rainfall thresholds for shallow landslide initiation at regional scale is presented. The model is capable of considering unsaturated conditions in the soil volume, by taking into account the effect of partial saturation in: a) the balance of mass for the pore water; b) the deformability of the solid skeleton; and, c) the soil shear strength. Starting from the simplified hypothesis of infinite slope, a series of numerical simulations was conducted in parametric form to determine the functional relationship between the critical rainfall intensity leading the slope to failure to rainfall duration, in terms of dimensionless variables. This has allowed to identify the functional dependence of the critical rainfall intensity on: a) event duration; b) slope geometry; c) mechanical properties of the soil cover; and, d) initial conditions in terms of pore water pressure distribution. The function thus obtained can be easily and efficiently implemented in GIS-based codes for the evaluation of physically-based, spatially-distributed critical rainfall thresholds.

Keywords: rainfall thresholds, shallow landslides, unsaturated soils, physically-based models.

1 Introduction and Motivations

Rainfall-induced shallow landslides, triggered by heavy rainstorms, represent a major issue in the evaluation of landslide hazard at the territorial scale. Starting from the pioneering work by [1], many Authors observed a clear correlation between shallow landslide occurrence and the characteristics of rainfall events, in terms of intensity and duration (see, *e.g.*, [2–4]). For this reason, an important aspect of the quantitative evaluation of the hazard related to shallow landslides is the assessment of the critical threshold of landslide initiation, defined as the minimum rainfall (in terms of intensity and duration) able to trigger the instability process.

Rainfall conditions that lead a slope to the limit equilibrium can be determined by means of empirical approaches or physically-based approaches. In empirical approaches, the intensity–duration thresholds are defined as power-law relations between the minimum values of the rainfall rate, q_z , and the corresponding duration, t_d , recorded during actual shallow landslides. Despite the

widespread use of such empirical approaches (see, *e.g.*, [5–7]), they present several intrinsic limitations. In particular, they are not capable of considering several key factors in the instability processes, such as:

- topographical and morphological characteristics of the slopes;
- physical and mechanical properties of the soil (unit weight, degree of saturation, shear strength, deformability, permeability);
- ratio between rainfall duration and characteristic time of the infiltration process.

To overcome such limitations in the definition of the critical rainfall thresholds, physically-based (PB) approaches have been recently developed (see, *e.g.*, [8, 9, 3, 10]). In general, such approaches couple a simplified mechanical model to evaluate the stability condition of the slope (based on the infinite slope hypothesis) with a hydraulic model to analyze the space-time evolution of the pore pressure within the soil volume. In particular, the physically-based model for the deterministic evaluation of $q_{z,crit}$ proposed by [10] is based on the following assumptions:

- a) limited soil thickness with respect to the slope length and constant slope angle;
- b) failure surface parallel to the topographic surface and at the contact between soil cover and bedrock;
- c) bedrock much less permeable than the soil cover (*i.e.*, treated as impervious);
- d) soil cover fully saturated; and,
- e) uniform rainfall intensity in space and time.

Under these assumptions, the infiltration process is governed by a diffusion equation, which admits a closed-form analytical solution [4].

The hypothesis of full saturation can be appropriate for wet regions, and/or fine-grained soil covers, for which surface tension at the water-air interface allows to maintain full saturation of the solid skeleton even in presence of high suction values. However, in dry climates and for coarse-grained soil covers, the degree of saturation S_r may be well below unity. In practice, the occurrence of low degrees of saturation in the superficial part of the slope is often neglected, both because of the increased complexity of the problem, and because considering a slope in fully saturated condition is on the safe side. However, it is now widely recognized that in slope stability analyses suction plays an important role, particularly in the initiation mechanism. For example, it is well known that prolonged rainfalls provoke a rapid drop of suction in the uppermost layer of soils with a consequential reduction of shear strength up to failure. In addition, the reduction of the degree of saturation of the soil affects significantly the infiltration process, as soil permeability strongly decreases with decreasing S_r , see, *e.g.*, [11].

For such reasons, the main goal of this work is to extend the work of ref. [10] by removing assumption d), properly taking into account the effects of partial saturation on the infiltration process and on the shear strength of the soil.

2 PB Model for Unsaturated Soil: Governing Equations

The PB model for unsaturated soil is based on the following uncoupled governing equations:

- a) *the balance of mass equation* for the unsaturated porous medium, providing the evolution of pore water pressure u_w with depth z and time t , during and after the rainfall event;
- b) *the limit equilibrium equation* for the evaluation of the shear stress τ and the safety factor F_s on the potential failure surface, under infinite slope assumption.

These equations are detailed in the following.

2.1 Balance of Mass Equation for the Porous Medium

In a one-dimensional setup, the balance of mass equation for the three-phase porous medium reads:

$$-S_w \frac{\partial \epsilon_v}{\partial t} + n \frac{\partial S_w}{\partial t} + \frac{\partial}{\partial z} \left\{ -k_s k_r \left(\frac{\partial \psi}{\partial z} + \frac{\partial \zeta}{\partial z} \right) \right\} = 0 \quad (1)$$

where: S_w is the degree of saturation of the soil; ϵ_v is the volumetric strain of the solid skeleton; n is the soil porosity; k_s is the hydraulic conductivity of the soil in saturated condition; k_r is the relative hydraulic conductivity; $\psi = u_w/\gamma_w$ is the pressure head, and ζ is the elevation head.

Eq. (1), representing a generalization of Richards equation to deformable porous media, governs the infiltration process and controls the pressure head evolution in space and time. The first two terms of the equation account for two storage mechanisms: the volumetric deformation of the solid skeleton and the variation of the degree of saturation with time. The first term disappears under the assumption of rigid solid skeleton. The second term vanishes under fully saturated condition. In this last case ($S_w=1$), Eq. (1) reduces to the 1-d consolidation equation controlling the infiltration process in a fully saturated soil.

In the present model, the degree of saturation S_w is linked to pore water suction via a simple, reversible soil–water characteristic curve, given in general terms by:

$$S_w = \begin{cases} S_w(\psi) < 0 & \text{for } \psi < \psi_{\text{aev}} \\ 1 & \text{for } \psi \geq \psi_{\text{aev}} \end{cases} \quad (2)$$

where ψ_{aev} is the air entry value pressure head of the solid skeleton. Accordingly, the second term of Eq. (1) can be rewritten as follows:

$$n \frac{\partial S_w}{\partial t} = n \frac{\partial S_w}{\partial \psi} \frac{\partial \psi}{\partial t} = C_s \frac{\partial \psi}{\partial t} \quad \text{where} \quad C_s = n \frac{\partial S_w}{\partial \psi} \quad (3)$$

Under the assumption of linear elastic behavior for the soil, the first term of Eq. (1) can be rewritten as:

$$\frac{\partial \epsilon_v}{\partial t} = \frac{1}{E_{ed}} \frac{\partial \sigma''_z}{\partial t} \tag{4}$$

where

$$\sigma''_z = \sigma_z - S_w \gamma_w \psi \tag{5}$$

is the z component of the average solid skeleton stress [13], and E_{ed} is the oedometric modulus.

Combining Eq. (1) with Eq. (4) and neglecting the term $\partial \sigma_z / \partial t$, very small as compared to the others, the following expression is obtained for the volumetric strain rate:

$$\frac{\partial \epsilon_v}{\partial t} = \frac{1}{E_{ed}} \left(-\gamma_w \psi \frac{\partial S_w}{\partial t} - \gamma_w S_w \frac{\partial \psi}{\partial t} \right) = -\frac{\gamma_w}{E_{ed}} \left(\frac{\psi}{n} C_s + S_w \right) \frac{\partial \psi}{\partial t} \tag{6}$$

Replacing Eq. (6) in Eq. (1) and setting $\bar{C}_s = n(\partial S_w / \partial u_w) = C_s / \gamma_w$, Eq. (1) reduces to the following PDE for the pore water pressure $u_w = u_w(z, t)$:

$$\left\{ \bar{C}_s + \frac{S_w}{E_{ed}} \left(\frac{u_w}{n} \bar{C}_s + S_w \right) \right\} \frac{\partial u_w}{\partial t} + \frac{1}{\gamma_w} \frac{\partial}{\partial z} \left\{ k_s k_r \left(-\frac{\partial u_w}{\partial z} + \gamma_w \frac{\partial \zeta}{\partial z} \right) \right\} = 0 \tag{7}$$

Eq. (7) is strongly non-linear, due to the dependence of S_w , \bar{C}_s and k_r on suction, and is typically solved by means of numerical methods (FE or FD) for any given initial and boundary conditions. Yet, a closed-form solution can be obtained [14] if the solid skeleton is rigid and the soil-water characteristic curve and the relative permeability are described by the following exponential relations proposed by Gardner [12]:

$$k = k_s \exp(\beta \psi) \tag{8}$$

$$S_w = S_{wr} + (1 - S_{wr}) \exp(\beta \psi) \tag{9}$$

For a typical infiltration process, the initial conditions for the unknown function u_w are given by:

$$u_w = \gamma(z - z_w) \tag{10}$$

where z_w is the water table depth. The boundary conditions at the ground surface ($z = 0$) and at the impervious boundary at the bottom of the soil cover ($z = d$) are given by:

$$v_z = k_s k_r \frac{\partial(\psi + \zeta)}{\partial z} = q_z f(t) \quad \text{at } z = 0 \tag{11}$$

$$v_z = 0 \quad \text{at } z = d \tag{12}$$

where q_z is the maximum rainfall rate and $f(t)$ a known function providing the rainfall history.

2.2 Limit Equilibrium Equation for the Soil Cover

Under the infinite slope assumption, the normal and tangential stresses acting on a potential failure surface at depth $z \leq d$ are obtained from the global translational equilibrium equations applied to a slice of arbitrary width:

$$\sigma_n = \gamma z \cos^2 \alpha \qquad \tau = \gamma z \sin \alpha \cos \alpha \qquad (13)$$

where $\gamma = (1 - n)\gamma_s + S_w n \gamma_w$ is the unit weight of the soil and α is the slope inclination.

From the Mohr–Coulomb failure criterium, written in terms of average skeleton stress, the following expression for the factor of safety is obtained:

$$F_s = \frac{\tau_f}{\tau} = \frac{c + \sigma_n'' \tan \phi}{\tau} = \frac{c + (\sigma_n - S_w \gamma_w \psi) \tan \phi}{\tau} \qquad (14)$$

where c and ϕ are the cohesion and the friction angle of the soil.

3 Governing Equations in Non – Dimensional Form

To investigate in a systematic manner the influence that different physical parameters may have on: *i*) the pore pressure distribution within the soil mass; *ii*) the factor of safety of the slope; and, *iii*) the critical rainfall intensity $q_{z,\text{crit}}$, *i.e.*, the rainfall intensity q_z that for a given rainfall duration t_d brings the slope to a limit equilibrium condition ($F_s = 1$), the governing equations have been recast in non–dimensional form. The solutions of the normalized equations in terms of dimensionless quantities can thus be applied to entire classes of problems that share geometric, kinematic and dynamic similarity properties.

Adopting the thickness h of the soil cover as a suitable length scale for the infiltration process, and noting that the time scale is provided by the saturated permeability of the soil, the following non–dimensional quantities can be defined:

$$\begin{aligned} T &= \frac{k_s t}{h} & Z &= \frac{z}{h} & P &= \frac{\psi}{h} & G &= \frac{\partial \zeta}{\partial z} \\ B &= \beta h & Q &= nh \frac{\partial S_w}{\partial \psi} & K &= \frac{k}{k_s} & R &= \frac{E_{\text{ed}}}{\gamma_w h} \\ I &= \frac{q_z}{k_s} & A &= \frac{\tan \alpha}{\tan \phi} & \Gamma &= \frac{\gamma}{\gamma_w} & C &= \frac{c}{\gamma_w h \sin \alpha \cos \alpha} \end{aligned} \qquad (15)$$

With the above definitions, the balance of mass equation (7) in non–dimensional form reads:

$$\left\{ Q + \frac{S_w}{R} \left(\frac{1}{n} CP + S_w \right) \right\} \frac{\partial P}{\partial T} + \frac{\partial}{\partial Z} \left\{ -K \left(\frac{\partial P}{\partial Z} + G \right) \right\} = 0 \qquad (16)$$

while the safety factor (13) of the slope is given by:

$$F_s = \frac{C}{\Gamma Z} + \left(1 - \frac{S_w P}{\Gamma Z} \right) \frac{1}{A} \qquad (17)$$

In Eq. (17), the quantity $\Gamma = \gamma/\gamma_w$ can be assumed as constant in most cases of practical interest.

4 Critical Rainfall Thresholds

The non-dimensional Eq. (16) has been solved numerically using the FE code Comsol Multiphysics v4.1. An extensive series of parametric simulations (648 analyses) have been carried out varying the most significant dimensionless groups in a range of values that covers most of practical cases of interest (see Tab. 1). The range of variability of each group has been defined from an extensive collection of data gathered from the archives of the Umbria Region Civil Protection Department. The results of such numerical study have been used to define the

Table 1. Values of the non-dimensional variables considered in the parametric study

Variable	Values
D	0.5, 5.0, 50.0, 500.0
A	0.49, 0.54, 0.58, 0.64, 0.70, 0.76, 0.79, 0.87, 0.94
B	3.45, 12.20, 17.10
Z_w	1.0, 0.8, 0.6
R	5830, 14500

dimensionless critical rainfall threshold, *i.e.*, the functional relationship providing – for a given set of geometrical and mechanical properties of the system and initial depth of water table $Z_w = z_w/h$ – the normalized critical rainfall intensity $I_c = q_{z,crit}/k_s$ as a function of the normalized rainfall duration $D = (k_s t_d)/h$:

$$I_c = \frac{q_{z,crit}}{k_s} = \hat{I}_c(D, A, B, R, Z_w) \quad (18)$$

The explicit expression for the function \hat{I}_c has been obtained from the numerical solution of Eq. (16) using the following procedure:

1. Assign a tentative range of value for the normalized rainfall intensity $I = q_z/k_s$, associated to a given rainfall duration D .
2. Compute the factor of safety F_s as a function of time T for different rainfall intensities I within the tentative range.
3. From the condition $\min(F_s) = 1$, identify I_c as the lowest rainfall intensity rate leading the slope to limit equilibrium condition for the assigned duration D .
4. Repeat steps 1–3 for different rainfall durations D and plot the couple of values (D, I_c) thus obtained in a bi-logarithmic plot (Fig. 1).

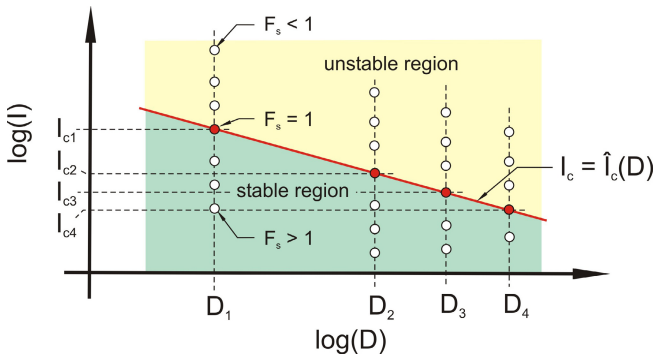


Fig. 1. Procedure for determining the normalized critical rainfall threshold $I_c = \hat{I}_c(D)$

5 Results and Discussion

Figures 2 to 4 presents in detail the results of a single FE simulation, carried out with the following data:

$$D = 5 \quad A = 0.76 \quad B = 17.10 \quad C = 0 \quad R = 5830 \quad Z_w = 1$$

The isochrones of normalized pore water pressure P during the transient infiltration process are shown in Fig. 2. The evolution of P and S_w with time T at different normalized depths Z is shown in Fig. 3. At the beginning of the process

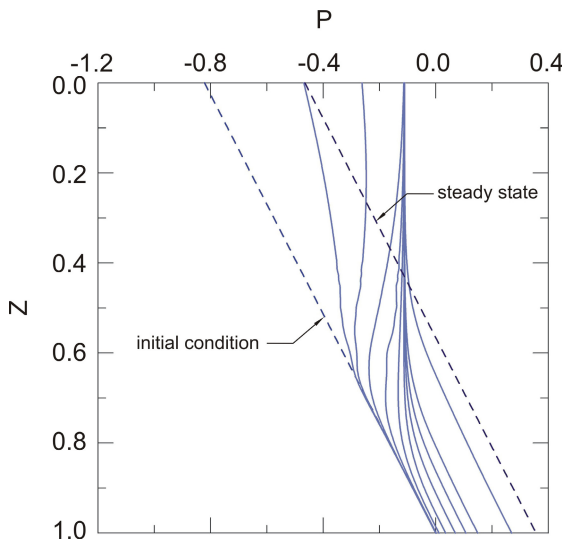


Fig. 2. Isochrones of normalized pore water pressure

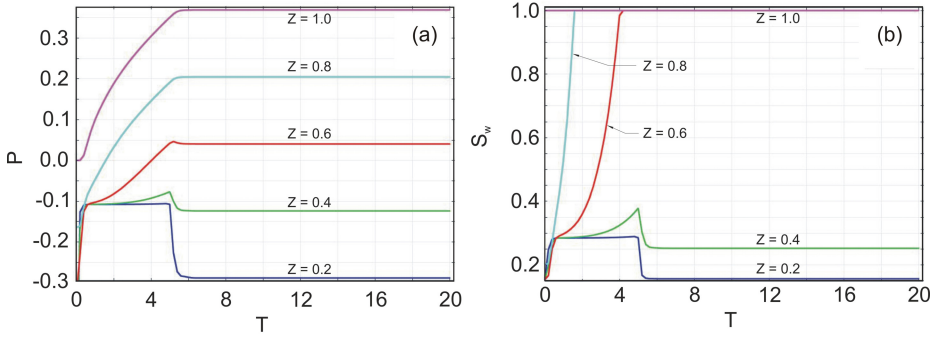


Fig. 3. Normalized pore pressure (a) and degree of saturation (b) *vs.* time at different depths

($T \leq D$), the downward flow causes a rapid drop of suction close to the ground surface. The pore water pressure increases monotonically on the entire depth of the soil layer, faster at shallow depths and slower close to the layer bottom. After the rainfall has ended ($T > D$) the pore water pressure remains stationary at depths $Z > 0.6$, while it drops at shallower depths, to reach the final steady-state conditions (Fig. 3a). A similar trend is shown by the time-histories of S_w in Fig. 3b. In the bottom part of the layer ($Z > 0.6$), the soil recovers a fully saturated state, while the upper part remains unsaturated although with a higher S_w . In the upper part of the layer S_w increases monotonically up to $T = D$, then decreases following the changes in P .

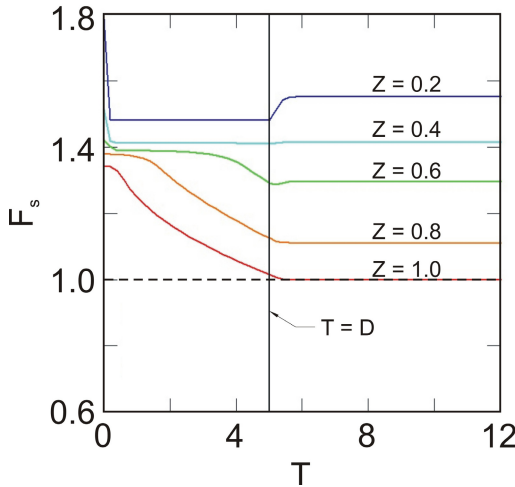


Fig. 4. Safety factor *vs.* time at different depths

Fig. 4 shows the evolution of the safety factor F_s with time T for different normalized depths. Consistently with the pore pressure and degree of saturation evolutions, during the rainfall event ($T \leq D$) F_s decreases monotonically. After the end of rainfall, the evolution of F_s with time depends on the depth considered. Close to the ground surface ($Z < 0.6$), consistently with the observed increase in suction, F_s experiences a slight increase up to the final stationary state. At higher depths, In the deeper layers, F_s decreases continuously before reaching the final asymptotic value. This effect is associated to the monotonic increase of pore water pressure and to the associated reduction in S_w . It is worth noting that, as observed by Salciarini *et al.* [10] for fully saturated soil layers, for relatively short rainfall events the minimum value of F_s is reached at the bottom of the soil layer ($Z = 1$) some time after the end of the event ($t_{crit} > t_d$).

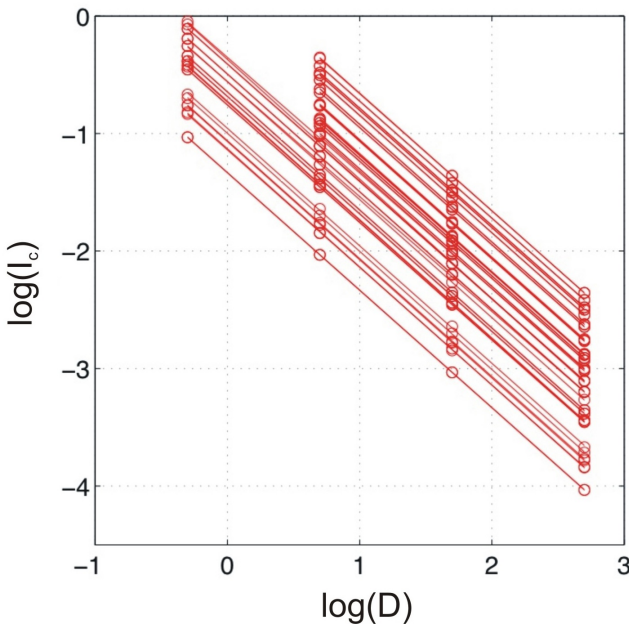


Fig. 5. Critical rainfall thresholds for different combination of the parameters A, B, R

Fig. 5 shows the critical rainfall thresholds numerically obtained – for varying slope geometries and soil properties (A, B, R) – by collecting all the couples of values (D, I_c) obtained from the subset of simulations performed with the initial condition $Z_w = 1$ (initial water table depth at the bottom of the layer). In all cases, the critical rainfall data can be interpolated quite accurately by the following expression:

$$\log I_c = q + m \log D \tag{19}$$

where m and q represent the slope and the intercept of the interpolating line in the bilogarithmic plot of Fig. 5. Eq. (19) is also equivalent to the following

power law, similar to the empirical rainfall thresholds available in literature:

$$I_c = 10^q(D)^m = \Xi(D)^m \tag{20}$$

The results of the parametric study indicate that the slope m of all critical rainfall thresholds varies in a very narrow range around the value $m = -1$ (Fig. 6a), while the coefficient $\Xi = 10^q$ experiences significant variations with changes in the normalized slope angle A and the soil–water retention coefficient B (Fig. 6b). In particular, Fig. 6b shows that Ξ decreases rapidly with increasing A and decreasing B . In fact, as the relative slope inclination increases, the slope can be driven to limit equilibrium condition even by rainfalls of low intensity. Moreover, a higher value of B corresponds to a lower degree of saturation, for given profile of suction; therefore, for higher B values, the rainfall intensity necessary to bring the slope at limit equilibrium is higher.

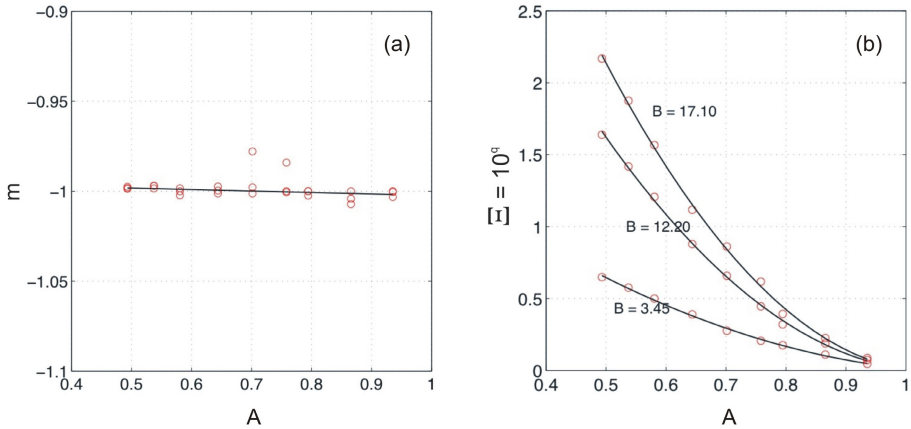


Fig. 6. Coefficients m (a) and Ξ (b) vs. normalized slope angle A

For the range of independent variables examined, the soil skeleton deformability (R) has practically no effect on the critical rainfall thresholds.

The dependence of the critical rainfall intensity on the initial pore water pressure field can be assessed by considering a second subset of the parametric study containing all the simulations performed with different initial positions of the water table (simulations performed with $A = 0.58, B = 12.20$).

Fig. 7a shows the normalized critical rainfall thresholds corresponding to Z_w varying from 0.6 to 1.0. As for the previous cases considered, the critical rainfall thresholds can be interpolated quite accurately by Eq. (19). The slope m of the interpolating lines remains almost constant and approximately equal to -1 , while the intercept q decreases as the Z_w increases. Again, Fig. 7 shows that Ξ decreases rapidly with increasing A . The reduction of Ξ with decreasing Z_w indicates that, as expected, the lower the initial depth of the groundwater table, the higher is the critical rainfall intensity.

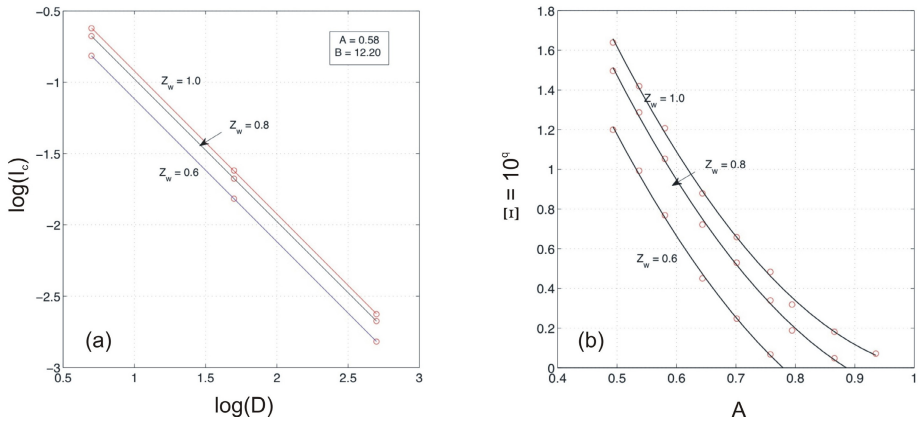


Fig. 7. Effect of initial conditions on: a) critical rainfall thresholds; b) coefficient Ξ

6 Conclusions

In this paper, a simple PB model has been used to investigate the effect of slope geometry, soil properties and initial conditions on rainfall intensity/duration thresholds. The development of the model is motivated by the need of extending existing models [10] to potentially unstable slopes in unsaturated soils.

A key result obtained from the results of an extensive program of parametric FE simulations is that the critical rainfall thresholds for unsaturated soil slopes can be expressed by the following power law in dimensionless form:

$$I_c(D, A, B, Z_w) = \Xi(A, B, Z_w)D^m \tag{21}$$

with $m \simeq -1$. The function thus obtained can be easily and efficiently implemented in GIS-based codes for the evaluation of physically-based, spatially-distributed critical rainfall thresholds, which represent a very useful tool for identifying potentially critical areas, setting up early-warning systems and/or designing appropriate protection measures.

Acknowledgements. The authors would like to thank Ms. Federica di Lorenzo for the help given in carrying out the parametric study. The financial support of the Project PRIN 2010–2011 “La mitigazione del rischio da frana mediante interventi sostenibili” funded by the *Italian Ministero dell’Università e della Ricerca* is gratefully acknowledged.

References

1. Caine, N.: The rainfall intensity–duration control of shallow landslides and debris flows. *Geografiska Annaler* 62, 23–27 (1980)
2. Crosta, G.B., Frattini, P.: Nonlinear oscillations and boundary-value problems for Hamiltonian systems. *Hydrol. Process.* 22(4), 473–477 (2007)
3. Frattini, P., Crosta, G.B., Sosio, R.: Approach for defining thresholds and return periods for rainfall–triggered shallow landslides. *Hydrol. Process.* 23, 1444–1460 (2009)
4. Baum, R.L., Godt, J.W.: Early warning of rainfall–induced shallow landslides and debris flows in the USA. *Landslides* 7, 259–272 (2010)
5. Glade, T., Crozier, M., Smith, P.: Applying probability determination to refine landslide–triggering rainfall thresholds using an empirical Antecedent Daily Rainfall model. *Pure and Applied Geophysics* 157, 1059–1079 (2000)
6. Chleborad, A.F., Baum, R.L., Godt, J.W.: Rainfall thresholds for forecasting landslides in the Seattle, Washington, Area – Exceedance and Probability. USGS Open-File Report 06-1064 (2006)
7. Valentino, R., Montrasio, L., Losi, G.L., Bittelli, M.: An empirical model for the evaluation of the degree of saturation of shallow soils in relation to rainfalls. *Canadian Geotechnical Journal* 48(5), 795–809 (2011)
8. Salciarini, D., Godt, J.W., Savage, W.Z., Baum, R.L., Conversini, P.: Modeling landslide recurrence in Seattle, Washington, USA. *Engineering Geology* 102(3-4), 227–237 (2006)
9. Godt, J.W., McKenna, J.P.: Numerical modeling of rainfall thresholds for shallow landsliding in the Seattle, Washington, area. *Reviews in Engineering Geology* 20, 121–136 (2008)
10. Salciarini, D., Tamagnini, C., Conversini, P., Rapinesi, S.: Spatially distributed rainfall thresholds for the initiation of shallow landslides. *Natural Hazards* 61, 229–245 (2012)
11. Lu, N., Likos, W.J.: *Unsaturated soil mechanics*, p. 556. John Wiley & Sons (2004)
12. Gardner, W.R.: Some steady state solutions of unsaturated moisture flow equations with applications to evaporation from a water table. *Soil Science* 85(4), 228–232 (1958)
13. Jommi, C.: Remarks on the constitutive modelling of unsaturated soils. In: Tarantino, Mancuso (eds.) *Experimental Evidence and Theoretical Approaches in Unsaturated Soils*, Trento, Italy, pp. 139–153 (2000)
14. Srivastava, R., Yeh, T.C.J.: Analytical solutions for one-dimensional, transient infiltration toward the water table in homogeneous and layered soils. *Water Resources Research* 27, 753–762 (1991)

Numerical Simulations of the Mechanical Contribution of the Plant Roots to Slope Stability

Barbara Maria Switala and Wei Wu

Institut für Geotechnik, Universität für Bodenkultur,
Vienna, Austria

barbara.switala@boku.ac.at

<http://www.baunat.boku.ac.at/489.html>

Abstract. Soil bioengineering methods in slope stabilisation are becoming more and more popular, when ecological solutions are desirable. Simple, numerical models were created in order to assess the mechanical contribution of the roots reinforcement to slope stability. Two- and three-dimensional analyses were conducted for different geometries of root architectures and different soil conditions. Obtained values of a factor of safety (FOS) are compared and discussed. From these data, it is possible to determine, which root reinforcement cases have the greatest impact on the stability of the slope.

Keywords: slope stability, root reinforcement, factor of safety, slip surface, bioengineering methods.

1 Introduction

Research on the role of bioengineering methods of slope stabilisation is relatively recent. Although some techniques are well known, there does not exist any precisely formulated design and calculation methods which would allow quantitative assessment. Nowadays, soil bioengineering methods are increasingly desirable due to its economical and ecological advantages. During recent years many interesting approaches have been developed and many tests have been conducted [1], [3], [5], [7, 8, 9, 10, 11, 12, 13, 14, 15, 16, 17]. The presence of vegetation on slopes minimise risk of shallow landslides, especially those induced by rainfall. Plants affect slope stability by different mechanisms. The most important and frequently investigated is the reinforcement of the soil with plant roots. This factor can be taken into account in different ways. Pioneering work by [12], [16,17], created a simple model containing many assumptions. However, it overestimates the increase of apparent cohesion due to presence of the roots in the soil. Due to it's simplicity, the model is commonly used and allows better understand of the problem and conduct simple preliminary studies. Second very important factor which has an impact on slope stability is evapotranspiration and related issue of water uptake from the soil, which leads to an increase in apparent cohesion.

Work presented in this paper compares results obtained from two- and three-dimensional analyses. These analyses allow asses of the mechanical contribution of the plant roots to the slopes stability under different conditions.

2 Mechanical Model of Soil Reinforcement by Plant Roots

2.1 Theory

Preliminary studies of the influence of vegetation on slope stability are conducted using simplified mechanical root models. [12], [16, 17] introduced a model of a soil-root system subjected to shear. According to their approach, the root's contribution to shear strength is dependent on the angle of shear distortion of the root, which is assumed to be initially perpendicular to the shear surface.

$$s_r = \sigma_r \tan \phi' + \tau_r = t_r (\cos \theta \tan \phi' + \sin \theta) \quad (1)$$

where s_r is the root's contribution to the shear strength and σ_r , τ_r are normal and shear stresses respectively, applied to the soil by T_r (tension in the root), ϕ' is the angle of internal friction and θ is the angle of shear distortion. If we consider all the roots in area A, then

$$t_r = \sum T_{ri}/A \quad (2)$$

where $\sum T_{ri}$ are the tension values summed for all roots present in the area A.

Tests conducted show that the quantity $(\cos \theta \tan \phi' + \sin \theta)$ can be assumed to be a constant value of 1.2 for the range of angles $\theta = 48 - 72^\circ$

The mechanical contribution of the root to the increase in shear strength of the soil is included in the Mohr-Coulomb failure criteria as an additional cohesion as follows [17]:

$$s^* = s + s_r = c' + \sigma' \tan \phi' + s_r \quad (3)$$

where s is the shear strength of the bare soil and c' is the cohesion of the bare soil.

The model created by [12], [16, 17] does not fully reflect reality, but shows an idealized case and confirms the statement that roots contribute to the shear strength of the soil.

Numerical models described here, are based on the three dimensional model of a slope proposed by [5], who considered three main types of roots morphology, according to [6]. [6] describes these as namely heart-, plate- and tap-like. [5] chose the following geometrical patterns corresponding to these morphologies. These are: semi-sphere, cylinder and cone respectively (Fig. 1).

The value of additional cohesion in the numerical models is chosen to be 10 kPa, which is an average value taken from experimental tests and literature [2], [5]. The whole slope is assumed to be composed of two (or three, taking into account bedrock) types of soil.




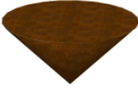


Class of root system	Real morphology	Geometrical approximation
<i>Heart root system</i>		
<i>Tap root system</i>		
<i>Plate root system</i>		

Fig. 1. Morphology and geometrical approximations of roots systems according to Köstler's classification, after [5].

2.2 Geometry and Boundary Conditions

The dimensions of the two- and three- dimensional models created in *SLOPE/W* and *FLAC^{3D}* respectively are presented in the Fig.2 and Fig.3. Two shapes of root architecture are considered: heart- and plate-like, as well as a uniformly distributed 0.5 m deep grass layer. Several cases are investigated. For each of the models the factor of safety (FOS) is calculated and compared, in order to determine the most favourable and unfavourable conditions. Slopes modelled are single or multi-layered constructions.

Two types of soil: sand and clay, as well as an impermeable bedrock layer, are chosen to the model. Their parameters are listed in the Tab.1

Table 1. Types and parameters of soils used in the calculations

Layer	Young Modulus	Poisson's ratio	Angle of friction	Cohesion	Unit weight
[-]	E [MPa]	ν [-]	φ [°]	c [kPa]	[kN/m ³]
Sand	20.0	0.30	42	1.0	16.0
Clay	6.0	0.25	20	8.0	13.0
Bedrock	5000.0	0.30	42	780.0	25.5
Clay with grass roots	6.0	0.25	20	18.0	13.0
Sand with grass roots	20.0	0.30	42	11.0	16.0

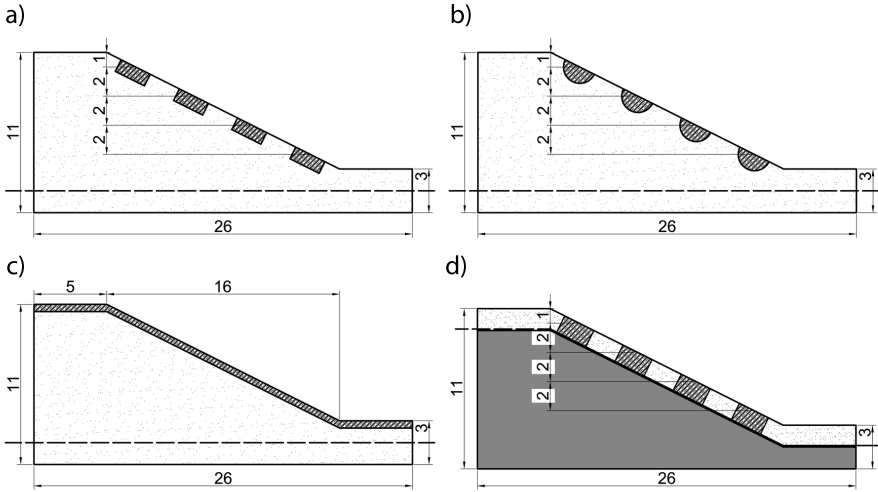


Fig. 2. Geometries of the input to the 2D and 3D numerical models: a) cylindrical shape of roots architecture (height: 0.7 m; diameter: 2.0 m), b) semi-spherical shape of roots architecture (diameter: 2.0 m), c) uniform vegetation cover (thickness: 0.5 m), d) rock slope with a sand layer and cylindrical shapes of roots architecture (height: 1.35 m, diameter: 2.0 m). Note that dash line stands for the water table, which is situated 1.5 m below the toe of the slope.

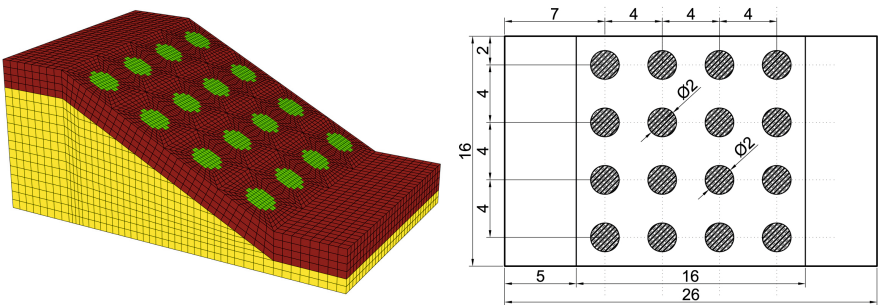


Fig. 3. Dimensions of the 3D model created in *FLAC^{3D}* (On the right-hand side the view on the model from the top as well as main dimensions are presented. A left-hand side of the model presents an example of a 3D model from *FLAC^{3D}*, which contains semi-spherical or cylindrical shapes of roots architecture).

3 Results and Discussion

3.1 Two-dimensional Model

The two-dimensional model of the root-reinforced slope is created in Slope/W. For the calculation of the factor of safety, the Spencer's limit equilibrium method is used. A diameter of the semi-circles is assumed to be 2.0 m, and the height of rectangles is: 0.7 m for the sand and clay slope and 1.35 m for slopes with impermeable bedrock. The factors of safety and shapes of the slip surfaces obtained for 2D analyses are shown in Fig.4 - Fig.6. A comparison of the results is presented in Tab.2.

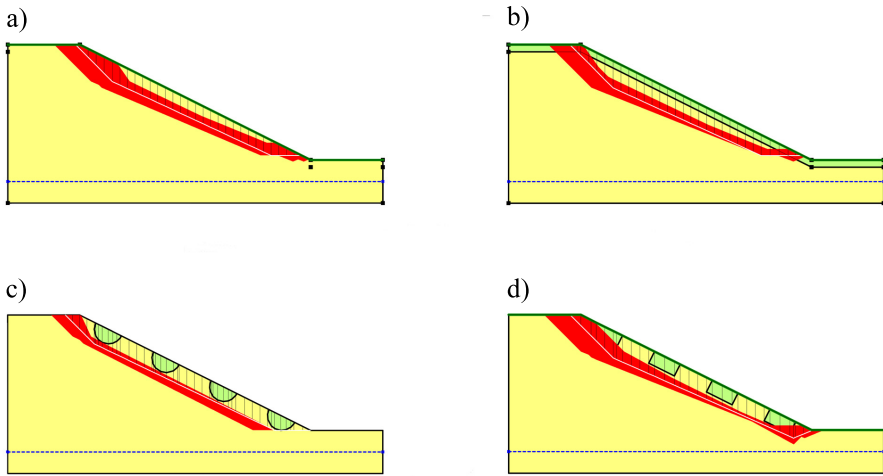


Fig. 4. Shapes of the slip surfaces and factors of safety values of the slope composed of sand: a) bare slope FOS = 1.403, b) uniform vegetation FOS = 1.530, c) semi-circular shape of roots archit. FOS = 1.404, d) rectangular shape of roots archit. FOS = 1.487.

Table 2. Results from 2D analysis: factors of safety for all considered types of soil and shapes of roots architecture and percent change in FOS related to the value obtained for the slope without vegetation (bare slope).

	Sand		Clay		Bedrock	
	FOS	Change [%]	FOS	Change [%]	FOS	Change [%]
Bare slope	1.403	-	1.616	-	1.409	-
Uniform vegetation	1.530	9.05	1.682	4.08	1.451	2.98
Semicircular roots	1.404	0.07	1.616	0.00	-	-
Rectangular roots	1.487	5.99	1.617	0.06	1.909	35.49

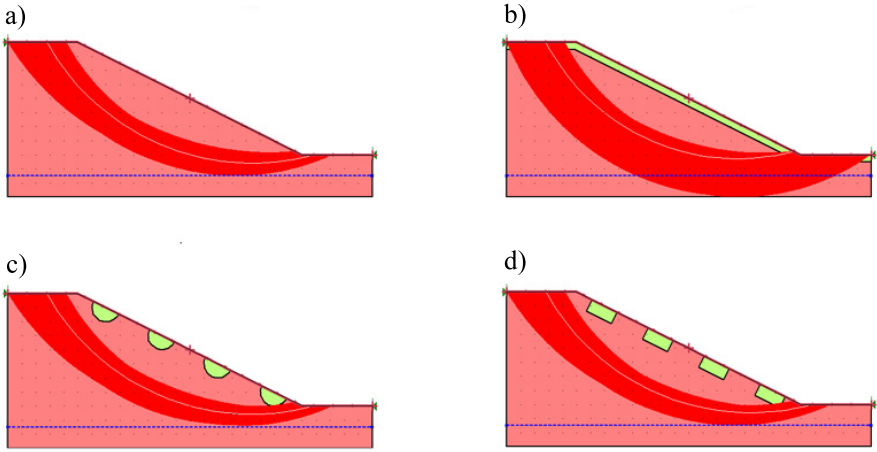


Fig. 5. Shapes of the slip surfaces and factors of safety values for the slope composed of clay: a) bare slope FOS = 1.616, b) uniform vegetation FOS = 1.682, c) semi-circular shape of roots archit. FOS = 1.616, d) rectangular shape of roots archit. FOS = 1.617.

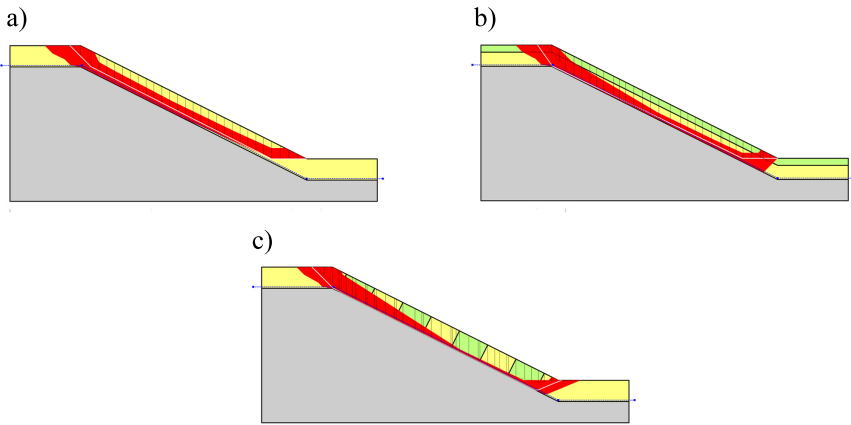


Fig. 6. Shapes of the slip surfaces and factors of safety values for the slope composed of impermeable bedrock overlaid by a sand layer: a) bare slope FOS = 1.409, b) uniform vegetation FOS = 1.451, c) rectangular shape of roots archit. FOS = 1.909.

The results show that the highest values of factor of safety (when compared to the bare slope), for sand and clay slopes, are achieved when the slope is uniformly vegetated. For the sand layer on impermeable bedrock, the highest increase in FOS is obtained for the case of rectangular shape of root architecture. In this case, roots are assumed to be 1.35 m deep, which is the depth of the slip surface.

This results in the increased "slice forces" used in limit equilibrium calculations. In all presented cases, the increase in FOS is caused by increased cohesion in the root zone. In clay slopes, where failure surface is very deep, the roots' presence have little or no impact on the stability of the slope (the failure surface do not usually cross the root zone).

3.2 Three-dimensional Model

The three dimensional model is developed using a Finite Difference Method code *FLAC^{3D}* version 3.0. In order to calculate a factor of safety (FOS), the procedure of shear strength reduction is used. This method is based on reduction of the shear strength of the soil in stages until the slope loose it's stability. FOS is then obtained by comparing initial and reduced parameters. The shapes of the root architecture which are considered are as follows: semi-spheres (diameter 2.0 m) and cylinders (diameter 2.0 m, height 0.7 m and 1.35 m for slopes composed of sand or clay and impermeable bedrock, respectively). Factors of safety and slip surfaces obtained in the 3D analyses are shown in Fig.7 - Fig.9. Comparison of the results is presented in the Tab.3.

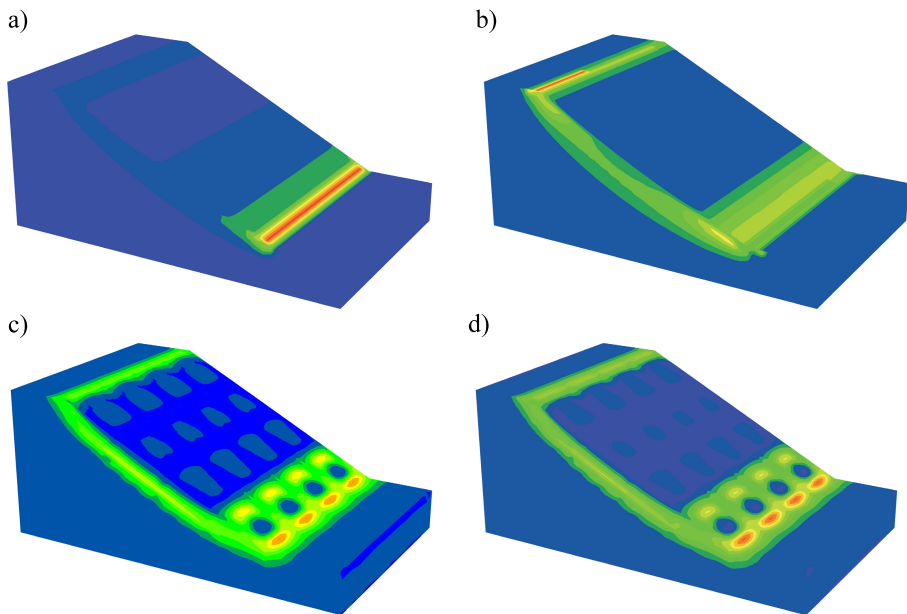


Fig. 7. Shapes of the slip surfaces and factors of safety values for the slope composed of sand: a) bare slope FOS = 1.44, b) uniform vegetation FOS = 1.52, c) semi-spherical shape of roots archit. FOS = 1.45, d) cylindrical shape of roots archit. FOS = 1.44.

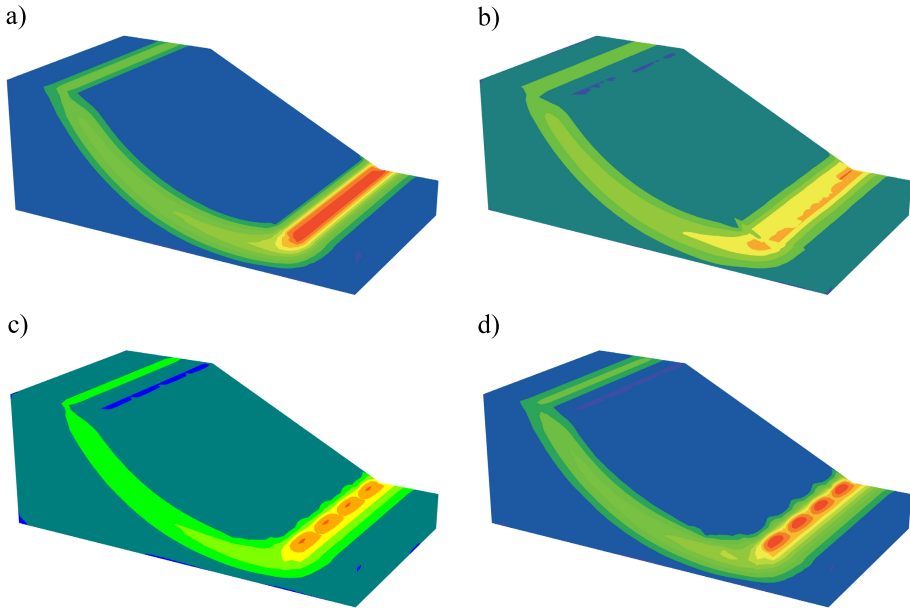


Fig. 8. Shapes of the slip surfaces and factors of safety values for the slope composed of clay: a) bare slope FOS = 1.87, b) uniform vegetation FOS = 1.91, c) semi-spherical shape of roots archit. FOS = 1.88, d) cylindrical shape of roots archit. FOS = 1.88.

Table 3. Results from 3D analysis: factors of safety for all considered types of soil and shapes of roots architecture and percent change in FOS related to the value obtained for the slope without vegetation (bare slope).

	Sand		Clay		Bedrock	
	FOS	Change [%]	FOS	Change [%]	FOS	Change [%]
Bare slope	1.44	-	1.87	-	1.38	-
Uniform vegetation	1.52	5.56	1.91	2.14	1.51	9.42
Semspherical roots	1.45	0.69	1.88	0.53	-	-
Cylindrical roots	1.44	0.00	1.88	0.53	1.66	20.28

A trend of the results obtained in the three-dimensional analysis is similar to the trend from two-dimensional analysis. For slopes composed of sand and clay, the highest FOS values are obtained for the uniformly vegetated slopes. Semi-spherical and cylindrical shapes of root systems have little or no impact on the stability of the slope. The highest increase in the FOS is observed for a sand layer on impermeable bedrock where roots reach the depth of the slip surface. This results in increased shear resistance of soil permeated by plant roots and thus a lower susceptibility to failure.

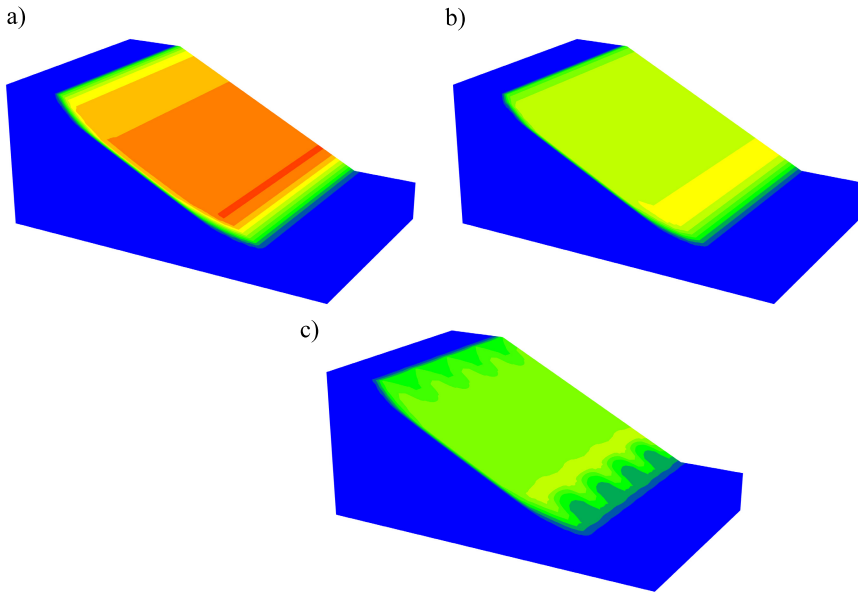


Fig. 9. Shapes of the slip surfaces and factors of safety values for the slope composed of impermeable bedrock overlaid by a sand layer: a) bare slope FOS = 1.38, b) uniform vegetation FOS = 1.51, c) cylindrical shape of roots archit. FOS = 1.66.

4 Conclusions

The simple, mechanical model of the vegetated slope showed that vegetation is important in the stability of the slope. The aim of the analysis is to investigate if different shapes of root architecture and different types of soil have an influence on the slope stability. Soil reinforcement by plant roots is most efficient for shallow slip surfaces, which may cross the root zone. In the presented cases, the increase in the FOS values due to the mechanical impact of vegetation on slope stability, is higher for slopes composed of sand, where the shear zone is usually shallow and parallel to the surface.

Acknowledgements. The research leading to these results has received funding from the People Programme (Marie Curie Actions) of the European Union's Seventh Framework Programme FP7/2007-2013/ under REA grant agreement n°289911.

References

1. Ali, N., Farshchi, I., Mu'azu, M.A., Rees, S.W.: Soil-Root Interaction and Effects on Slope Stability Analysis. *Electronic Journal of Geotechnical Engineers* 17, 319-328 (2012)

2. Comino, E., Druetta, A.: In situ Shear Tests of Soil Samples with Grass Roots in Alpine Environment. *American Journal of Environmental Sciences* 5(4), 475–486 (2009)
3. Fan, C.C., Su, C.F.: Role of roots in the shear strength of root-reinforced soils with high moisture content. *Ecological Engineering* 33, 157–166 (2008)
4. Itasca Consulting Group: FLAC 3D Version 3.0 User's Guide, Minneapolis (2005)
5. Kokutse, N., Fourcaud, T., Kokou, K., Lac, P.: 3D Numerical Modelling and Analysis of the Influence of Forest Structure on Hill Slopes Stability. In: Proceedings to the INTERPRAEVENT International Symposium Disaster Mitigation of Debris Flows, Slope Failures and Landslides, Niigata, Japan, pp. 561–567 (2006)
6. Köstler, J.N., Brückner, E., Bibelriether, H.: Die Wurzeln der Waldbäume. Untersuchungen zur Morphologie der Waldbäume in Mitteleuropa. P.Parey, Hamburg (1968)
7. Mickovski, S.B., Stokes, A., van Beek, R., Ghestem, M., Fourcaud, T.: Simulation of direct shear tests on rooted and non-rooted soil using finite element analysis. *Ecological Engineering* 37, 1523–1532 (2011)
8. Schwarz, M., Lehmann, P., Or, D.: Quantifying lateral root reinforcement in steep slopes—from a bundle of roots to tree stands. *Earth Surface Processes and Landforms* 35, 354–367 (2010)
9. Stokes, A., Atger, C., Bengough, A.G., Fourcaud, T., Sidle, R.C.: Desirable plant root traits for protecting natural and engineered slopes against landslides. *Plant Soil* 324, 1–30 (2009)
10. Thomas, R., Pollen-Bankhead, N.: Modelling root-reinforcement with a fiber-bundle model and Monte Carlo simulation. *Ecological Engineering* 36, 47–61 (2010)
11. Tiwari, R.C., Bhandary, N.P., Yatabe, R., Bhat, D.R.: New Numerical scheme in the finite-element method for evaluating the root-reinforcement effect on slope stability. *Geotechnique* 63, 129–139 (2013)
12. Waldron, L.J., Dakessian, S.: Soil reinforcement by roots, calculation of increased soil shear resistance from root properties. *Soil Science* 132(6), 427–435 (1981)
13. Wan, Y., Xue, Q., Zhao, Y.: Mechanism Study and Numerical Simulation on Vegetation Affecting the Slope Stability. *Electronic Journal of Geotechnical Engineers* 16, 741–751 (2011)
14. Wilkinson, P.L., Anderson, M.G., Lloyd, D.M.: An integrated hydrological model for rain-induced landslide prediction. *Earth Surface Processes and Landforms* 27, 1285–1297 (2002)
15. Wilkinson, P.L., Anderson, M.G., Lloyd, D.M., Renaud, J.: Landslide hazard and bioengineering: towards providing improved decision support through integrated numerical model development. *Environmental Modeling & Software* 17, 333–344 (2002)
16. Wu, T.H.: Investigation of landslides on Prince of Wales Island, Alaska. *Geotechnical Engr. Report N°5*, Dept. of Civil Engr. Ohio State University, p. 94. Columbus (1976)
17. Wu, T.H., McKinell, W.P., Swantson, D.N.: Strength of tree roots and landslides on Prince of Wales Island, Alaska. *Canadian Geotechnical Journal* 16, 19–33 (1979)

Study on Morphological Characteristics of Coarse Particles in Sliding Zones of Huangtupo Landslide in Three Gorges Reservoir Area, China

Jinge Wang, Wei Xiang, and Shun Wang

Three Gorges Research Center for Geohazard, Ministry of Education,
China University of Geosciences, Wuhan, China
wangjinge1985@gmail.com

Abstract. The coarse particles (defined as particle size between 0.25 mm and 2 mm here) in sliding zones of Huangtupo landslide in Three Gorges Reservoir Area are taken as study objects. Particle size distribution and particle profiles of samples are firstly obtained through sieving tests and digital imaging respectively. Combined with fractal theory, the fractal dimensions of particle size distributions and particle profiles are calculated quantitatively. Scanning electron microscopy and energy disperse spectroscopy are employed to capture the micrograph and test the mineral composition of samples. Tests and analysis results indicate that the particle size distributions and profiles of samples have fractal characteristics, and the fractal dimensions can be used as quantitative analytical index for the evolution of sliding zones. As the continuous development of sliding zones, the particle mass – size fractal dimension increase and the profile fractal dimension decrease. The special surface characteristics of particles can also indirectly reflect the stress and deformation conditions during the failure and evolution of the sliding zones.

Keywords: Three Gorges Reservoir, Huangtupo landslide, Sliding zones, Morphological characteristics, Fractal.

1 Introduction

Sliding zones of landslide indicate the relative weak regions where have already failed and might fail again in the future. They are usually composed with complex soil and rock mixture, which form under compressive and shearing stress state environment. Skempton and Petley [1] are almost the earliest researchers study the structure of sliding zones. They find the sliding zones formed in different environments and times have significant different structures. Wen's study [2] indicate that the structures of sliding zone soils can not only control the physical- mechanical properties of the sliding zones, but also have great significance on the reveal of the formation, evolution and the stability of landslide.

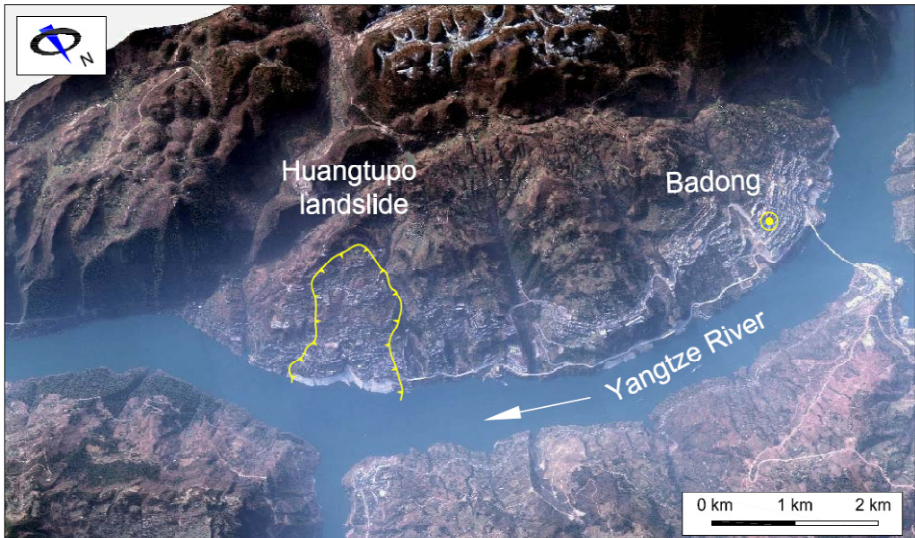


Fig. 1. Image of Huangtupo landslide

Huangtupo landslide locates in Badong County of Hubei Province, China (See Figure 1). It is one of the largest and most harmful wading landslides in Three Gorges Reservoir Area. The study on this landslide starts from the proposal of the construction of the Three Gorges Project. Deng et al. [3] proposed a three-stage model involving mass rock creep – primary landsliding – partial reactivation to describe the evolutionary process of huangtupo landslide based on field investigation and electrical resistivity survey. Wen et al [4] studied the physical and chemical effects of groundwater in reducing shear strength in sliding zones of Huangtupo landslide, they propose the shear strength reduction could have resulted from physical and chemical processes involving hydrolyses, argillation of marls fragments, dissolution of calcite, and transformation of illite to interlayered illite and smectite. According to the investigation data from the Hubei Survey and Design Institute for Geohazard Engineering [5], there are several layers of sliding zones with different thicknesses and ranges developed in Huangtupo landslide. These sliding zones divide the sliding body to several parts, which lead to the landslide structure extremely complex. Until now, it is still very difficult to obtain a common understanding of the nature and stability of this landslide. The components of sliding zones exposed by boreholes are mainly silty clay with sands and gravels, in which, the content of coarse particles with grain size larger than 0.25 mm is more than 50%. Because the coarse particles in sliding zones

experienced the whole process of landslide failure and evolution, the study on morphological characteristics of coarse particles in sliding zones can provide a new thinking for the analysis of failure and evolution of landslide.

2 Geologic Setting and Sampling

According to the existing investigation report [5], Huangtupo landslide is composed with 4 main parts, namely No.1 adjacent to river sliding debris, No.2 adjacent to river sliding debris, Garden Spot Landslide and Transformer Station Landslide (Fig.2), the total area is about $135 \times 10^4 \text{ m}^2$ and total volume is about $6934 \times 10^4 \text{ m}^3$. As many other landslides in the reservoir area, Huangtupo landslide is a wading landslide which means the toe area of the sliding body is under the highest 175 m water level of the reservoir. Because of the initial impoundment and annually water level fluctuation, the adjacent to river sliding debris directly effect by the reservoir water, which are the most dangerous area in Huangtupo landslide.

Investigation data shows that the bedrocks of Huangtupo landslide are mainly gray limestone and gray pelitic limestone of Badong formation (T2b). The lower part of sliding mass is dense soil and rock debris originated from gray limestone. The upper part of sliding mass is loose soil and rock debris originated from gray pelitic limestone. Boreholes expose two sliding zones in the landslide. The main sliding zone locates between sliding body and bed rock, the secondary sliding zone locates in the sliding mass between dense and loose debris. As we know, sliding zones of large scale landslides are buried deeply in sliding body. Because of the limit of investigation technology, sliding zone soils are relatively difficult to obtain. However, the field testing site, constructed by Three Gorges Research Center for Geohazard (Ministry of Education, China) locates on Badong County, Hubei province. The underground tunnel group of the testing site is totally constructed in Huangtupo landslide. The tunnels built in the landslide can not only expose the original characteristics of the sliding zones, but also can provide the possibility to obtain sufficient sliding zone soil for laboratory and in situ tests. The soil samples for this research are collected from the 745 m tunnel face of the main tunnel and the 196 m – 210 m section of TP4 investigation channel, which locates in No.1 and No.2 adjacent to river sliding debris respectively (see Figure 2).

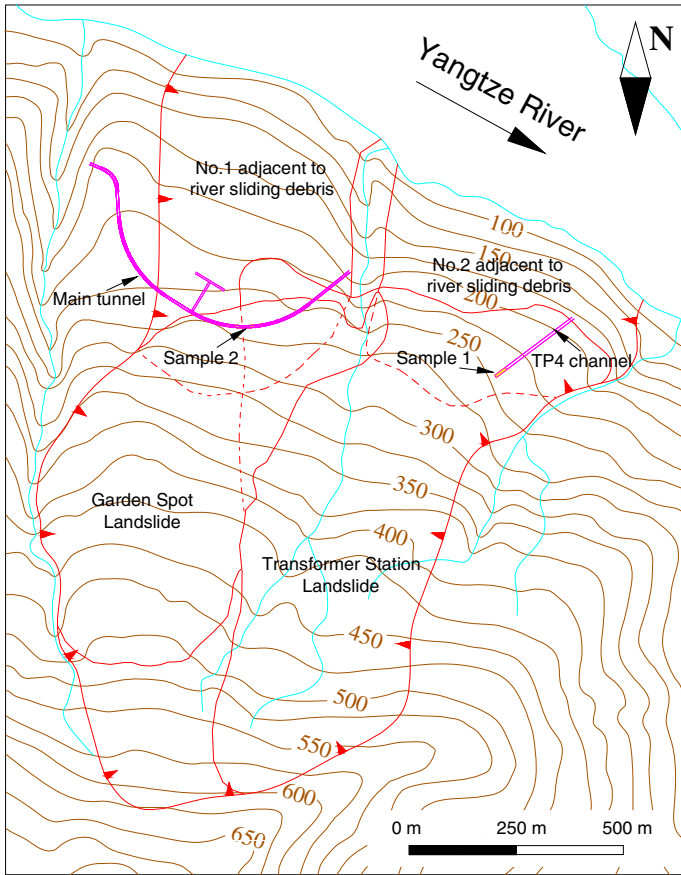


Fig. 2. Plan view of Huangtupo landslide and sampling locations

3 Particle Size Distribution of Sliding Zone Soils

Particle size distribution of sliding zone soil samples 1 and 2 are tested by sieving method. The hole sizes of the standard sieve content 20 mm, 10 mm, 5 mm, 2 mm, 1 mm, 0.5 mm, 0.25 mm and 0.075 mm. Gravels larger than 20 mm are not taken into count. Results of sieving tests for samples 1 and 2 are plotted in the following figure 3. Plotting the particle size distribution data on logarithmic coordinate system can obtain following Figure 4.

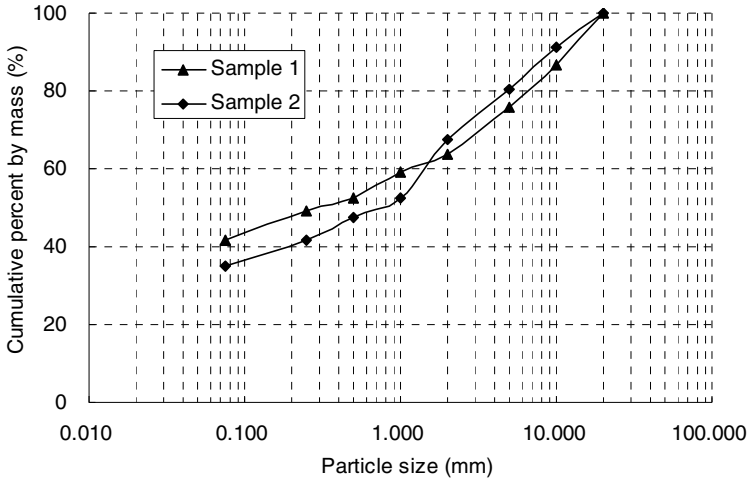


Fig. 3. Particle size distribution curves of sample 1 and 2

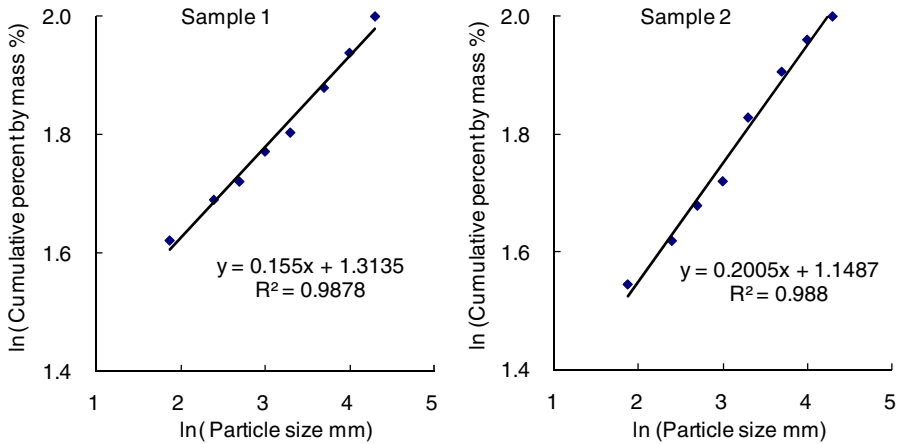


Fig. 4. Particle size distribution data on logarithmic coordinate system

The linear relation of particle mass and size of above samples on logarithmic coordinate system indicate the particle size distribution of sliding zone soil samples have fractal characteristic. The particle size distribution of soils can be quantitatively expressed by particle mass – particle size fractal dimensions. Tyler et al. [6] derived a

following particle mass – particle size fractal model under the assumption that the soils particles density are similar.

$$\frac{M(r < R)}{M_T} = \left(\frac{R}{R_L} \right)^{3-D} \quad (1)$$

where $M(r < R)$ is the total mass of soil particles with the size smaller than R ; M_T is the total mass of soil sample; R_L is the largest particle size, D is the particle mass – particle size fractal dimension.

On the base of above model, the particle mass – size fractal dimension of sample 1 and 2 can be calculated as 2.845 and 2.800. Larger fractal dimension value indicates the soils content more small particles and less large particles.

4 Shape Characteristics of the Coarse Particle

In the engineering practice, the shapes of soil particles are commonly described qualitatively by adjectives such as spherical, block, sheet and so on. Kaye [7] studied the profiles of different kinds of small particles by fractal theory. The study results indicate the profiles of the particles also have fractal characteristics. The pseplicity of particles can be quantitatively expressed by profile fractal dimension. Box counting method [7] is employed to calculate the fractal dimension of sliding zone samples. The profile fractal dimension based on box counting method is defined as following equation 2.

$$D = -\lim_{r \rightarrow 0} \frac{\ln N(r)}{\ln r} \quad (2)$$

where D is the fractal dimension of profile; $N(r)$ is the number of boxes that can fully cover the profile of the particle; r is the side length of boxes used to cover the profile of the particle.

Fig.5 shows the magnified photos of coarse particles in different size ranges from sample 1. Choosing and digitizing 10 particles from each size range randomly can obtain typical profiles of particles shows in figure 6. The fractal dimension of each typical profile is calculated by box counting method and shows in table 1. Calculation results indicate the fractal dimensions decrease with decreasing the particle size.

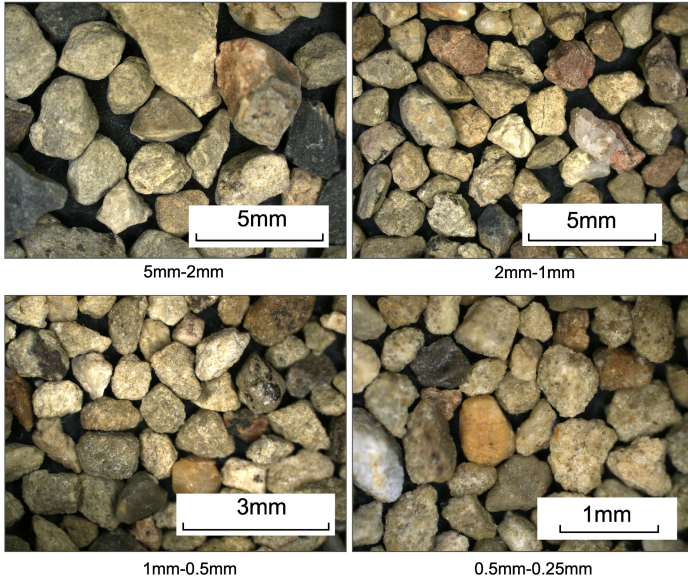


Fig. 5. Magnified photos of coarse particles

5mm-2mm										
2mm-1mm										
1mm-0.5mm										
0.5mm-0.25mm										

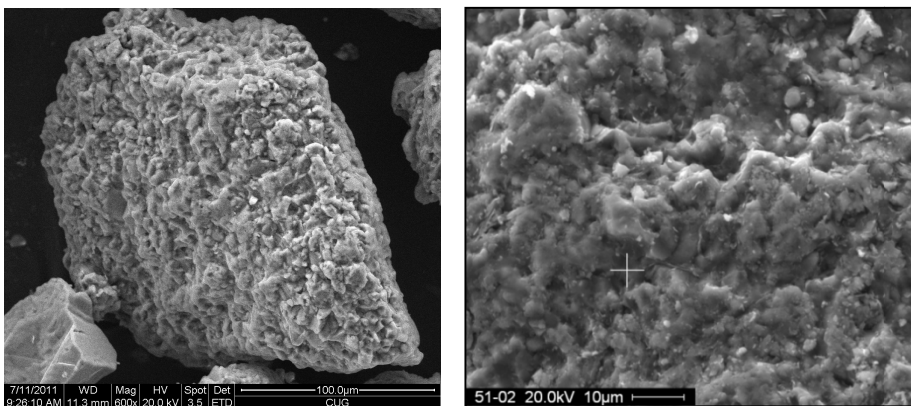
Fig. 6. Typical profiles of particles

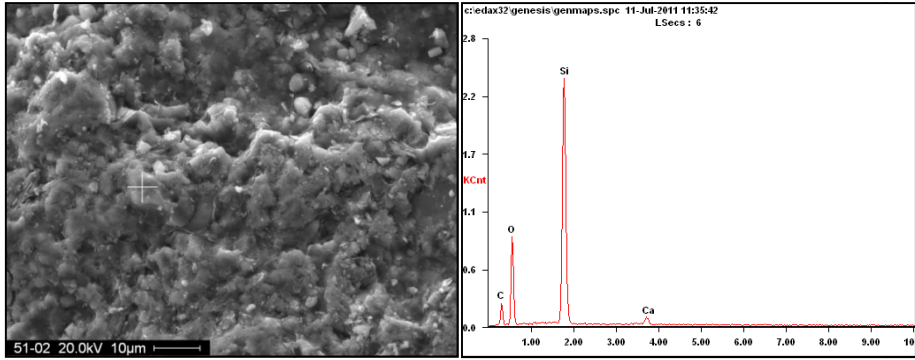
Table 1. Fractal dimensions of each typical profile

Samples	Particle size	5mm–2mm	2mm–1mm	1mm–0.5mm	0.5mm–0.25mm
1		1.0402	1.0345	1.0079	1.0052
2		1.0252	1.0154	1.0177	1.0172
3		1.0128	1.0455	1.0295	1.0280
4		1.0610	1.0102	1.0196	1.0206
5		1.0239	1.0327	1.0342	1.0158
6		1.0356	1.0131	1.0174	1.0234
7		1.0108	1.0410	1.0292	1.0226
8		1.0291	1.0171	1.0181	1.0235
9		1.0663	1.0309	1.0185	1.0030
10		1.0176	1.0473	1.0308	1.0061
Mean value		1.0323	1.0288	1.0223	1.0165

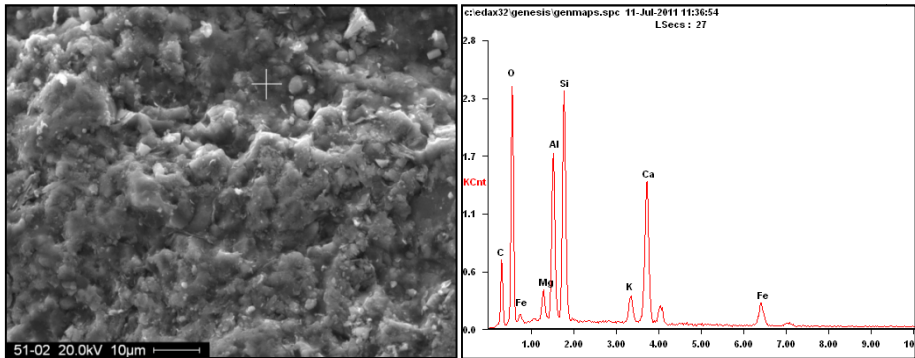
5 Surface Characteristics of the Coarse Particle

Since the scanning electron microscopy (SEM) is imported into geology field, it is widely used to study the micro surface characteristics of soil and rock particles and their forming environment [8, 9, 10]. SEM is employed to observe and capture the micro pictures of the surface of coarse particle in sliding zone samples of Huangtupo landslide. This device can not only be used to observe the microstructure, but also can test the element content of the micro targets though Energy disperse spectroscopy. After the preliminary classification, the original rocks of coarse particles in sliding zones of Huangtupo landslide are mainly pelitic limestone and pelitic siltstone.

**Fig. 7.** SEM photos of typical pelitic siltstone particle



Element	Wt%	At%
C K	30.79	42.81
O K	36.37	37.96
SiK	31.16	18.53
CaK	01.68	00.70



Element	Wt%	At%
C K	24.17	36.48
O K	37.20	42.16
MgK	01.74	01.30
AlK	08.07	05.42
SiK	11.23	07.25
K K	01.86	00.86
CaK	11.06	05.00
FeK	04.67	01.51

Fig. 8. Energy disperse spectroscopy test result of typical pelitic siltstone particle

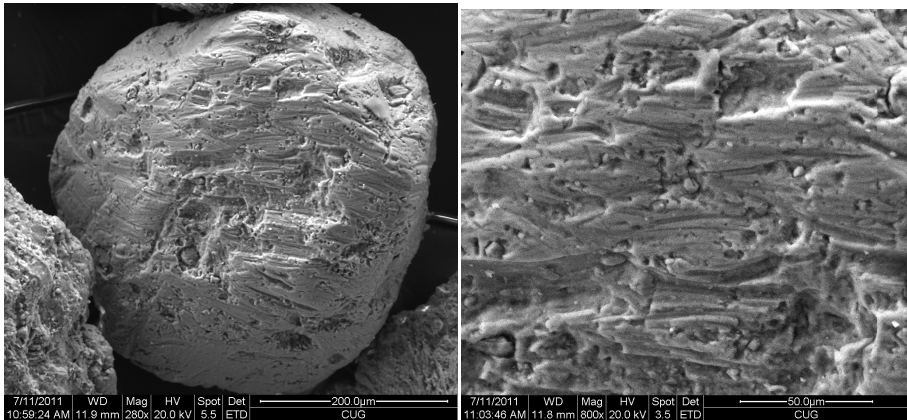
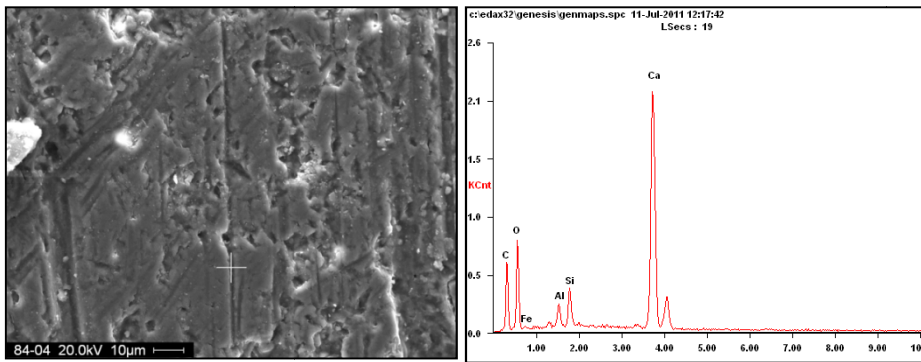


Fig. 9. SEM photos of typical pelitic limestone particle



Element	Wt%	At%
C K	26.83	42.04
O K	32.73	38.50
FeL	04.37	01.47
AlK	01.97	01.37
SiK	02.99	02.00
CaK	31.13	14.62

Fig. 10. Energy disperse spectroscopy test result of typical pelitic limestone particle

Several particle samples of both kinds are selected to implement SEM tests. In order to clean the attachment on the surface of samples, all particles are firstly immersed in distilled water for 24 hours and then boiling for 30 minutes. Figure 7 to 11 are the typical results of SEM and Energy disperse spectroscopy tests for particle samples.

From Figure 7, we can find that the typical pelitic siltstone particle has relative lower psephticity and obvious edges and corners. The surface is rough and full of concaves and convexes. Energy disperse spectroscopy test results shows in figure 8 indicate the element component of concaves are mainly O, Al, Si, K, Ca and Fe, the

element component of convexes are mainly Si and O. So, we can conclude that the convexes of the particle samples are quartz, which has higher hardness and can preserve in the mechanical friction and chemical erosion process during the development of sliding zones. On the contrary, the concaves are mainly pelitic materials with relative lower hardness.

Figure 9 shows the surface characteristics of typical pelitic limestone particles. Compared with pelitic siltstone particles, their pseplicity are relative higher, and the surfaces are smoother. Particularly, the surfaces of pelitic limestone particles develop a lot of linear scratches, which are resulting from the friction during the failure and shearing of sliding zones. Energy disperse spectroscopy test indicates the component of the region near the scratch is mainly O, Fe, Al, Si and Ca, which are typical element of pelitic limestone (Figure 10).

6 Discussion

Particles size distribution is an important structural characteristic for soils. In the sedimentology field, the method that using particles size distribution of sedimentary debris to inverse the original sedimentation environment and geological evolution history of study area is widely used. Different particles size distributions of soils are not only related to the stress history and physical–chemical environment, but also depend on their mineral component and physical–chemical properties. The sliding zone soils, although forms in special environment, are also like this. Generally, the formation of sliding zones of rock slope is the process of the original soft rock fragment into clastic particles. During the original soft rock fragment step by step, particle size decrease and the particle number increase gradually. This process can be regarded as the inverse process of rock formation, which is a typical self-similar iteration process [11, 12]. So, the particle size distribution of sliding zone soils theoretically has fractal characteristics, above results of sieving tests can also support this opinion. According to the rule that the particle mass – size fractal dimension increase as the development of rock fragmentation, the particle mass – size fractal dimension of sliding zone soils can be used as a quantitative analytical index for the evolution of sliding zones. For example, higher particle mass – size fractal dimension indicate longer evolution history or stronger fragmentation.

The profile and surface characteristics of clastic particles are also commonly used in sedimentology field to identify the evolution history of sedimentary environment. The surfaces of clastic particles like the videotape to record their stress history and physical–chemical environment in the geological history. As we know, pseplicity is one of the main parameters to describe the particle shape characteristic. Generally, lower pseplicity indicate the particles have not experience long transport distance or intense friction condition. As the transport distance or friction action increase, the pseplicity of particles increase with the abrasion of edges and corners, the profile of particles also change to round gradually. Because the coarse particles in sliding zones are under the compressive shearing environment, their pseplicity will increase with the continual shearing action. According to this opinion, the profile fractal dimension

of particles in sliding zones can be used as another quantitative analytical index for the evolution of sliding zones. Lower profile fractal dimension indicates higher pseplicity of particles and larger deformation or more intense stress condition of sliding zones. The profile fractal dimensions of coarse particles in sliding zone samples calculated in above section indicate the fractal dimensions decrease with decreasing the particle size, which means small particles have experienced more shearing actions.

The special striated surface characteristics of coarse particles are resulted from the friction during the shearing process of sliding zones, the depth and density of scratches are depending on the intensity of extrusion and shearing force. So, the surface characteristics of coarse particles in sliding zones can be used as a quantitative analytical index for the stress state of the evolution of sliding zones. The extending direction and overlapping situation can also reflect the sliding direction and times.

7 Conclusions

Tests and analysis results indicate that the particle size distribution and shape characteristics of coarse particle samples from sliding zones of Huangtupo landslide have fractal characteristics. The particle size distribution and shape characteristics can be quantitatively expressed by particle mass – particle size fractal dimensions and profile fractal dimension respectively. Considering the failure process and mechanism of the sliding zones in landslide, the mass – size fractal dimension and profile fractal dimension of coarse particles in sliding zones can be used as quantitative analytical indexes for the study on the formation and evolution of sliding zones. Higher particle mass – size fractal dimension indicates the sliding zone soils content more small particles and less large particles, which means the sliding zones experienced longer evolution history or stronger fragmentation. Lower profile fractal dimension indicates the particles have higher pseplicity, which means the sliding zones have experienced larger deformation or more intense stress condition. The profile fractal dimensions decrease with the decreasing of particle size indicates the small particles have experienced more shearing actions. The surface characteristics of coarse particles in sliding zones such as the depth and density of scratches and their overlapping situation can also reflect the stress state and the sliding direction and times of sliding zones.

References

1. Skempton, A.W., Petley, D.: The strength along structural discontinuities in stiff clays. In: Proceedings of the Geotechnical Conference on Shear Strength of Natural Soils and Rocks, Norway, vol. 2, pp. 29–46. Norwegian Geotechnical Institute, Oslo (1967)
2. Wen, B.P., Aydin, A.: Microstructural study of a natural slip zone: quantification and deformation history. *Engineering Geology* 68(3-4), 289–317 (2003)
3. Deng, Q.L., Zhu, Z.Y., Cui, Z.Q., et al.: Mass Rock Creep and Landsliding on the Huangtupo Slope in the Reservoir Area of the Three Gorges Project, Yangtze River. *Engineering Geology* 58(1), 67–83 (2000)

4. Wen, B.P., Chen, H.Y.: Mineral Compositions and Elements Concentrations as Indicators for the Role of Groundwater in the Development of Landslide Slip Zones: a Case Study of Large-scale Landslides in the Three Gorges Area in China. *Earth Science Frontiers* 14(6), 98–106 (2007)
5. Yang, S.S., Chen, H.Y.: Investigation Report of Huangtupo landslide area in Badong County. Hubei Survey and Design Institute for Geohazard Engineering, Hubei Province (2001)
6. Tyler, S.W., Wheatcraft, S.W.: Fractal scaling of soil particle size distributions: analysis and limitations. *Soil Science Society of America Journal* 56(2), 362–369 (1992)
7. Kaye, B.H.: A random walk through fractal dimensions. VCH Publishers, Inc., New York (1989)
8. Krinsley, D.H., Doornkamp, J.C.: Atlas of Quartz Sand Surface Textures. Cambridge University Press, Cambridge (2011)
9. Bull, P.A., Culver, S.J.: An application of scanning electron microscopy to the study of ancient sedimentary rocks from the Saionia Scarp, Sierra Leone. *Palaeogeography, Palaeoclimatology, Palaeoecology* 26, 159–172 (1979)
10. Dowdeswell, J.A.: Scanning electron micrographs of quartz sand grains from cold environments examined using Fourier shape analysis. *Journal of Sedimentary Research* 52(4), 1315–1323 (1982)
11. Turcotte, D.L.: Fractals and fragmentation. *Journal of Geophysical Research* 91(B2), 1921–1926 (1986)
12. Rieu, M., Sposito, G.: Fractal fragmentation, soil porosity, and soil water properties: I. Theory. *Soil Science Society of America Journal* 55(5), 1231–1238 (1991)

Study of a Model Slope Reinforced with Jute

Aniruddha Sengupta and Saurabh Kumar

Department of Civil Engineering, IIT Kharagpur, Kharagpur 721302 India
sengupta@civil.iitkgp.ernet.in,
er.saurabh009@gmail.com

Abstract. This paper presents the results of laboratory model tests and corresponding numerical analyses carried out on a model slope representing an actual embankment, which failed on several occasions after overnight heavy rainfall. A study is performed by reinforcing the slope with thin jute strips of 1 mm diameter. The numerical simulation of the model tests is performed by a commercial program called FLAC. The responses of the model slope with the jute strips are observed under different intensities and duration of rainfall. Significant improvement in the deformation and the factor of safety of the slope is observed both in the numerical analyses and the laboratory experiments when jute strips are utilized as a slope protection measure. The study indicates that the stability of the embankment can be improved significantly at a low cost by reinforcing it with jute strips.

Keywords: Embankment, Physical modelling, Soil reinforcement, Jute strips, Slope failures.

1 Introduction

The repeated failure of the road and the railway embankments in the state of West Bengal in India is the main focus of the present study. Several road and train accidents have occurred in the recent past causing loss of property and human life. Figure 1 shows one such embankment failure adjacent to a highway bridge at a place called Dankuni near Kolkata in West Bengal. In all the cases, the failure occurred after overnight continuous heavy rainfall. The investigating agencies have blamed them on the sudden subsidence of the embankment due to the pore water pressure buildup within the embankment and its foundation [1, 2, 3]. The site inspections in most of the cases revealed formation of several gullies and wet areas on the slope of the embankments by the seepage of the rainwater. This kind of slope failure after prolonged and/or heavy rainfall is not very uncommon throughout the world and several cases have been reported in the literature [4, 5, 6]. But only a very few solutions have been proposed at present on the topic.

One of the major constraints during the rehabilitation of these embankments is that the roadways or the railways located on top of the failed embankments cannot be closed for very long time. The most common remedial measures include construction of filters/drains and rockfill stabilizing berms on the slopes and installation of closely

spaced piles or sheet pile cutoff wall near the toes of the embankment. Besides above traditional methods, inserting piles and soil anchors on the slope [7, 8] have been also found to be effective ways to stabilize a slope. The roadways and the railways have several hundreds of kilometers of susceptible embankment, but these remedial measures have been implemented only at the places of past accidents, not throughout the whole susceptible area due to exorbitant cost associated with them and/or lack of sufficient funding. This has prompted a fresh look at a cheaper but effective alternative remedial measure to prevent embankment slope failures.



Fig. 1. Embankment Failure adjacent to a bridge approach at Dankuni, West Bengal (India)

Jute is a vegetable fiber that is produced from plants in the genus *Corchorus*. It is one of the most affordable natural fibers. The jute fiber comes from the stem and ribbon (outer skin) of the jute plant. The fibers are first extracted by retting. After the retting process, the stripping begins. In the stripping process, non-fibrous matter is scraped off and the fibers from within the jute stem are grabbed. Jute fibers are composed primarily of the plant materials cellulose and lignin. Jute is a rain-fed crop with little need for fertilizer or pesticides. Jute needs a plain alluvial soil and standing water. The suitable climate for growing jute (temperatures from 20°C to 40°C and relative humidity of 70%–80%) is offered by the monsoon climate, during the monsoon season. India is the world's largest producer of jute. In 2011, India produced 2,000,000 tons of jute. Production of jute is concentrated mostly in Indian state of Assam, Bihar, West Bengal and Bangladesh. Beside India and Bangladesh, jute is also produced in China, Vietnam, Myanmar, Thailand, Egypt, Zimbabwe and Uzbekistan. In the past, the utilization of jute fibre, though readily available and cheap, has been limited by its low durability. But recent researches are indicating that

the tensile strength, hydrophobicity and resistance against biological and chemical degradations of jute fibres can be significantly enhanced by proper treatment [9]. Properly treated jute can be utilized in the field for long term benefits.

The objective of this paper is to find out the performance of jute reinforced slope in terms of its stability during different rainfall events. In this connection it may be noted that Grimshaw [10], Yoon [11], Hengchaovanic, and Nilaweera [12] have shown that the roots of small plants like certain shrubs and grasses can act as very good soil reinforcements and planting them on the slopes can enhance stability of the slope. Since no field data are available and field tests are discouraged to avoid difficulties associated with the daily operation of the roadways and the railways, it is decided to perform laboratory model tests and numerical modeling of the slope failure mechanisms occurring within the embankment to assess the effect of rainfall on the embankment with and without jute reinforcement. This paper presents the results of laboratory model tests and the corresponding numerical simulation of the scaled model slope with and without jute reinforcements. The jute fibres utilized in the model study are purchased from the local market.

2 Properties of the Soil and Jute Reinforcement

2.1 Properties of the Test Soil

The test soil used for the model study in the laboratory is obtained from the failed embankment at Dankuni (West Bengal). Besides bag (loose) samples, three undisturbed tube samples from the mid height of the embankment are collected and brought to the laboratory for the determination of their properties. Several standard laboratory tests are performed to determine the properties and the classification of the soil. The laboratory specific gravity tests indicate that the soil has a specific gravity of 2.63. The saturated hydraulic conductivity k_s obtained from the falling head permeability tests is 8.27×10^{-4} cm/s. This value is further used to establish a relationship between the hydraulic conductivity and the suction empirically using Van Genuchten method [13]. The shear strengths of the soil are obtained from the conventional drained direct shear tests. The tests show that the soil has a cohesion (c') of 0.5kPa and an effective internal angle of friction (ϕ') of 25.7° . The grain size distribution of the soil is shown in Figure 2. The sieve analyses indicate that the soil contains 23.77% fines and the rest is sand. The liquid limit and the plasticity index of the fines are 21% and 6.45%, respectively. The UCSC classification of the embankment soil is SM-SC (silty sand). A summary of all the relevant engineering properties of the soil is given in Table 1. The soil-water characteristic curve (SWCC) for the soil is determined by following the standard test method [14, 15] using tensiometers. The soil is first dried and then known amount of water is added to it. Every time, the corresponding suction force measured by a tensiometer is noted down. The procedure is repeated for the different water content of the soil. Figure 3 shows the SWCC curve for the embankment soil.

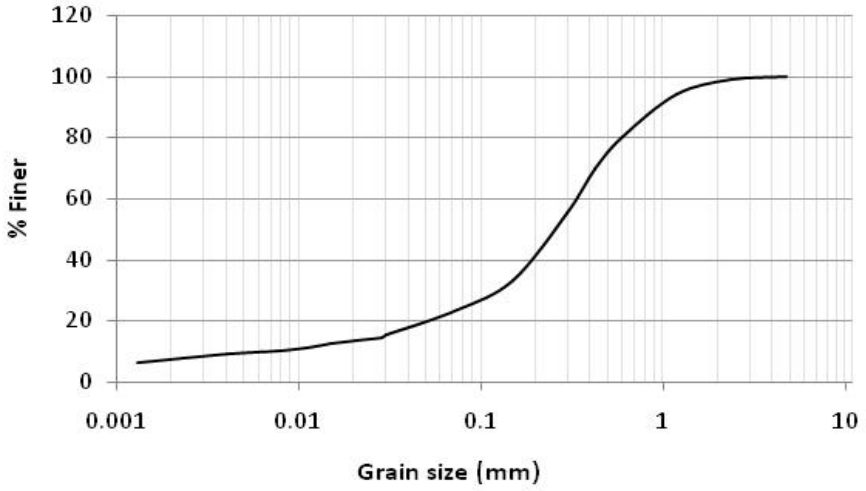


Fig. 2. Grain Size Distribution of the Soil

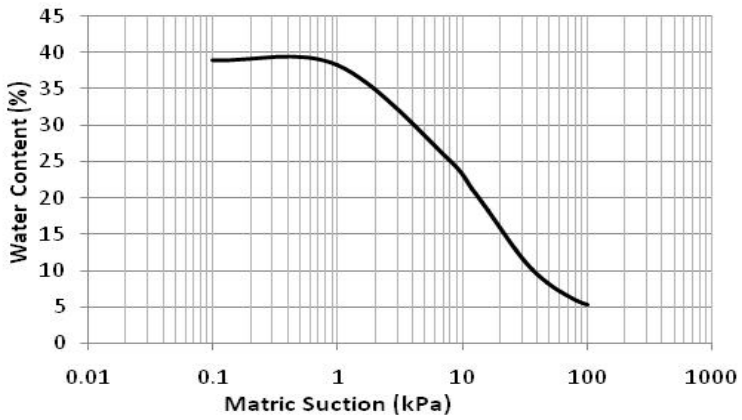


Fig. 3. SWCC Curve of the Soil

Table 1. Material Properties of the Soil

Material Properties	Values
Plastic limit (PL)	14.55%
Liquid limit (LL)	21%
Plasticity index (PI)	6.45%
Soil classification	“ SM-SC ”
Coeff. of permeability, K_{sat} .	8.27×10^{-4} cm/sec
Dry unit weight, γ_{dry}	14.5 kN/m ³
Saturated unit weight, γ_{sat}	18.67 kN/m ³
Cohesion, c'	0.5 kPa
Angle of internal friction, ϕ'	25.7°
Modulus of elasticity, E	5110 kPa
Poisson's ratio, ν	0.25

Table 2. Mechanical Properties of Jute Fibres

Material Parameter	Value
Density, ρ	1.35 gm/cc
Young's Modulus, E	20 GPa
Poisson's ratio, ν	0.38
Shear Modulus, G	7.24 GPa
Tensile Strength, T	393 MPa

2.2 Properties of Jute Reinforcement

Thin jute strips or tassels are considered in the present study for the mitigation of the slope. Each jute tassel consists of a number of jute fibres tied to each other at the top. The jute tassels are of 220mm in length and 10mm in diameter. A total of four such jute tassels are placed along the width of the model slope. The spacing between two jute tassels is 100mm. The typical mechanical properties of the jute fibre produced in

India is adopted from Ahmed and Vijayarangan [16] and given in Table 2. The embedment depth of each jute tassel is 200mm. The cross sectional area, the bond area, and the moment of inertia of each jute tassel are $7.86 \times 10^{-5} \text{ m}^2$, $6.3 \times 10^{-3} \text{ m}^2$, and $4.91 \times 10^{-10} \text{ m}^4$, respectively. The load carrying capacity, the bond skin friction and the bond resistance (bond skin friction \times circumferential area/ spacing \times factor of safety) for each jute tassel are 31kN, 4933kPa and 1033.2kN, respectively for a factor of safety of 1.5.

3 Laboratory Model Tests

3.1 Test Setup

A test setup has been prepared to conduct the model tests in the laboratory. The main components of the test setup are a test tank made up of plexiglass and a supporting steel frame holding the rain simulator on top of the test tank. The test chamber, having inside dimensions of 1.2m \times 1.0m in plan and a height of 0.15m on the front side and 0.80m on the other three sides, is supported directly on two concrete platforms.



Fig. 4. Front View of a Jute Reinforced Slope

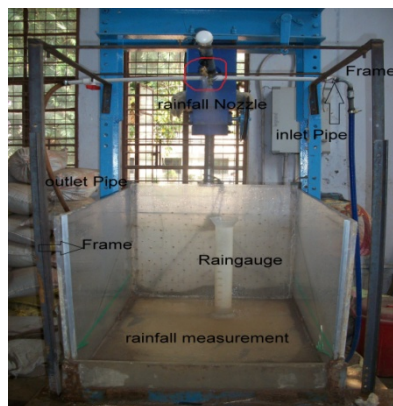


Fig. 5. Rainfall Simulator

The plexiglass walls have a thickness of 16mm. All the joints are glued as well as reinforced with steel angles and the box may be considered to be rigid. Figure 4 shows the laboratory model test setup. A 1:10 scaled model of the actual embankment slope is constructed within the test tank. The embankment slope is constructed with the soil collected from the failed embankment at Dankuni. Due to the symmetry, only one side slope of the embankment is modeled in the laboratory. The slope is prepared in 5 to 6 lifts maintaining a uniform dry unit weight of 14.5kN/m^3 . In the laboratory tests, the 1-g scaling law has been utilized. The grain size distribution, the strengths and the density of the soil are modeled same as in the original embankment. Though the slope of the embankment to be provided depends strongly on the shear strength of the embankment material, a 2(H):1(V) slope is most common for the railway and the road way embankments in India [1,2]. However, the field survey done after the embankment failures indicate that the actual slopes are varying between 1.4:1 and 2:1. Typical height of such embankments is between 2m and 5m. Three slope angles, 1.25(H):1(V), 1.5:1 and 2:1 with a height of 0.4m are considered in the laboratory model tests. The finished surface of the slope is prepared by hand modeling tools. At the bottom of the slope, a 0.15m thick foundation of the same soil is provided. The width of the slope is same as the width of the test tank. In the cases of the model slope reinforced with the rows of jute tassels, holes are first dug at the designated places by inserting a 10mm hollow pipe and then the jute reinforcements are inserted in places. Once the jute reinforcements are in place, the holes are backfilled with the same soil as necessary. Four jute tassels at a spacing of 100mm are considered in a row. A total of four such rows are considered. The spacing between the rows is also kept at 100mm. The first row of jute tassels is placed on the slope at 170mm from the toe. The second row of jute tassels is placed on the slope at 270mm from the toe. The third and fourth rows of jute tassels are placed on the slope at 370mm and 470 mm from the toe. After the construction, the slope is fully saturated by adding water. The front and the back sides of the plexiglass test chamber are double walled with a gap in between. The inner walls (the walls adjacent to the slope) are perforated to allow water in and out of the test tank. The gap between the backside walls is continuously filled with water and it is allowed to percolate into the constructed soil slope within the test chamber. The water coming out of the slope is drained away from the front. The water is supplied to the slope continuously throughout the tests to maintain a steady water level at the toe elevation of the slope as observed in the actual field. During the saturation process and during the tests, the pore water pressure/ suction pressures within the constructed embankment are measured by T5-7 tensiometers. In order to study the behaviour of the slope with and without jute reinforcements during different intensity of rainfall, a rainfall simulator has been installed over the test tank. The rainfall simulator (Fig. 5) consists of a centrifugal pump which pumps water from a reservoir to a network of pipes fitted with spray nozzles. The spray nozzles are located in such a way that the whole slope within the tank gets a uniform rainfall. The pressure of water inside the pipes is controlled by a valve. Thus rainfall of different intensity may be simulated by turning the valve appropriately. A rain gauge is used to measure the rainfall intensity and to calibrate the rainfall simulator before the tests. The tests are conducted at 50mm/hr.,

100mm/hr. and 150mm/hr. rainfall intensities. These rainfall intensities are significantly higher than the recorded historic highest intensity of rainfall of 32mm/hr. in the area [17]. The deformations along the centerline of the slope are measured at 50 mm interval by a Laser Displacement Transducer (LDT). The development of the matric suction at different points within the slope with and without jute reinforcements at different intensities of rainfall are monitored by the digital tensiometers. The progressive failures and the development of cracks within the slope are also observed after different intensities of rainfall.

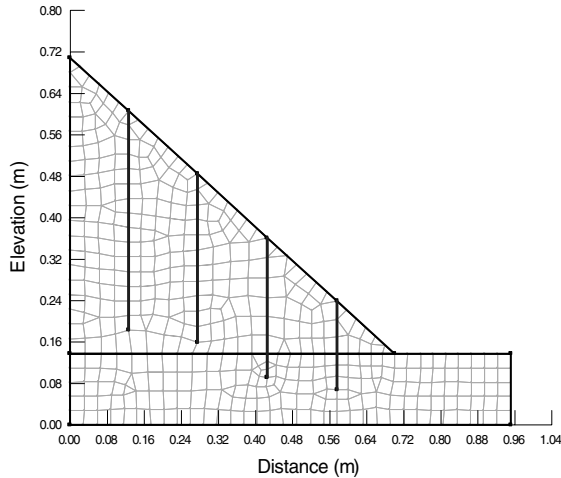


Fig. 6. Modeling of the slope & the Reinforcements

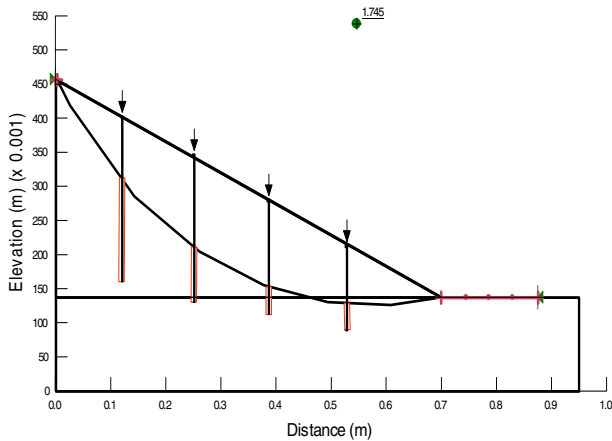


Fig. 7. A Typical Slip Surface

4 Numerical Analysis

The behavior of the scaled model slopes tested in the laboratory is numerically evaluated by a commercial finite element software called GEO-STUDIO [18]. The SEEP/W, SLOPE/W and SIGMA/W modules of the program are utilized to study the behavior of the slope. A plane strain condition is assumed for all the analyses. The soil slope is discretized in the numerical analyses by the standard two dimensional quadrilateral and triangular elements (Fig. 6). The material properties assumed for the soil in the numerical analyses are given in Table 1. The jute reinforcements are modeled as anchor elements (Fig. 6). The anchor elements are one-dimensional axial elements. The anchors can yield in tension or compression, but they cannot sustain a bending moment. The numerical program utilized in this study is two-dimensional; the three-dimensional effect of regularly spaced elements (anchors) is accommodated by scaling their material properties in the out-of-plane direction. The properties of the jute reinforcements are given in Table 2. The boundary conditions in the stress analyses assume that the nodes on all the sides are on roller and the nodes at the bottom are fixed in all directions.

Before the stability analyses of the slope, the initial conditions of the pore-water pressures are obtained by a transient seepage analysis using the SEEP/W program. The result of the transient analysis is then imported into the stability analysis model. The negative pore water pressure distribution within the slope is computed under a given intensity and duration of rainfall. Before the transient seepage analysis is carried out, a steady-state analysis is done to achieve a hydrostatic condition within the slope and the foundation. In the transient analyses, the infiltration rate is determined by dividing the amount of rainfall in an event by the total duration of the rainfall event and applied to the slope boundary as a surface flux. The transient analysis is carried out for the different infiltration rate and the results are recorded at 2.4 hours interval. The transient analysis program, SEEP/W, is formulated on the basis that the flow of water through both saturated and unsaturated soil follows Darcy's law. The Darcy's law is also applied to the flow of water through unsaturated media. The only difference is that under the unsaturated flow condition, the hydraulic conductivity is no longer a constant, but varies with the changes in the water content and indirectly varies with the changes in the pore-water pressure. The general governing differential equation for a two-dimensional seepage is expressed as:

$$\frac{\partial}{\partial x} \left(k_x \frac{\partial H}{\partial x} \right) + \frac{\partial}{\partial y} \left(k_y \frac{\partial H}{\partial y} \right) + Q = \frac{\partial V}{\partial t} \quad (1)$$

where, H = total head, k_x , k_y = hydraulic conductivity in the x and y directions, Q = applied boundary flux, V = volumetric water content, and t = time. This equation states that the difference between the flow (flux) entering and leaving an elemental volume at a point in time is equal to the change in the storage of the soil media.

The program is formulated for the conditions of constant total stress (σ); that is, there is no loading or unloading of the soil mass. It also assumes that the pore-air pressure, u_a , remains constant at an atmospheric pressure during the transient processes. This means that $(\sigma - u_a)$ remains constant and has no effect on the change in the volumetric water content. The changes in the volumetric water content are consequently dependent only on the changes in the $(u_a - u_w)$ stress state variable, and with u_a remaining constant, the change in the volumetric water content is a function of only the pore-water pressure (u_w) changes. As a result, the governing differential equation (Eqn. 1) used in the SEEP/W finite element formulation reduces to the following:

$$\frac{\partial}{\partial x} \left(k_x \frac{\partial H}{\partial x} \right) + \frac{\partial}{\partial y} \left(k_y \frac{\partial H}{\partial y} \right) + Q = m_w \gamma_w \frac{\partial H}{\partial t} \quad (2)$$

where, m_w and γ_w are the slope of the storage curve and the unit weight of water. The SLOPE/W program considers the unsaturated shear strength conditions when the suction pressures exist or the pore-water pressures are negative. The following equation for the shear stress as proposed by Vanapalli, et. al. [19] based on the soil water characteristics curve is utilized in the present study.

$$\tau = c' + (\sigma_n - u_a) \tan \phi' + (u_a - u_w) \left[\left(\frac{\theta_w - \theta_r}{\theta_s - \theta_r} \right) \tan \phi' \right] \quad (3)$$

where, c' = effective cohesion of the soil, σ_n = normal stress, u_a = pore-air pressure, u_w = pore-water pressure, ϕ' = effective friction angle of the soil. In the above equation, θ_w is the volumetric water content, θ_s is the saturated volumetric water content, and θ_r is the volumetric water content at the residual condition. When the water content is at saturation ($\theta_w = \theta_s$), 100% of the suction contributes to the strength. When the water content is at the residual value ($\theta_w = \theta_r$), the suction makes no contribution to the strength. Thus the water content function is used in essence to apportion the suction contribution to the strength. The above equation (Eqn. 3) is used in the present analyses for the computation of the stresses. The above equation is similar to that proposed by Lu, et al. [20, 21]. The factor of safety is then calculated by

$$FS = \frac{\sum \tau_r}{\sum \tau_m} \quad (4)$$

where, $\sum \tau_r$ is the summation of the resisting shear stresses computed from the Mohr-Coulomb equation and the corresponding material parameters. $\sum \tau_m$ is the summation of the mobilized shear stresses.

The slope stability analysis is performed using four well known limit equilibrium methods, that is, Morgenstern & Price method, Janbu's method, ordinary method of slice and Bishop's simplified method [18]. The above limit equilibrium methods are different in how they are handling the four inter-slice forces to make the equilibrium equations determinate. The Morgenstern & Price method allows one to define the relationship between the inter slice forces and satisfies both the force and the moment

equilibrium equations. The Janbu's simplified method assumes the inter slice forces to be horizontal and satisfies the force equilibrium equations only. The ordinary method of slice or Fellenius method assumes no inter-slice forces and satisfies the moment equation only. The Bishop's simplified method assumes the inter slice forces to be horizontal and satisfies only the moment equilibrium condition. In the present analyses, the minimum factor of safety obtained by applying the above four methods is reported for each case. Fig. 7 shows a typical slip surface predicted by the numerical analyses for the case of a jute reinforced model slope.

5 Results and Discussions

The maximum deformations within the three slopes (2:1, 1.5:1 and 1.25:1) under fully saturated condition with and without jute reinforcements as obtained from the laboratory model tests and the numerical analyses are shown in Table 3 below. The laboratory model tests in general show more deformations than the values predicted by the numerical analyses. However the differences between the two are not significant. The results of both, laboratory model tests and numerical analyses, show that the slope deformations reduce significantly with the inclusion of the jute reinforcements in the slope. For 2:1 slope, the maximum deformation reduces from 12.5mm to 4.4mm with the inclusion of four rows of jute reinforcements. For 1.5:1 slope, the deformation reduces from 17.7mm to 9.6mm. For 1.25:1 slope, four rows of jute reinforcements reduce the maximum deformation from 33.8mm to 18.5mm. These reductions in the slope deformation are significant. Figures 8(a) and (b) show the deformations (in the vector form) of the 1.25:1 slope without and with four rows of jute reinforcements from the numerical analyses. The formation of the slip plane is quite prominent in the case of slope without any reinforcement. But for the case of slope with jute reinforcements, the slip plane is not properly forming. The development of the suction pressures within a slope without and with jute reinforcement and their subsequent reduction at different intensities of rainfall are of interest. In the laboratory model tests, the suction pressures at different elevations along the middle of the slope at a depth of 50mm from the surface are measured with the electronic tensiometers. Figure 9 below shows graphically the reduction of the suction pressures measured for a 2:1 unreinforced slope during 50, 100 and 150mm/hr. intensities of rainfall over 30minutes of duration. The experimental results are also compared with those predicted numerically.

In general the suction pressures measured during the tests are higher than those predicted by Geo –slope using Vanapalli, et al s' equation and SWCC curve developed for the same soil. The numerical analyses indicate that the suction pressures reduce to zero after 12mins, 15mins and 24mins of 50mm/hr, 100mm/hr and 150mm/hr rainfall but the model tests show a suction pressure between 5-7kPa remains even after 30minutes of rainfall.

Table 3. Comparison of the Maximum Deformation of the Saturated Slopes obtained from the Numerical Analyses and the Laboratory Model Tests

Slope	Maximum Deformation (mm)							
	Without Jute Reinforcement		With 2-rows of Jute Reinforcements		With 3-rows of Jute Reinforcements		With 4-rows of Jute Reinforcements	
	Exp. Value	Num. value	Exp. Value	Num. value	Exp. Value	Num. value	Exp. Value	Num. value
2:1	12.5	9.8	10.6	7.6	8.5	5.6	4.4	2.3
1.5:1	17.7	14.6	16.6	13.7	13.4	7.8	9.6	4.6
1.25:1	33.8	25.8	29.2	22.4	24.8	14.6	18.5	11.8

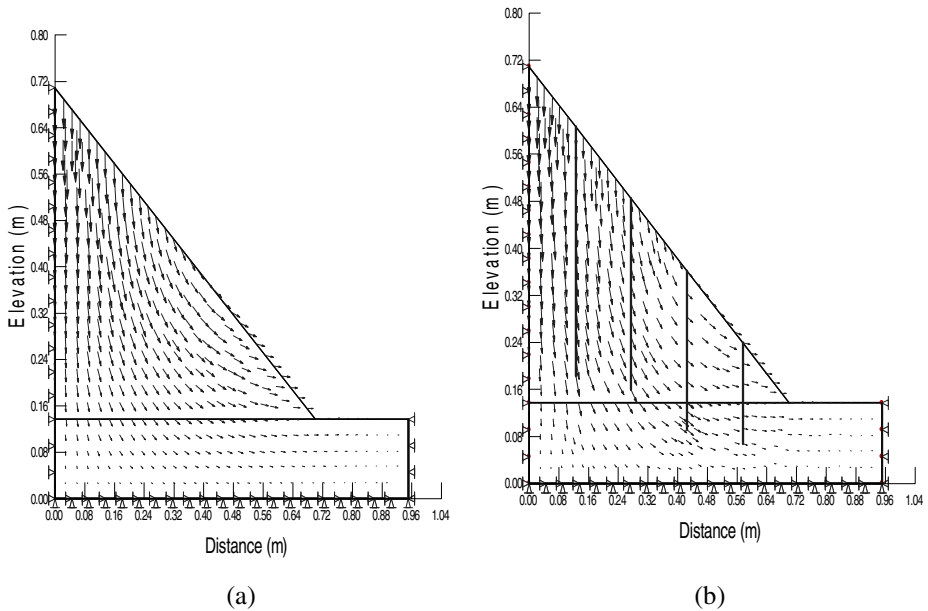


Fig. 8. Deformation Vector of a 1.25:1 Slope obtained from the Numerical Analyses (a) without and (b) with 4-Rows of Jute Reinforcements

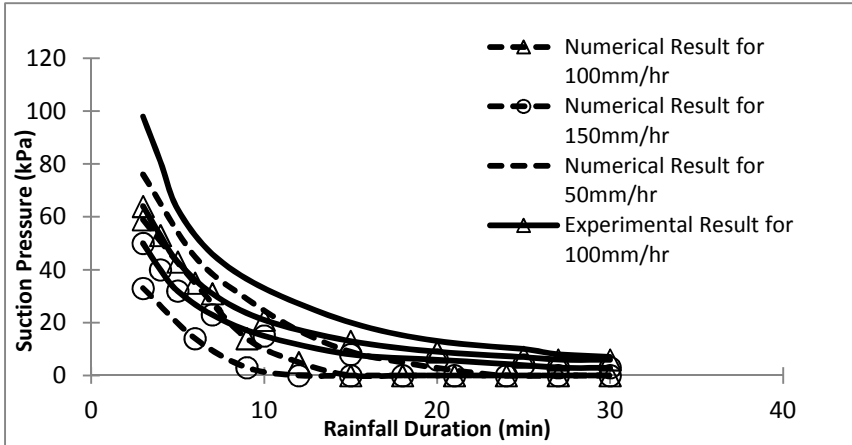


Fig. 9. Suction Pressures in a 2:1 Unreinforced Slope at Different Intensities of Rainfall

Figure 10 shows graphically the reduction of the suction pressures measured for a 2:1 slope with 4-rows of jute reinforcements during 50, 100 and 150mm/hr. intensities of rainfall over 30minutes of duration. The experimental results are also compared with those predicted numerically. In general the suction pressures are higher with 4-rows of jute reinforcement as compared to those for the unreinforced slope. The suction pressures at the end of 30minutes of rainfall are between 10-14kPa for 4-rows of jute reinforced slope corresponding to 5-7kPa for the unreinforced slope. The numerical analyses of 4-rows of jute reinforced slope indicate that the suction pressures reduce to zero after 18, 21 and 30minutes of 50, 100 and 150mm/hr. of rainfall as compared to 12, 15 and 24minutes of 50, 100 and 150mm/hr. rainfall in case of the unreinforced slope. The results clearly show that the jute reinforcements not only reducing the deformation of the slope but also increasing the overall suction pressures within the slope.

Though the deformation of the slope is a very important factor especially for the railway embankments, but these embankments are designed by traditional limit equilibrium methods which are based on stresses, that is, factor of safety approach. The minimum factor of safety requirement for these embankments under a saturated or flooding condition is 1.2 [1, 2]. These embankments are typically not designed to retain water as they remain in moist to dry condition throughout the year except during rainy seasons (July to September). The historical maximum rainfall intensity in this part of the world (lower Gangetic basin) is 32mm/hr [17]. Since the rainfall data are incomplete and not available for sufficient years, the rainfall intensities for this study are very conservatively assumed to be 50mm/hrs, 100mm/hrs and 150mm/hr. The factor of safety for the 2:1 slope for these three rainfall intensities up to a maximum duration of 30 minutes are computed numerically and shown in Fig. 11 below.

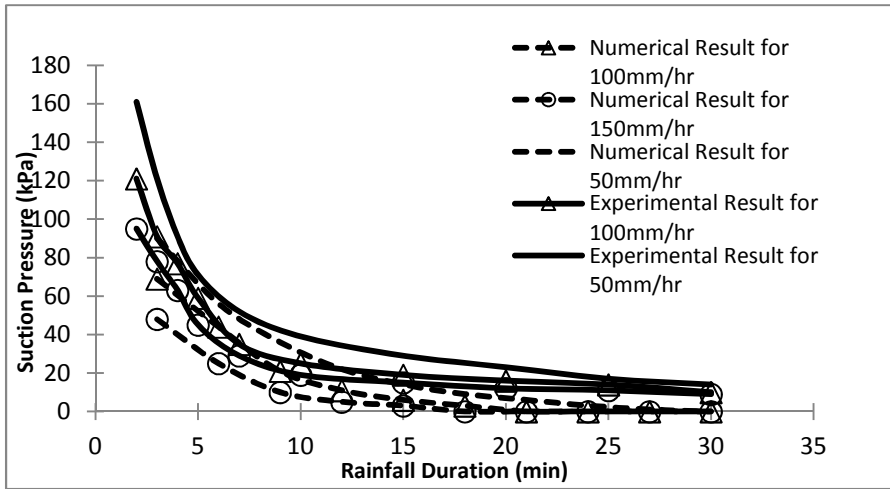
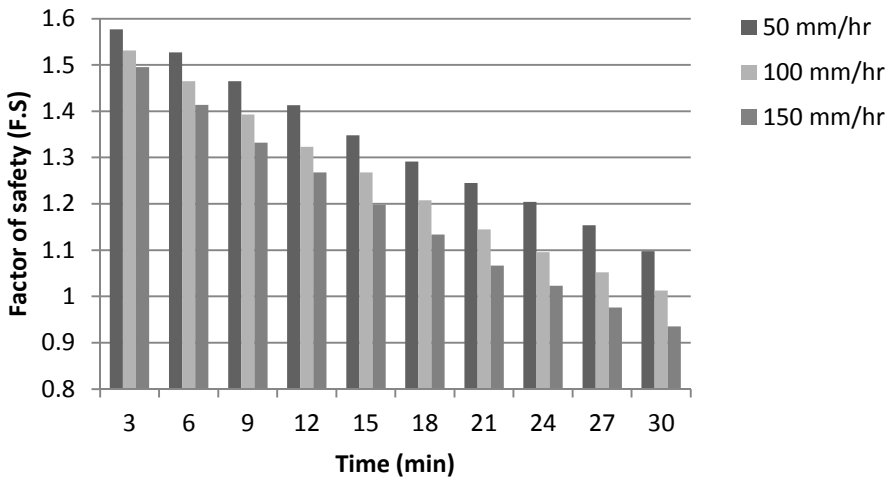


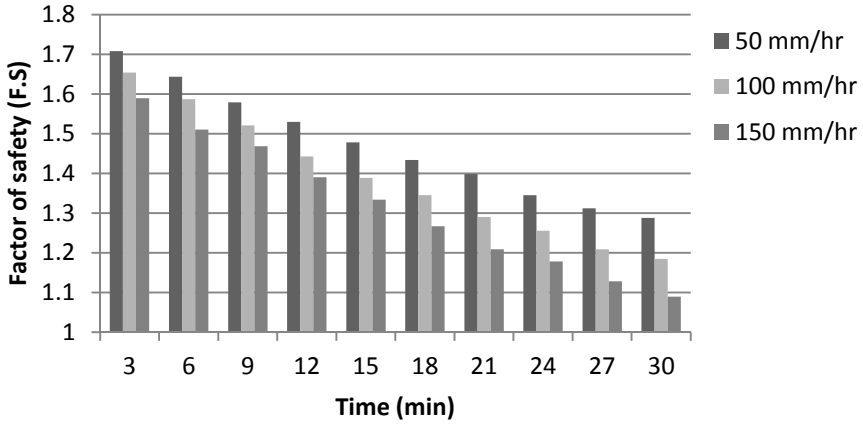
Fig. 10. Suction Pressures in a 2:1 Slope with 4-Rows of Jute Reinforcements at Different Intensities of Rainfall

The theoretical factors of safety of the saturated slopes with and without jute reinforcements are given in Table 4 below. Table 4 shows that a typical 2:1 unreinforced slope is barely stable after 30minutes of 50mm/hr intensity of rainfall. But the same slope reinforced with 4 rows of jute reinforcements will yield a factor of safety of 1.5 even after 30 minutes of continuous 50mm/hr rainfall.

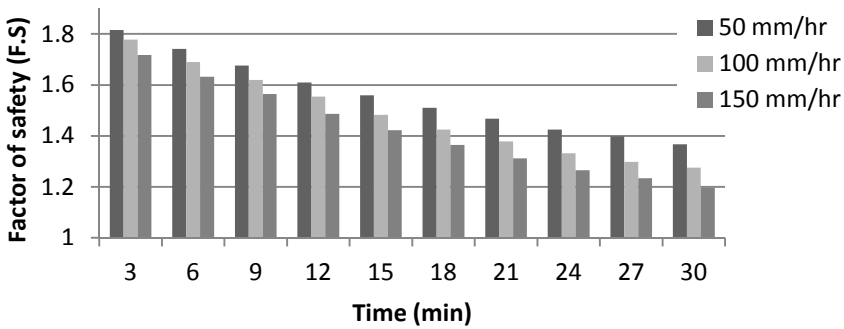


(a)

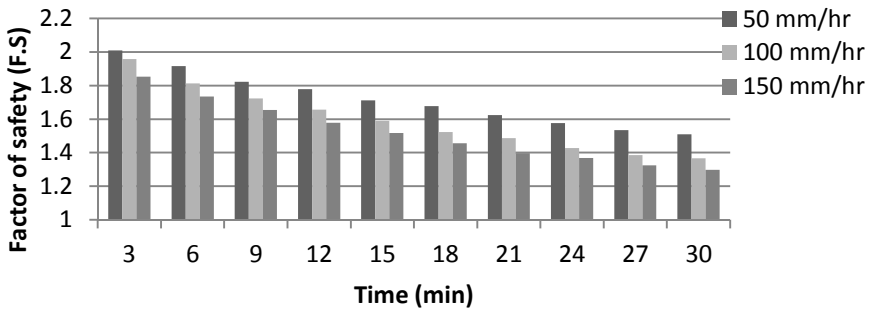
Fig. 11. Factor of Safety of 2:1 Slope for Different Intensity and Duration of Rainfall (a) without Reinforcement, (b) with 2-Rows, (c) with 3-Rows, and (d) with 4-Rows of Jute Reinforcements



(b)



(c)



(d)

Fig. 11. (continued)

Table 4. Variation of the Factor of Safety with respect to the Slope and the Jute Reinforcement

Slope	Factor of Safety			
	Without Jute Reinforcement	With 2-Rows of Jute Reinforcements	With 3-Rows of Jute Reinforcements	With 4-Rows of Jute Reinforcements
2:1	0.973	1.133	1.239	1.336
1.5:1	0.826	0.982	1.106	1.232
1.25:1	0.686	0.775	0.879	1.061

The above table shows that the 1.25:1 saturated slope will not be stable with or without jute reinforcements. The 1.5:1 and 2:1 saturated slopes, though not stable without any jute reinforcements, will meet the minimum factor of safety requirements with 4-rows of jute reinforcements.

6 Conclusions

From all the model tests performed in the laboratory and corresponding numerical analyses, it is clear that the inclusion of the jute reinforcements on a slope significantly reduces the deformation of the slope in a fully saturated condition. The jute tassels act as tensile reinforcements and increase the resistance along the probable slip surfaces. Consequently, the stability of the soil slope is improved.

Both the model tests and the numerical analyses indicate that planting four rows of jute reinforcements on the slope increase the overall suction pressures within a slope and significantly improve the stability of the slope as compared to the slope without and with 2- rows and 3-rows of jute reinforcements.

The deformations of the slope computed by the numerical analyses are found to be reasonably close to those observed in the model tests performed in the laboratory. Both show that the maximum deformation/ settlement may be reduced by more than half by planting four rows of jute reinforcements on the embankment slopes.

The results confirm that the plantation of jute strips or tassels in the slope may significantly improve the slope stability and may be considered as an environment friendly and a low cost slope stabilization measure.

References

1. RDSO: Rehabilitation of Weak Formation between Gour Malda and Malda Town on Malda Division Eastern Railway. Consultancy Report No: GE-20, Geotechnical Engineering Directorate, RDSO, Lucknow, India (1998)
2. RDSO: Rehabilitation of Unstable Formation between Gour Malda and Jamirghata Stations, Malda Division, Eastern Railway. Consultancy Report No. RDSO/2011/GE:CR-0157, Geotechnical Engineering Directorate, RDSO, Lucknow, India (2011)

3. Sengupta, A.: Numerical Study of a Failure of a Wall. *Intl. J. of Geotechnical & Geological Engg.* 30, 1025–1034 (2012)
4. Fowze, J.S.M., Bergado, D.T., Soralump, S., Voottipreux, P.: Rain-triggered landslide hazards and mitigation measures in Thailand: From research to practice. *Journal of Geotextiles and Geomembranes* 30, 50–64 (2012)
5. Au, S.W.C.: Rain-induced slope instability in Hong Kong. *Engineering Geology* 51(1), 1–36 (1998)
6. Fourie, A.B.: Predicting rainfall-induced slope instability. *Proceedings of the Institution of Civil Engineers –Geotechnical Engineering* 119(4), 211–218 (1996)
7. Ausilio, E., Conte, E., Dente, G.: Stability analysis of slopes with piles. *Comput. Geotech.* 28, 591–611 (2001)
8. Rowe, R.K., Poulos, H.G.: A method for predicting the effect of piles on slope behaviour. In: *Proc. 3rd Intl. Conf. on Numerical Methods in Engineering* 3, Aachen (1979)
9. Saha, P., Manna, S., Sen, R.K., Roy, D., Adhikari, B.: Durability of lignocellulosic fibers treated with vegetable oil–phenolic resin. *Carbohydrate Polymers* 87, 1628–1636 (2012)
10. Grimshaw, R.G.: Vetiver grass—its use for slope and structure stabilization under tropical and semitropical conditions. In: *Vegetation and Slopes*, pp. 26–35. Institution of Civil Engineers, London (1994)
11. Yoon, P.K.: Important biological considerations in use of vetiver grass hedge rows (VGHR) for slope protection and stabilization. In: *Proc. Int. Conf. on Vegetation and Slopes*, Oxford, England (1994)
12. Hengchaovanich, D., Nilaweera, N.: An assessment of strength properties of vetiver grass roots in relation to slope stabilization. In: *Proceedings of the First International Conference on Vetiver*, pp. 153–158. Office of the Royal Development Projects Board, Bangkok (1996)
13. Van Genuchten, M.T.: A closed form equation for predicting the hydraulic conductivity of unsaturated soils. *Soil Sci. Soc. Am. J.* 44, 892–898 (1980)
14. ASTM: Standard guide for measuring matric potential in the vadose zone using tensiometers. ASTM Standard D3404-91. American Society of Testing materials, West Conshohoken, PA (2004)
15. Fernando, M.A.M.: Nature of soil–water characteristic curve for plastic soils. *Journal of Geotechnical and Geoenvironmental Engineering (ASCE)* 131(5), 654–661 (2005)
16. Ahmed, K.S., Vijayarangan, S.: Elastic property evaluation of Jute-glass fibre hybrid composite using experimental and CLT approach. *Indian Journal of Engineering and Material Sciences* 13, 435–442 (2006)
17. IMD: Monsoon 2012: A Report. IMD MET Monograph No. 13/2013, Pai, D.S., Bhan, S.C. (eds.) National Climate Centre, Indian Meteorological Department, Government of India, Pune, India (2012)
18. GEO-SLOPE Intl. Ltd.: Seepage Modeling with SEEP/W: An Engineering Methodology. 2007 edition. GEO-SLOPE Intl. Ltd., Calgary (2007)
19. Vanapalli, S.K., Fredlund, D.G., Pufahl, D.E., Clifton, A.W.: Model for the prediction of shear strength with respect to soil suction. *Canadian Geotechnical Journal* 33(3), 379–392 (1996)
20. Lu, N., Wayllace, A., Oh, S.: Infiltration-induced seasonally reactivated instability of a highway embankment near the Eisenhower tunnel, Colorado, USA. *Engineering Geology* 162, 22–32 (2013)
21. Lu, N., Sener-Kaya, B., Wayllace, A., Godt, J.W.: Analysis of rainfall-induced slope instability using a field of local factor of safety. *Water Resources Research* 48, W09524 (2012), doi:10.1029/2012WR011830

Soil Nailing, the Variable Static System of the Future

Michael Auer

J. Krismer Handels GmbH, Rum, Austria
office@krismer.at

Abstract. Every time we build new constructions, changes occur in the natural environment around the project area. The importance of geotechnics in the design and realisation of several protection measures has increased. Many new construction techniques have been developed to realise big projects in and with the construction material named soil. The development of stone columns, the manufacture of big retaining walls and dams of reinforced soil or the so-called Mixed-in-place method can be cited as examples.

An always greater meaning is recently assumed by soft soil nailing in the increase of the stability of natural slopes. Until now the construction standards only poorly considered this construction technique, hence determining the adoption of very different approaches for the calculation of these passive anchors. Because of the continuous increase in the number of soil nailing projects, it is necessary that at least a construction guideline for the construction and the design of passive nails is introduced in the norms. As the writing of the EC7 has not been yet completed, the inclusion of one chapter on soil nailing should not be problematic and would recognise the importance of this intelligent system. The following points should be included in the guideline:

- Maximum admissible horizontal nail spacing in soft soil,
- The nail rows must be placed within a certain vertical offset,
- The determination of the pull-out resistance must be included in the geological report,
- Only experienced companies must be admitted to perform these works,
- A satisfying protection against corrosion must be guaranteed especially at the nail heads,
- The specific boring method for the excavation with the injections method, or the creation of boreholes with the auger or the hammer drill, must be determined depending on the soil type,
- The stability analyses must contain the following points:
 1. Analysis of the global stability,
 2. Analysis of the loads acting along the soil axis and especially at the nail head,
 3. Analysis of the adequate bond length of the nail,

4. Analysis of the deformation,
5. Analysis of the adequate protection against surface erosion

The bearing capacity of soil nailing is a deformation-dependent factor and must be measured consequently. The previous is surely not a comprehensive list of the necessary points to include in such a guideline (and additional suggestions are therefore welcome), but this article should suggest all colleagues, who use this construction method, that the attention on the special issues raised by this variable static system is growing and that a uniform building practice should be established.

Soil Nailing as an Overall System

A statically effective soil nailing is achieved if the sliding body is reduced to a monolith thanks to the closely spaced soil nails. The tensile load resulting from the self-weight of the sliding body, net of the counteraction resulting from the friction along the shear surface, is deviated along the bond length of the soil nails behind the slip surface. The monolithic character of the sliding body is ensured by the limitation of the horizontal offset of the nails. A statement concerning exclusively the GEWI-nails is made in the following.

Soil Nails

Soil nails are a passive integrated construction system for the stabilisation of loose soils. The employment of soil nailing for the provision of adequate stability in embankment construction is convenient with respect to other methods. This method is frequently used in the field of cut slopes in road construction. The installation of soil nails does not normally present problems during construction and the interference with the natural environment of this support system is considerably lower than, for instance, for retaining structures requiring large foundations. Surface shaping can be uncoupled from the stability increase and interpreted as an effective erosion protection and greening technique. Another great advantage of this construction method is that the reinforcements can be constructed already during the slope excavation and their static function is then fully exploited after a sufficient curing time. No provisional support is therefore necessary as, for instance, in case of excavations. Soil nails are inserted with a special boring machine in two different ways. The first possibility is the GEWI-nail which is installed in previously excavated boreholes using spacers. Two flexible tubes along the nail axis distribute the injection material in the cavity around the tension member. A concrete cylinder is formed, which is clearly bounded by the surrounding soil, with a steel reinforcement in the middle, the GEWI-BAR. After careful secondary grouting, the remaining cavities between the soil and the concrete cylinder are occluded. The diameter of the entire nails is clearly recognisable

and remains constant over the whole length, provided that the boreholes are sufficiently stable. On the other hand there are also the so-called injection bore anchors. A hollow cylinder with outer thread is used as steel tension member. A suspension is grouted through this hollow cylinder during the boring process, which rinses and simultaneously supports the cavity. As soon as the necessary boring depth is reached, the resulting hole will be grouted from its bottom. The resulting concrete-soil mix hardens with time and forms an irregular cylindrical body due to the injection method adopted.

This fact is also beneficial to the pull-out resistance of this type of nails. Therefore, this system is mainly adopted in soils with little or no natural short-term shear strength. The final decision on which nail type is to be used in certain ground conditions depends on the characteristics of the subsoil and can only be made in individual cases. The design of soil nailing interventions is based on the same static model for both types of nails. The construction method has only a very limited influence on the static efficiency, provided it meets the technical requirements of the nail manufacturer.

The Soil Nail Static System

Basically, it is always important to keep in mind that a soil nail alone is not effective. Soil nailing is subject to clear geometric limitations. Besides an adequate length of the soil nails, the nail grid and the geometric arrangement of the nail rows is of crucial importance. Only the bearing capacity of the whole soil nailing system can be mobilised. In extensive experiments, the structural behaviour of soil nails was investigated. The outcome of these experiments was that the shallow soil layer on the slope surface supported with soil nails plays only a minor role in the statics of the system, similarly to the case of reinforced soil. It is much more important to provide the soil with a supporting skeleton by the insertion of the concrete cylinder, thanks to which the sliding body can be anchored. The sliding soil mass encloses the soil nails and tries to pull them from the rear stable soil by means of its self-weight.

The nails are primarily aligned in the direction of the tensile forces, as the soil is incapable of carrying the shear load generated by the ground settlement. During the occurrence of this deformation pattern, the friction forces are induced and mobilised between the soil and the soil nail. If the overall length of the nails has been correctly estimated, the friction mobilised along the bond length of the nails in the stable part of the slope is sufficient to prevent the nail pull-out.



Fig. 1. The diameter of the grout is not uniquely defined and can change consistently along the nail axis

Schematische Darstellung des Druckgewölbes bei einer Bodenvernagelung

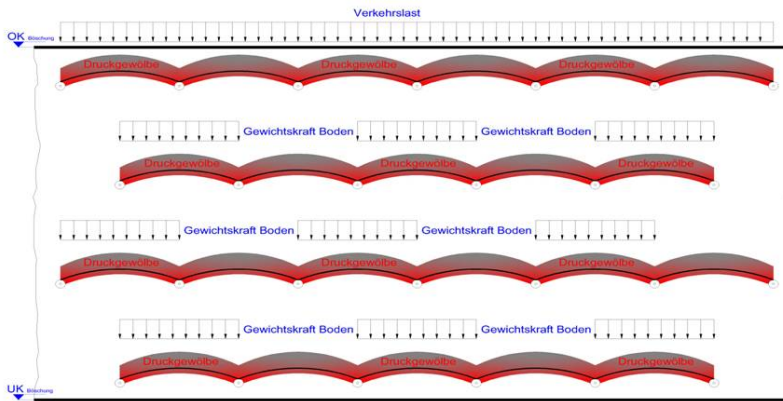


Fig. 2. Schematic display of the pressure arches in the soil nailing

This is the mode of action of an individual nail. However, its range of influence is geometrically very limited. This effect must be subsequently spread over the entire slope, so that the whole manufacture complies with the static requirements. Making use of several soil nails in a geometrically convenient arrangement, the sliding soil forms a monolithic body, which is held by the nails crossing the failure surface and which can serve as a gravity wall or a toe support of a slope.

Passive System Means Deformations

For the mobilisation of the shaft friction a certain slope deformation is necessary. This actually represents the most difficult problem in the correct design of soil nailing.

At first some issues must be clarified:

- Are deformations acceptable and if so, to what extent?
- How large is the impact of these deformations on the surrounding buildings?
- How large is the impact of the soil deformations on its shear parameters?
- What happens if the dilatancy angle is overcome and the ground begins to move?
Is it then still supported by a passive system?

Using an example, it will be explained that under certain conditions a passive soil nailing can be theoretically stable, but the occurring deformations, mobilised by the resisting forces, are too large and incompatible. In the following example a path is cut in the middle of a 38 degree greened slope.

that the deformation occurring before the complete mobilisation of the resistances between soil and soil nails is too large, thus damaging the shotcrete lining. A finite element stability analysis clearly shows that the deformations due to achieve sufficient stability are incompatible with global stability, although in the previous assessment a sufficient stability factor was determined.

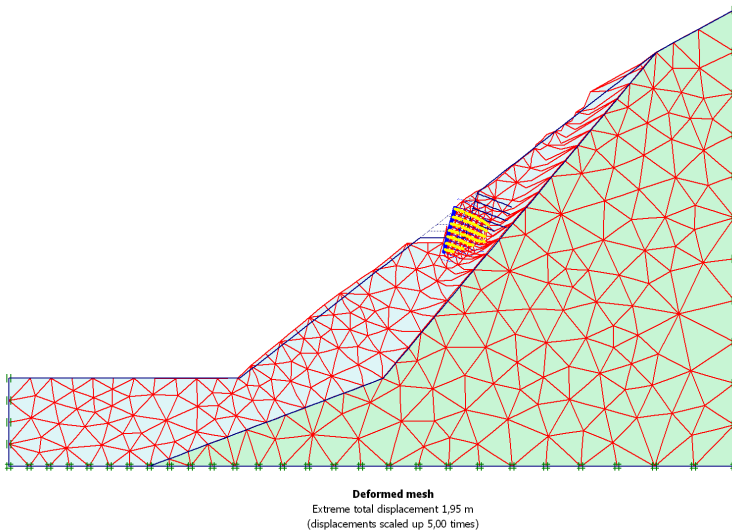


Fig. 6. Over prediction of deformation by finite Elements

The soil parameters are reduced until slope failure occurs and the pull-out resistance of the soil nails is fully mobilised. The factor of safety calculated this way must comply with the requirements of the building codes. In the present case, although the safety factor is about 1.25, slope failure occurs. The occurring deformations are excessively large. A deformation larger than one meter is obtained in the previous analysis at the required value of factor of safety. The height of the range of possible failure initiation is clearly visible in the slope above the protection system. The soil mass loading the system is astonishingly large, if considered over its whole height. Soil deformation lasts as long as equilibrium between the loading and the resisting forces is established. In the present case, soil nails could support the sliding soil mass at a calculated safety factor of about 1.25. However, it requires incompatible soil deformations to fully mobilise the bearing capacity of the soil nails. An alternative solution with passive soil nails is shown in Figure 9. In this variant even the soil portion above the actual construction is reinforced, having the advantage that, since the beginning of the excavation of the cut, no large stresses are transferred to the construction.

The support of the excavation is managed with few reinforcements, although the whole slope is supported with passive nails. Also in the finite element analysis an adequate safety factor is obtained.

In the area of failure initiation, the soil behaves as a monolith due to the closely spaced soil nailing and the sliding of the whole soil mass above the cut is prevented. Therefore, the loads on the reinforcements are reduced and, due the presence of much smaller deformations, equilibrium is established between the loading and resisting forces, as required. It must be also mentioned that, in the variant II, the driving forces require generally large resistances in the reinforcements. Therefore, a construction method comprising exclusively passive soil nails is useless in the present case. In this case, the use of prestressed anchors and appropriately designed wales in the horizontal direction is probably the much more efficient system. The prestress force prevents any ground deformation and is designed according to the load actually occurring at failure. The present example shows how large is the influence on the expected deformations in the reinforcement of otherwise unstable slopes and embankments on the choice of the right reinforcement system.

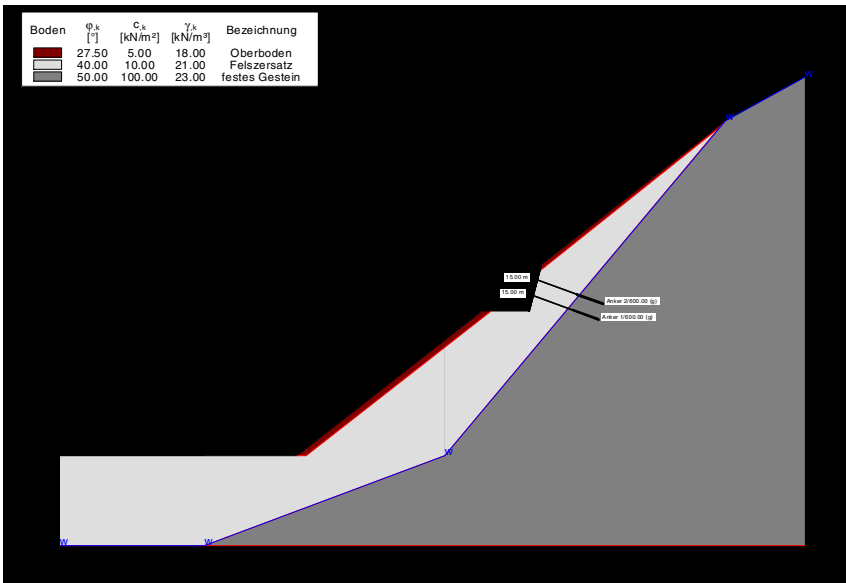


Fig. 9. The most optimized solution by prestressed anchors

There are some types of structures, such as "reinforced soil", in the field of soil and foundation engineering whose effectiveness is determined by the occurring deformations. These structures can be grouped together as the bearing capacity of their reinforcements must be mobilised to work properly. For this reason, the static design

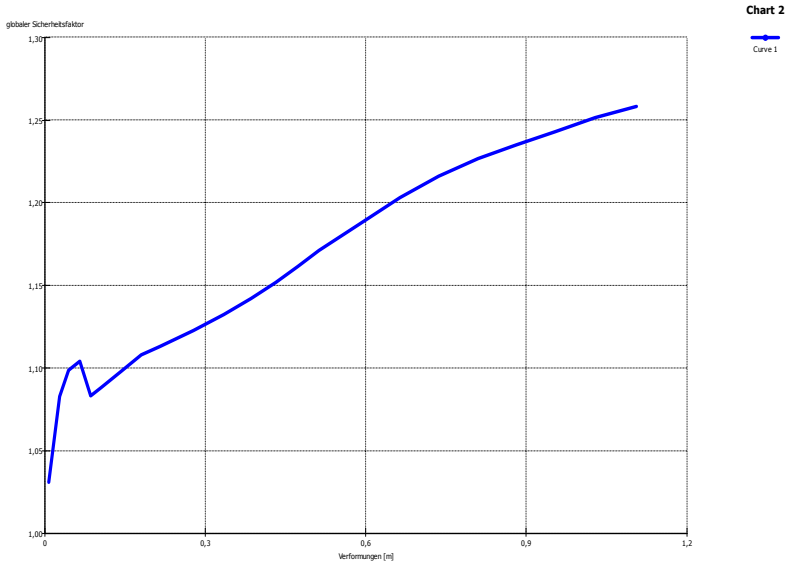


Fig. 10. Change of the safety factor with deformation

of such structures should always include an analysis of the expected deformations. This is especially important when flexible systems are friction-locked to the nail heads at the surface of a slope reinforced with soil nailing.

A second example shows how large is the influence of the choice of the right surface protection on the structural behaviour of the global soil nailing system. Deep cuts into the ground were necessary in this case to build a connection point. These road embankments exhibit some deep weathering traces on the surface and should be protected permanently. In one location of the planned intervention a state of deep soil instability was stated. This location is to be reinforced by soil nailing combined with a net on the surface. The proposed approach is to use soil nails placed in a 2.50 x 2.50 m raster. A high strength steel mesh MW 150 x 85 mm, presenting random orientation and elaborate texture, is used as surface protection.

The mesh is locally friction-locked to the nail heads. An idea can be proposed to reinforce the embankments, which descends from the careful study of the geological reports. To remediate to the inadequate protection against erosion, instead of a steel mesh, a three-dimensional steel grid system might be used.

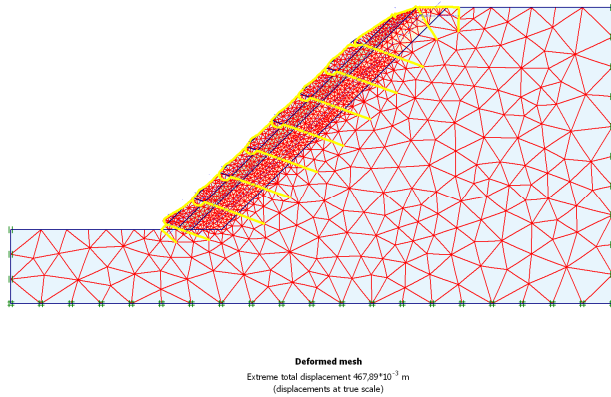


Fig. 11. Protection by a 2-dimensional Net

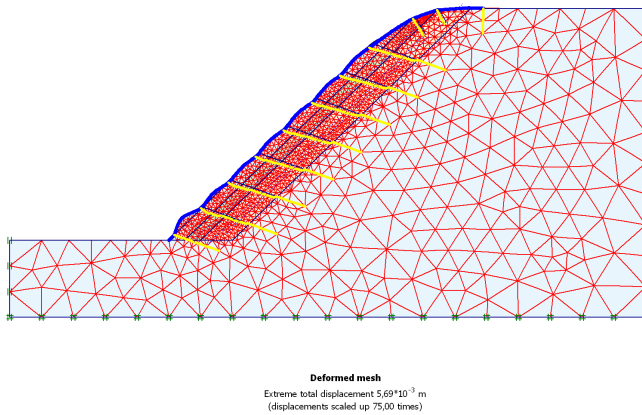


Fig. 12. Protection by a 3-dimensional steel grid system “System Krismer”

From the geological report it can be seen that the expected instability and the associated slope failure are caused mainly by the progressive weathering of the soil. Therefore, this problem cannot be solved by the steel meshes. Another consideration to be made is that a static effective soil nailing must always obey the building codes. Therefore, the nail spacing in the horizontal direction must be reduced to 1.50 m. Based on finite element analyses conducted in a relevant section and within the framework of this static survey, some qualitative statements are made to help increase slope stability thanks to a convenient nail configuration and to the adoption of different solutions at the ground surface.

Soil Condition

In the study area, the slopes have been excavated with an inclination of about 45 degree. The thin-stratified rock emerges from the slope with an inclination below 45 degree. Significant land movements parallel to the slope are observed which are composed of rock slices with different thicknesses. For the following calculations a weathering depth of 3 m is assumed, the soil parameters taking lower values with progressing depth from the ground surface. The shear bond between grout and local soil was estimated by a boundary skin friction t_{Gr} as indicated above, which depends on the soil layers crossed by the soil nails.

Table 1. Geotechnical data of the slope

The following soil stratification is assumed:		
Completely weathered rock:		
	Friction angle:	$\phi = 30^\circ$
	Cohesion	$c = 5 \text{ kN/m}^2$
	Unit weight	$\gamma = 18 \text{ kN/m}^3$
	Limit skin friction	$t_{gr} = 50 \text{ kN/m}^2$
Highly weathered rock:		
	Friction angle:	$\phi = 33^\circ$
	Cohesion:	$c = 10 \text{ kN/m}^2$
	Unit weight:	$\gamma = 19 \text{ kN/m}^3$
	Limit skin friction:	$t_{gr} = 80 \text{ kN/m}^2$
Slightly weathered rock:		
	Friction angle:	$\phi = 35^\circ$
	Cohesion:	$c = 20 \text{ kN/m}^2$
	Unit weight:	$\gamma = 20 \text{ kN/m}^3$
	Limit skin friction:	$t_{gr} = 150 \text{ kN/m}^2$
Hard rock:		
	Friction angle:	$\phi = 50^\circ$
	Cohesion:	$c = 100 \text{ kN/m}^2$
	Unit weight:	$\gamma = 22 \text{ kN/m}^3$
	Limit skin friction:	$t_{gr} = 1 \text{ kN/m}^2$

Stability analyses of such slopes with conventional geotechnical commercial software, in which the friction angles are solely replaced, are not correct. In fact, the mathematical formulation of such software is not suitable for rock slopes. In this case, to be able to assess slope stability, the analyses are to be conducted with the finite element method which provides information on the deformation obtained by iteratively changing the soil properties in an unfavourable way. Furthermore, the influence of the different surface systems on the global stability of the soil nailing system must be investigated. The slope toe is assumed to be completely submerged by water. The unstable area is clearly visible and reflects the local conditions quite accurately.

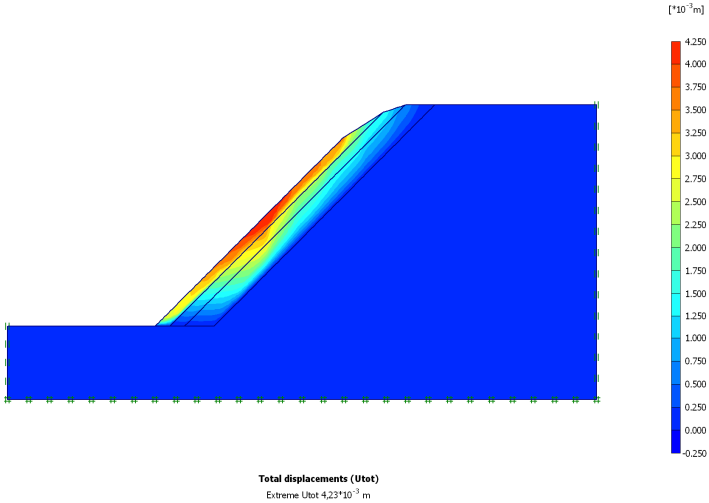


Fig. 13. Picture of the instable area on the slope

The heavily weathered soil layer at the top of the slope tends to slide in the area shown in red (Figure 14). This area must be reinforced with a horizontal nail spacing of 1.5 m. The values of ϕ_0 and c_0 are calculated from the value of M_{sf} and the corresponding input values ϕ' and c' in the finite elements analysis. The values of ϕ' and c' are progressively reduced during the calculation until the serviceability limit state is reached. The safety factor M_{sf} calculated this way must be large enough to meet the following conditions:

$$\phi_0 = \tan^{-1}(\tan\phi'/M_{sf}) \leq \tan^{-1}(\tan \phi / \gamma_\phi) \tag{1}$$

$$c_0 = c'/M_{sf} \leq c/\gamma_c \tag{2}$$

with γ_c and $\gamma_\phi = 1.25$

ϕ and c correspond to the values of the geological report. The graph shows the safety variation with respect to the deformations occurring during each iteration step until a failure condition is reached. The curve shows a monotonic increase of the safety factor with corresponding increase of deformation up to a global safety factor of 2.0. The deformation necessary to reach this safety factor is acceptable. The global long-term stability of these slopes is guaranteed by the present reinforcement system. Due to the three-dimensional nature of the system, the steel grid can be considered rigid. To determine the flexural strength in the three-dimensional steel grid, the moment of inertia of the lower and upper wires were simply approximated by using the Huygens–Steiner theorem. The stiffening effect of the diagonal wires and the layer of gravel serving as drainage were not considered. Figure 16 illustrates the influence of the horizontal nail spacing on the soil nails’ loading. The force distribution along the nail axis is displayed in the Figure. The nails are numbered starting from the second

nail from the bottom and in the upward direction. The nails have a total length of 5 m and penetrate approximately 1.50 m of bedrock. The maximum load occurs in the 5th nail and has a value of 80.57 kN/m, whereas the global factor of safety is 2.0. Since the calculation is always performed for a slope section with a depth of 1 m, this value must be multiplied by the horizontal nail spacing a_h .

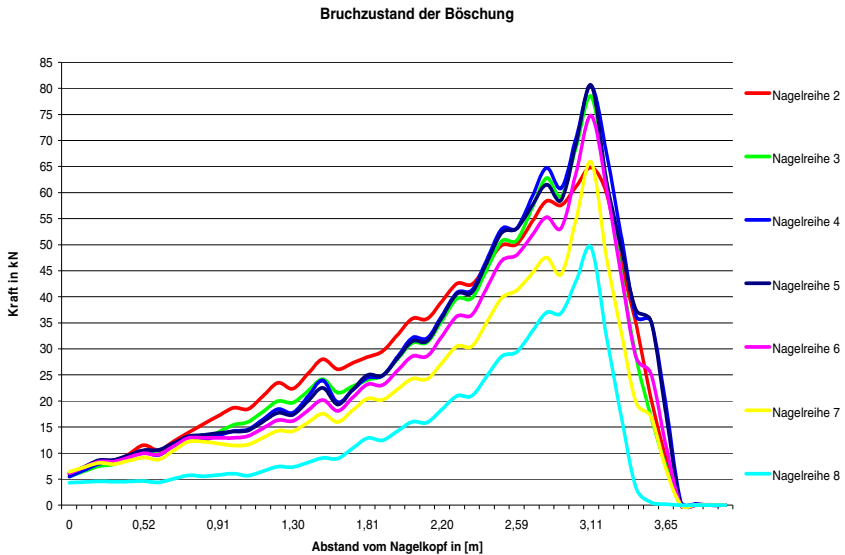


Fig. 14. Tension in the nails from top to the bottom

$$a_h = 1.50 \text{ m} \Rightarrow N_{\text{vorh,max}} = 80.57 \text{ kN/m} \times 1.5 \text{ m} = 120.86 \text{ kN}$$

$$a_h = 2.50 \text{ m} \Rightarrow N_{\text{vorh,max}} = 80.57 \text{ kN/m} \times 2.5 \text{ m} = 201.43 \text{ kN}$$

The fact that this computational model comes very close to reality is also confirmed by the diagram of the tensile stresses recorded in the soil nails. The maximum tensile forces in the individual nails have the same order of magnitude, thus indicating that the sliding events are due to compact ground layers with an orientation parallel to the slope. Therefore, the force is consistently distributed along the soil nails. In the following, the influence of the surface reinforcement on the overall system is described. For this purpose, the calculation is performed at the same section with a flexible wire mesh as ground surface protection. The diagram points out the location of maximum horizontal deformation. The negative sign indicates the direction of the deformation (to the left). It is to stress that the deformations calculated this way take place already at a safety factor of 1.5. Even performing further iterations with largely increased deformations, no higher factor of safety could be achieved.

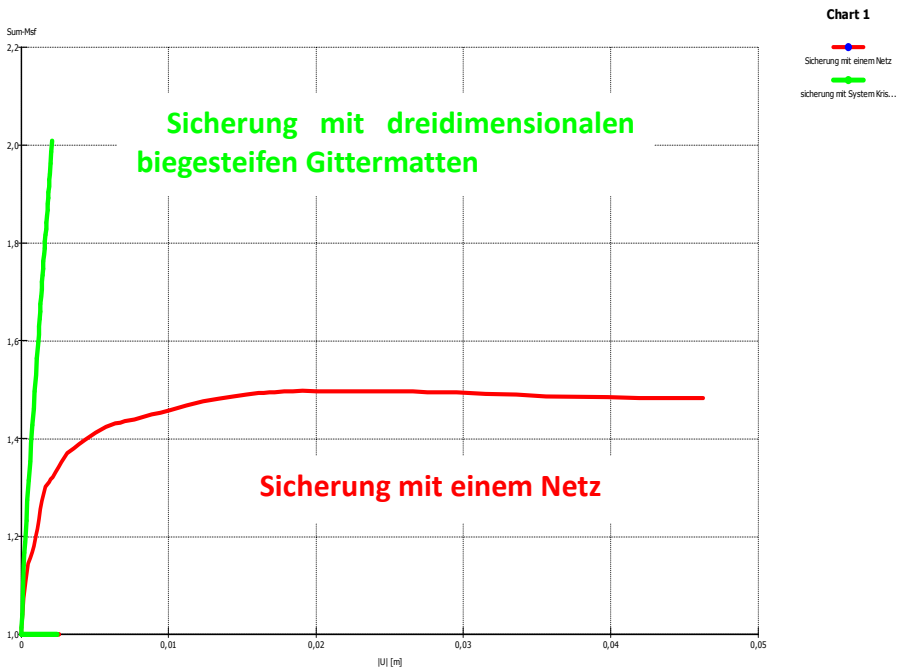


Fig. 15. Change of the safety factor with deformation

The diagram shows the progression of the safety factor with progressing deformation which occurs at each iteration step up to failure in both surface protection systems. Larger deformations occur in the variant with wire mesh lining. At the same time, the safety factor of this variant is lower than that calculated with a rigid, three-dimensional steel grid system. The curve plot of this variant shows a monotonic increase of the safety factor with similarly increasing deformation, up to a global safety factor of 2.0. The deformations needed to reach this safety factor are admissible. The global, long-term stability of these slopes with the present protection system is guaranteed. Due to the three-dimensionality of the protection system, the membrane structure composed by the steel grid can be considered rigid. To determine the flexural strength in the three-dimensional steel grid, the moment of inertia of the lower and upper wires were simply approximated by using the Huygens–Steiner theorem. The stiffening effect of the diagonal wires and the layer of gravel serving as drainage were not considered. A comparison of the two curves illustrates the relationship between the stiffness of the surface lining and the deformation of the sliding body. It should be noted that, in this case, a horizontal nail spacing of more than 1.50 m is not taken into account. A larger spacing would significantly increase the deformation.

Stability Analyses

Similarly to other construction systems in the field of soil and foundation engineering, the bearing capacity of passive soil nails depends on the degree of deformation. It is therefore essential to measure these deformations and to observe their effects on the overall system. These two examples have shown to what extent the global stability of a soil nailing system is dependent on the occurring deformations.

Nail Stability

The pull-out resistance of soil nails is still carried out on the same basis of tensile tests of prestressed anchors. However, these methods involve a source of error. In addition to the requirement that the determination of the pull-out resistance of soil nails be part of the geological report, the choice of appropriate test parameters for soil nails is of great importance. Within the framework of this article, we can only list the most significant features of such a test method.

- The test is performed on nails that are specially prepared for the test.
- The nature of the test is destructive, i.e., the nail should be pulled-out completely.
- The grout length to be investigated must be exactly defined.
- The test load must be the pull-out resistance adopted in the nails' design which depends on grout length of the nail to be tested.
- The counterfort is in the form of a frame with edge length a , which corresponds to the horizontal nail spacing a_h : $a = a_h$.
- The number of nails to be tested depends - in relation to the construction area - on the expected number of different substrates. A certain amount of nails are to be tested for each group in which some of the individual nail forces are subdivided.
- If the calculated values are significantly lower than those adopted in the design, a stability condition must be achieved before the construction project begins.

This is just a list of the main points and does not claim to be complete.

Summary

Soil nailing is a very flexible and easily constructible reinforcement system. It does not preclude any possible design of the natural slope surface and offers the opportunity of stabilizing endangered slopes and hillsides with relatively low economic cost. However, the bearing capacity of soil nailing is limited and an extraordinary effort must be made sometimes to ensure adequate stability. The lack of building codes devoted to this construction method allows currently different approaches to the design of soil nailing, meaning that there are very different solutions for the same problem. This could be avoided in the future thanks to the creation of a guideline for soil nailing that comprises the main design and construction rules. In the future building codes should be sufficient to dedicate a chapter to this construction method, thus eliminating the uncertainties that arise by dealing with soil nailing.

Acknowledgements. The author wishes to acknowledge MEng. Enrico Soranzo for the English translation of the paper.

Author Index

- Acharya, Madhu Sudan 29, 49, 163
Albaba, Adel 95
Alcántara-Ayala, Irasema 179
Auer, Michael 29, 49, 163, 307
- Cabrera, Miguel Angel 57, 141
Chareyre, Bruno 95
- Eichenberger, John 107
- Fern, James 107
Ferrari, Alessio 107
- Gollin, Devis 57
Graeber, Peter-Wolfgang 195
Graf, Frank 29, 163
Guo, Jinxing 195
Guo, Xiaogang 1
- Hasan, Issa 195
Herrmann, Hans J. 131
- Jakubczyk, Aleksandra 11
- Kaitna, Roland 57
Kumar, Saurabh 289
- Laloui, Lyesse 107
Lambert, Stéphane 95
Lehane, Barry Michael 229
Lei, Guoping 211
Leonardi, Alessandro 131
Li, Xia 11
Liu, Qingbing 19, 229
- Marshall, Alec M. 73
Matziaris, Vasileios 73
Mendoza, Miller 131
Meng, Xiannan 119
Murillo-García, Franny Giselle 179
- Nicot, François 95
- Peng, Chong 141
- Qiong, Nie 239
- Salciarini, Diana 253
Sengupta, Aniruddha 289
Shuixiang, Du 239
Soranzo, Enrico 85
Switala, Barbara Maria 163, 265
- Tamagnini, Claudio 253
Tamagnini, Roberto 85, 151, 163
Tang, Huiming 211
te Kamp, Lothar 29, 49, 163
- Wang, Jinge 275
Wang, Shun 19, 275
Wang, Yongqi 119
Wittel, Falk K. 131
Wu, Wei 1, 19, 29, 49, 57, 85, 141, 151, 163, 211, 265
- Xiang, Wei 19, 163, 229, 239, 275
- Yu, Hai-Sui 11, 73